X-ray Spectral Studies and Development of a Polarimeter for Accretion powered Pulsars

Hemanth M

September 04, 2023

X-ray Spectral Studies and Development of a Polarimeter for Accretion powered Pulsars

by

Hemanth M

This dissertation is submitted for the degree of

Doctor of Philosophy

to

Jawaharlal Nehru University

New Delhi, India

Under the supervision of

Supervisor Prof. Biswajit Paul

Co-supervisor Prof. Vikram Rana

Raman Research Institute

CV Raman Avenue, Sadashivanagar

Bengaluru, India

September 04, 2023

Hemanth M
X-ray Spectral Studies and Development of a Polarimeter for Accretion powered Pulsars
Documentation, September 04, 2023
Supervisors: Prof. Biswajit Paul and Prof. Vikram Rana

Raman Research Institute
Department of Astronomy and Astrophysics
CV Raman Avenue, Sadashivanagar
Bengaluru 560 080
Karnataka, India

Declaration

I hereby declare that the work presented in this thesis titled "**X-ray Spectral Studies and Development of a Polarimeter for Accretion powered Pulsars**" is the result of the investigations carried out by me under the supervision of **Prof. Biswajit Paul** and the co-supervision of **Prof. Vikram Rana** at the **Astronomy and Astrophysics Group**, **Raman Research Institute**, **Bengaluru**, **India**. I further declare that the work presented in this thesis has not been submitted for the award of any other degree or diploma of any other University or Institution. Keeping with the general practice, due acknowledgements have been made wherever the work described is based on other investigations. I have also run the thesis through the **Ouriginal** plagiarism software

Bengaluru, September 04, 2023

Hemanth M

Certified by

Prof. Biswajit Paul
Thesis Supervisor

Raman Research Institute
Bengaluru 560 080
Karnataka, India

Prof. Vikram Rana
Thesis Co-supervisor

Raman Research Institute
Bengaluru 560 080
Karnataka, India

Certificate

This is to certify that the dissertation entitled "**X-ray Spectral Studies and Development of a Polarimeter for Accretion powered Pulsars**" submitted by **Hemanth M** for the award of the degree of Doctor of Philosophy to Jawaharlal Nehru University is his original work. This has not been submitted or published for any other degree or qualification to any other university.

Prof. Tarun Souradeep	**Prof. Biswajit Paul**	**Prof. Vikram Rana**
Director	Thesis Supervisor	Thesis Co-supervisor
Raman Research Institute	Raman Research Institute	Raman Research Institute
Bengaluru 560 080	Bengaluru 560 080	Bengaluru 560 080
Karnataka, India	Karnataka, India	Karnataka, India

Acknowledgement

I extend my appreciation to Prof. Biswajit Paul for providing me with diverse problems in the field of X-ray pulsar astronomy to work on and express my gratitude for his professionalism during my PhD journey. I thank Prof. Shiv Sethi for his immense support during the first-year coursework. I am grateful to Prof. Biswajit Paul and Prof. Vikram Rana for introducing me to various data analysis techniques and to the field of X-ray detector development. To the members of the X-ray astronomy lab, including Rishin, Gopalakrshina, Krishnamurthy, Irshad, Harikrishna, Ketan, Manish, Mamatha, Sandhya, Rajagopala, Shreenandini, and Puttaswamy, I extend my sincere appreciation for their valuable assistance with POLIX related activities. I would like to acknowledge and thank my collaborators, including Ashwin, Pragati, Kinjal, Manish, Rahul, Abhishek, and Ajith for their support in the scientific data analysis. I thank Peter Kretschmar, Chandrayee Maitra, Andrea Santangelo, and Paolo Soffitta for hosting me during the international visits. I thank Silpa, Saikat, Tanuman, and Agnibha for the insightful discussions. I am grateful to my mother Lekha K, for financial assistance during times of need. I would like to express my thanks to Manjunath for their assistance in accessing the facilities of the library.

List of publications

1. H. Manikantan, B. Paul, and V. Rana (2023). “An investigation of the ‘10 keV feature’in the spectra of accretion powered X-ray pulsars with NuSTAR”. in: *Monthly Notices of the Royal Astronomical Society* 526.1, pp. 1–28
2. H. Manikantan, B. Paul, K. Roy, and V. Rana (2023). “Changes in the distribution of circum-binary material around the HMXB GX 301-2 during a rapid spin-up episode of the neutron star”. In: *Monthly Notices of the Royal Astronomical Society* 520.1, pp. 1411–1416
3. H. Manikantan, B. Paul, R. Sharma, P. Pradhan, and V. Rana. "Energy dependence of Quasi-periodic oscillations in accreting X-ray pulsars". Submitted to *Monthly Notices of the Royal Astronomical Society*.
4. H. Manikantan, M. Kumar, B. Paul, and V. Rana (2023). “Investigating the orbital evolution of the eccentric HMXB GX 301–2 using long-term X-ray light curves”. In: *Monthly Notices of the Royal Astronomical Society* 527.1, pp. 640–650

Hemanth M	**Prof. Biswajit Paul**	**Prof. Vikram Rana**
Research Scholar	Thesis Supervisor	Thesis Co-supervisor
Raman Research Institute Bengaluru 560 080 Karnataka, India	Raman Research Institute Bengaluru 560 080 Karnataka, India	Raman Research Institute Bengaluru 560 080 Karnataka, India

Bengaluru, September 04, 2023

List of Figures

List of Tables

Synopsis

This thesis reports some characteristics of accreting X-ray pulsars (XRPs) deduced primarily from X-ray spectroscopy and describes in detail some aspects of the development of an X-ray polarimeter instrument. The thesis comprises seven chapters. Chapters 1 and 2 introduce the observed characteristics of XRPs, data analysis techniques, and the astronomical X-ray observatories we utilized to study them. Chapter 3 discusses the observational studies of XRP characteristics near the Neutron star. This includes the work on *'10 keV feature'*. Chapter 4 discusses the studies of Quasi-periodic Oscillations in XRPs and the accretion disk corona in 4U 1822–37. In Chapter 5, the evolution of the extended binary reprocessing environment of GX 301–2 during a long spin-up episode of the pulsar in 2019 and the long-term evolution of the binary orbit of GX 301–2 are discussed. Chapter 6 discusses the development and tests of an X-ray polarimeter POLIX for a dedicated astronomical X-ray polarimetry satellite mission of the Indian Space Research Organization (ISRO). Chapter 7 summarises all the works and discusses related future scopes.

XRPs are binary stellar systems where a rapidly spinning Neutron Star (NS) captures matter from a main-sequence companion by a process called accretion. The gravitational energy lost by accreted matter is emitted as X-ray photons. The strong magnetic fields of the NS and misaligned rotation turn the XRP into a pulsating X-ray source. Having a pulsating X-ray source in a binary orbit with a companion opens up options for studying the physical characteristics, environment, and evolution of binary stellar systems. The properties of the companion stars, like the stellar winds in early-type giants and equatorial disks in Be stars, and the accretion disk could be probed by assessing the X-rays from pulsars reprocessed from these sites (Paul, 2017). The X-rays emitted by galactic pulsars travel through the ISM before reaching the observer, thereby giving information about the constitution and density of the ISM. XRPs are also important as probes of fundamental physics in extreme environments that are not reproducible in a human-built laboratory/facility. The X-ray photons emitted by them carry information on the properties of matter at extremely high temperatures ($\sim 10^{6-7}$ K), magnetic fields (10^{12} G, which is a trillion times that of the earth's surface magnetic field), and extreme gravitational fields. The notable discovery of Cyclotron Resonance Scattering Feature (CRSF) in the observed photon energy spectrum of an XRP (Trümper, Kahabka, et al., 1986) gave

evidence for the quantized cyclotron orbits of electrons in extreme magnetic field conditions near the surface of the neutron star.

Observational studies of XRPs (Chapters 3,4,5)

The vicinity of pulsar (Chapter 3)

XRPs are fuelled by matter from the companion. The accreting matter spirals in, forming concentric rings of varying radii around the NS called the accretion disk. However, the angular momentum of the incoming matter is conserved. The strong surface magnetic field (10^{12} G) of the NS influences the accretion process near the NS, resulting in truncation of the accretion disk. At the distance of a few 1000 km from the NS, the accretion disk is truncated and the accreted matter is channelled towards the NS magnetic poles along the field lines. The fast-flowing accreted matter dumps most of its kinetic energy near the magnetic poles, usually in a region called the accretion column. The photons emitted from the column base are up scattered by the high-velocity ($\sim 0.1c$) infalling matter within the column, resulting in the emission of harder X-rays. The photons escape the accretion column preferentially in the direction of the magnetic field or orthogonal to it, giving a directionality. When the magnetic axis of the pulsar is oblique to its rotation axis, it manifests to the observer as stable, periodically pulsing X-ray photon bunches. The emitted photon spectrum from the XRP accretion column depends on several factors, including the magnetic field strength, the characteristics of incoming plasma, and the accretion rate. On top of this, the XRP emission is reprocessed by matter in the local environment, mostly from the wind and surface of the companion star, and the accretion disk, and absorbed by the metal-rich ISM through which they reach the observer.

The '10 keV' spectral feature in XRPs

The observed photon energy spectra of most XRPs have general characteristics. All of them show a photon distribution having the shape of a powerlaw modified by a high energy cutoff. Many show Cyclotron Resonance Scattering Features (CRSFs), atomic emission lines, absorption by neutral Hydrogen, and soft excess. The physical mechanisms responsible for these spectral features are well established.

A peculiar observed spectral feature that still has no consensus about is a relatively broad spectral feature at 10 keV, known by the name 'The 10 keV feature' (*TKF*). *TKF* appears as a hump/dip/wiggle in the spectrum always at/near 10 keV (Coburn et al., 2002). It is generally modelled with a gaussian absorption/emission or a

combination of the two when it is encountered, but no correlations have been seen on its occurrence. Various observatories have observed this feature in multiple instances of the same source, but not all observations of any given source demonstrate its presence consistently. Additionally, this feature has been observed in sources with distinct accretion and neutron star parameters, and there is currently no known explanation for it. Furthermore, the 10 keV feature has frequently been identified through the combined spectral fitting of data from different instruments, which have a gap in spectral coverage within the 10–15 keV region. To explore the presence of the '10 keV feature' in more detail, we conducted a thorough investigation using *NuSTAR* observations of many accreting X-ray pulsars. *NuSTAR* is an imaging-spectroscopic instrument that provides wide and uninterrupted spectral coverage surrounding the 10 keV region. We analyzed spectra from a total of 58 observations of 30 different sources using a standard continuum model and then scrutinized them for signs of the '10 keV feature'. We found its presence in 16 out of 58 *NuSTAR* observations. It could be fitted with a Gaussian absorption model centred around 10 keV. The details of this study are described in Chapter 3.

The accretion disk (Chapter 4)

A search for Quasi-periodic intensity oscillations

In Roche lobe overflown XRPs, the accretion disk extends from about a few 1000 km radial distance from the NS to the inner Lagrangian point of the binary. The Keplerian orbital frequency of a test particle orbiting a $1.4M_{\odot}$ NS at a distance of a few 1000 km from the NS is of the order of mHz. Interestingly, this is the frequency range at which XRPs exhibit quasi-coherent oscillations in the X-ray intensity (oscillation periods ranging from a few tens of seconds to a few hundred seconds) called Quasi-periodic Oscillations (QPOs). If one generated the Fourier power spectral density (PSD) from the X-ray lightcurve of an XRP, several features could be observed in the PSD. These include the narrow spike at $\nu_{\rm spin}$ corresponding to the NS spin frequency, a continuum (aperiodic variability) originating from the accretion disk, and sometimes, the concentration of Fourier power in a narrow frequency band called the QPO.

We extensively searched 95 archival *NuSTAR* and XMM-*Newton* observations of XRPs. We detected QPOs in 8 observations of 5 sources. QPOs were detected in 4U 1626–67, IGR J19294+1816, V0332+53, Cen X–3 and XTE J1858+034. QPOs in XRPs are generally modelled with the Keplearian Frequency (KFM) and Beat Frequency models (BFM). KFM models QPOs as inhomogeneities in the inner accretion disk periodically absorbing the X-ray photons from NS. BFM models QPOs as periodic modulation in the accretion rate due to inhomogeneities in the inner accretion disk.

The applicability of the models could be tested based on the QPO/spin frequency and photon energy dependence of QPO strength. We found that BFM explains the observed QPO properties in all the detections better than KFM. A related spectral phenomenon of the inner accretion disk is the reprocessed emission from the inner accretion disk, usually called the soft excess. Soft excess is usually modelled with a blackbody of $kT < 1$ keV. In all the sources in which we found the QPO, we analysed the spectrum and constructed the energy dependence of QPO strength. We found soft excess only in 4U 1626–67, where the QPO also shows enhanced strength.

Structure of Accretion Disk Corona in 4U 1822–37

Accretion disk corona (ADC) is a hot dense gaseous region originating from the accretion disk and surrounding the compact object. ADCs are believed to be ubiquitous in X-ray binaries with Blackhole as the compact object, with their observational signatures being hard-powerlaw emission and hard X-ray lags. In XRPs, however, ADC has been observed only in one source, 4U 1822–37. It is an XRP that is viewed edge-on and is therefore expected to exhibit a complete eclipse if the X-ray emission originates from the relatively small region near the NS. However, 4U 1822–37 exhibit partial eclipses, indicating the presence of an extended emission region, hypothesised to be ADC. We analysed the non-simultaneous pointed X-ray observations of 4U 1822–37 from *XMM-Newton* (2001, 2017) and *NuSTAR* (2018) in the combined energy range of 0.5–50 keV. We characterized the partial eclipse profiles of the source in various energy ranges, indicative of the geometry and characteristics of the ADC. We found that the ADC characteristics differ from what has been reported earlier from observations made with *EXOSAT*, *RXTE* and *ASCA* observatories (Hellier and Mason, 1989; Heinz et al., 2001).

The extended binary environment and the binary orbit (Chapter 5)

The reprocessing environment of GX 301–2

GX 301–2 is an HMXB with a Supergiant companion. In addition to the expected transient spin-up/down behaviour, GX 301–2 shows occasional steady spin-up episodes. The occasional spin-up episodes exhibited by GX 301–2 usually happen after a periastron passage and stay for the whole binary orbit. The latest of this was in 2019 when there was a steady two orbits long spin-up episode during which the pulsar spin frequency increased by about 2%. The pulsar flux increased during the episode, making it possible to use data from the All-sky X-ray monitor *MAXI* to look into the reprocessing environment of the pulsar. Using *MAXI* time-resolved spectroscopy, we probed the evolution of the reprocessing environment of GX 301–2 during the spin-up episode. We found a significant deviation in the characteristics

of the reprocessing environment during the spin-up episode in comparison to the long-term average properties.

The orbital evolution of GX 301–2

High Mass X-ray Binaries (HMXBs) are X-ray binaries in which the companion is an early-type massive star ($>$10 $M_{\odot}$). They are assumed to be the young stage of X-ray binaries post a Supernova explosion. The peculiarity of the companions in HMXBs is their mass loss rates of $10^{-(6\text{ to }7)}$ $M_{\odot}$ yr^{-1}, which signifies about $10^6 - 10^7$ yr lifetime for them. Even though the strong stellar wind causes loss of mass from the binary and endorses an orbital expansion, unlike expectations, the measured orbits of $> 90\%$ HMXBs are known to be decaying. This decay in orbit is primarily speculated to be driven by mass transfer between the stars, mass loss from the binary post the compact object interaction and tidal interactions.

Despite the absence of pointed observations of the entire binary orbit, Doroshenko, Santangelo, Suleimanov, et al. 2010 estimated the orbital decay rate of the eccentric HMXB GX 301–2 using pulse time of arrival analysis. However, this method faces challenges due to the pulsar's luminosity-dependent spin-up trend and frequent switches between spin-up and spin-down episodes, which suggest that the pulse period derivative is not constant within an orbit. Fortunately, GX 301–2 has a peculiar characteristic in that it shows an X-ray flare about 1 d before the periastron passage of the NS in every 42 d binary orbit. We employed a different approach, whereby long-term light curves from All-sky X-ray monitors were analyzed to time pre-periastron flare peaks over nearly 30 years. The resulting orbital decay rate was found to be $\dot{P}$ of $= -(1.98 \pm 0.28) \times 10^{-6}$ s s^{-1}, indicating one of the swiftest orbital decays witnessed in an HMXB. This study explores and discusses the potential explanations for the observed decay rate.

Developement of an X-ray polarimeter (Chapter 6)

The astronomical X-ray observatories generally have imaging, timing and spectral capabilities, and have advanced significantly on these capabilities. However, X-ray polarimetry has lagged behind and is still in a rudimentary stage. X-rays from cosmic sources can be polarized due to characteristics such as Synchrotron emission in strong magnetic fields, scattering, etc. *IXPE* polarimeter launched in December 2021 already gave glimpses of surprising polarization measurements in the 2–8 keV energy band in various cosmic X-ray sources. *X-ray Polarimeter Satellite* (*XPoSat*) is an upcoming small satellite mission of the Indian Space Research Organisation (ISRO) dedicated for astronomical X-ray polarimetry. *XPoSat* (Paul, 2022) carries

two scientific payloads; the primary instrument is the Thomson scattering X-ray polarimeter named the Indian X-ray POLarimeter (POLIX), operating in 8–30 keV and the other instrument is a spectroscopy-timing capable instrument named X-ray Spectroscopy and Timing (XSPECT) operating in 0.8–15 keV. POLIX utilizes the property that the angular distribution of Thomson-scattered photons is characterized by their polarization. The linearly polarized photon undergoing Thomson scattering in a material is preferentially scattered in the direction orthogonal to the direction of X-ray polarization. Though other polarimetry techniques exist, Thomson scattering is the most suitable in the 8–30 keV energy range where POLIX will operate.

POLIX uses the combination of a Collimator, a Beryllium scattering block, surrounding proportional counter X-ray detectors and a spinning satellite to fulfil the task. To restrict the field of view of POLIX to a source and thereby restrict the background photons from other parts of the sky, POLIX uses an Aluminium collimator which facilitates a $3^\circ \times 3^\circ$ field of view on the sky. The photons from the source fall into the low *Z* Beryllium scatterer placed below the collimator. The scattered photons are detected using four large Xenon-filled proportional counters surrounding the scatterer. The proportional counter detectors are arranged so the X-ray photon-detecting anode cells sit vertically to the Be scatterer plane. The whole satellite is spun about the viewing axis of POLIX at a modest rate of 0.2 rpm. Each vertical detection element in the proportional counters probes a full azimuthal distribution of scattered photons every 5 minutes. The azimuthal distribution of scattered photons probed by each detector cell is then shifted and added to construct the overall azimuthal photon distribution. If a significant fraction ($B/(2A+B)$) of the photons are linearly polarized with a polarization angle $\phi_{\rm pol}$, then the azimuthal distribution of photons will take the form:

$$C(\phi) = A + B\sin^2(\phi - \phi_{\rm pol}) \tag{0.1}$$

Chapter 6 includes the details of fabrication, assembly, gas filling, post-assembly tests and the environmental tests of the POLIX Qualification Model (QM) proportional counters.

The proportional counter fabrication and assembly

POLIX uses four proportional counters, each having twelve X-ray detection cells. Each cell of the proportional counter could be viewed essentially as a gas-filed grounded cylinder with a high voltage (HV) supplied anode wire running along its axis. Each proportional counter has four major mechanical parts: the Detector housing, the Aluminized Mylar window, the Mylar window support plate and

the Wireframe. The cuboid made by the Aluminium detector housing chamber, the aluminium-coated Mylar window, and the window support top plate form an enclosed volume inside which a Wireframe is secured and pressurized with a Xenon-based gas mixture. The Wireframe is designed to divide the proportional counter volume into twelve anode cells and 30 veto cells, each separated by a boundary of grounded cathodes. Since the cell on which the photon has deposited its energy has to be identified, the proportional counters of POLIX should be position-sensitive. High-resistivity Nichrome wire is used for the anode to achieve this position sensitivity. The Wireframe is first secured to the housing using Titanium screws. Then a 50 mum thick Mylar window with two Viton® O-rings, one each on the top and bottom, is sandwiched between the housing and The Mylar support window (or Top plate). The Top plate has openings that facilitate the entry of X-ray photons into the detector chamber through the Mylar window. Fixed on the rear side of the housing is a gas port which can be used for evacuating and filling gas to the detector chamber and then closed shut with an Aluminium button. A total of six proportional counters were assembled for POLIX, of which four are Flight models (FM), and two are Qualification (QM) cum spare Flight models.

Tests and application of the Room Temperature Vulcanizing material

The 12 anodes and 50 anti-anodes in each Wireframe are secured to the frame using a Teflon cylindrical bush. Since 6 of the anodes and all anti-anodes must be separately attached to a pin fixed to the Teflon bush, conducting wires soldered to the pins and connecting two different anodes are required for serial connectivity. However, solder joints are susceptible to breakage during vibration tests and must be reinforced. A prospective material is Room Temperature Vulcanizing (RTV) Silicone, a durable, flexible seal resistant to mechanical/chemical impacts. However, introducing a new material to the detector chamber can contaminate the gas mixture and compromise the detector's performance. The procured RTV was therefore tested in a Qualification model (QM) detector before its application across all detectors. The tests of the impact of the introduction of the RTV material on the detectors were evaluated by monitoring the reduction in gas gain over several weeks. We found that the gas gain was not affected by the introduction of RTV material; hence, it was used during the fabrication of all the Wireframes.

Leak tests and Gas filling

The assembled proportional counters will have to be filled with 800 Torr (1.05 atm) gas mixture of 90% Xenon, 9% Argon and 1% Methane. Due to its high atomic number, Xenon has a large photoelectric absorption cross-section, assisting photon absorption. The secondary electron cloud, however, should drift to the avalanche

region with minimal scattering, for which a low Z Argon gas is mixed. The ions will finally recombine and neutralize the cathode, emitting photons in the process, which can produce stray pulses in the detector. Methane is therefore added as a quench gas. Methane gas molecules have weaker electron affinity, and they can collisionally de-excite the ions or absorb the recombination photons and dissociate into Carbon instead of generating new electron-ion pairs. However, multiple locations in the detector are susceptible to generating leaks during the assembly process, which can reduce the gas pressure inside the detector volume. Therefore, we perform a threefold leak test on each detector: a mass spectrometer leak detector to find and localize leaks, a positive pressure test primarily to expose the Mylar window to space pressure gradient, and the gas port leak test.

Environmental tests of the Qualification model

Environmental tests are performed on the payloads to asses and verify their performance in the harsh launch and in-orbit environments. This section explains the performance of POLIX Qualification models during the vibration tests and Thermal-vacuum tests.

Sinusoidal and random vibration tests were performed on the payload on three axes. Pre-vibration tests and radioactive source data were acquired, and the position ratio histograms and pulse height amplitude histograms were constructed. After vibration, the data was collected and then cross-checked for any anomaly. During the Thermal-vacuum tests, the QM model was exposed to multiple temperature cycles under vacuum. The source data from a mounted X-ray generator was used to verify the detector's performance during various temperature settings. The details of the environmental tests and validation of the detectors using acquired source data are explained.

Hemanth M	**Prof. Biswajit Paul**	**Prof. Vikram Rana**
Research Scholar	Thesis Supervisor	Thesis Co-supervisor
Raman Research Institute	Raman Research Institute	Raman Research Institute
Bengaluru 560 080	Bengaluru 560 080	Bengaluru 560 080
Karnataka, India	Karnataka, India	Karnataka, India

Bengaluru, September 04, 2023

Contents

1 Introduction

Accreting X-ray pulsars (XRPs) are amongst the brightest cosmic X-ray sources with X-ray flux hovering around a few to a few 100s of mCrab (1 crab = 10^{-9} ergs s^{-1} keV^{-1} cm^{-2}). Their bright nature makes them feasible targets for very detailed investigations of individual objects. XRPs are binary stellar systems in which a spinning neutron star (NS) captures matter from a main-sequence companion by the process called accretion. The gravitational potential energy of the accreted matter is the source of energy for the emitted X-ray photons. The X-ray photons emitted by them carry information on the properties of matter at extremely high temperatures ($\sim 10^6$ to 10^7 K), magnetic fields (10^{12} G, which is a trillion times that of the earth's surface magnetic field) and extreme gravitational fields. The notable discovery of Cyclotron Resonance Scattering Feature (CRSF) in the observed photon energy spectrum of an XRP (Trümper, Kahabka, et al., 1986) gave evidence for the quantized cyclotron orbits of electrons in extreme magnetic field conditions near the surface of the Neutron star. Other than their contribution to astrophysics, XRPs are also important as probes of fundamental physics in extreme environments that are not reproducible in a laboratory setting, at least in the near future.

An X-ray detector must be positioned above the Earth's atmosphere to study XRPs or any other cosmic X-ray source. Earth's atmosphere absorbs most cosmic X-rays rendering a ground-based X-ray observatory impossible. The two possibilities that have been exploited are balloon-borne X-ray detectors and instrument onboard satellites. The latter option is highly favoured among the scientific community due to its exceptional pointing stability and capability to conduct prolonged observations. The first of its kind was *Uhuru* (1970) which discovered the first known accretion powered X-ray pulsar Cen X–3 (Giacconi, Gursky, Kellogg, Schreier, et al., 1971) and Her X–1 (Tananbaum et al., 1972). Following *Uhuru*, more than 30 satellite-borne X-ray observatories have flown till now. The astronomical X-ray observatories flown until recently, generally possess imaging, timing and spectral capabilities (Refer Chapter 2). All known physical characteristics of XRPs have been deciphered from analysis of the observed X-ray spectral and timing data.

The widely adopted model for X-ray pulsars is a rotating NS of radius $R_{\rm NS} \sim 10$ km having a strong surface magnetic field of the order of 10^{12} G accreting matter from

the companion star via its stellar wind or Roche lobe overflow (Sturrock, 1971). The magnetic field lines emanate from the poles of the NS. A magnetic boundary surrounding the NS could be defined within which the magnetic pressure is the predominant factor affecting the accretion flow. The expression for radial distance (Alfven radius) to the magnetic boundary (See Fig. 13 of Nagase 1989) for spherical accretion approximation is given by (Frank, King, and Raine, 2002)

$$r_{\rm M} = 5.2 \times 10^8 \ \mu_{30}^{4/7} \dot{M}_{16}^{-2/7} m_{\rm NS}^{-1/7} \ \ {\rm cm} \tag{1.1}$$

where, μ_{30} is the magnetic dipole moment in unit of 10^{30} G cm^3, $\dot{M}_{16}$ is the accretion rate in 10^{16} g s^{-1} and $m_{\rm NS}$ is the mass of NS in units of $M_\odot$. Inside $r_{\rm M}$, the magnetic pressure dominates over the ram pressure of accretion flow, causing the accretion flow to channel along the field lines onto the magnetic poles. The accretion flow (composed of plasma) gains kinetic energy at the expense of gravitational energy as it falls along the field lines and deposits its energy onto the poles. X-rays are emitted near these magnetic poles and the misaligned spin and magnetic axes of the NS manifests as pulsation to the observer. In a simple dipolar approximation, the pulsar can be visualized as a rotating NS with two beams of emission from either pole (See Fig. 1 of Sturrock 1971).

The characteristics of emission from the NS are related to the properties of plasma in strong magnetic fields and radiative processes in action in such magnetised plasma. From a simple blackbody consideration, typical X-ray luminosity ($L_{\rm x}$) and polar cap area of (about 1% of the NS surface area) the effective temperature of X-ray emission at the polar caps is ~ 10 keV (Harding and Lai, 2006). However, the spectra of X-ray pulsars do not generally have the characteristic shape of a blackbody but rather resemble non-thermal emission (White, Swank, et al., 1983). Eddington luminosity demands a critical luminosity beyond which the infalling matter into the NS is blown away due to radiative pressure dominating ram pressure. For a steady spherical accretion rate of $\dot{M}$ into a NS of mass $m_{\rm NS}$ (in units of $M_\odot$) is given by

$$L_{\rm Edd} = 4\pi c G m_{\rm NS} m_p / \sigma_T \approx 10^{38} \ {\rm ergs \ s^{-1}} \tag{1.2}$$

where G is the gravitational constant in CGS units and $\sigma_T = 6.7 \times 10^{-25}$ cm^2 is the Thomson scattering cross-section, m_p is the mass of the proton in g and c is the speed of light in cm s^{-1}. In the case of an XRP, the spherical accretion geometry is replaced with an emission spot of surface area $0.1 \times R_{\rm NS}^2$, and consequently, the Eddington luminosity for spherical accretion ($L_{\rm Edd} \approx 10^{38}$ ergs s^{-1}) gets modified to a critical luminosity $L_{\rm crit} \approx 10^{36}$ erg s^{-1}, beyond which the accreted matter to an XRP is stopped by radiation. Most of the accreting XRPs exhibit X-ray luminosity ($L_{\rm x}$)

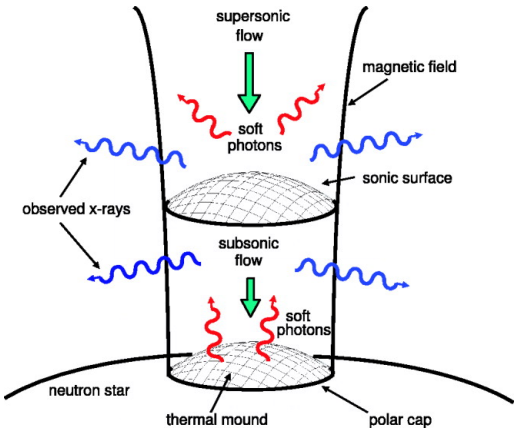

Fig. 1.1: A schematic diagram illustrating the structure of the accretion column. (Fig. credits: Becker et al., 2007)

beyond $L_{\rm crit}$. In such cases of $L_{\rm x} > L_{\rm crit}$, the radiation pressure acting against the infalling matter causes a 'radiative shock' to form several $R_{\rm NS}$ above the NS surface (Harding and Lai, 2006). Within this radiative shock, the kinetic energy of accreted matter is transformed into thermal energy. The hot matter in the shock cools by bremsstrahlung emission, cyclotron emission or Compton scattering, and settles below the shock front onto the NS poles in a thermal mould. The shocked region where the cooling proceeds is hypothesized to have a cylindrical geometry and is called the accretion column (See Fig. 1.1 for an illustration). The photons generated from the thermal mould and the cooling process are also inverse-Compton up-scattered in the accretion column, resulting in the generation of hard (high-energy) X-rays. The generated photons, depending on their polarization state have different scattering cross sections encountered while travelling parallel to or perpendicular to the magnetic fields, which is perpendicular to the NS surface near the poles (Nagase, 1989). The structure of the accretion column and geometry of magnetic fields influence the emission of photons perpendicular to the magnetic field lines (fan beam) or parallel to the magnetic field lines (pencil beam) (White, Swank, et al., 1983). A small fraction of XRPs, however, exhibits $L_{\rm x} << L_{\rm crit}$, where the radiation pressure is not strong enough to produce a radiative shock. In such cases, the Coulomb collisions of infalling protons with the NS atmosphere cause the formation of a Coulomb shock near the NS surface where the accretion impacts, creating a hotspot on the NS that emits X-rays. Such hotspots produce relatively softer (low energy) X-rays compared to the accretion column. Details of the accretion processes near the XRP poles have been discussed extensively in literature (Davidson et al., 1973; Nagase, 1989; Becker et al., 2007).

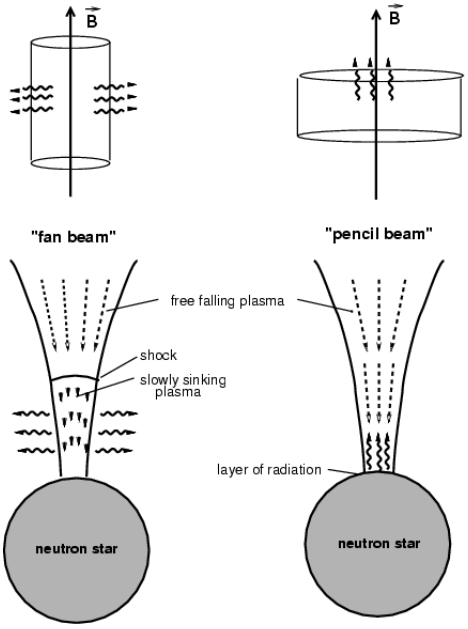

Fig. 1.2: An illustration of different X-ray beaming patterns. (Fig. credits: Schönherr et al., 2007)

Spectroscopy is a data analysis technique often employed to study the emission processes at the NS poles. The observed spectra of the high $L_{\rm x}$ XRPs ($L_{\rm x} > L_{\rm crit}$) are generally represented with a power-law continuum having photon index Γ, modified beyond a high energy cutoff $\rm E_c$ by an exponential decay of the form $\exp[(E - E_c)/E_f]$ (White, Swank, et al., 1983). The high energy cutoff is generally observed above 20 keV. The spectra of low $L_{\rm x}$ XRPs ($L_{\rm x} << L_{\rm crit}$) generally exhibit a two-component spectral structure (Mushtukov, Suleimanov, et al., 2021). Few XRPs (GX 304–1, 1A 0535+036) that exhibit a wider range of X-ray luminosities spanning either side of $L_{\rm crit}$ have exhibited the transition from power-law to the two-component spectral structure when their luminosity drops below $L_{\rm crit}$. Other than the continuum emission, spectroscopy has also revealed the presence of CRSF as a consequence of the strong NS surface magnetic field (Refer Staubert et al., 2019, for a recent review of CRSF in XRPs). Another analysis technique to understand the properties of the emission from NS poles is the pulsations themselves. The spin periods of XRPs are observed to vary from a few seconds (~ 1.24 s of Her X–1) to ~ 2.8 hr of 4U 0114+65. The shape of X-ray pulse profiles, which are constructed by X-ray timing techniques (Refer Chapter 2), indicates the emission geometry. The generally regarded axially symmetric fan beam and pencil beam emission mechanisms in X-ray pulsars (Fig. 1.2) show distinct pulse profiles.

The matter funnelled to the NS at the magnetospheric radius $r_{\rm M}$ (eq. 1.1) could get accreted or propelled away depending on whether the Keplerian orbital frequency

at $r_{\rm M}$ is larger or smaller than the NS spin frequency $\nu_{\rm NS}$. For convenience, a widely used representation is the corotation radius $r_{\rm co}$, which is defined as the radial distance from NS at which the Keplerian orbital frequency around the NS becomes equal to $\nu_{\rm NS}$. $r_{\rm co}$ is derived from Keplers's third law as

$$r_{\rm co} = \frac{G m_{\rm NS}}{2\pi\nu_{\rm NS}} \tag{1.3}$$

For $r_{\rm M} > r_{\rm co}$, the NS cannot capture fast spinning matter and due to the centrifugal force, it is expelled without accreting to the poles. This is called the Propeller regime. The opposite is true for $r_{\rm M} < r_{\rm co}$, and it is called the accretion regime. The propeller regime acts as a quiescent state of the source, during which the source is switched off, while the source is visible during the accretion regime as it is actively accreting matter. Either of these phenomena facilitates angular momentum exchange between the accreting matter and the NS, causing the NS to spin faster (spin-up) or slower (spin-down). The torque exerted by accretion on the NS, affecting its spin state, is called the accretion torque. The mode of accretion determines the accretion torque exerted on the NS. A detailed treatment of the accretion torque in different scenarios and the change in spin rate of the NS are given in Rappaport et al. (1977) and Nagase (1989).

The mass of the main sequence companion star in XRPs could be assessed by observing the companion in UV/Optical bands or by determining the dimension of the binary orbit by pulse arrival time delays of the pulsar in its orbit. XRPs are broadly classified into two kinds based on the mass of their companion; Low-mass X-ray binaries (LMXBs) and High-mass X-ray binaries (HMXBs). In LMXBs, the companion star is a main sequence late spectral type, has a mass below 1 $M_\odot$ and accretion to the NS is facilitated via Roche lobe overflow (RLO) through the inner Lagrangian point of the compact binary orbit. Eggleton (1983) gives the expression for approximate Roche lobe radius $R_{\rm L}$ for the companion star of mass $m_{\rm C}$, mass ratio $q = m_{\rm C}/m_{\rm NS}$ and orbital separation a as

$$R_{\rm L} = a\left[\frac{0.49q^{2/3}}{0.6q^{2/3} + \ln(1+q^{1/3})}\right] \tag{1.4}$$

Because RL overflown matter cannot reach the NS without getting rid of its angular momentum, an accretion disk is formed around the NS to facilitate angular momentum exchange (Frank, King, and Raine, 2002). XRPs like 4U 1626-67 ($P_{\rm orb} \sim 42$ min), 4U 1822–37 ($P_{\rm orb} \sim 5.6$ hr) and Her X–1 ($P_{\rm orb} \sim 1.7$ d) fall into this category. The friction between particles in a viscous accretion disk causes the accretion disk to heat up and emit soft X-rays. They are also called disk-fed XRPs. For a fundamental

prescription of the accretion disk, one can refer to the α thin disk (Shakura et al., 1973). However, the NS emission dominates in XRPs and the accretion disk emission is subdued in observations. The evaporation of the inner accretion disk due to the NS irradiation is hypothesized to produce the accretion disk corona (ADC) in the LMXB 4U 1822–37. For sufficiently inclined orbits, the relatively small XRP emission is completely eclipsed by the companion star in a certain orbital phase range. The presence of relatively large bright ADC, however, shows excess emission during the eclipses due to scattered photons. In Chapter 4, we report the temperature structure of the ADC of 4U 1822–37, by characterizing its eclipse profiles.

HMXBs are of two kinds, Sg-HMXBs (wind-fed XRPs) in which the strong stellar wind (mass loss rates of 10^{-4} to 10^{-6} $M_\odot$ yr^{-1}) of a main sequence O/B type companion is captured by the NS in orbit by Bondi-Hoyle accretion (Lewin et al., 1997) and Be-HMXBs in which the dense circumstellar matter of a main sequence Be-type companion star is intercepted by the NS at the periastron in an eccentric orbit. XRPs like GX 301–2 and Vela X–1 are Sg-HMXBs in which the NS is embedded within the strong stellar wind of the companion. The semi-major axis (a) of the binary orbit in which the NS has mass $m_{\rm NS}$ and companion has mass $m_{\rm C}$ could be expressed as a function of the binary orbital period ($P_{\rm orb}$) by Kepler's third law as

$$a = \left[\frac{G(m_{\rm NS} + m_{\rm C})P_{\rm orb}^2}{4\pi^2}\right]^{1/3} \tag{1.5}$$

Some of the Sg-HMXBs having relatively small orbital periods have accretion powered by the RLO instead of the stellar wind because of the compact binary orbit, and subsequent formation of an accretion disk. XRPs like LMC X–4 ($P_{\rm orb} \sim 1.4$ d), Cen X–3 ($P_{\rm orb} \sim 3.1$ d) and SMC X–1 ($P_{\rm orb} \sim 3.9$ d) falls into this category. Be-HMXBs have long eccentric orbits and they show Type-I (normal) or Type-II (giant) outbursts and long quiescent periods (Caballero and Wilms, 2012). Unlike RLO, a persistent accretion disk is not usually formed, but accretion episodes may be facilitated by the formation of transient accretion disks due to interaction between the rotating magnetosphere of the NS and the stellar wind of the companion (Nagase, Hayakawa, et al., 1982). XRPs like XTE J19294+276 and KS 1947+300 are Be-HMXBs. Since LMXBs (RLO) and Sg-HMXBs (strong stellar wind and/or RLO) have stable accretion reservoirs, they are usually persistent while Be-HMXBs are transients. A shred of observational evidence for the presence of accretion disks in XRPs is the Quasi-periodic oscillations (QPOs) exhibited by them (Refer James et al. 2010 and Raman et al. 2021) in both transient as well as the persistent sources. Quasi-periodic oscillations in XRPs are intensity oscillations exhibited at a narrow range of frequencies ($\delta\nu$)

around a central frequency $\nu_{\rm QPO}$ of a few to a few 100 mHz. The difference between pulsations and QPOs is the spread in their observed frequency. While the pulsations are coherent, QPOs are more spread out with $\nu_{\rm QPO}/\delta\nu \lessapprox 5$. Because the accretion disk does not cross the magnetosphere to reach the NS, the inner accretion disk is at a distance $r_{\rm M}$, and mHz QPOs in XRPs are therefore hypothesized to be originating from inhomogeneities in the inner accretion disk from simple Keplearian orbit consideration (eq. 1.5). In Chapter 4, our search for the presence of QPOs in XRPs and their energy-dependent characteristics are described.

The characteristics of companion stars like the mass, temperature, and elemental abundance of the stellar wind could be studied from Optical/UV observations of the companion. Since the emission from NS travels through the binary environment and interstellar medium (ISM) before reaching the observer, absorption by them leaves signatures in the X-ray spectrum. Spectroscopy of the XRP has been successful in probing the characteristics of the binary environment. The radiative transfer equation for a beam of radiation travelling through an absorptive medium is given by

$$I_\nu = I_{\nu 0}\,\exp(-\tau) = I_{\nu 0}\,\exp\left(-\int_0^d \alpha\; dz\right) = I_{\nu 0}\,\exp(-\sigma N) \tag{1.6}$$

I_ν is the observed intensity and $I_{\nu 0}$ is the intensity emitted by the NS, the constituents in the binary environment and inter-stellar medium contributes to attenuation coefficient α via the photoelectric cross-section of each atom σ in cm^2 and a column density of N along the line of sight (LOS) in atoms cm^{-2}, resulting in absorption of the original intensity by the factor $\exp(-\tau)$, τ is called the optical depth. The density of absorbing matter is generally measured in column density N, and for convenience, it is expressed in terms of the count of hydrogen atoms, called the equivalent hydrogen column density N_H. Large absorption column densities (N_H $\sim$10^{23} cm^{-2}) have been observed in Sg-HMXBs due to their strong stellar winds, and they appear as strong soft X-ray absorption. Due to enhanced photoelectric absorption cross section σ at certain frequencies (depending on the element), absorption edges are also observed alongside large N_H (White, Swank, et al., 1983). Another tracer for the circumbinary environment of XRPs is the Kα emission lines from abundant iron atoms in the spectrum that appear around 6.4 keV. The iron Kα emission lines are hypothesized to originate beyond a few $R_{\rm NS}$ which is the binary environment due to reprocessing, because Kα emission from fully ionized plasma in the accreting matter would be close to 7 keV, and then from the NS surface would be largely redshifted (to ~ 5.5 keV). The ionization state of iron atoms in the

reprocessing site could be deduced by probing the central energy of the iron Kα, Lα emission lines and iron absorption edge (Nagase, Hayakawa, et al., 1982). XRPs are not resolvable by imaging and therefore, getting information on the geometry is largely through exploiting indirect techniques like the presence of absorption and atomic lines in the spectrum (Islam and Paul, 2014), time delay of the reprocessed photons with respect to the NS pulsations (Bykov et al., 2021), properties of the reprocessed emission during the eclipse (Aftab et al., 2019) and through polarimetric observations (Tsygankov, Doroshenko, Poutanen, et al., 2022).

Because of the redistribution of matter (and hence angular momentum redistribution) between the binary components, mass loss from the companion, and tidal interaction between the two, the orbits of XRPs are also known to evolve over time. In the evolutionary time scale, LMXBs are old systems and HMXBs are young systems. This is supported by the fact that HMXBs are found in the star-forming spiral arms of Milkyway, while LMXBs are found in the galactic bulge and globular clusters. A generally assumed evolution scenario (Fig. 1.3) is as follows: The massive star in a binary comprising of Zero Age Main Sequence Stars (ZAMS) undergoes Type-II supernova explosion after transferring some of its mass to the companion, with the NS receiving natal kick of ~ 100 km s^{-1}, causing an eccentric orbit. The NS then accretes from the wind of the companion and at this stage, it is an HMXB. Due to the redistribution of angular momentum and tidal interactions, the binary orbit decays and the companion star is able to fill its RL (eq. 1.4) and subsequently overflow. At this stage, it is an LMXB. The low magnetic field fast-spinning millisecond LMXB XRPs are believed to have evolved to their current state due to prolonged accretion of matter, decaying the surface B field and spinning up the NS. For detailed discussion on the evolution of XRPs, the reader is reffered to Tauris et al., 2006.

The presence of coherent pulses from NS is a useful probe to track the binary orbit and its evolution. The time of arrival of the coherent pulses emitted by the XRP is modified by i) the binary orbit and ii) the relative movement between the observer and the XRP, of which (ii) could be predicted and corrected for by the process called *barycentric correction*. Modification to the X-ray pulses by (i) is often exploited to determine the binary parameters of XRPs. For an XRP with spin period P and its higher order derivatives $\dot{P}$, $\ddot{P}$, ..., the time of arrival of the $n_{\rm th}$ pulse is given by

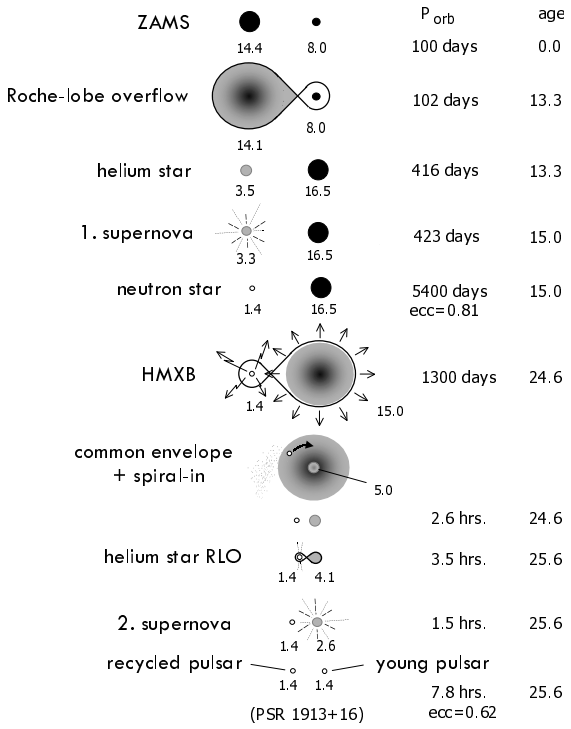

Fig. 1.3: An illustration of the evolutionary phases of an XRP. (Fig. credits: Tauris et al., 2006)

$$t_n = T_0 + \sum_{i=0}^{n} P_i + \frac{a_x \sin i}{c} F(e, \omega, \tau, \theta) \tag{1.7}$$

$$\sum_{i=0}^{n} P_i = nP_0 + \frac{1}{2} n^2 P_0 \dot{P} + \frac{1}{6} n^3 P_0^2 \ddot{P} + \dots$$

P_0 is the spin period at epoch T_0, a_x is the semi-major axis, i is the orbital inclination, e is the eccentricity of the orbit, ω is the longitude of periastron, τ is the time of periastron passage and θ is the mean anomaly. By fitting the function given by eq. 1.7 to the photon time of arrivals, the best fitting binary parameters e, ω, τ, θ could be determined (Raichur et al., 2010a). The binary orbit of XRPs also manifests as orbital intensity modulation (GX 301−2, EXO 2030+375) and eclipses (Her X–1, 4U 1538-52). Such recurring patterns in orbital X-ray intensity profiles are also exploited to derive the binary parameters of XRPs (Islam and Paul, 2016). The evolution of binary parameters so determined is usually found to differ from expectations. For example, Sg-HMXBs have strong mass loss rates of $10^{-(6 \text{ to } 7)}\ M_\odot$ yr^{-1} which suggests an orbital expansion, and unlike expectations, the measured

orbits of most of the HMXBs are known to be decaying. Chapter 5 describes our effort to determine the orbital period decay rate of an HMXB GX 301–2.

The studies mentioned before have exploited the timing and spectral studies to gather insights on XRPs. The X-ray instruments have advanced significantly from the first X-ray observatory, achieving sub-arc min resolution images (*Chandra X-ray Observatory*) through X-ray telescopes, $E/\Delta E \sim 200$ photon energy spectral resolution (XMM-$Newton$/RGS) through Reflection gratings and cooled semiconductors and μs timing resolution (*NICER*). An area under-explored or underdeveloped primarily due to its photon-hungry nature and gradually rising recently is X-ray polarimetry. The NASA-ASI collaborative mission *Imaging X-ray Polarimetry Explorer* (*IXPE*) launched in 2021 has already been providing interesting results in the 2–8 keV energy band and the ISRO mission *X-ray Polarimetry Satellite* (*XPoSat*) described in Chapter 6 operating in 8–30 keV is the next in queue to be launched in second half of 2023. X-ray polarimetry window adds an extra degree of freedom to the study of X-ray sources, the prospects of polarimetry in XRPs are described in Meszaros et al. (1988).

In this thesis, we have utilized the timing and spectral observational data of XRPs to understand some of the properties of individual sources and some properties of XRPs as a whole. The thesis is organized into six chapters. Chapter 2 introduces various X-ray observatories and data analysis techniques that were utilized in this thesis. Chapter 3 discusses a peculiar spectral feature observed in the X-ray pulsars, whose origin is usually attributed to improper modelling of the X-ray emission from NS. Chapter 4 discusses some observational phenomena related to accretion disks, which includes the studies of energy-dependent properties of the Quasi-Periodic Oscillations exhibited XRPs and the structure of accretion disk corona (ADC) in 4U 1822–37. In Chapter 5, the short-term evolution of the binary reprocessing environment and the long-term evolution of the binary orbit of the HMXB GX 301–2 are discussed. Chapter 6 describes the development and some of the tests of the X-ray polarimeter POLIX, which is an instrument onboard *XPoSat*, a dedicated X-ray polarimetry satellite mission of ISRO. Chapter 7 provides a summary of all the works described in this thesis and future scopes.

2 X-ray Observatories and Data Analysis Techniques

Space-based X-ray observatories are inevitable for performing observational X-ray astronomy. The X-ray observatories carry instruments that are capable of detecting X-ray photons and recording their spatial information (imaging), time of arrival (timing), and photon energy (spectroscopy). X-ray detectors work by converting the energy absorbed from an incident X-ray photon into an electrical pulse. Generally, an X-ray detector has photon sensitive area exposed to the patch of the sky having the astrophysical source of interest through collimators, slits or telescopes. A photon absorbed in the sensitive material generates charged carriers. The generated charge carriers are restricted from recombination, and trapped into a Coloumbic well by applying electric fields, and then read out in solid-state detectors, or read out after avalanche multiplication in proportional counters. In scintillation detectors, the X-ray photon incident on a luminescent material produces photons in the visible range, which are collected using photomultiplier tubes (PMTs), and the number of visible photons signifies the energy of the incident X-ray photon. Each detected X-ray photon is called an event. Localization of events for imaging requirements is achieved by segmenting the detector collection area into smaller physical units and distinguishing the events read out from different units. The time of arrival of photons is tagged to each event using an onboard clock, providing timing capability in proportional counters, scintillation detectors, and CdTe/CZT solid-state detectors. In solid-state CCD detectors, the accuracy of time-tagging of events is limited by the charge transfer duration. The amount of primary charge carriers generated by the absorbed photon carries information on the photon energy and hence spectroscopic capability. In this thesis, we also present some work towards the development of detectors that measure the linear polarization of incident X-ray photons, which is discussed in detail in Chapter 6. Usually, the instruments are designed such that they excel in one or more of these capabilities. For example, a large number of photons has to be collected to perform rigorous timing analysis or polarimetry, and hence the detectors in such observatories are made with large geometrical collecting areas (eg: *RXTE*/PCA and *Astrosat*/LAXPC), which results in the increase of background photons and subsequent low signal-to-noise ratio (SNR) spectral data. For spectroscopic requirements, low readout noise Solid State CCDs are preferred, and their smaller

pixel size has the advantage in imaging, however, their low geometric area reduces the amount of photons that can be collected. With the advent of X-ray telescopes, CCD detectors are also improving on photon collection by coupling to the X-ray telescopes. A quantity called *quantum efficiency* (*QE*) is also defined for detectors, which signifies the ratio of photons registered by the detector to the total number of incident photons. A general entity used to express the photon collection capability of an X-ray observatory is its *effective area*, which is the product of the geometric area of the telescope mirror, mirror reflectivity, and the detector quantum efficiency.

In a broad sense, astronomical X-ray observatories could be classified into observatories for pointed observations and All-sky monitors based on the target area of the sky from which it is collecting photons. For pointed observations, the detectors are exposed for long exposures to a small patch of the sky that has the source(s) of interest. All-sky monitors have larger fields of view and they scan the entire sky or a large part of the sky with short exposure detection of small sky patches. Pointed observations give high signal-to-noise ratio observations from a particular point source in the sky, while the all-sky monitors help in the regular monitoring of bright X-ray sources and the detection of transient events like gamma-ray bursts (GRBs), transient X-ray binaries and Active galactic nuclei (AGNs). In this thesis, we have utilized data from pointed observations of XRPs made by the observatories *XMM-Newton*/PN and *NuSTAR* and long-term data from the All-sky monitors *RXTE*/ASM, *Swift*/BAT and *MAXI*/GSC.

It is essential to extract useful science data from the instrument's raw data and this process is called Data Reduction. Some space-based observatories encounter interruptions in their operations, affecting the continuous acquisition of useful scientific data. For example, the detectors are switched off to prevent damage when the observatory passes through dense charged particle regions near the South Atlantic (South Atlantic Anomaly or SAA). The continuous data acquisition is also interrupted when the target source is occluded by the Earth. Therefore, the events recorded by the detector should also be filtered for 'good time intervals' (GTIs). Also, the detectors may exhibit short or long-term changes in their characteristics, which should be corrected while extraction of scientific products. The science products generally contain the timing, spectral, and imaging information of the target source (Refer Sec. 2.2). Data reduction is generally performed at the mission team end for the All-Sky Monitors and at the user end with the latest calibration files for pointed observatories.

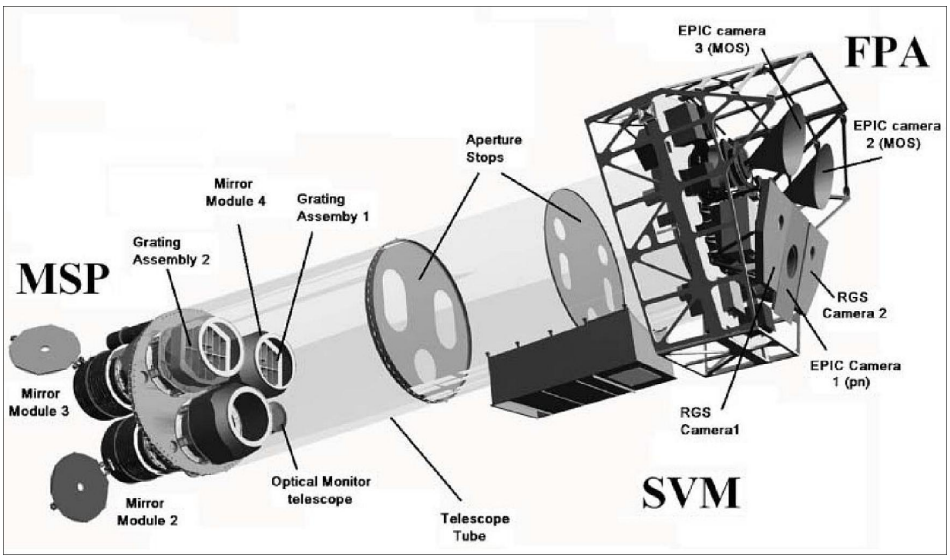

Fig. 2.1: Schematic diagram of *XMM-Newton* observatory. (Fig. credits: ESA/XMM-Newton)

2.1 X-ray Astronomy Missions utilized in this work

2.1.1 X-ray Multi-Mirror Mission (*XMM*-Newton)

The *XMM*-Newton (Jansen et al., 2001) is an X-ray astronomical mission of the European Science Agency (ESA) launched in 1999 and operational as of 2023. The X-ray observatory hosts three Wolter Type I X-ray telescopes focusing the X-rays into three sets of CCD detectors directly and two sets of CCD detectors through Reflection gratings. The peculiar characteristic of *XMM*-Newton is its concentrically nested multiple Wolter Type I mirrors, which aids in improving the number of source photons collected, or an improved effective area. Each telescope carries 58 concentric mirror shells with a focal length of 7.5 m. The XMM-Newton carries four scientific instruments; two sets of EPIC-MOS (0.2–10 keV), EPIC-PN (0.5–10 keV), two sets of RGS (0.33–2.5 keV), and one OM (Optical/UV Monitor) (170-650 nm). The X-ray photons from two telescopes have half of their flux split into two MOS CCDs and two RGS CCD strips, while a single PN CCD array receives interrupted flux from the third mirror. A schematic diagram of the *XMM*-Newton observatory is shown in Fig. 2.1. The observatory is placed in an elliptical high-altitude orbit with apses varying from 6000 km to 115,000 km.

European Photon Imaging Camera - PN (EPIC-PN)

The EPIC-PN instrument collects photons from one of the three telescope modules of *XMM-Newton* and has imaging, timing, and spectroscopic capabilities. The EPIC-PN comprises twelve monolithic 3×1 cm Si CCD wafers arranged in two rows, each having 64×198 pixels. The PSF of the telescope of EPIC-PN is about 13" FWHM. Due to the high satellite orbit altitude, the detectors suffer from solar soft protons background (Read et al., 2003). These energetic protons also get occasionally focused by the optics into the detectors and these events cannot be distinguished from X-ray photons and the data during such episodes are manually removed during the data reduction. The event time tagging accuracy of the EPIC-PN varies from 7 μs to 200 ms depending on the mode of operation of the instrument (by switching off different CCDs and sacrificing event localization to reduce the event processing time). In the Burst mode of operation, the EPIC-PN can operate without pile-up to observe bright sources with a maximum count rate of 60,000 cts s^{-1}. The multi-mirror focusing and unobstructed beam to EPIC-PN translates to a large effective area of about 2000 cm^2 at 2 keV. The EPIC-PN operates in 0.5–10 keV, with a spectral resolution E/dE ~ 40 at 6 keV.

2.1.2 Nuclear Spectroscopic Telescopic Array (*NuSTAR*)

The *NuSTAR* (Harrison et al., 2013) is a Small Explorer (SMEX) X-ray astronomy mission of the National Aeronautics and Space Administration (NASA) launched in 2012 into a low earth orbit and is operational as of 2023. The X-ray observatory operating in 3–79 keV consists of a pair of Wolter Type I telescopes coupled to a pair of identical Cadmium Zinc Telluride (CdZnTe) pixel detectors and is the first hard X-ray focusing telescope. The hard X-ray focussing is achieved through multi-layer mirrors made of high Z materials and grazing incidence of X-ray photons, facilitated by a long ~ 10 m focal length.

Each X-ray telescope of NuSTAR is made with 133 Wolter Type I multi-layer mirror shells (Petre et al., 1985). The X-ray telescopes have a focal length of 10.14 m and provide an angular imaging resolution of 18" FWHM. The two X-ray telescopes are co-aligned with their own 2×2 array of CdZnTe detectors at their focal planes, achieved with a deployed extendable mast and a laser aspect metrology system installed at the optics and detector ends (Fig. 2.2). The CdZnTe detector arrays are surrounded by an active Cesiun-Iodide (CsI) scintillation-based anti-coincidence shield. The detector arrays are identical and are called Focal Plane Modules A (FPMA) and B (FPMB). Each CdZnTe detector element in an FPM has a size of

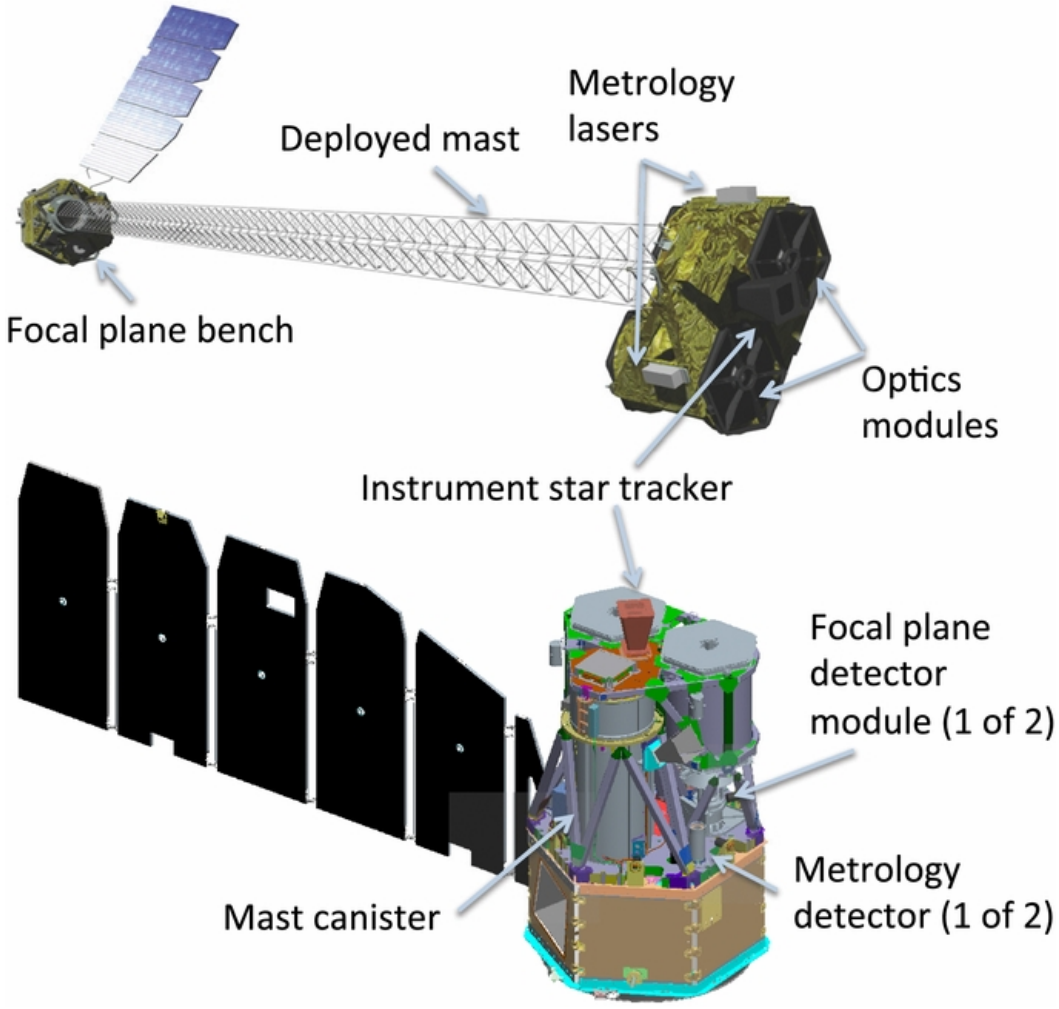

Fig. 2.2: Schematic diagram of the *NuSTAR* observatory in mast-secured condition (Bottom) and mast-deployed condition (Top). (Fig. credits: Harrison et al. 2013)

$20 \times 20 \times 2$ mm^3 and is divided into 32×32 pixels, with each pixel having a separate readout. The processing time for each event detected in a detector element is 2.5 ms, facilitating the operation of detectors at relatively large count rates of 400 events s^{-1} on each detector module without pileup. Each event is time-stamped with a precision of 2 μs. The spectral resolution is 400 eV FWHM below 50 keV.

2.1.3 Rossi X-ray Timing Explorer *(RXTE)*

The RXTE was an X-ray astronomy satellite mission of NASA that was operational from 1996 to 2011. The satellite was launched in late 1995 into a 580 km altitude low-earth orbit. RXTE carried three scientific instruments onboard; the Proportional Counter Array (PCA) (Jahoda et al., 1996) sensitive in 2–60 keV, the High Energy X-ray Timing Experiment (HEXTE) sensitive in 15–250 keV and the All-Sky Monitor (ASM) sensitive in 1.5–12 keV.

The All-Sky Monitor (ASM)

The ASM (Levine, Bradt, et al., 1996) comprised three Scanning Sky Cameras (SSC). Each SSC comprised an 8-wire position-sensitive proportional counter (PSPC) that was coupled to an Aluminium Slit Coded Aperture Mask. The shadow pattern of the X-ray sky cast by the coded mask on the PSPC was inverted using known shadow patterns to produce the intensities and directions of the X-ray sources in the sky. The SSCs were mounted on their own motorized rotation assembly which allowed the ASM to view different regions of the sky. A schematic of the ASM is shown in Fig. 2.3. Each PSPC was constructed with eight carbon-coated quartz anode wires and pressurized with 1.2 atm of the 95% Xenon and 5% CO_2 mixture. ASM accumulated lightcurves with 90 s (dwell) bin size in the 1.5-–12 keV energy range. The long-term dwell/orbit/day averaged lightcurves of about 300 astrophysical X-ray sources from 1996 to 2011 are available for download in the ASM Quick-look results website[1].

2.1.4 The Neil Gehrel's Swift Observatory (*Swift*)

The *Swift* observatory (Gehrels et al., 2004) is a Medium Explorer (MIDEX) mission of NASA for gamma-ray burst (GRB) astronomy launched in 2004 into a 585 km

[1] http://xte.mit.edu/asmlc/ASM.html

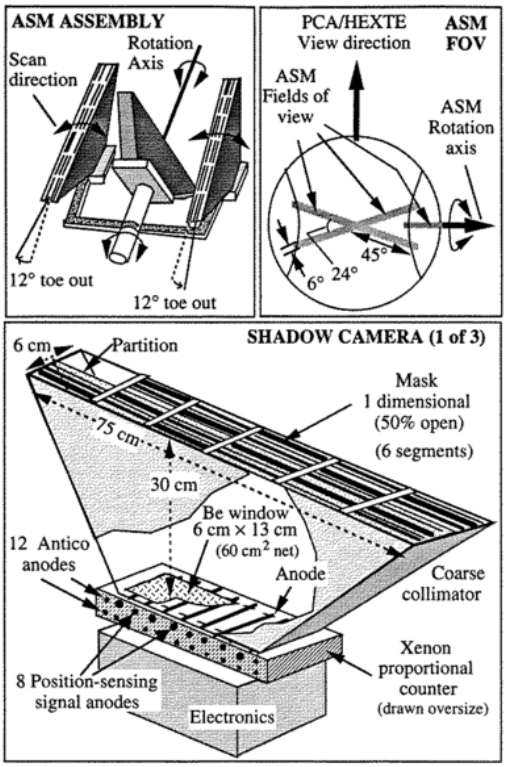

Fig. 2.3: Schematic diagram of the *RXTE*/ASM instrument. (Fig. credits: Levine, Bradt, et al. 1996)

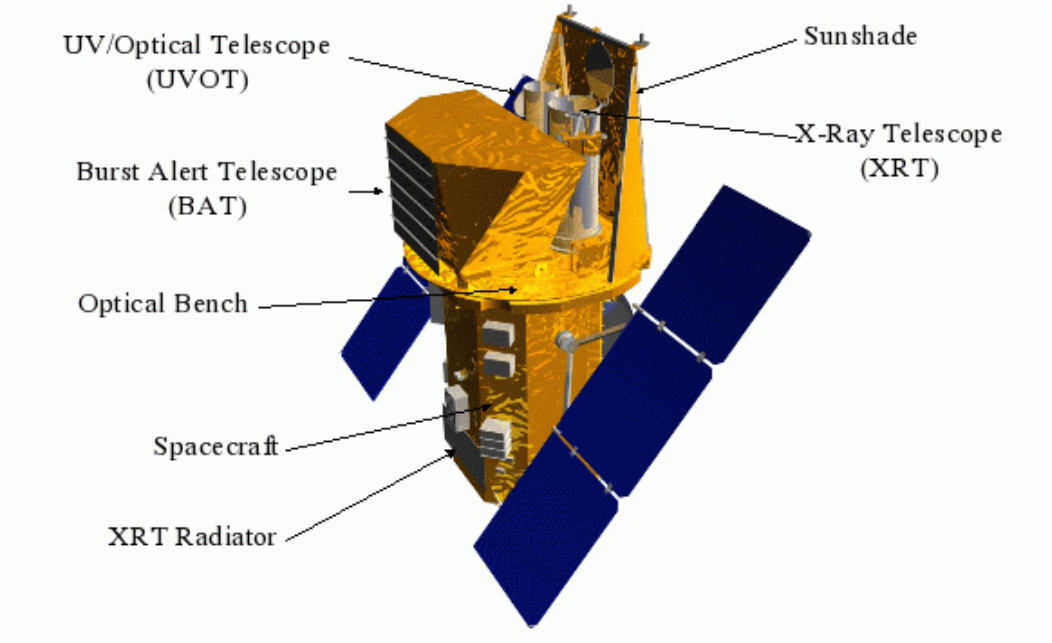

Fig. 2.4: Schematic diagram of the *Swift* observatory. Shown are the three scientific instruments onboard (UVOT, XRT and BAT). (Fig. credits: UKSSDC)

altitude low-earth orbit. The *Swift* carries three scientific instruments viz., the Burst Alert Telescope (BAT), the X-ray Telescope (XRT), and the Ultraviolet-Optical Telescope (UVOT). *Swift* was designed for GRB detections and their after-glow observations. A GRB that is triggered by the BAT instrument is localized first and the quick slewing capability ($\lesssim 90$ s) of the *Swift* allows follow-up multi-wavelength pointed observations of the GRB location using the XRT and UVOT instruments. A schematic diagram of *Swift* observatory is shown in Fig. 2.4.

The Burst Alert Telescope (BAT)

The BAT (Barthelmy et al., 2005) comprises a CdZnTe detector array consisting of 32,768 detector elements, each having a size of $4 \times 4 \times 2$ mm, placed 100 cm below a D-shaped Coded Aperture Mask Array constructed with 52,000 lead tiles, each tile having dimensions of $5 \times 5 \times 1$ mm. The FOV of BAT varies from 1.94 str for 10% coding fraction to 2.85 str for 0% coding fraction. BAT observes about 87% of the sky every day. The pattern of the shadow cast by the Coded Aperture on the detector array is inverted using known shadow patterns to produce the image of the X-ray sky, which helps in the localization of the GRBs. Even though the *Swift*/BAT instrument was designed for GRB alerts, the large FOV of the BAT and sky coverage of *Swift* makes it a hard X-ray monitor while waiting for GRBs. The BAT X-ray monitor

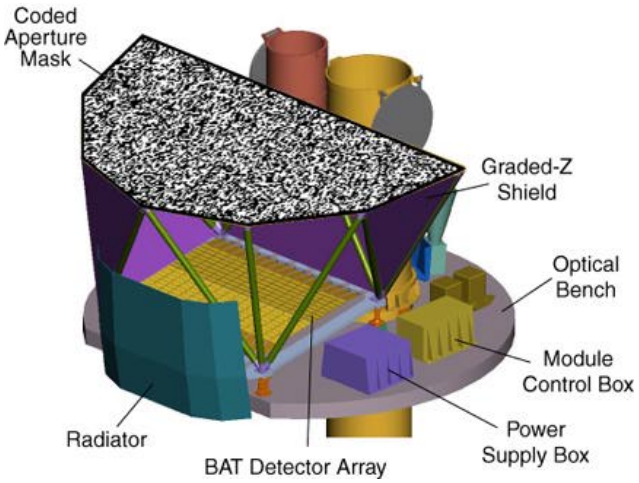

Fig. 2.5: Schematic diagram of the Burst Alert Telescope (BAT) onboard the *Swift* observatory. (Fig. credits: swift.gsfc.nasa.gov)

works in the 15–150 keV energy range and has been operational since 2006. The long-term daily/orbit averaged lightcurves of about 1000 astrophysical X-ray sources are available on the BAT monitor webpage[2].

2.1.5 Monitor of All-Sky X-ray Image (*MAXI*)

The *MAXI* (Matsuoka et al., 2009) is an X-ray astronomy instrument installed on the Japanese Experiment Module (Kibbo-EF) onboard the International Space Station (ISS). *MAXI* comprises of two scientific payloads; the Gas Slit Camera (GSC) (Mihara, Nakajima, et al., 2011) and the Solid-state Slit Camera (SSC) (Tomida, Tsunemi, Kimura, Kitayama, Matsuoka, Ueno, Kawasaki, Katayama, Miyaguchi, Maeda, et al., 2011b). Both GSC and SSC are X-ray Slit cameras, GSC has gas proportional counter detectors operating in 2–30 keV while SSC has CCD detectors operating in 1.5–12 keV. The GSC was designed to perform as an All-sky X-ray monitor, and the SSC produces X-ray sky maps with fine spectral resolution.

The Gas Slit Camera (GSC)

The GSC instrument on the *MAXI* (Mihara, Nakajima, et al., 2011) comprises twelve gas-filled position-sensitive proportional counters (PSPC), each integrated with their own Slit-Slat collimator. Each Slit-Slat collimator acts like a pin-hole camera. GSC is configured in two groups in which each group contains six cameras which are called

[2] https://swift.gsfc.nasa.gov/results/transients/BAT_current.html

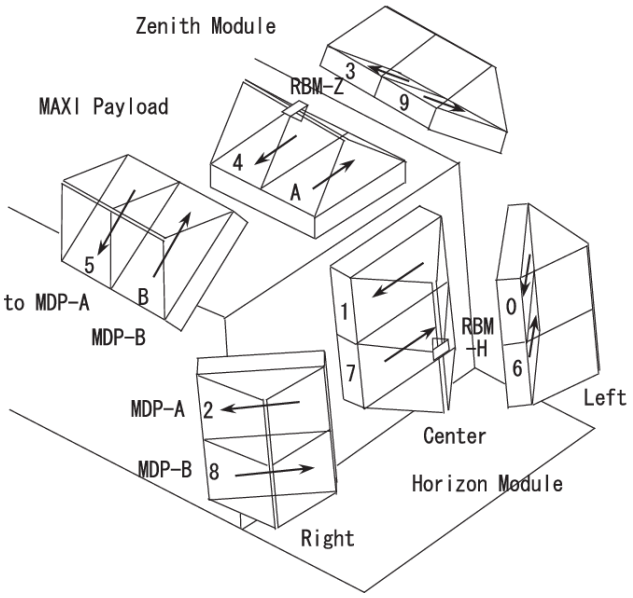

Fig. 2.6: Schematic diagram of the *MAXI*/GSC showing its horizontal and zenith camera modules. (Fig. credits: Mihara, Nakajima, et al., 2011)

the horizontal and zenith modules and each module has a large FOV of $1.5 \times 160^{\circ}$ FWHM. They are configured such that one module covers the sky in the tangential direction of the ISS motion while the other covers the sky in the orthogonal direction (See Fig. 2.6). In every 92 m orbit of the ISS, each camera covers 95% of the sky. The PSPCs on GSC have six $10\ \mu$m thick resistive Carbon wire anode cells, ten Tungsten wire veto cells in a Titanium container, and a Beryllium X-ray window. Each PSPC is filled with a gas mixture of 99% Xe and 1% CO_2 at 1.4 atm pressure. The twelve PSPCs have a combined geometrical detection area of 5350 cm^2. The long-term 6 hr/orbit/day lightcurves of X-ray sources in 2–20 keV are available[3]. Additionally, the spectral resolution of 16% FWHM at 6 keV makes GSC capable of performing spectroscopy.

2.2 Data Analysis Techniques

In this work, we have performed the time series and spectral analysis of X-ray pulsars to extract information about the underlying physical mechanisms behind the observed phenomena. This section describes various data analysis techniques and software packages that were utilized in this thesis. All the science data products used

[3] http://maxi.riken.jp/top/lc.html

in X-ray astronomy are generally stored in FITS (Flexible Image Transport System) file format for historical reasons.

2.2.1 Time Series Analysis

A basic science data in X-ray astronomy is the lightcurve, which is the X-ray counts observed from a source plotted as a function of time ($c(t_n)$). The lightcurve carries useful information of the underlying physical mechanisms in action, for instance, the coherent pulsations from XRPs appear as periodic modulation in the light curve, and variable accretion in a binary orbit appears as variation in intensity during the binary orbit. To study X-ray pulsations, the lightcurves are usually barycentric corrected and corrected for contribution from background photons. We have used the XRONOS tool `lcurve` to plot the lightcurves.

Power Spectral Density

The Fourier power spectral density (PSD) expresses a lightcurve as a superposition of sine waves of different frequencies. The concentration of power against a particular frequency or a range of frequencies is indicative of oscillations in the intensity at those frequencies (time scales). The features exhibited by XRPs are the coherent pulsations that appear as very narrow spikes, the Quasi-Periodic Oscillations (QPOs) that appear as relatively broad features, and the broadband low-frequency noise. For a lightcurve $c(t_n)$, where n $\in [0, 1, 2, \ldots, N-1]$, a discrete Fourier power spectral density (PSD) could be constructed by

$$C^2(f_k) = \frac{1}{N}\left|\sum_{n=0}^{N-1} c_n e^{-i\frac{2\pi nk}{N}}\right| \quad ; \; k \in [0, 1, 2, \ldots, N-1]$$

The PSD ($C^2(f_k)$) signifies the distribution of signal power over different frequencies (k). For faster computation, the PSD is generally generated using an FFT algorithm. The PSDs are generally normalized to fractional rms^2 Hz^{-1} and an expected Poisson white noise level of $2/\langle c(t_n)\rangle$ is also subtracted from the generated PSD. For an evenly sampled lightcurve $c(t_n)$, the Nyquist criterion limits the maximum frequency to which the PSD could be generated to $1/2\Delta$t (Δt $= t_n - t_{n-1}$) and frequency resolution δf to $1/n\Delta$t. We generated the PSDs using the XRONOS tool `powspec`[4]. To improve the signal-to-noise ratio of the PSD, PSDs were generated from smaller

[4] https://heasarc.gsfc.nasa.gov/lheasoft/ftools/fhelp/powspec.txt

lightcurve segments and then averaged, albeit with a limitation on the frequency resolution Δf. For an excellent review of Fourier techniques on X-ray time series, the reader is referred to Van der Klis (1989). PSDs suffer from the drawback that the oscillations having non-sinusoidal profiles cause leakage of power into harmonics. Gaps in the lightcurve that are common in X-ray astronomy also impact the PSD generation. Therefore, alternate techniques like Epoch folding and Lomb-Scargle are also often employed for X-ray timing analysis.

Lomb-Scargle Periodogram

A similar method used to generate a Fourier-like power density spectrum, widely utilized to detect periodicities in the lightcurve $c(t)$, is the Lomb-Scargle (LS) periodogram (Lomb 1976 and Scargle 1982). LS does this by constructing multiple sinusoidal lightcurves, each one using sine waves of a particular frequency, and fitting each of them to the actual lightcurve. The sine wave frequency corresponding to the best fitting curve based on least squares and the best fitting frequency is indicative of the underlying periodicity (VanderPlas, 2018). LS outputs fitting statistics for different trial frequencies. LS periodograms are utilized for lightcurves with uneven gaps. Also, trial lightcurves with non-sinusoidal wave patterns could also be constructed using higher-order harmonics. The error on the LS peak is expressed based on False Alarm Probability (FAP), which is the probability of a non-periodic lightcurve giving a particular LS power. The FAP levels for different powers of an LS periodogram are usually computed using the Bootstrap method. In this thesis, we have used the python-*Astropy* Lomb-Scargle Periodogram package to generate the Lomb-Scargle periodograms.

Folding Period Method

The most utilized technique for detecting pulsations from X-ray lightcurves is the Epoch folding search (Leahy, 1987). In this technique, the lightcurve $c(t_n)$ is folded into a preset number (N) of phase bins using a trial period P_j. The folded profiles C_i are scaled by the exposure time in each phase bin and have units of cts s^{-1}. C_is are constructed for a range of trial periods of interest. For each folded profile C_i, the sum of squares of the difference between C_i and the mean value C scaled by their respective errors is estimated, and the corresponding statistic (S) is plotted as a function of the trial periods. It is represented by

$$S = \sum_{n=1}^{N} \frac{(C_i - C)^2}{\sigma_i} \; ; \; i \in 1, 2, \ldots, N$$

$$C = \frac{1}{N} \sum_{i=1}^{N} C_i$$

Now, a distribution of S plotted as a function of the trial periods P_j is constructed. In the event of a lack of periodicity in the lightcurve, S could be associated with a noise amplitude, which is a random variable with χ^2 distribution with $N-1$ degrees of freedom. A deviation of S from the noise corresponding to any period could be associated with the detection of periodicity. We use the XRONOS tool *efsearch* for searching for pulsation and *efold* to view the folded profile at the detected period.

2.2.2 Spectral Analysis

The term photon spectrum refers to the photon flux expressed as a function of photon energy and has units of cts s^{-1} cm^{-2} keV^{-1}. The spectrum carries useful information on underlying photon emission processes (See Chapter 1) and it is deduced by comparing the data with physically motivated models. Usually, the photon energies in the X-ray band are expressed in electron volts (eV), with the current spectroscopic instruments sensitive from a few 100 eV to a few 100 keV. An X-ray spectroscopic instrument records photon energies (E) in terms of equivalent voltage levels called invariant pulse height amplitudes (PI). The spectral data output of the X-ray spectroscopy instrument when it is observing a target source could be viewed as the source emission spectrum convoluted with the instrument response. The instrument response is encoded in two files namely the Redistribution Matrix File (RMF) and the Ancillary Response File (ARF). RMF is a matrix that holds unitless scale values for pairs of E and PI, while ARF holds the instrument effective area in cm^2 as a function of E.

Due to the poor spectral resolution of the X-ray instruments relative to the sharp spectral features, deconvolving the instrument output (in PI) to meaningful physical data (in E) is often impossible. Instead, the physical model to be tested against the data is first convolved with the instrument response and the convolved model is then compared with the instrument data. This procedure is called forward-folding. The

expected spectral response C(PI) produced by the detector for an incident source photon energy spectrum M(E) is given by

$$C(PI) = \int M(E) \cdot RMF(PI, E) \cdot ARF(E)\, dE \tag{2.1}$$

C(PI) generated for various sets of model parameters are fitted against the observed C(PI) and the best-fitting model parameters are estimated using the least square method. Due to the photon counting nature of X-ray instruments, the errors on each spectral bin are Poisson distributed, and for relatively bright sources the best fitting model selection using least squares transforms to χ^2 minimization (likelihood maximization) technique. There are several spectral fitting packages available for X-ray astronomy, viz., ISIS, Sherpa, and Xspec. We have used the Xspec package (Arnaud, 1996) and its python version PyXspec (Gordon et al., 2021) in this thesis. Xspec provides a good collection of physical spectral models that could be tested against the observed data.

3 The vicinity of X-ray pulsar[a]

[a]The findings discussed in this chapter are part of a paper published in the journal MNRAS.

3.1 10 keV feature in the XRP spectra

The spectrum of Accreting X-ray Pulsars (XRPs) generally have a smooth broad-band continuum with a high energy cut-off along with some additional features like narrow K-shell emission lines of iron, thermal soft excess, cyclotron absorption line, etc. (See White, Swank, et al. 1983 and Nagase 1989). The X-ray spectral continuum carries information related to the photon generation mechanism and physical conditions at the X-ray emission site. Generally, we parameterize the X-ray spectral continuum using a set of simplified empirical models. The spectral continuum of XRPs is generally described by a powerlaw having high energy cutoff (Nagase, 1989). The lack of 'perfect' theoretical models for representing the observed XRP spectra is owed to the complexity involved with the consistent calculation of the coupled radiation transfer and magneto-hydrodynamics equations of the accretion flow (the accretion flow dynamics and radiation transfer are inter-dependent) at the location of origin of emergent spectra (Isenberg et al. 1998, Orlandini 2006). In addition to the powerlaw continuum, the physical origins of most of the observed XRP spectral features are well established, viz., the narrow fluorescence emission lines especially from iron, Cyclotron Resonance Scattering Feature (CRSF) due to electron-cyclotron resonance in the super-strong magnetic field near the surface of neutron star ($B_{NS} \sim 10^{12}$ Gauss) (Harding 2003, Staubert et al. 2019), photoelectric absorption of the soft X-rays by the interstellar medium and(or) circum-stellar/circum-binary matter, absorption edges, soft excess of thermal origin due to hard X-rays reprocessed by the inner accretion disk (Paul, Nagase, et al. 2002, Hickox et al. 2004), etc.

High signal-to-noise ratio (SNR) data and the broad-band spectral coverage delivered by present-day X-ray space observatories facilitate detailed examination of characteristic features in XRP spectra. In this work, we explore the mysterious feature found in XRP spectra, introduced as a distinct spectral feature by Coburn et al. (2002) called as "*The feature at 10 keV*" or the "*10 keV feature*" (hereafter *TKF*). *TKF* appears as a bump or depression or wiggle around 10 keV in the residuals to the best fit spectral model and is generally modelled as a gaussian emission or gaussian

absorption or a combination of these two models. This spectral feature has been observed in multiple XRP sources across different observatories viz., *Ginga* (Mihara 1995), *RXTE* (Coburn et al., 2002), *BeppoSAX* (Doroshenko, Santangelo, Doroshenko, et al., 2017), *Suzaku* (Rivers et al., 2009) and *NuSTAR* (Fürst, Pottschmidt, Wilms, Tomsick, et al., 2013). The appearance of *TKF* in spectra from multiple observatories rules out the possibility of its instrumental origin. The most suspected reason for the origin of *TKF* is the common usage of over-simplified and imperfect phenomenological spectral continuum models to describe the high statistics X-ray spectral data from the sensitive modern observatories (See Coburn et al. 2002, Vasco et al. 2013, and Doroshenko 2017). Reports of detection of *TKF* are sporadic, which impacts the selection of sources in an organized manner for its study. For instance, *TKF* may be reported in the spectrum of a particular source with data from a specific instrument (observatory) but may not be reported in the spectrum from another instrument. No particular pattern has been observed in the occurrence of *TKF* until now.

The broad-band (3−79 keV) focussing X-ray telescope *Nuclear Spectroscopic Telescope Array* (*NuSTAR*) is an instrument well suited to study the *TKF*, as it covers the 10 keV spectral region by a factor of a few on either side with good spectral resolution and low background levels. Additionally, there is the availability of a large archival *NuSTAR* spectral data of multiple XRPs. We selected some of the bright XRPs for which *NuSTAR* archival observations were available and then surveyed the available literature for spectral analysis studies of these chosen sources with different instruments. All the previous report(s) of detection of *TKF* in these sources were noted down. We then tried to model the available *NuSTAR* spectra of these XRPs with a suitable continuum model and check for the presence of *TKF* in them.

Since Coburn et al. (2002) presented *TKF* as a distinct spectral feature, it has been extensively reported in spectral analysis of XRPs. Generally, an extra model component with a gaussian absorption profile or a gaussian emission profile or a combination of the two is used to account for the residuals remaining at ~ 10 keV following the spectral fits. Coburn et al. (2002) also pointed out the residuals resembling *TKF* that were visible in spectral fits to *Ginga* observations of XRPs (Mihara, 1995). We surveyed the literature containing spectral analysis of XRPs in the following manner. First, the X-ray observatories covering the spectral band 5–20 keV and having an adequate spectral resolution to resolve *TKF* (which usually turns up as a broad feature) are screened. This confines the survey to the Large Area Counter instrument on *Ginga* (*Ginga*/LAC) spanning 1.5–37 keV with $\sim 18\%$ spectral resolution (Turner et al., 1989), the Proportional Counter Array (*RXTE*/PCA) covering 2–60 keV with $\sim 18\%$ spectral resolution and High Energy X-ray Timing Experiment (*RXTE*/HEXTE) covering 15–250 keV with $\sim 15\%$ spectral resolution

onboard *Rossi X-Ray Timing Explorer* (Jahoda et al., 1996), the High Pressure Gas Scintillation Proportional Counter (HPGSPC) (Manzo, G. et al., 1997) and Phoswich Detection System (PDS) (Frontera et al., 1997) instruments on-board *BeppoSAX* (Boella et al., 1997) covering 4–120 keV, the Joint European X-Ray Monitor (JEM-X) instrument on-board *INTEGRAL* covering 4–35 keV with $\sim 10\%$ spectral resolution (Lund et al., 2003), *Suzaku*/XIS (X-ray Imaging Spectrometer) with 0.2–12 keV coverage and $\sim 2\%$ spectral resolution, and *Suzaku*/HXD (Hard X-ray Detector) with 10–70 keV coverage and spectral resolution of 3.0 keV (Koyama, Tsunemi, et al. 2007 and Takahashi et al. 2007 respectively), *NuSTAR* (Harrison et al., 2013) and AstroSAT-*LAXPC* (Large Area X-ray Proportional Counters) covering 3–80 keV with $\sim 10\%$ spectral resolution (Antia et al., 2017). For the selected bright XRPs, we searched for the reported spectral analysis results using data from the aforementioned X-ray observatories.

A summary of the published results in the context of the *TKF* is given in Table 3.1. Out of the 30 selected sources given in the table, *TKF* has been reported at least once in 9 sources viz., Vela X–1, Her X–1, XTE J1946+274, 4U 1907+09, 4U 1538–52, Cep X–4, SMC X–1, GX 304–1 and EXO 2030+375. A graphical depiction of the survey is shown in Fig. 3.1. It is most commonly observed with *RXTE*-PCA observatory and for powerlaw continuum having a high energy cutoff `highecut`[1] (See Fig. 3.1). However, analysis of the same data by different groups also sometimes has given contrasting results regarding *TKF* (See for example Vybornov et al. 2017, Fürst, Pottschmidt, Miyasaka, et al. 2015 and Bhargava et al. 2019).

References for Table 3.1 – [1]La Barbera, A., Santangelo, A., et al. (2003) [2]Orlandini, Fiume, Frontera, et al. (1998) [3]Choi et al. (1996) [4]Mihara (1995) [5]Kreykenbohm, I. et al. (2002) [6]Wang (2014b) [7]Schanne et al. (2007) [8]Fürst, Pottschmidt, Wilms, Tomsick, et al. (2013) [9]Maitra and Paul (2013b) [10]Odaka et al. (2013) [11]Fuerst et al. (2013) [12]Klochkov, Staubert, et al. (2007) [13]Fiume et al. (1998) [14]Gruber et al. (2001) [15]Enoto et al. (2008) [16]Vasco et al. (2013) [17]Varun, Maitra, et al. (2019) [18]Rodes-Roca, J. J. et al. (2009) [19]Hemphill, Rothschild, Cheatham, et al. (2019) [20]Fürst, Falkner, et al. (2018) [21]Suchy, Fürst, et al. (2012) [22]Doroshenko, V. et al. (2010) [23]La Barbera, A., Segreto, A., et al. (2005) [24]Kreykenbohm, Pottschmidt, et al. (2004) [25]Mukherjee and Paul (2004) [26]Coburn et al. (2002) [27]Rivers et al. (2009) [28]Tendulkar et al. (2014) [29]Cusumano et al. (2000) [30]Hemphill, Rothschild, Caballero, et al. (2013) [31]Mukherjee, Bapna, et al. (2006) [32]Doroshenko, Doroshenko, et al. (2008) [33]Nagase, Corbet, et al. (1992) [34]Devaraj et al. (2022) [36]Jaisawal and Naik (2016a) [37]Baum et al. (2017) [38]Lutovinov, Tsygankov, Suleimanov, et al. (2015) [39]Makishima, Mihara, Ishida, et al. (1990) [40]Kreykenbohm, Mowlavi, et al. (2005) [41]Tsygankov, Lutovinov, Churazov, et al. (2006) [42]Ferrigno, Carlo et al. (2016) [43]Shtykovsky, Lutovinov, Tsygankov, et al. (2019) [44]Roy et al. (2017) [45]Orlandini, Fiume, Del Sordo, et al. (1999) [46]Mukherjee, Raichur, et al. (2006) [47]Clark, Woo, et al. (1990) [48]Robba et al. (2000) [49]Jaisawal and Naik (2016b) [50]Tomar et al. (2021) [51]Doroshenko (2017) [52]Kreykenbohm, Kretschmar, et al. (1998) [53]Pradhan, Maitra, Paul, Islam, et al. (2014a) [54]Filippova et al. (2005) [55]Burderi et al. (2000) [56]Vybornov, V. et al. (2018) [57]Doroshenko, Tsygankov, et al. (2017) [58]Tsygankov and Lutovinov (2005b) [59]Saavedra et al. (2022) [60]Sharma, Sharma, et al. (2022) [61]Jaisawal, Naik, Epili, et al. (2021) [62]Barnstedt, J. et al. (2008) [63]La Barbera, Baushev, et al. (2004) [64]Orlandini, Dal Fiume, et al. (1998) [65]Owens et al. (1997) [66]Iwakiri, Terada, et al. (2012) [67]Fürst, Pottschmidt, Wilms, Kennea, et al. (2014) [68]Naik, Callanan, et al. (2006) [69]Galloway et al.

[1]The model is explained in Section. 3.1.2

Tab. 3.1: For each source spectrum from the particular observatory, the spectral model used to fit the continuum in the literature is given. If a *TKF* was used for the spectral fit, then the cell is given in bold fonts. Whether the *TKF* is modelled like a dip (gaussian absorption) or a hump (gaussian emission) is shown with letters A (absorption) and E (emission), respectively. If the authors have not reported the presence of *TKF* for any observation, but residuals resembling *TKF* are visible in their best fit model, it is indicated with the letter R (residuals).

Source	Ginga	RXTE	BeppoSAX	INTEGRAL	Suzaku	NuSTAR	Astrosat	NuSTAR (*This work*)
Her X–1	PL[4]	HEC[14]	BPLHEC[13]	HEC[12]	NPEX[15]	**HEC[11] (A)**	HEC[110]	NPEX, HEC
	NPEX[71]	**HEC[16] (E)**	–	–	–	–	–	**FDC (A)**
	–	HEC[26] (R)	–	–	–	–	–	–
Vela X–1	NPEX[4]	**NPEX[5] (A)**	**NPEX[1] (E)**	CPL[6]	compTT[9]	**FDC[8] (A)**	–	**compTT (A)**
	PL[3]	HEC[26]	NPEX[2]	CPL[7]	NPEX[10]	**FDC,HEC,NPEX,compTT[158] (A)**	–	CPL, compTT, HEC
	–	FDC[52]	compTT[51]	–	–	–	–	–
XTE J1946+274	–	**FDC[105] (A)**	**FDC[112] (E)**	**FDC[105] (A)**	HEC[84]	**HEC,FDC,NPEX,compTT[34] (A)**	–	**HEC (A)**
	–	NPEX[111]	–	–	–	–	–	–
	–	HEC[26]	–	–	–	–	–	–
KS 1947+300	–	compTT[69]	compTT[68]	HEC[58]	CPL[113]	CPL[67]	–	HEC, NPEX
4U 1907+09	**NPEX[4] (A)**	**HEC[26] (A)**	HEC[29]	CPL[30]	**FDC,HEC,NPEX[27] (E)**	**HEC, CPL[157] (A)**	HEC[81]	**compTT (A)**
	–	–	–	–	NPEX[84]	–	–	–
4U 1538–52	NPEX[4] (R)	HEC[46]	HEC[48]	**CPL[30] (E)**	–	HEC[19]	FDC[17]	NPEX
	NPEX[71]	**CPL[18] (A)**	–	–	–	–	–	–
	HEC[47]	**HEC[26] (A)**	–	–	–	–	–	–
Cep X–4	NPEX[71]	**FDC[97] (E)**	–	–	NPEX[95]	FDC[93]	–	compTT, NPEX
	HEC[94]	–	–	–	–	FDC[96]	–	–
	HEC[114]	–	–	–	–	**FDC[98] (E)**	–	–
4U 1626-67	–	HEC[26]	HEC[51]	–	NPEX[66]	HEC[83]	–	FDC
	–	–	HEC[64]	–	HEC[82]	–	–	–
	–	–	CPL[65]	–	NPEX[80]	–	–	–
SMC X–2	–	–	–	–	–	NPEX[36]	–	compTT, NPEX
IGR J17544–2619	–	–	–	–	–	nthcomp[99]	–	NPEX
IGR J16393–4643	–	–	–	–	HEC[104]	CPL[103]	–	**NPEX (A)**
2S 1553–542	–	BPL[115]	–	–	–	CPL[116]	–	FDC
RX J0520.5–6932	–	–	–	–	–	FDC[28]	–	**CPL,NPEX (A)**
Cen X–3	HEC[33]	HEC[26] (R)	compTT[51]	PCH[54]	FDC[84]	NHC[50]	–	**HEC (A)**
	–	–	PCH[32] (R)	PCH[55]	NHC[50]	–	–	–
	–	–	HEC[63]	–	–	–	–	–
GX 301–2	NPEX[4]	HEC[25]	NHC[23]	FDC[22]	FDC[21]	NPEX[20]	–	NPEX
	–	HEC[26]	–	FDC[24]	–	–	–	–
	–	–	–	HEC[54]	–	–	–	–
XTE J1829–098	–	–	–	–	–	CPL[43]	–	NHC
V 0332+53	HEC[39]	CPL[38]	–	compTT[37]	–	compTT[56]	–	HEC, NHC, NPEX, compTT
	NPEX[4]	CPL[41]	–	CPL[40]	–	compTT[57]	–	–
	NPEX[71]	–	–	HEC[42]	–	–	–	–
	–	–	–	HEC[54]	–	–	–	–
XTE J1858+034	–	HEC[31]	–	HEC[32]	–	compTT[33]	–	NPEX
4U 1700-67	HEC[115]	2PL[117]	HEC[141]	–	NPEX[116]	NHC[118]	–	**NPEX (A)**
	–	–	–	–	NHC[116]	–	–	–
LMC X–4	HEC[120]	HEC[123]	HEC[122]	HEC[125]	HEC[127]	compTT[128]	–	**NPEX (A)**
	NPEX[4]	–	PL[124]	HEC[126]	–	–	–	NPEX, FDC, compTT
	HEC[121]	–	–	–	–	–	–	–
IGR J17329–2731	–	–	–	PL[119]	–	HEC[119]	–	NPEX
SMC X–1	HEC[133]	HEC[129]	HEC[132]	–	CPL[134]	**FDC[130] (E)**	–	HEC, FDC
	–	–	CompTT[132]	–	–	NPEX[131]	–	–
GRO J1008–57	–	CPL[138]	–	CPL[136]	NPEX[135]	NPEX[137]	–	NPEX
	–	–	–	CPL[138]	CPL[138]	2compTT[140]	–	–
GX 304–1	–	HEC[146]	–	HEC[145]	FDC[141]	2compTT[144]	–	PL
	–	FDC,NPEX[141]	–	CPL[147]	NPEX[141]	–	–	–
	–	**HEC,CPL[148] (E)**	–	–	NPEX[142]	–	–	–
	–	–	–	–	HEC[143]	–	–	–
1A 0535+26	–	CPL[85]	–	CPL[85]	CPL[85]	CPL[86]	–	FDC, PL, 2compTT
	–	HEC[87]	–	HEC[87]	NPEX[84]	2compTT[89]	–	–
	–	PL[88]	–	HEC[91]	–	CPL[90]	–	–
GRO J2058+42	–	–	–	–	–	FDC[153]	FDC[154]	**compTT (A)**
	–	–	–	–	–	compTT[155]	–	NHC
1E 1145.1–6141	–	HEC[74]	–	CPL[72]	–	CPL[73]	–	CPL
OAO 1657–415	HEC[70]	–	CPL[45]	HEC[62]	HEC[49]	CPL[59]	PL[61]	CPL
	–	–	–	–	HEC[53]	CPL[60]	–	–
EXO 2030+375	–	**HEC[76] (A)**	–	**HEC[77] (A,E)**	HEC[78]	**CPL[75] (A)**	HEC[79]	NPEX
	–	HEC[92]	–	compTT[106]	HEC[101]	HEC[79]	–	**CPL (A), NPEX (A)**
	–	HEC[156]	–	HEC[107]	–	HEC[100]	–	–
IGR J19294+1816	–	PL[151]	–	PL[44]	–	compTT[109]	HEC[108]	NPEX, PL
	–	PL[152]	–	–	–	–	–	–

NOTE– PL: powerlaw, 2PL: double powerlaw, HEC: PL with `highecut`, FDC: PL with Fermi-Dirac cutoff, NHC: `newhcut`, CPL: `cutoffpl`, NPEX: Negative Positive Exponential, BPL: Broken powerlaw, BPLHEC: Broken powerlaw with `highecut`, compTT: comptonization model, 2compTT: double compTT NOTE– 4U 1700–37 is not an established XRP, but it is included because of the reported CRSF.

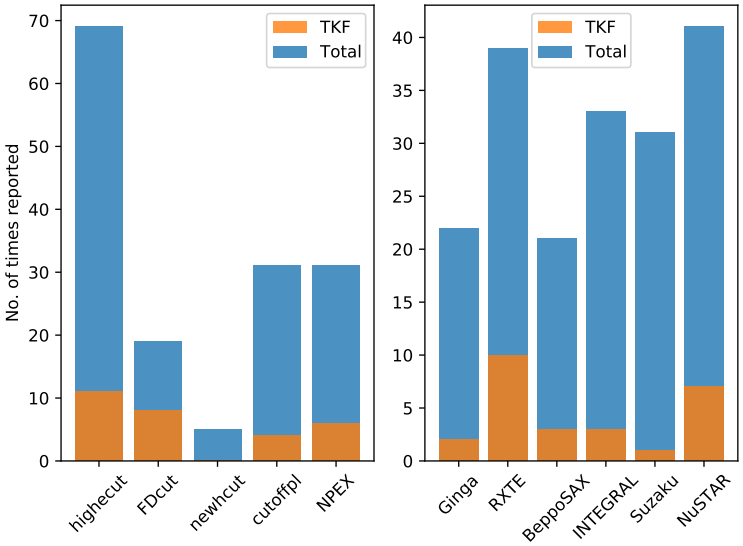

Fig. 3.1: The bar chart shows the specifics of the performed survey (Table 3.1). The distribution of reports of *TKF* for different continuum models, and from different observatories[2] are shown.

(2004) [70]Kamata et al. (1990) [71]Makishima, Mihara, Nagase, et al. (1999) [72]Ferrigno et al. (2008) [73]Ghising et al. (2022) [74]Ray et al. (2002) [75]Tamang et al. (2022) [76]Wilson, Finger, and Camero-Arranz (2008b) [77]Klochkov, D. et al. (2008) [78]Naik and Jaisawal (2015) [79]Jaisawal, Naik, Gupta, et al. (2021) [80]Iwakiri, Pottschmidt, et al. (2019) [81]Varun, Pradhan, et al. (2019) [82]Camero-Arranz et al. (2012) [83]D'Aí et al. (2017) [84]Maitra and Paul (2013a) [85]Caballero, Pottschmidt, et al. (2013) [86]Ballhausen et al. (2017) [87]Caballero, Kretschmar, et al. (2007) [88]Rothschild, Markowitz, et al. (2013) [89]Tsygankov, Doroshenko, Mushtukov, Suleimanov, et al. (2019) [90]Mandal et al. (2022) [91]Sartore et al. (2015) [92]Epili et al. (2017) [93]Fürst, Pottschmidt, Miyasaka, et al. (2015) [94]Koyama, Kawada, et al. (1991) [95]Jaisawal and Naik (2015b) [96]Bhargava et al. (2019) [97]McBride et al. (2007) [98]Vybornov et al. (2017) [99]Bhalerao et al. (2015) [100]Fürst, Kretschmar, et al. (2017) [101]Naik, Maitra, et al. (2013) [103]Bodaghee et al. (2016) [104]Islam, Maitra, et al. (2015) [105]Müller, S. et al. (2012) [106]Camero Arranz, A. et al. (2005) [107]Martínez Núnez, S. et al. (2003) [108]Raman et al. (2021) [109]Tsygankov, Doroshenko, Mushtukov, Lutovinov, et al. (2019) [110]Bala, Bhattacharya, et al. (2020) [111]Heindl et al. (2001) [112]Doroshenko, Santangelo, Doroshenko, et al. (2017) [113]Ballhausen, Ralf et al. (2016) [114]Mihara, Makishima, et al. (1991) [115]Pahari et al. (2012) [116]Tsygankov, Lutovinov, Krivonos, et al. (2016) [116]Jaisawal and Naik (2015a) [117]Seifina et al. (2016) [118]Bala, Roy, et al. (2020) [119]Bozzo et al. (2018) [120]Levine, Rappaport, et al. (1991) [121]Woo, Clark, Levine, et al. (1996) [122]La Barbera, Burderi, et al. (2001) [123]Naik and Paul (2003) [124]Naik and Paul (2004b) [125]Lutovinov, Tsygankov, Revnivtsev, et al. (2004) [126]Tsygankov and Lutovinov (2005a) [127]Hung et al. (2010) [128]Shtykovsky, Lutovinov, Arefiev, et al. (2017) [129]Inam et al. (2010) [130]Pike et al. (2019) [131]Brumback et al. (2020) [132]Naik and Paul (2004a) [133]Woo, Clark, Blondin, et al. (1995) [134]Pradhan, Maitra, and Paul (2020) [135]Yamamoto, Mihara, et al. (2014) [136]Wang (2014a) [137]Bellm et al. (2014) [138]Kühnel et al. (2013) [139]Naik, Paul, et al. (2011) [140]Lutovinov, Tsygankov, Molkov, et al. (2021) [141]Yamamoto, Sugizaki, et al. (2011) [142]Jaisawal, Naik, and Epili (2016) [143]Pradhan, Paul, et al. (2021) [144]Tsygankov, Rouco Escorial, et al. (2019) [145]Klochkov, Doroshenko, et al. (2012) [146]Devasia et al. (2011) [147]Malacaria, Klochkov, et al. (2015) [148]Rothschild, Kühnel, et al. (2017) [149]Haberl and Day (1992) [150]Reynolds et al. (1999) [151]Rodriguez et al. (2009) [152]Roy et al. (2017) [153]Kabiraj and Paul (2020) [154]Mukerjee et al. (2020) [155]Molkov et al. (2019) [156]Reig and Coe (1999) [157]Tobrej et al. (2023) [158]Diez et al. (2022)

[2]Remark: Reports with residuals resembling *TKF* visible in the best fit model were counted for the bar chart on the right-hand side of the figure.

Many of the results mentioned before include combined spectral analysis using data from more than one instrument (except *Ginga*/LAC, *NuSTAR*, and *AstroSat*/LAXPC), often with a gap around 10–15 keV which is above the energy range of the imaging instruments and below the energy range of the scintillator detectors. We have analyzed archival data of 58 *NuSTAR* observations of 30 bright XRPs to probe the *TKF*. The *NuSTAR* observations cover either side of the 10 keV with a single instrument, thus reducing systematic effects of cross-normalization of different instruments.

In Sec. 3.1.1, a brief description of *NuSTAR* instrument, the Data reduction steps followed, and a log of the *NuSTAR* observations that we have used for spectral analysis in this work are given. Sec. 3.1.2 explains the details of the spectral analysis performed. The results of the analysis and its discussion are given in Sec. 3.1.3.

3.1.1 Instrument, Observations and data-reduction

NuSTAR is an X-ray imaging spectroscopic observatory that covers the energy band by a factor of a few on either side of 10 keV with the same telescope and detector, making it an ideal instrument to probe the *TKF*. *NuSTAR* is the first hard X-ray focusing telescope and it provides spectral coverage in the 3–79 keV bandpass. The spectral resolution below 50 keV is 400 eV FWHM, which is excellent for studying the relatively broad *TKF* feature. In addition, the uninterrupted broadband coverage from the instrument aids in modelling the spectral continuum in the best possible manner.

We followed the standard data reduction steps from the *NuSTAR* Data Analysis Software Guide[3] to extract the calibrated and screened source and background products. The task nupipeline v0.4.6 of HEASoft v6.25[4] was first run on the raw data to obtain the filtered and calibrated data. Calibration database CALDB v1.0.2[5] was used for this purpose. Using DS9[6], circular source and background region files are generated. The task `nuproducts` was then run to extract the source and background energy spectra as well as the Redistribution Matrix File (RMF) and Auxiliary Response File (ARF). The extracted source spectrum was checked against the background spectrum, and the background-dominated energy range was excluded from the spectral analysis. A set of two spectra from two detector modules FPMA and FPMB were obtained for

[3] https://heasarc.gsfc.nasa.gov/docs/nustar/analysis/nustar_swguide.pdf
[4] https://heasarc.gsfc.nasa.gov/docs/software/heasoft/
[5] https://heasarc.gsfc.nasa.gov/docs/heasarc/caldb/nustar/
[6] https://sites.google.com/cfa.harvard.edu/saoimageds9

each observation. The spectra were then re-binned with the tool ftgrouppha[7] using the optimal binning scheme by Kaastra et al. (2016)[8]. Both the FPMA and FPMB spectra are fitted together in XSPEC v12.10.1 (Arnaud, 1996), with an instrument relative normalization constant parameter left free to vary and all other model parameters tied together across both the spectra.

A catalogue of the sources and corresponding *NuSTAR* observation IDs used in this work is given in Table 3.2.

3.1.2 Time-averaged spectroscopy

We have performed the time-averaged spectral analysis on the *NuSTAR* pointed observations of sources listed in Table 3.2 in the 3–79 keV spectral band unless otherwise specified. The light curves of some of the observations showed the presence of flares (See Table 3.2). In those cases, the flare and out-of-flare spectra were separately generated and then analysed[9]. The spectra were fitted with a composite model of the following form

$$\frac{dN}{dE} = e^{-\sigma_{\rm abs}(E)} \times \left(f e^{-\sigma_{\rm abs,local}(E)} + (1-f) \right) \times [\ \text{continuum}(E) \times \text{gabs}_{\rm TKF}(E) + \text{gaussian}_{\rm Fe}(E) + \text{bbody(E)}\ ] \times \text{gabs}_{\rm CRSF}(E) \tag{3.1}$$

$e^{-\sigma_{abs}(E)}$ denotes absorption by the interstellar medium (ISM) and was modelled with the Tuebingen-Boulder ISM absorption model (`tbabs`) using ISM abundances from Wilms et al. (2000) and photoelectric absorption cross-sections from Verner et al. (1996). For the observations in which the galactic absorption column density towards the source could not get constrained by the fit, the absorption column density was frozen to the galactic line of sight value obtained from the tool *w3nh*[10]. Local absorption was modelled by multiplying the spectrum with a partial covering absorption model of the form $f e^{-\sigma_{\rm abs,local}(E)} + (1-f)$. The implication of this modified Tuebingen-Boulder ISM absorption model (`tbpcf`) is that only a fraction f of the total X-ray flux is absorbed, while the remaining fraction $(1-f)$ of the flux travels unabsorbed (See Maitra and Paul, 2013a). The redshift parameter of `tbpcf`

[7] https://heasarc.gsfc.nasa.gov/lheasoft/help/ftgrouppha.html
[8] We verified that the best fit spectral parameters have no significant variation when using this binning scheme, compared to grouping with a minimum of 25 counts per bin.
[9] We consider any spike in the light curve as a flare if the ratio of the peak count rate of the spike to the average count rate outside the spike is greater than 3.
[10] https://heasarc.gsfc.nasa.gov/cgi-bin/Tools/w3nh/w3nh.pl

Tab. 3.2: *NuSTAR* Observations catalogue with the details of the source and observation IDs used in this work. The observation IDs having flare in the light curve have the letter '*F*' super-scripted.

Obs. Sn.	Source	*NuSTAR* Obs. ID	start (DATE-OBS)	stop (DATE-END)	exposure (ks)	FPMA count rate (cts s^{-1})
1	Her X–1	30002006002	2012-09-19 08:26:07	2012-09-20 01:06:07	27.7	34
2		30002006005	2012-09-22 04:26:07	2012-09-22 18:36:07	21.9	90
3		10202002002	2016-08-20 04:31:08	2016-08-21 06:21:08	36.6	80
4	Vela X–1	10002007001	2012-07-09 13:16:07	2012-07-09 23:06:07	10.8	135
5		30002007002	2013-04-22 12:16:07	2013-04-22 20:11:07	7.14	67
6		30002007003	2013-04-22 20:11:07	2013-04-23 19:06:07	24.5	43
7		90402339002^{F}	2019-01-10 04:11:09	2019-01-11 02:26:09	36.0	41
8	XTE J1946+274	90401328002	2018-06-24 11:26:09	2018-06-25 15:36:09	47.2	36
9	KS 1947+300	80002015002	2013-10-21 18:36:07	2013-10-22 05:46:07	18.36	72
10		80002015004	2013-11-22 21:26:07	2013-11-23 09:31:07	18.59	82
11		80002015006	2013-12-09 15:51:07	2013-12-10 07:41:07	27.29	65
12	4U 1907+09	30401018002	2018-08-01 12:41:09	2018-08-03 07:41:09	78.86	7
13	4U 1538–52	30201028002	2016-08-11 19:11:08	2016-08-12 19:16:08	11.1	7
14	Cep X–4	80002016002	2014-06-18 22:01:07	2014-06-19 20:11:07	40.4	44
15		80002016004	2014-07-01 10:16:07	2014-07-02 07:26:07	41.16	12
16	4U 1626-67	30101029002	2015-05-04 12:26:07	2015-05-05 20:41:07	65.0	15
17	SMC X–2	90102014002	2015-09-25 21:51:08	2015-09-26 11:21:08	24.51	19
18		90102014004	2015-10-12 21:41:08	2015-10-13 12:06:08	23.06	9
19		90101017002	2015-10-21 21:31:08	2015-10-22 11:16:08	26.72	6
20	IGR J17544–2619	30002003003	2013-06-19 09:31:07	2013-06-19 23:41:07	26.3	26
21	IGR J16393–4643	30001008002	2014-06-26 02:21:07	2014-06-27 05:31:07	50.57	0.54
22	2S 1553–542	90101002002	2015-04-03 11:36:07	2015-04-04 01:46:07	27.42	19
23	RX J0520.5–6932	80001002002	2014-01-22 20:16:07	2014-01-23 11:36:07	27.75	14
24		80001002004	2014-01-24 23:56:07	2014-01-25 18:31:07	33.2	16
25	Cen X–3	30101055002	2015-11-30 18:11:08	2015-12-01 05:01:08	21.4	65
26	GX 301–2	30001041002	2014-10-29 07:41:07	2014-10-29 22:01:07	38.2	12
27		30101042002^{F}	2015-10-04 08:01:08	2015-10-04 22:41:08	35.7	19
28	XTE J1829–098	90401332002	2018-08-16 02:11:09	2018-08-16 18:01:09	27.8	6
29	V0332+53	80102002008	2015-09-30 22:51:08	2015-10-01 09:46:08	18.1	37
30		80102002010	2015-10-04 23:36:08	2015-10-05 11:51:08	20.1	21
31		90202031002	2016-07-30 18:01:08	2016-07-31 06:31:08	25.2	12
32		90202031004	2016-07-31 18:06:08	2016-08-01 06:46:08	25.0	10
33	XTE J1858+034	90501348002	2019-11-03 06:56:09	2019-11-04 08:31:09	43.7	17
34	4U 1700–37	30101027002^{F}	2016-03-01 10:21:08	2016-03-02 07:31:08	38.0	23
35	LMC X–4	30102041002^{F}	2015-10-30 01:01:08	2015-10-30 12:46:08	24.5	13
36		30102041004	2015-11-04 19:46:08	2015-11-05 05:56:08	21.9	10
37		30102041006	2015-11-11 11:16:08	2015-11-11 22:36:08	22.9	3
38		30102041008^{F}	2015-11-27 09:16:08	2015-11-27 20:31:08	20.3	10
39	IGR J17329–2731	90301012002	2017-08-29 15:36:09	2017-08-30 02:36:09	20.8	3
40	SMC X–1	30202004002	2016-09-08 21:26:08	2016-09-09 09:06:08	22.5	21
41		30202004004	2016-09-19 07:11:08	2016-09-19 19:06:08	21.2	15
42		30202004006	2016-10-01 00:56:08	2016-10-01 12:01:08	20.4	1.52
43		30202004008	2016-10-24 19:31:08	2016-10-25 07:36:08	20.8	24
44	GRO J1008–57	80001001002	2012-11-30 08:41:07	2012-11-30 17:31:07	12.4	227
45	GX 304–1	90401326002	2018-06-03 05:56:09	2018-06-04 12:06:09	58.1	0.21
46	1A 0535+26	80001016002	2015-02-11 04:11:07	2015-02-11 16:21:07	21.4	36
47		80001016004	2015-02-14 01:36:07	2015-02-14 17:31:07	29.7	14
48		90401370001	2018-12-26 02:41:09	2018-12-27 12:11:09	54.9	68
49	GRO J2058+42	90501313002	2019-03-25 07:06:09	2019-03-25 19:26:09	20.4	38
50		90501313004	2019-04-11 00:11:09	2019-04-11 22:11:09	38.6	42
51		90501336002	2019-08-28 12:36:09	2019-08-29 09:26:09	38.5	4
52	1E 1145.1–6141	30501002002	2019-07-23 10:56:09	2019-07-24 07:26:09	44.2	7.3
53	OAO 1657–415	30401019002	2019-03-25 07:06:09	2019-06-13 08:01:09	74.7	7.6
54	EXO 2030+375	90201029002	2016-07-25 08:36:08	2016-07-26 17:11:08	56.7	2.6
55		90701336002	2021-11-08 03:31:09	2021-11-08 17:56:09	23.5	71
56		80701320002	2021-08-30 00:56:09	2021-08-31 03:56:09	32.4	194
57	IGR J19294+1816	90401306002	2018-03-02 21:56:09	2018-03-03 20:06:09	40.6	0.06
58		90401306004	2018-03-16 03:11:09	2018-03-17 01:31:09	40.4	2.1

model was fixed to 0. The soft excess was modelled with a blackbody spectrum model *bbody*. *TKF* was modelled with a gaussian absorption model `gabs`.

The spectral continuum is modeled with a physical comptonization model like `compTT` (Titarchuk, 1994) or one of the following phenomenological powerlaw based continuum models:

$$\texttt{powerlaw} = A \times E^{-\Gamma}$$

$$\texttt{cutoffpl} = A \times E^{-\Gamma} \exp\left(-\frac{E}{E_{\rm cut}}\right)$$

$$\texttt{powerlaw} \times \texttt{mplcut} = \begin{cases} A \times E^{-\Gamma} \exp\left(-\frac{(E-E_{\rm cut})^2}{(0.1E_{\rm cut})^2}\right) & E < E_{\rm cut} \\ A \times E^{-\Gamma} \exp\left(-\frac{E-E_{\rm cut}}{E_{\rm fold}}\right) \exp\left(-\frac{(E-E_{\rm cut})^2}{(0.1E_{\rm cut})^2}\right) & E \geq E_{\rm cut} \end{cases}$$

$$\texttt{powerlaw} \times \texttt{FDcut} = \begin{cases} A \times E^{-\Gamma} & E < E_{\rm cut} \\ A \times E^{-\Gamma} \times 1/\left[1 + \exp\left(-\frac{E-E_{\rm cut}}{E_{\rm fold}}\right)\right] & E \geq E_{\rm cut} \end{cases}$$

$$\texttt{powerlaw} \times \texttt{newhcut} = \begin{cases} A \times E^{-\Gamma} & E \leq E_{\rm cut} - \Delta E \\ c_0 + c_1 E + c_2 E^2 + c_3 E^3 & E_{\rm cut} - \Delta E < E < E_{\rm cut} + \Delta E \\ A \times E^{-\Gamma} \exp\left(-\frac{E-E_{\rm cut}}{E_{\rm fold}}\right) & E \geq E_{\rm cut} + \Delta E \end{cases}$$

$$\texttt{NPEX} = (A_1 \times E^2 + A_2 \times E^{-\Gamma}) \exp\left(-\frac{E}{E_{\rm cut}}\right)$$

`highecut` (White, Swank, et al., 1983) represents a powerlaw continuum modified by an exponential roll-off above energy E_{cut}. `mplcut` (Coburn et al., 2002) is a slightly modified version of `highecut` wherein the abrupt break in continuum at E_{cut} is smoothed out with a gaussian absorption model (`gabs` in XSPEC). Similarly, `FDcut` (Tanaka, 2005) has a Fermi-Dirac distribution-like function and `newhcut` (Burderi et al., 2000) has a third-order polynomial function to smoothen the kink at E_{cut}[11]. `NPEX` (Mihara, 1995) is a combination of two cutoff powerlaw functions, with the photon-index of one of the powerlaw components fixed to 2. `NPEX` mimics saturated inverse Compton scattering. We used `compTT` over the superior spectral models like `nthcomp` and `thcomp` because of its wide usage in the literature for modelling XRP

[11] We have consistently used ΔE=5 keV for the `newhcut` model throughout the analysis.

spectra in comparison to the other two. CRSF is modelled with a gaussian absorption profile (`gabs`) and iron fluorescence line with simple gaussian (`gaussian`). `newhcut` and `FDcut` are local models installed into XSPEC. All other spectral models used in this work are available in XSPEC[12].

Spectral analysis and Model selection Methodology

Our aim is to search for the best fitting composite spectral model for each *NuSTAR* observation (Table 3.2) and check if it contains the *TKF* model component. We employed a two-step spectral fitting process invoking the Akiake Information Criterion (Akaike, 1998) for finding the best fitting model. The AIC score for a model fit is given by

$$\mathrm{AIC} = 2n - 2ln(L_{\max}) = 2n + \chi^2_{\min}$$

Here, $L_{\max}$ is the maximum value of likelihood and $-2ln(L_{\max}) = \chi^2_{\min}$ is the equivalent minimum value of the fit statistic, and n is the number of model parameters. As evident from the equation, AIC score will be low for a model that fits the data well, but it increases with the complexity of the model (based on the number of model parameters). We compared the AIC scores of all the composite models derived from equation 3.1 after they were fitted to the spectrum of each observation, and chose the best fitting model based on the lowest AIC score.

Since the primary interest of this work is to identify the presence/absence of a spectral feature near 10 keV, we employed a two-step spectral fitting procedure so that importance is given to the 10 keV spectral band in the selection of the best fitting composite model.

Training and Validation

We performed an initial manual fit on the broadband spectrum of each observation (Table 3.2) to identify the presence of iron fluorescence line(s) and CRSF(s) in the spectrum. The spectrum from each observation in 3–15 keV (the *TKF* band) and 3–79 keV (broadband) was treated as two separate data sets, and we named them the 'Training' data set and the 'Validation' data set, respectively.

[12]https://heasarc.gsfc.nasa.gov/xanadu/xspec/manual/Models.html

The 3–15 keV training data set spectra were fitted with every possible composite model combination derived from

$$\frac{dN}{dE} = e^{-\sigma_{abs}(E)} \times \left(f e^{-\sigma_{\rm abs,local}(E)} + (1-f) \right) \times$$
$$[\text{continuum}(E) \times \text{gabs}_{TKF} + \text{gaussian}_{\rm Fe}(E) + \text{bbody}(E)] \quad (3.2)$$

The combinations were identified, ensuring that the continuum, `tbabs` and `gaussian` (if iron emission line is present) were included in all of them. Since the cutoff energy of most pulsars is beyond 15 keV, continuum models without a high energy cutoff (`powerlaw`, `cutoffpl`, `NPEX` and `compTT`) were only used for training. A total of 32 composite model candidates (without high energy cutoff continuum models) were tested on each training set.

The performance of each candidate model on the training set was evaluated based on AIC. Only those models were considered in which all the spectral parameters were within the globally accepted ranges. The accepted ranges of various spectral model parameters were chosen as follows: galactic absorption column density as per the source, partial covering absorption column density less than 10^{25} atoms cm^{-2}, powerlaw index between 0 and 3, high energy cutoff between 0 and 40 keV, T_0, kT and τ of `compTT` between 0.01–5 keV, 2–100 keV and 0.01–100, respectively, the line centre and line width of iron fluorescence emission between 6.2–6.8 keV and 0–1 keV, respectively, temperature kT of `bbody` between 0.01 and 3 keV, and the centre and width of the `gabs` used to model the *TKF* between 9–12 keV and 0–3 keV, respectively.

The best fitting training model so identified (having the lowest AIC), along with other models within 5% AIC score (or sometimes 10% AIC in case the 5% does not contain multiple candidates) were selected for fitting the 3–79 keV broadband validation data set. The validation was performed after including the extra `gabs` or `cyclabs` model component(s) to account for CRSF(s). If any of the training-screened composite models contain a simple `powerlaw` continuum, in addition to it, the same composite model after modifying with different kinds of high energy cutoff (`mplcut`, `newhcut`, `newhcut`) was also tested on the validation data set. The best-fitting composite model on the validation data set was selected based on the lowest AIC score and best fitting spectral parameters within the accepted ranges.

However, it was observed in some spectral data sets that none of the best-fitting training models would fit the validation data set well. In those cases, the training was skipped and single-step validation was performed using all the possible 56

composite model combinations derived from equation 3.2 (including the high energy cutoff continuum models) and the best-fitting model was selected following the same model screening procedure.

We report the presence of *TKF* only when all the best fitting composite model(s) on the validation data set within the top 5% AIC contain *TKF* model component.

The rest of this section briefs the details of each source and explains the spectral analysis performed on their *NuSTAR* observations. In each observation, the background-dominated spectral range is excluded from the fitting process. The figure showing the best fitting model (the unfolded spectrum and model in $\mathrm{E}\frac{dN}{dE}$ as solid curves, the contribution of additive model components as dotted curves) and residuals to the best fit model for one observation containing *TKF* and one observation not containing *TKF*, based on availability, of each source are also shown. In case *TKF* is required in the fit, a third panel showing the significance of *TKF* is also included. The data points from the FPMA instrument are shown in black and FPMB is shown in red. The fit statistic is χ^2 distributed in all the observations except Obs. Sn.45. The tables containing best fit spectral parameter values for each observation are given across four tables in Section. 3.1.4.

Her X–1

Hercules X–1 is a moderately bright, persistent, eclipsing intermediate mass X-ray binary (IMXB) pulsar with 1.24 s spin period (Tananbaum et al., 1972) located 6.6 kpc away, hosting a NS and a 2.3 $\mathrm{M}_{\odot}$ optical companion (Hz Her) in a low eccentricity orbit. Nearly edge-on view of the binary manifests as periodic ~ 1.7 d intensity variation in the X-ray light curve in the form of eclipses. In addition, it also exhibits a 35 d intensity modulation due to absorption by a precessing warped accretion disk (Giacconi, Gursky, Kellogg, Levinson, et al., 1973). The first ever report of CRSF in an XRP spectrum was with the balloon observations of Her X–1 (Trümper, Pietsch, et al., 1978). The broadband spectrum of Her X–1 is usually modelled with an absorbed powerlaw continuum with iron fluorescence lines, modified by CRSF at $\sim$ 38 keV (See Xiao et al., 2019).

We analysed the spectra from the observations Obs. Sn.1, 2 and 3 (Table 3.2). Obs. Sn.1 spans the eclipse and out of eclipse orbital phases of the binary. Therefore, the time average spectrum and out-of-the-eclipse phase spectrum of Obs. Sn.1 were analyzed. Galactic absorption towards the source could not be constrained by the fit, therefore we fixed it to the galactic value of 1.5×10^{20} atoms cm^{-2}. The iron emission line region is complex, and we modelled it with the combination of a narrow and

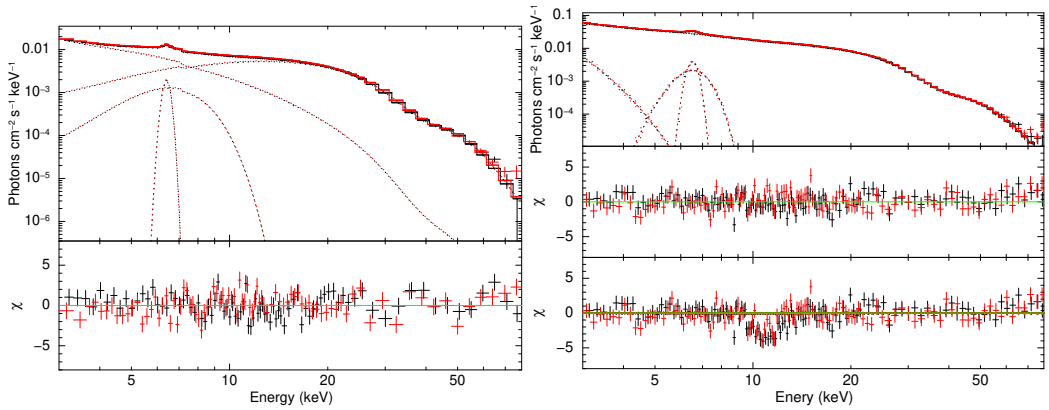

Fig. 3.2: Left: Spectral fit on Her X–1 Obs. Sn.1 with `NPEX` continuum model, having no *TKF*. The top panel shows the best-fit model and the bottom panel shows the residuals to the best-fit model. Right: Spectral fit on Her X–1 Obs. Sn.2. with `FDcut` continuum model, having *TKF*. The top panel shows the best-fit model, the middle panel shows the residuals to the best-fit model, and the bottom panel shows the residuals when the strength of the `gabs` component modelling *TKF* is set to 0.

a broad `gaussian` (adopted from Fuerst et al. 2013). CRSF at ~ 38 keV was fitted with a `gabs` model.

None of the best fitting training models could fit the validation data sets of Obs. Sn.2 and 3. Therefore, single-step fitting was performed on Obs. Sn.2 and 3 skipping training. The best-fitting models on the time-averaged and out-of-eclipse spectrum of Obs. Sn.1 does not contain *TKF*. The best fitting models on Obs. Sn.2 and 3 contain *TKF*.

The spectral parameters of the best fitting models for all three observations are given in Tables 3.4 and 3.5. The spectral fit for the time-averaged spectrum of Obs. Sn. 1 (having no *TKF*) and Obs. Sn. 2 (having *TKF*) are shown in Fig. 3.2.

Vela X–1

Vela X–1 (4U 0900-40) is a bright and persistent eclipsing HMXB pulsar hosting a NS and a B-type Super-giant stellar companion, located 1.9 kpc away. The XRP has a spin period of ∼283 s, and the binary has an orbital period of ∼8.9 d. Even though the typical X-ray luminosity of the pulsar is about 4×10^{36} erg s^{-1}, the relatively compact orbital separation keeps the pulsar embedded in the clumpy stellar wind of the companion, and this shows up as strong variability in XRP luminosity. CRSF has been detected in the source spectrum at two energies, with the fundamental line at ~ 25 keV and its harmonic at ~ 55 keV (See Kreykenbohm, I. et al. 2002 and

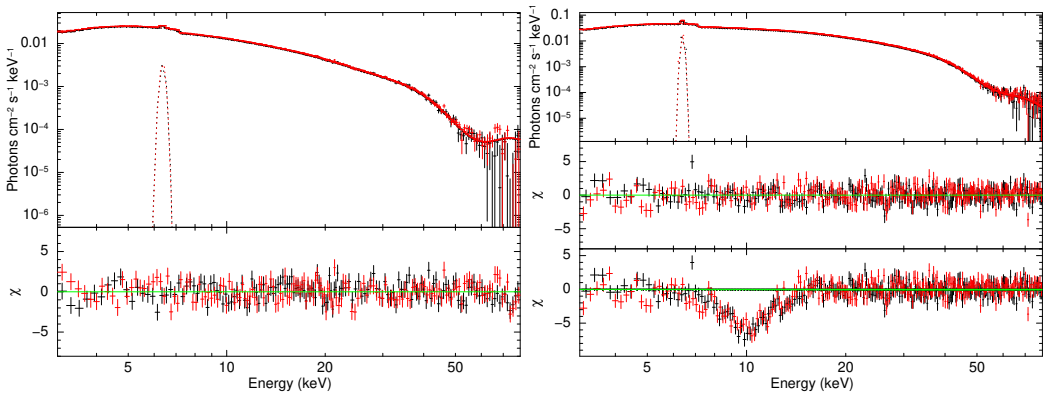

Fig. 3.3: Left: Spectral fit on Vela X–1 Obs. Sn.5 with `cutoffpl` continuum model, having no *TKF*. The top panel shows the best-fit model and the bottom panel shows the residuals to the best-fit model. Right: Spectral fit on Vela X–1 Obs. Sn.4. with `compTT` continuum model, having *TKF*. The top panel shows the best-fit model, the middle panel shows the residuals to the best-fit model, and the bottom panel shows the residuals when the strength of the `gabs` component modelling *TKF* is set to 0.

references therein, Maitra and Paul 2013b, and Fürst, Pottschmidt, Wilms, Tomsick, et al. 2013).

We analyzed the spectra from four observations Obs. Sn.4, 5, 6, and 7 (Table 3.2). Because of the presence of flare in Obs. Sn.7, we analysed the flaring state spectra of Obs. Sn.7. We could not get satisfactory fits for the time-averaged and out-of-flare-state spectra due to the presence of a narrow absorptive feature around 7 keV. Galactic absorption towards the source could not be constrained by the fit, therefore we fixed it to the galactic value of 3.7×10^{21} atoms cm^{-2}. Iron line emission was fitted with a `gaussian` model. The fundamental CRSF at ∼25 keV and its harmonic at ∼50 keV were fitted with two `gabs` model components. Iron fluorescence line was present, which was fitted with a `gaussian`. The width of CRSF was not constrained by the fit in Obs. Sn.4, it was thus fixed to the average width obtained from other observations. The width of CRSF was not constrained by the fit in the best fitting model containing *TKF* in Obs. Sn.6, it was fixed to the width from the best fitting model on Obs. Sn.6 not containing *TKF*.

The best fitting models on Obs. Sn.5 and 7 do not contain *TKF*, while the best fitting model on Obs. Sn.4 contains *TKF*. Even though the best fitting model Obs. Sn.6 contains *TKF*, there also exists a similar well-fitting model in which *TKF* is absent.

The spectral parameters of the best fitting models for all four observations are given in Tables 3.4 and 3.5. The spectral fit for the time-averaged spectrum of Obs. Sn. 4 (having TKF) and Obs. Sn.2 (having no TKF) are shown in Fig. 3.3.

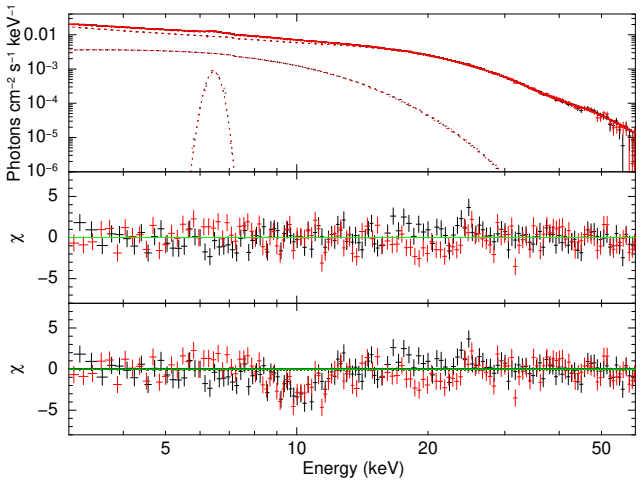

Fig. 3.4: Spectral fit on XTE J1946+274 Obs. Sn.8 using `mplcut` model, having *TKF*. The top panel shows the best-fit model, the middle panel shows the residuals to the best-fit model, and the bottom panel shows the residuals when the strength of the `gabs` component modelling *TKF* is set to 0.

XTE J1946+274

XTE J1946+274 is a transient HMXB pulsar at a distance of 9.5 ± 2.9 kpc, in which the binary hosts the NS and a Be-type stellar companion. The pulsar has a spin period of about 15.8 s, and the binary has an orbital period of about 169 d (See Doroshenko, Santangelo, Doroshenko, et al., 2017, and references therein). Interaction between the circumstellar equatorial disk of the Be companion and the pulsar at the periastron in a moderately eccentric orbit results in violent X-ray outbursts which appear as variability in the long-term X-ray light curve (Wilson, Finger, Coe, and Negueruela, 2003). CRSF has been reported in the source spectrum at ~ 38 keV (Heindl et al. 2001, Maitra and Paul 2013a, Doroshenko, Santangelo, Doroshenko, et al. 2017, Devaraj et al. 2022) and also at ~ 25 keV (Müller, S. et al., 2012).

We analyzed the 3–60 keV spectrum from Obs. Sn.8 (Table 3.2). Iron fluorescence line was present, which was fitted with a `gaussian`. CRSF centred around 40 keV was fitted with `gabs`.

The best fitting model on Obs. Sn.8 contains *TKF*.

The spectral parameters of the best fitting models for Obs. Sn.8 is given in Tables 3.4 and 3.5. The spectral fit for the time-averaged spectrum of Obs. Sn.8 (having TKF) is shown in Fig. 3.4

KS 1947+300

KS 1947+300 is a transient HMXB pulsar hosting the NS and Be-companion star in an almost circular orbit. The binary orbital period is about 41.5 d, and the pulsar has a spin period of 18.8 s (Fürst, Pottschmidt, Wilms, Kennea, et al., 2014, and references therein). CRSF was first reported in the *NuSTAR* spectrum of the source by Fürst, Pottschmidt, Wilms, Kennea, et al. (2014), but this discovery is debated (Doroshenko, Piraino, et al., 2020).

Fürst, Pottschmidt, Wilms, Kennea, et al. (2014) reported that the absorption feature detected in Obs. Sn.10 (for `highecut` model) could be CRSF. However, in a revisit of the same data and earlier *BeppoSAX* observations, Doroshenko, Piraino, et al. (2020) reported that a two-component `compTT` continuum model does not show such a prominent absorption feature and hence questioning the claim of CRSF.

We analyzed the spectra from three observations Obs Sn.9, 10 and 11 (Table 3.2), the same ones reported in Fürst, Pottschmidt, Wilms, Kennea, et al. (2014) and Doroshenko, Piraino, et al. (2020). The three observations covered the increase, peak and decline phase of the 2013 outburst of the source. Galactic absorption column density could be constrained by the fit. Iron fluorescence line was fitted with a `gaussian`.

None of the best fitting training models could fit the validation data sets of Obs. Sn.9 and 10. Therefore, single-step fitting was performed on Obs. Sn.9 and 10 skipping training. The best models for validation were based on the top 10% AIC on the training data set of Obs. Sn.11 because only one model was in the top 5% AIC. The best fitting models on Obs. Sn.9 and 10 do not contain *TKF*. The best-fitting model from training-validation on Obs. Sn.11 also does not contain *TKF*. We did not include the claimed *CRSF* feature around 10 keV during the fitting process and the best fitting models on all three observations do not contain an absorptive feature around 10 keV. Thus, our analysis indicates towards the result of Doroshenko, Piraino, et al. (2020) that the CRSF feature is not present.

The spectral parameters of the best fitting models for all three observations are given in Tables 3.4 and 3.5. The spectral fit for the time-averaged spectrum of Obs. Sn. 9 (having no *TKF*/CRSF) is shown in Fig. 3.5.

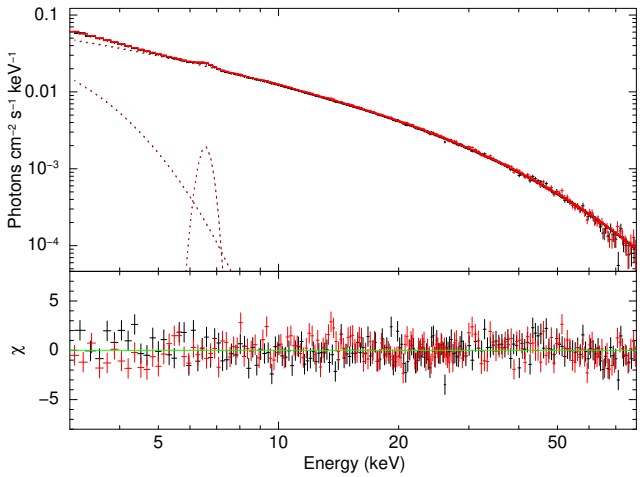

Fig. 3.5: Spectral fit on KS 1947+300 Obs. Sn.9 using `mplcut` model, having no *TKF*/CRSF. The top panel shows the best-fit model and the bottom panel shows the residuals to the best-fit model.

4U 1907+09

4U 1907+09 (X 1908+075) is a persistent HMXB pulsar with the NS accreting matter from the wind of an O-type Super-giant (Cox et al. 2005, Marshall et al. 1980). The HMXB has a relatively short orbital period of about 8 d, and the pulsar has a spin period of about 437.5 s (Makishima, Kawai, et al., 1984). The fundamental CRSF at 18 keV and its harmonic at 36 keV have been reported in the source (Cusumano et al., 2000).

We analyzed the 3–45 keV spectrum from one *NuSTAR* observation Obs. Sn.12 (Table 3.2). Iron fluorescence line was present, which was fitted with a `gaussian`. We used two `gabs` components centred at 18 keV and 36 keV respectively, to model the fundamental and harmonic CRSF, respectively.

All the training fits left absorption-like residuals between 5 and 10 keV. An absorptive feature around 8 keV has been reported by Tobrej et al. (2023). We, therefore, lowered the allowed *TKF* model centre between 6 and 9 keV. None of the best fitting training models could fit the validation data set of Obs. Sn.12. Therefore, single-step fitting was performed skipping training. The best fitting model on Obs. Sn.12 contains *TKF*, centred around 8 keV at a lower centre value than other cases.

The spectral parameters of the best fitting models for Obs. Sn.12 is given in Tables 3.4 and 3.5. The spectral fit for the time-averaged spectrum of Obs. Sn.12 (having TKF) is shown in Fig. 3.6.

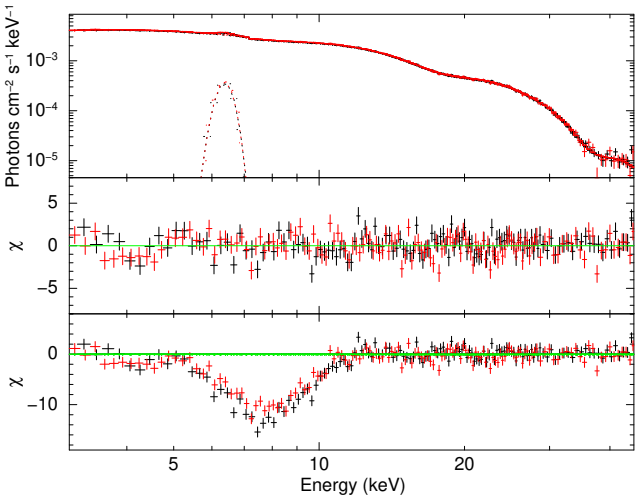

Fig. 3.6: Spectral fit on 4U 1907+09 Obs. Sn.12 with `CompTT` continuum model, having *TKF*. The top panel shows the best-fit model, the middle panel shows the residuals to the best-fit model, and the bottom panel shows the residuals when the strength of the `gabs` component modelling *TKF* is set to 0.

4U 1538–52

4U 1538–52 (4U 1538–522) is a bright, persistent eclipsing HMXB pulsar 6.6 kpc away, in which the NS accretes matter from the stellar wind of B-type Super-giant companion. The pulsar has a spin period of 526 s, and the binary has a relatively short orbital period of 3.73 d (See Malacaria, Jenke, et al. 2020, Hemphill, Rothschild, Cheatham, et al. 2019, and references therein.). CRSF has been reported in the source spectrum at ∼22 keV and ∼49 keV (Hemphill, Rothschild, Cheatham, et al., 2019).

We analyzed the spectrum from one observation of the source Obs. Sn.13 (Table 3.2). The light curve indicated that this *NuSTAR* observation spans the ingress, eclipse, and egress phases of the binary. Therefore, we extracted two sets of spectra: i) the time-averaged spectrum of the entire observation, and ii) the spectrum of the out-of-eclipse phase (∼11 ks of data covering ingress and egress phases).

Galactic absorption towards the source could not be constrained by the fit, therefore we fixed it to the galactic value of 7×10^{21} atoms cm^{-2}. Iron line emission was fitted with a `gaussian` model. CRSF at ∼22 keV is fitted a `gabs` model.

The best fitting models on both the time-averaged and out-of-eclipse spectra do not contain *TKF*.

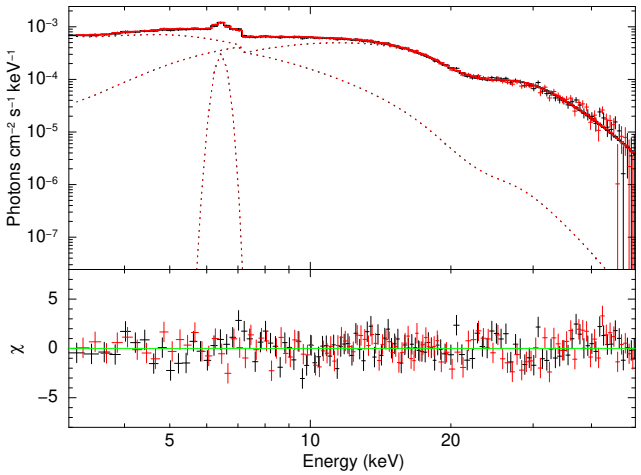

Fig. 3.7: Spectral fit on time average spectrum of 4U 1538–52 Obs. Sn.13 covering the eclipse and out-of-eclipse phases, with `NPEX` continuum model, having no *TKF*. The top panel shows the best-fit model and the bottom panel shows the residuals to the best-fit model.

The spectral parameters of the best fitting models for Obs. Sn.13 is given in Tables 3.4 and 3.5. The spectral fit for the time-averaged spectrum of Obs. Sn. 13 (having no TKF) is shown in Fig. 3.7.

Cepheus X–4

Cep X–4 (GS 2138+56) is a transient HMXB pulsar with $P_{spin} \sim 66.2$ s located 3.8 kpc away, in which the NS accretes from a Be-type stellar companion in a 20 d binary orbit (See Bonnet-Bidaud et al. 1998, Vybornov et al. 2017, and references therein.). CRSF has been found in the source at 30 keV (Mihara, Makishima, et al., 1991), and the asymmetric line profile of CRSF in the *NuSTAR* spectra was described with a combination of two Gaussian absorption model components centred at ~ 30 keV and ~ 19 keV respectively (Fürst, Pottschmidt, Miyasaka, et al., 2015).

We analyzed the 3–60 keV spectra from two observations Obs. Sn.14 and 15 (Table 3.2). Obs. Sn.14 probed the peak luminosity phase of the outburst of the source in 2014, while Obs. Sn.15 covered the luminosity decline phase of the same outburst. Iron line emission was fitted with a `gaussian` model. The CRSF at ∼22 keV having an asymmetric profile is fitted with the combination of two `gabs` models (Bhargava et al., 2019).

The best fitting models on both observations do not contain *TKF*.

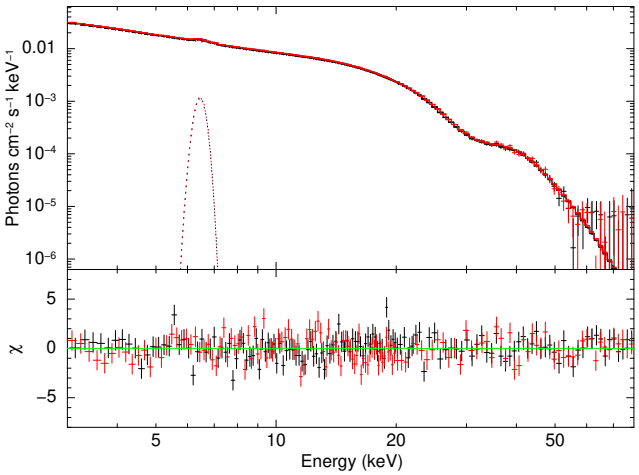

Fig. 3.8: Spectral fit on Cep X–4 Obs. Sn.14 with `compTT` continuum model, having no *TKF*. The top panel shows the best-fit model and the bottom panel shows the residuals to the best-fit model.

The spectral parameters of the best fitting models for both the observations are given in Tables 3.4 and 3.5. The spectral fit for the time-averaged spectrum of Obs. Sn. 14 (having no TKF) is shown in Fig. 3.8.

4U 1626-67

4U 1626-67 is an XRP in a Low mass Ultra-compact XRB (UCXB) pulsar hosting the NS having a spin period of 7 s (McClintock et al., 1977) and 0.04 $M_\odot$ companion star, with a short binary orbital period of about 42 minutes (Middleditch et al., 1981). CRSF has been reported in the spectrum at 37 keV (Orlandini, Dal Fiume, et al., 1998). Another peculiarity of the spectrum is the presence of low energy soft excess, which is usually modelled with a blackbody component of kT $\sim$ 0.6 keV (See Kii et al., 1986).

We have analyzed the spectrum from the observation Obs. Sn.16 (Table 3.2). All the powerlaw continuum models having a high energy cutoff could fit the spectrum well. Prominent residuals resembling absorption present at 37 keV could be flattened with `gabs`, which could be identified as the CRSF. The iron emission line was visible, and `gaussian` was used to fit it.

None of the best fitting training models could fit the validation data set of Obs. Sn.16. Therefore, single-step fitting was performed on Obs. Sn.16 skipping training. The best fitting model on Obs. Sn.16 does not contain *TKF*.

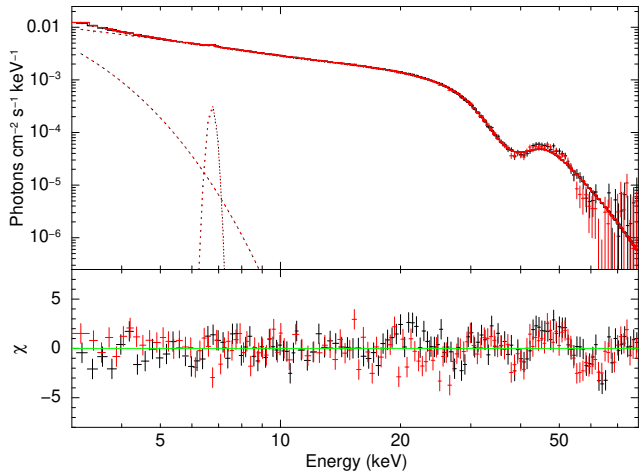

Fig. 3.9: Spectral fit with `FDcut` model on 4U 1626-67 Obs. Sn.16, having no *TKF*. The top panel shows the best-fit model and the bottom panel shows the residuals to the best-fit model.

The spectral parameters of the best fitting models for Obs. Sn.16 is given in Tables 3.4 and 3.5. The spectral fit for the time-averaged spectrum of Obs. Sn.16 (having no TKF) is shown in Fig. 3.9.

SMC X–2

SMC X–2 (2S 0052-739) is a bright transient HMXB XRP in the Small Magellanic Cloud (SMC) dwarf galaxy, located 65 kpc away (Li et al., 1977). The binary hosts the pulsar having spin period ~ 2.37 s (Corbet et al., 2001) and an O-type stellar companion (Crampton et al., 1978) in a 28.6 d orbit (Schurch et al., 2008). The X-ray spectrum is generally modelled with an absorbed powerlaw continuum modified by CRSF centred at ~ 27 keV (Jaisawal and Naik, 2016a).

We analysed the spectrum from three observations Obs. Sn. 17, 18 and 19 (Table 3.2) that probed the outburst of the source in 2015. Iron fluorescence line was present, which was fitted with a `gaussian`. CRSF at ~ 27 keV was fitted with a `gabs`. The width of CRSF was not constrained by the fit in Obs. Sn.19, it was thus fixed to the average width obtained from other observations.

The best fitting models of all three observations did not require *TKF*.

The spectral parameters of the best fitting models for Obs. Sn.17, 18 and 19 are given in Tables 3.4 and 3.5. The spectral fit for Obs. Sn.17 (having no TKF) is shown in Fig. 3.10.

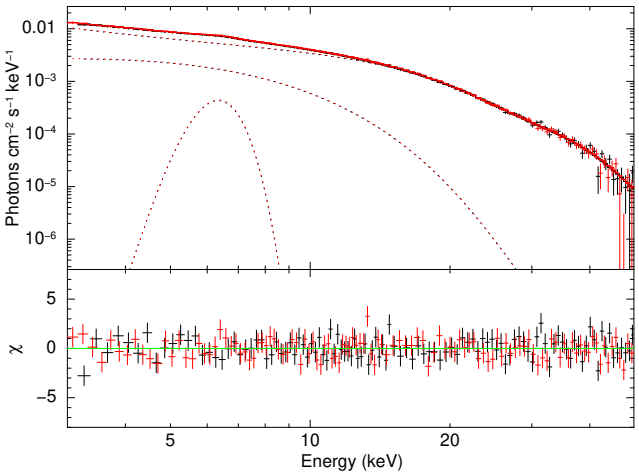

Fig. 3.10: Spectral fit on SMC X–2 Obs Sn.17 with `compTT` continuum model, having no *TKF*. The top panel shows the best-fit model and the bottom panel shows the residuals to the best-fit model.

The spectral parameters of the best fitting models for Obs. Sn.17, 18 and 19 are given in Tables 3.4 and 3.5. The spectral fit for Obs. Sn.17 (having no TKF) is shown in Fig. 3.10.

IGR J17544–2619

IGR J17544–2619 is a Super-giant fast X-ray transient located 4 kpc away (See Rampy et al., 2009, and references therein) in which, the NS in an HMXB accretes from the wind of an O-type Super-giant companion. The binary has an orbital period of 5 d (Clark, Hill, et al., 2009), and the NS has an (unconfirmed) spin period of 71.5 s (Drave, Bird, Townsend, et al. 2012 and Drave, Bird, Sidoli, et al. 2014). The spectrum is usually modelled with a combination of low energy thermal blackbody component and a high-energy non-thermal comptonization component, modified by fundamental CRSF at 17 keV and its harmonic at 30 keV (Bhalerao et al., 2015).

We analysed the 3–40 keV spectrum from Obs. Sn.20 (Table 3.2). The spectrum was dominated by background photons above 40 keV. CRSF present at $\sim$ 18 keV was modelled with a `gabs`.

The best fitting model on Obs. Sn.20 does not contain *TKF*.

The spectral parameters of the best fitting models for Obs. Sn.20 is given in Tables 3.4 and 3.5. The spectral fit for Obs. Sn.20 (having no TKF) is shown in Fig. 3.11.

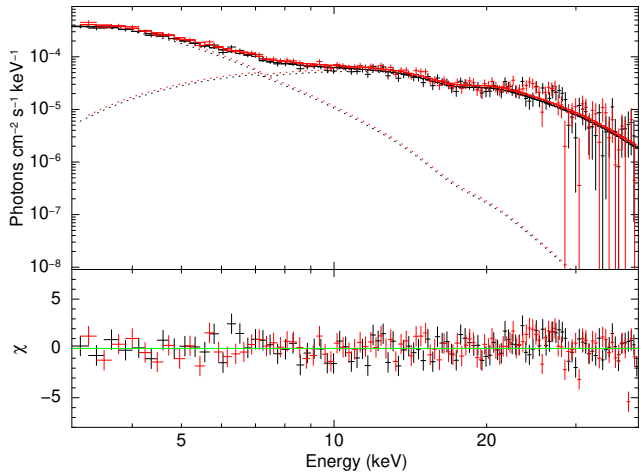

Fig. 3.11: Spectral fit on IGR J17544–2619 Obs Sn.20 with `NPEX` continuum model, having no *TKF*. The top panel shows the best-fit model and the bottom panel shows the residuals to the best-fit model.

IGR J16393–4643

IGR J16393–4643 is an HMXB pulsar in which the NS accretes from the wind of a stellar companion of an unknown spectral class. The pulsar has a spin period of 911 s, and the binary has an orbital period of ∼3.7 d (See Thompson et al., 2006, and references therein). It shows an unusual partial eclipse (Islam, Maitra, et al., 2015) which has also been interpreted to be the absorption of X-rays in the stellar corona with a grazing line of sight to the source (Kabiraj, Islam, et al., 2020). Galactic ISM heavily obscures photons from the source and the broadband spectrum is usually modelled with a heavily absorbed powerlaw continuum modified by CRSF at 30 keV (Bodaghee et al., 2016).

We analysed the 3–50 keV spectrum from Obs. Sn.21 (Table 3.2). The pointed observation is contaminated by stray light from a nearby source GX 340+0, but we have taken care of this during the selection of the source region. Galactic absorption towards the source could not be constrained by the fit, therefore we fixed it to the galactic value of 2.15×10^{21} atoms cm^{-2}. CRSF present at $\sim$ 30 keV was modelled with a `gabs`.

The best fitting model on Obs. Sn.21 contain *TKF*.

The spectral parameters of the best fitting models for Obs. Sn.21 is given in Tables 3.4 and 3.5. The spectral fit for Obs. Sn.21 (having TKF) is shown in Fig. 3.12.

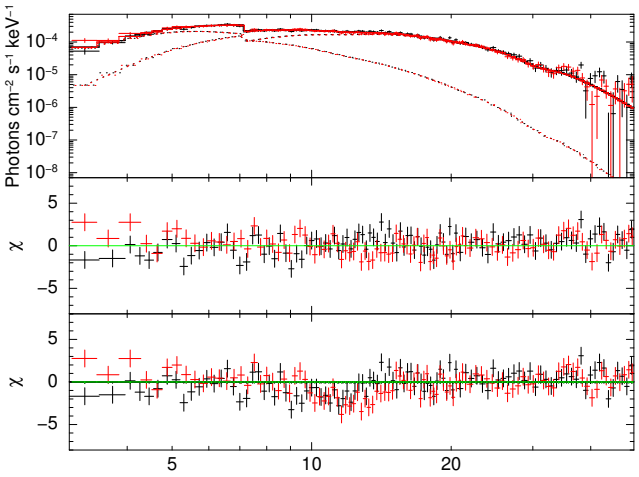

Fig. 3.12: Spectral fit on IGR J16393–4643 Obs Sn.21 with `NPEX` continuum model, having *TKF*. The top panel shows the best-fit model, the middle panel shows the residuals to the best-fit model, and the bottom panel shows the residuals when the strength of the `gabs` component modelling *TKF* is set to 0.

2S 1553–542

2S 1553–542 is a transient HMXB pulsar located at a distance of 20 ± 4 kpc on the far-side arms of Milkyway (Tsygankov, Lutovinov, Krivonos, et al. 2016 and Lutovinov, Buckley, et al. 2016). It consists of a NS with a spin period of 9.3 s accreting from a Be-type companion star in a 31 d binary orbit (See Kelley et al., 1983, and references therein). CRSF has been reported in the source at ~ 24 keV (Tsygankov, Lutovinov, Krivonos, et al., 2016).

We analysed the 3–50 keV spectrum from Obs. Sn. 22 (Table 3.2). Iron line emission was fitted with a `gaussian` model. CRSF at ~ 28 keV was fitted with `gabs`.

Since a high energy cutoff was present below 15 keV, the models containing a high energy cutoff were also included while fitting the training data set. The best fitting model on Obs. Sn. 22 does not require *TKF*.

The spectral parameters of the best fitting models for Obs. Sn.22 is given in Tables 3.4 and 3.5. The spectral fit for Obs. Sn.22 (having no TKF) is shown in Fig. 3.13.

RX J0520.5–6932

RX J0520.5–6932 is a transient XRP in the Large Magellanic Cloud (Schmidtke et al., 1996). The HMXB hosts the NS with spin period of ~ 8 s (Vasilopoulos et al., 2014) in a 24.4 d orbit around a Be-type companion star (See Coe et al. 2001, Kuehnel

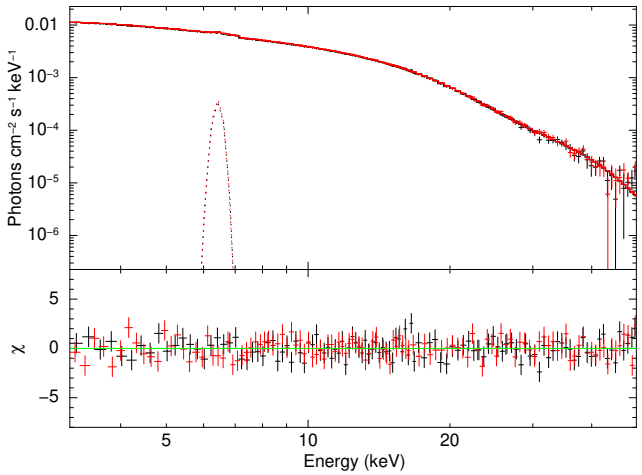

Fig. 3.13: Spectral fit on 2S 1553–542 Obs. Sn.22 with `FDcut` continuum model, having no *TKF*. The top panel shows the best-fit model and the bottom panel shows the residuals to the best-fit model.

et al. 2014, and references therein). CRSF has been reported in the spectrum at 31 keV (Tendulkar et al., 2014).

We analyzed the spectrum from two observations Obs. Sn.23 and 24 (Table 3.2). The spectra are background-dominated above 55 keV in both observations. Also, FPMA and FPMB spectra showed cross-calibration anomalies in 3-4 keV for Obs. Sn.23. Hence we analyzed the 3–55 keV spectrum of Obs. Sn.23 and 4–55 keV spectrum of Obs. Sn.24. Galactic absorption towards the source could not be constrained by the fit, therefore we fixed it to the galactic value of 2×10^{21} atoms cm^{-2}. Iron emission line was fitted with a `gaussian`. CRSF at ~ 30 keV was fitted with a `gabs`.

The best fitting models on both observations contain *TKF*.

The spectral parameters of the best fitting models for Obs. Sn.23 and 24 are given in Tables 3.4 and 3.5. The spectral fit for Obs. Sn.23 (having TKF) is shown in Fig. 3.14.

Cen X–3

Cen X–3 is a bright and persistent HMXB pulsar that hosts a NS that accretes from the wind of an O-type companion star. The binary has an orbital period of about 2.1 d (Schreier et al., 1972), and the NS has a spin period of 4.8 s (Giacconi, Gursky, Kellogg, Schreier, et al., 1971). CRSF is present in the source at 30 keV (See Tomar et al., 2021, and references therein).

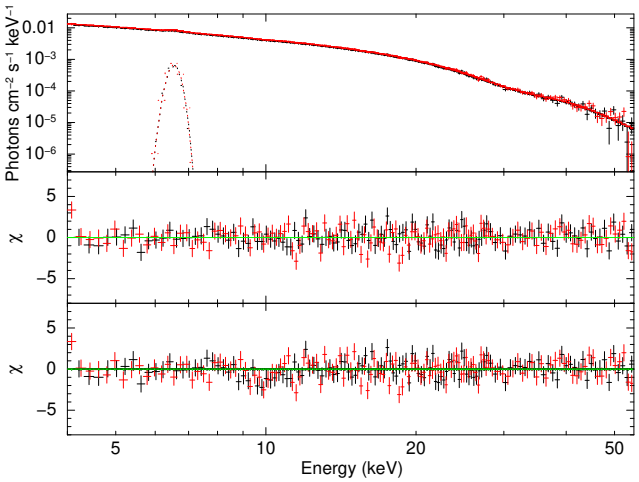

Fig. 3.14: Spectral fit on RX J0520.5–6932 Obs. Sn.23 with `cutoffpl` continuum model, having *TKF*. The top panel shows the best-fit model, the middle panel shows the residuals to the best-fit model, and the bottom panel shows the residuals when the strength of the `gabs` component modelling *TKF* is set to 0.

We analysed the 3–60 keV *NuSTAR* spectrum from Obs. Sn.25 (Table 3.2). Iron emission line was fitted with a `gaussian`. CRSF present at ~ 30 keV was fitted with a `gabs`.

Since a high energy cutoff was present below 15 keV, the models containing a high energy cutoff were also included while fitting the training data set. None of the best fitting training models could fit the validation data set of Obs. Sn.25. Therefore, single-step fitting was performed skipping training. The best fitting model on Obs. Sn.25 contain *TKF*.

The spectral parameters of the best fitting models for Obs. Sn.25 is given in Tables 3.4 and 3.5. The spectral fit for Obs. Sn.25 (having TKF) is shown in Fig. 3.15.

GX 301–2

GX 301–2 is a bright HMXB pulsar located ~ 4 kpc away, hosting a NS accreting from the wind of a hyper-giant 35 $M_\odot$ donor star. The pulsar has a relatively long spin period of ~ 680 s, and the binary has an eccentric orbit with an orbital period of 41 d which is manifested as periodic flares during the periastron passage of the NS (See Doroshenko, V. et al., 2010, and references therein). Its broadband spectrum is usually modelled by a powerlaw continuum modified by two distinct CRSFs at 35 keV and 55 keV (See Nabizadeh et al., 2019, and references therein).

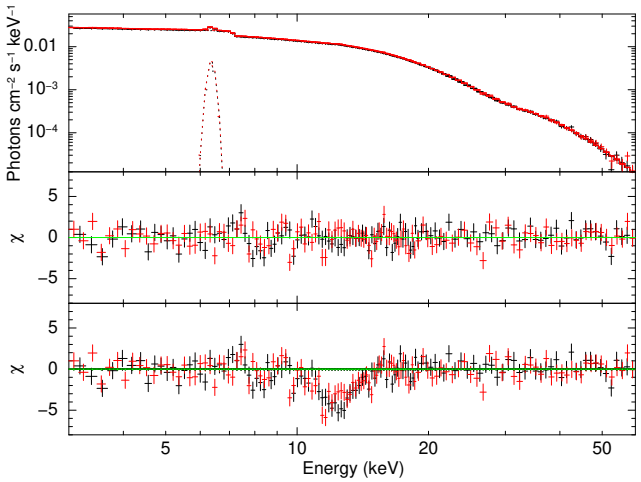

Fig. 3.15: Spectral fit with `mplccut` model on Cen X–3 Obs. Sn.25, having *TKF*. The top panel shows the best-fit model, the middle panel shows the residuals to the best-fit model, and the bottom panel shows the residuals when the strength of the `gabs` component modelling *TKF* is set to 0.

We analysed the 3-65 keV spectra from two observations Obs. Sn.26 and 27 respectively in Table 3.2. Since Obs. Sn.27 contains a flare, and therefore we analysed time-averaged, flare and out-of-flare spectra separately. Iron fluorescence line was present in all the spectra, which were fitted with a `gaussian`. The width of the iron emission line was not constrained by the fit in the out-of-flare-state spectrum of Obs. Sn.38 and we fixed it to 10 eV. Two CRSFs were present at ~ 30 keV and ~ 50 keV, and those were fitted with two `gabs`. The width of CRSF at 50 keV could be constrained in Obs. Sn.27 out-of-flare state and the flaring state spectrum of Obs. Sn.27. Therefore, it was frozen to the CRSF width obtained from time-averaged spectrum of Obs. Sn.27.

The best fitting models on none of the spectra contain *TKF*.

The spectral parameters of the best fitting models for Obs. Sn.26 and 27 are given in Tables 3.4 and 3.5. The spectral fit for Obs. Sn.26 (having no TKF) is shown in Fig. 3.16.

XTE J1829–098

XTE J1829–098 is a transient XRP having a spin period of 7.8 s. Even though the nature of the binary is considered an HMXB based on the observed hard spectrum, the classification of the companion is still uncertain. Assuming an O- or B-type nature to the companion, Halpern et al. (2007) estimated the distance to the binary as 10 kpc. The binary orbital period is considered to be the outburst recurrence

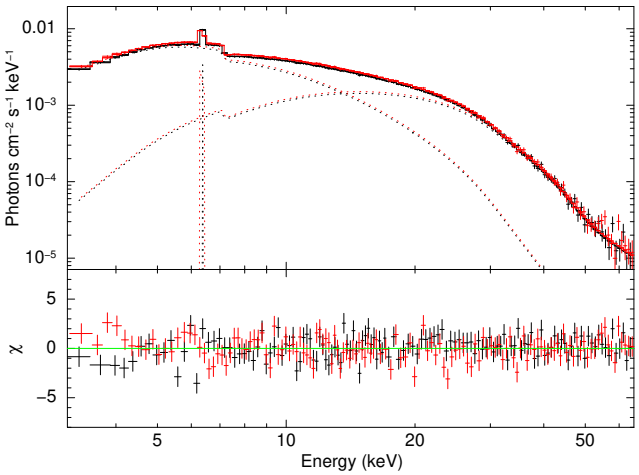

Fig. 3.16: Spectral fit using `mplcut` model on GX 301–2 Obs. Sn.26, having no *TKF*. The top panel shows the best-fit model and the bottom panel shows the residuals to the best-fit model.

interval of ~ 246 d. Its broadband spectrum is usually modelled with a powerlaw continuum, and a CRSF was reported at ~ 15 keV (See Shtykovsky, Lutovinov, Tsygankov, et al., 2019, and references therein).

We analyzed the 3–40 keV *NuSTAR* spectrum of the source (Obs. Sn.28 in Table 3.2) that probed an outburst of the source in 2018. The ISM absorption column density could be constrained by the fit, and the iron fluorescence line was fitted with a `gaussian`. This could be interpreted as the CRSF. The cutoff energy of the best fit powerlaw with high energy cutoff models is close to ~ 10 keV. Moreover, the CRSF present at ~ 15 keV would impact the *TKF* estimation. Therefore we performed direct validation to find the best-fitting model without *TKF*.

The spectral parameters of the best fitting models for Obs. Sn.28 is given in Tables 3.4 and 3.5. The spectral fit for Obs. Sn.28 (having no TKF) is shown in Fig. 3.17.

V0332+63

V 0332+53 is a bright transient HMXB pulsar located 7 kpc away hosting an O-type stellar companion and the NS having a spin period of 4.4 s. The binary has an eccentric orbit with an orbital period of 34 d. This is one of the few pulsars that exhibit multiple harmonics of the CRSF in the spectrum. The spectrum is usually modelled by a powerlaw continuum modified by a CRSF at 28 keV and its two harmonics at 49 keV and 72 keV respectively (See Tsygankov, Lutovinov, Churazov, et al., 2006, and references therein).

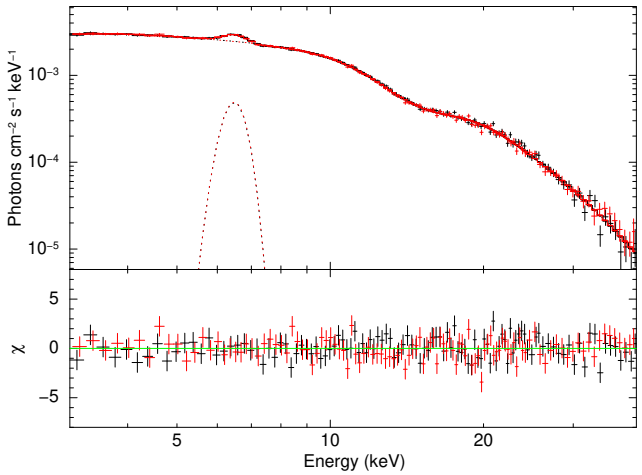

Fig. 3.17: Spectral fit using `newhcut` model on XTE J1829–098 Obs. Sn. 28, having no *TKF*. The top panel shows the best-fit model and the bottom panel shows the residuals to the best-fit model.

We analysed the 3–55 keV spectrum from the four observations Obs. Sn.29, 30, 31 and 32 (Table 3.2). Iron fluorescence line was present in all the spectra, which were fitted with a `gaussian`. The width of the iron emission line was not constrained by the fits and we fixed it to 10 eV. CRSF at ~ 28 keV and its first harmonic at ~ 56 keV fitted with `cyclabs`. We also tried using `gabs` to fit the CRSF, but it left residuals at high energies. The width of harmonic CRSF could not be constrained in the best fit models on Obs. Sn.29 and 30 containing *TKF*. Therefore, it was fixed to the CRSF width obtained from the best fit models on Obs. Sn.29 and 30 that does not contain *TKF*.

The best-fitting models on Obs. Sn.29 and 32 do not contain *TKF*. Even though the best fitting model Obs. Sn.30 and 31 contain *TKF*, there also exist similar well-fitting models in which *TKF* is absent.

The spectral parameters of the best fitting models for Obs. Sn.29, 30, 31 and 32 are given in Tables 3.6 and 3.7. The spectral fit for Obs. Sn.30 (having no TKF) is shown in Fig. 3.18.

XTE J1858+034

XTE J1858+034 is a transient Be-XRP with spin period ~ 221 s located ~ 10 kpc away. The regular outburst period of ~ 380 s is considered as the orbital period of the binary. The broadband spectrum is generally modelled by a powerlaw continuum with a cutoff at high energy, modified by iron fluorescence line at 6.5 keV and CRSF at ~ 48 keV (See Malacaria, Kretschmar, et al., 2021, and references therein).

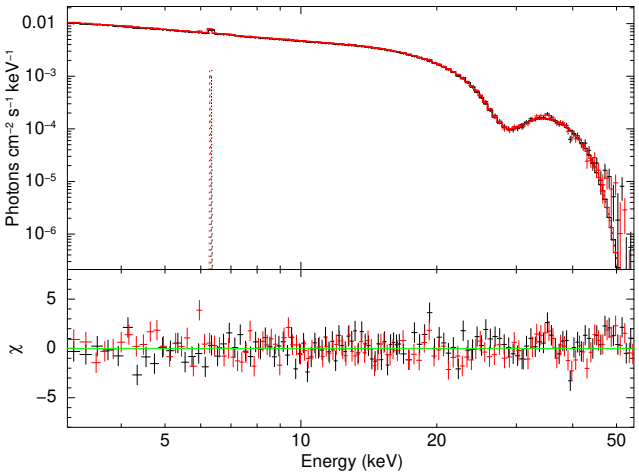

Fig. 3.18: Spectral fit on V 0332+53 Obs. Sn.30 with `newhcut` continuum model, having no *TKF*. The top panel shows the best-fit model and the bottom panel shows the residuals to the best-fit model.

We analysed the 5–55 keV spectrum of the source. The spectrum is background-dominated above 55 keV, and the FPMA/FPMB spectra below 5 keV showed cross-calibration anomalies. Iron fluorescence line was present, which was fitted with a `gaussian`. CRSF centred around 50 keV was fitted with `gabs`.

The best-fitting models on Obs. Sn.33 does not contain *TKF*.

The spectral parameters of the best fitting models for Obs. Sn.33 is given in Tables 3.6 and 3.7. The spectral fit for Obs. Sn.33 (having no TKF) is shown in Fig. 3.19.

4U 1700–37

4U 1700–37 is a transient HMXB in which a NS accretes from the wind of a supergiant O-type star in a 3.5 d binary orbit. Even though coherent pulsations were reported at 67 s from Tenma observation during a flare, none of the other observatories has detected pulsations in the subsequent observations. The spectrum of 4U 1700–37 is usually modelled with powerlaw continuum models, and CRSF has been reported at two different energies of 16 keV (Bala, Roy, et al., 2020) and 37 keV (Reynolds et al., 1999).

Obs. Sn.34 (Table 3.2) contains a flare as evident from the light curve. We, therefore, analysed the 3–79 keV *NuSTAR* time-averaged, flare and out-of-flare spectra from Obs. Sn.34. Galactic absorption towards the source could not be constrained by the fit, therefore we fixed it to the galactic value of 5×10^{21} atoms cm^{-2}. Iron fluorescence line was present, which is fitted with a `gaussian`. The width of the

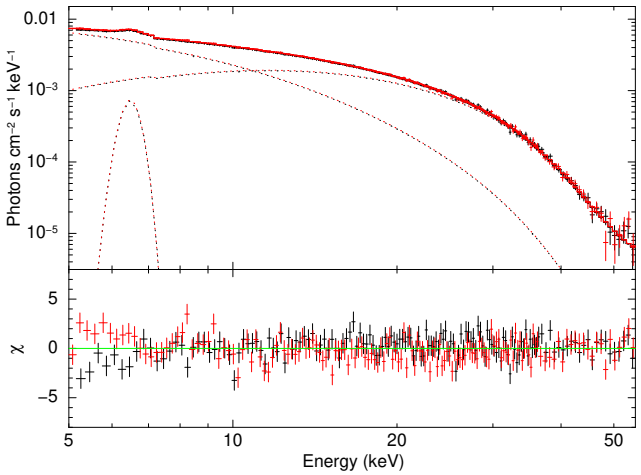

Fig. 3.19: Spectral fit using `NPEX` continuum model on XTE J1858+034 Obs. Sn.33, having no *TKF*. The top panel shows the best-fit model and the bottom panel shows the residuals to the best-fit model.

iron emission line was not constrained by the fit and we fixed it to 10 eV. CRSF at ~ 16 keV was fitted with a `gabs` model. The width of CRSF was not constrained by the fit in the flaring state spectrum, it was thus fixed to the width obtained from the time-averaged spectrum.

The best fitting models on the time-averaged, flaring state and out-of-flare state spectrum of Obs. Sn.34 contains *TKF*.

The spectral parameters of the best fitting models for Obs. Sn.34 is given in Tables 3.6 and 3.7. The spectral fit for Obs. Sn.34 (having TKF) is shown in Fig. 3.20.

LMC X–4

LMC X–4 is a persistent flaring HMXB pulsar (P_{spin}∼13.5 s) located ~ 50 kpc away in the Large Magellanic Cloud (LMC) satellite galaxy, hosting a NS pulsar that accretes from the disk-fed matter of an O-type companion star in a 1.4 d orbit. The spectrum of LMC X–4 is usually fitted with powerlaw continuum models with fluorescence lines of iron (Levine, Rappaport, et al., 1991).

We analysed six spectra from four *NuSTAR* observations Obs. Sn.35, 36, 37 and 38 (Table 3.2). Obs. Sn.35 and 38 have flares in the light curves, and therefore the separated flare and out-of-flare spectra were independently analysed. Galactic absorption towards the source could not be constrained by the fit, therefore we fixed it to the galactic value of 8×10^{20} atoms cm^{-2}. Iron fluorescence line was present in all the spectra, which were fitted with a `gaussian`. The width of the iron emission

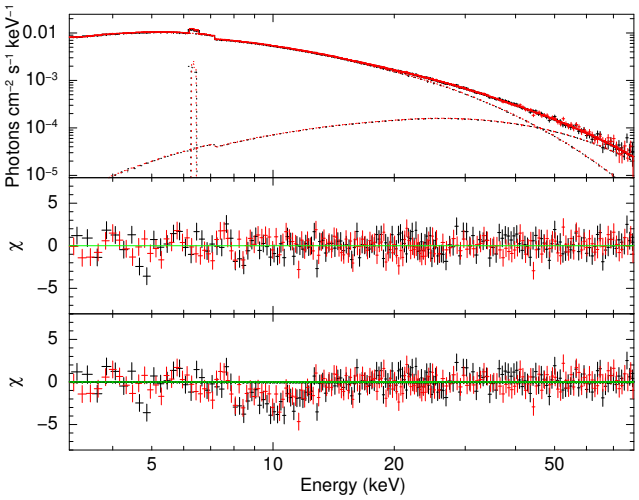

Fig. 3.20: Spectral fit using `NPEX` continuum model on 4U 1700–37 Obs. Sn.34 time-averaged spectrum, having *TKF*. The top panel shows the best-fit model, the middle panel shows the residuals to the best-fit model, and the bottom panel shows the residuals when the strength of the `gabs` component modelling *TKF* is set to 0.

line was not constrained by the fit in the out-of-flare-state spectrum of Obs. Sn.38 and we fixed it to 10 eV.

The best fitting models on the time-averaged and flaring-state spectrum of Obs. Sn.35, and time-averaged spectrum of Obs. Sn.38 contain *TKF*. The best fitting model on the out-of-flare-state spectrum of Obs. Sn.38 does not contain *TKF*. Even though the best fitting models on the out-of-flare-state spectrum of Obs. Sn.35, the flaring-state spectrum of Obs. Sn.38 and time-averaged spectra of Obs. Sn.36 and 37 contain *TKF*, there also exist similar well-fitting models in which *TKF* is absent.

The spectral parameters of the best fitting models for Obs. Sn.35, 36, 37 and 38 are given in Tables 3.6 and 3.7. The spectral fit for the time-averaged spectrum of Obs. Sn.35 (having TKF) and out-of-flare-state spectrum of Obs. Sn.35 (having no TKF) are shown in Fig. 3.21.

IGR J17329–2731

IGR J17329–2731 is a transient XRP in a Symbiotic X-ray Binary (SyXB) hosting the slow spinning ~ 6680 s pulsar accreting from the wind of a late M-type giant stellar companion. The source is estimated to be at a distance of 2.7 kpc. The broadband spectrum is modelled with a powerlaw continuum modified by CRSF at ~ 21 keV and iron fluorescence lines (Bozzo et al., 2018).

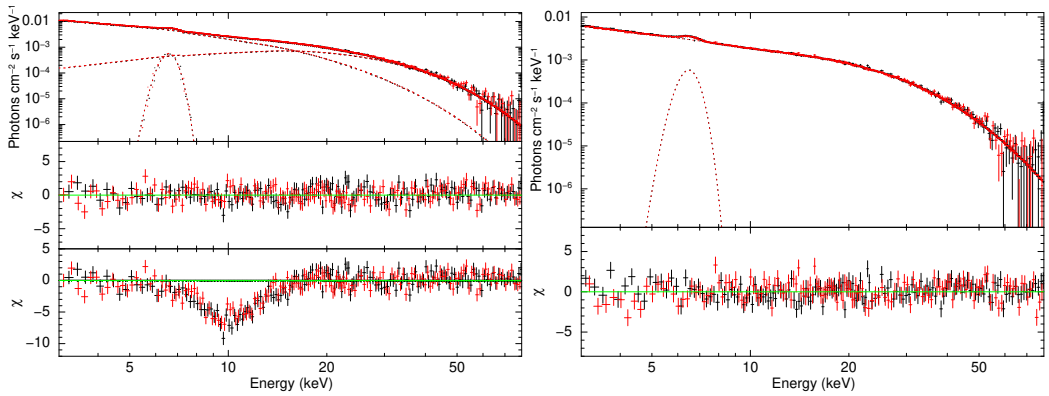

Fig. 3.21: Left: Spectral fit on LMC X–4 Obs. Sn.35 time-averaged spectrum. with `NPEX` continuum model, having *TKF*. The top panel shows the best-fit model, the middle panel shows the residuals to the best-fit model, and the bottom panel shows the residuals when the strength of the `gabs` component modelling *TKF* is set to 0. Right: Spectral fit on LMC X–4 Obs. Sn.35 out-of-flare state spectrum with `FDcut` continuum model, having no *TKF*. The top panel shows the best-fit model and the bottom panel shows the residuals to the best-fit model.

We analysed the 3–55 keV spectrum from the observation Obs. Sn.39 (Table 3.2). Galactic absorption towards the source could not be constrained by the fit, therefore we fixed it to the galactic value of 3×10^{21} atoms cm^{-2}. Iron fluorescence line was present, which is fitted with a `gaussian`. The width of the iron emission line was not constrained by the fit and we fixed it to 10 eV. CRSF at ~ 22 keV was fitted with a `gabs` model.

The best fitting models on Obs. Sn.39 does not contain *TKF*.

The spectral parameters of the best fitting models for Obs. Sn.39 is given in Tables 3.6 and 3.7. The spectral fit for Obs. Sn.39 (having no TKF) is shown in Fig. 3.22.

SMC X–1

SMC X–1 is an HMXB pulsar in the Small Magellanic Cloud located ~ 61 kpc away. This eclipsing binary consists of a ~ 0.7 s NS pulsar in ~ 3.89 d orbit around a B-type Super-giant companion star and is one of the few HMXBs that accrete via Roche lobe overflow. The broadband spectrum is usually modelled by absorbed powerlaw models and iron fluorescence line (See Pike et al., 2019, and references therein).

We analysed the spectra of SMC X–1 from four *NuSTAR* observations Obs. Sn.40, 41, 42 and 43 (Table 3.2). Galactic absorption towards the source could not be constrained by the fit, therefore we fixed it to the galactic value of 5×10^{21} atoms cm^{-2}. Iron fluorescence line was present, which is fitted with a `gaussian`.

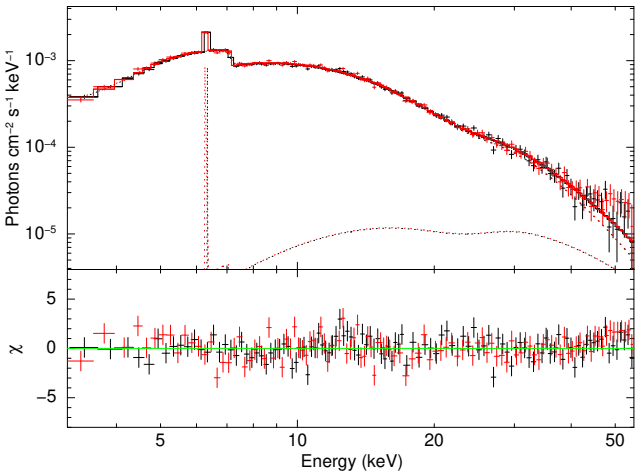

Fig. 3.22: Spectral fit on IGR J17329–2731 Obs. Sn.39 using `NPEX` continuum model, having no *TKF*. The top panel shows the best-fit model and the bottom panel shows the residuals to the best-fit model.

The best fitting models on Obs. Sn.40, 41 and 42 do not contain *TKF*. Even though the best fitting models on Obs. Sn.43 could contain *TKF* there also exists a similar well-fitting model in which *TKF* is absent.

The spectral parameters of the best fitting models for Obs. Sn.40, 41, 42 and 43 are given in Tables 3.6 and 3.7. The spectral fit for the time-averaged spectrum of Obs. Sn.40 (having no TKF) is shown in Fig. 3.23.

GRO J1008–57

GRO J1008–57 is a transient HMXB pulsar located ∼5 kpc away, hosting a ~ 94 s pulsar and a Be-type stellar companion. The source shows regular outbursts at a period of ~ 249 d, interpreted as the binary orbital period. The spectrum is usually modelled with powerlaw continuum modified by CRSF at ~ 78 keV (See Kühnel et al. 2013, Bellm et al. 2014 and references therein).

We analysed the 3–79 keV *NuSTAR* spectrum from Obs. Sn.44. Galactic absorption towards the source could be constrained by the fit. Iron fluorescence line was present, but fitting it with a `gaussian` line left residuals in the iron region. This could be attributed to improper modelling of the complex iron fluorescence emission region, as the presence of lines at 6.4 keV, 6.6 keV and 7 keV have been reported in the *Suzaku* observations in Yamamoto, Mihara, et al. (2014). Therefore, we used a combination of two `gaussian` models to fit the complex iron region (similar to 3.1.2). The cyclotron line parameters could not be constrained by the fit, therefore

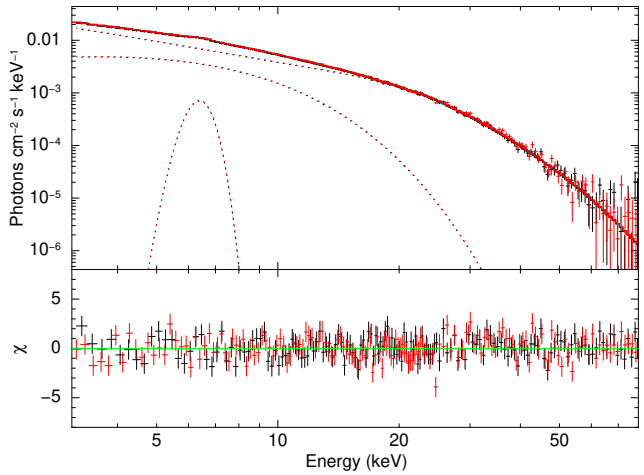

Fig. 3.23: Spectral fit performed on SMC X–1 Obs. Sn.40 using `mplcut` continuum model, having no *TKF*. The top panel shows the best-fit model and the bottom panel shows the residuals to the best-fit model.

we froze the CRSF line energy to the best fit value obtained by Bellm et al. (2014) from simultaneous *Suzaku*/HXD (20–100 keV) and *NuSTAR* (3–79 keV) spectra.

None of the best fitting training models could fit the validation data sets in Obs. Sn.44. Therefore, single-step fitting was performed on Obs. Sn.44, skipping training. The best fitting model on Obs. Sn.44 does not contain *TKF*.

The spectral parameters of the best fitting models for Obs. Sn.44 is given in Tables 3.6 and 3.7. The spectral fit for Obs. Sn.44 (having no TKF) is shown in Fig. 3.24.

GX 304–1

GX 304–1 is a transient Be-XRP located ~ 2 kpc away that hosts the ~ 272 s pulsar and Be-type companion star in a long ~ 133 d orbit. It exhibits regular Type-I outbursts during its periastron passage. The luminosity of the source varies over a wide range spanning several orders of magnitude like other Be-XRPs. CRSF has been detected in the high luminosity outburst-state spectrum at ~ 54 keV, which was modelled with a powerlaw continuum model (Yamamoto, Sugizaki, et al., 2011). The low luminosity spectrum is modelled by a two-component comptonization model (Tsygankov, Rouco Escorial, et al., 2019).

We analysed the 3–25 keV *NuSTAR* spectrum from Obs. Sn.45, during which the source was in a low-luminosity state. The spectrum is dominated by background photons above 25 keV. This observation has poor photon statistics, with an average count rate of ~ 0.21 counts s^{-1} and a total exposure of ∼58 ks (See Table 3.2).

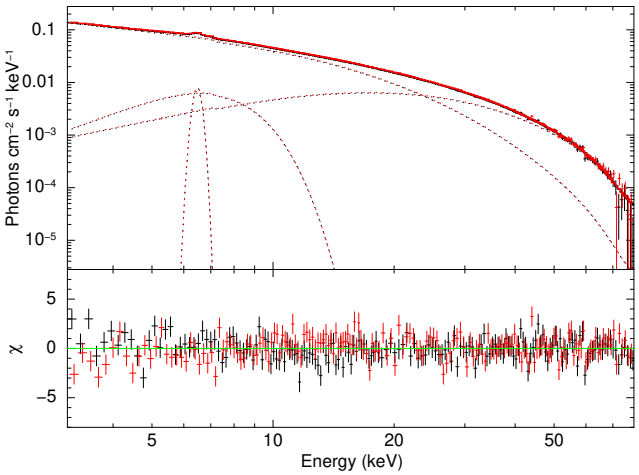

Fig. 3.24: Figure showing spectral fit using `NPEX` continuum model on GRO J1008–57 Obs. Sn.44, having no *TKF*. The top panel shows the best-fit model and the bottom panel shows the residuals to the best-fit model.

Therefore we re-binned the spectrum such that it has a minimum of 1 count per energy bin and have used Cash-statistic (cstat in XSPEC) as the fit statistic for analysing this *NuSTAR* observation.

We found that some of the model combinations given in Sec. 3.1.2 could fit the training and validation sets. However, as discussed in Tsygankov, Rouco Escorial, et al. (2019), the spectrum of GX 304–1 shows a transition from single powerlaw to double powerlaw, when the source luminosity drops by ~ 2 orders of magnitude. We found that double powerlaw models could also fit the spectrum. The best fitting model on Obs. Sn.45 does not contain *TKF*.

The spectral parameters of the best fitting models for Obs. Sn.45 is given in Tables 3.6 and 3.7. The spectral fit for Obs. Sn.45 (having no TKF) is shown in Fig. 3.25.

1A 0535+26

1A 0535+26 is a transient HMXB pulsar located 2 kpc away that hosts the pulsar spinning with a period of 104 s in an eccentric and long 110 d orbit around the Be-type stellar companion. It exhibits regular Type-I outbursts during the periastron passage and Type-II outbursts due to companion stellar activity. It is known to exhibit long out-of-flare states as well (See Ballhausen et al. 2017, and references therein), and the source flux, therefore, spans several orders of magnitude. The source spectrum shows fundamental CRSF at about 45 keV and first harmonic at about 100 keV (See Sartore et al., 2015, and references therein). The high luminosity level spectra are usually modelled with powerlaw continuum models (Mandal et

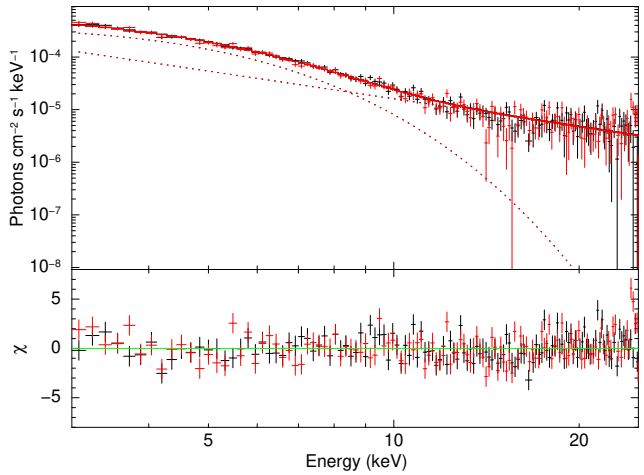

Fig. 3.25: Spectral fit using `NPEX` continuum model performed on GX 304–1 Obs. Sn.45, having no *TKF*. The top panel shows the best-fit model and the bottom panel shows the residuals to the best-fit model.

al., 2022) while the low luminosity spectra are modelled with a two-component comptonization model (Tsygankov, Doroshenko, Mushtukov, Suleimanov, et al., 2019).

We analysed spectra from three *NuSTAR* observations of the source, Obs. Sn.46, 47 and 48 (Table 3.2). Obs. Sn. 47 and 48 were dominated by background photons above 50 keV. Galactic absorption towards the source could not be constrained by the fit in Obs. Sn.48, therefore we fixed it to the galactic value of 4×10^{21} atoms cm^{-2}. Iron fluorescence line was present in Obs. Sn.46 and 47, which were fitted with a `gaussian`. CRSF at ~ 45 keV was fitted with a `gabs` model in Obs. 46 and 48, and it was not required in Obs. Sn.47. The width of CRSf could not be constrained by the fit in Obs. Sn.48, therefore it was fixed to the best fit value obtained from Obs. Sn.46.

All the models that could fit Obs. Sn.48 by Training/Validation gave systematic wavy residuals in 3–20 keV, regardless of the best fitting models having no *TKF*. Therefore, Obs. Sn.48 was fitted manually with a two-component `CompTT` model (See Tsygankov, Doroshenko, Mushtukov, Suleimanov, et al. 2019), and it does not contain *TKF*.

The spectral parameters of the best fitting models for Obs. Sn.46, 47 and 48 are given in Tables 3.6 and 3.7. The spectral fit for the time-averaged spectrum of Obs. Sn.46 (having no TKF) is shown in Fig. 3.26.

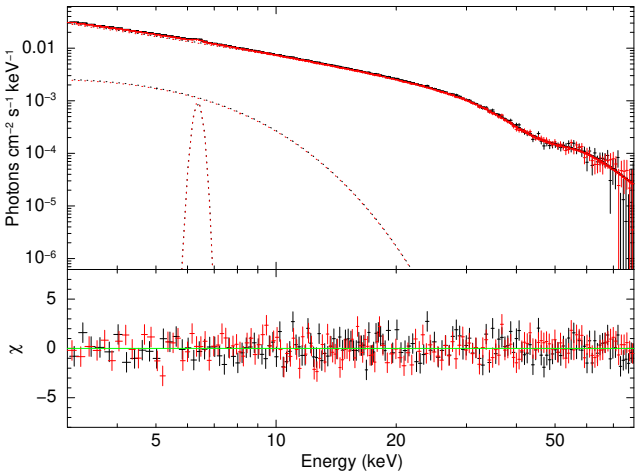

Fig. 3.26: Spectral fit using `FDcut` continuum model performed on 1A 0535+26 Obs. Sn.46, having no *TKF*. The top panel shows the best-fit model and the bottom panel shows the residuals to the best-fit model.

GRO J2058+42

GRO J2058+42 is a bright transient HMXB pulsar with P_{spin}∼198 s located 9 kpc away, hosting the pulsar and a Be-type companion star (Wilson, Weisskopf, et al., 2005). The binary orbital period of this system is ambiguous due to the ambiguity in the perceived intensity levels of successive outbursts. An outburst interval of 55 d is interpreted as the orbital period when each outburst is assumed to be occurring due to the periastron passage, or 110 d if the successive outbursts are distinguishable, with one from the apastron and the next from the periastron. Molkov et al. (2019) reported the presence of CRSF at $\sim$ 10 keV and two of its harmonics at $\sim$ 20 keV and $\sim$ 30 keV in the *NuSTAR* spectrum in a narrow spin phase interval. The presence of spin phase-dependent CRSF and two of its harmonics were later reported by Mukerjee et al. (2020) in the *Astrosat* spectrum as well. However, analysis of the spin-phase averaged *NuSTAR* spectrum by Kabiraj and Paul (2020) didn't require these CRSF lines. The presence of the possible CRSF near 10 keV makes it almost impossible to detect *TKF* even if it exists.

We analysed the spectra from three *NuSTAR* observations of the source Obs. Sn.49 (3–79 keV), 50 (3–79 keV) and 51 (3–50 keV) (Table 3.2). Galactic absorption towards the source could not be constrained by the fit, therefore we fixed it to the galactic value of 6×10^{21} atoms cm^{-2}. Iron fluorescence line was present, which is fitted with a `gaussian`. No significant residuals resembling the reported CRSF line were visible during the fitting, probably because it becomes evident only if one performs spin-phase resolved spectroscopy (See Molkov et al. 2019).

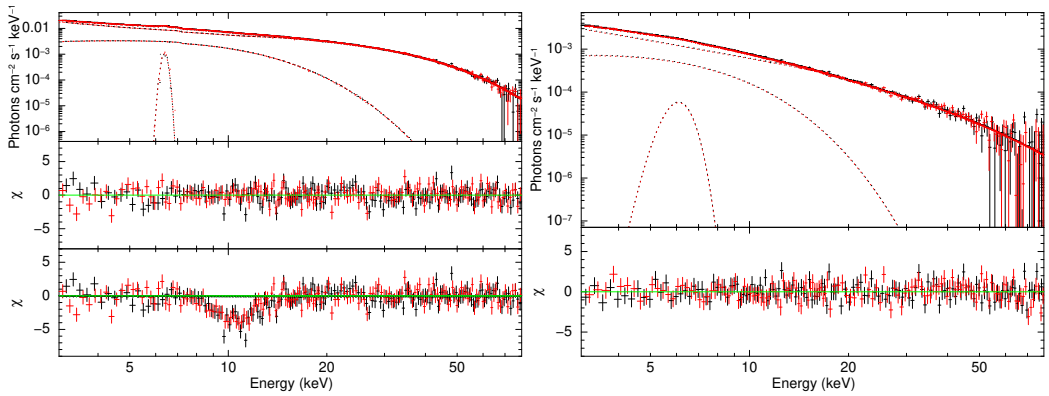

Fig. 3.27: Left: Spectral fit on GRO J2058+42 Obs. Sn.49 with `compTT` continuum model, having *TKF*. The top panel shows the best-fit model, the middle panel shows the residuals to the best-fit model, and the bottom panel shows the residuals when the strength of the `gabs` component modelling *TKF* is set to 0. Right: Spectral fit on GRO J2058+42 Obs. Sn.51 with `newhcut` continuum model, having no *TKF*. The top panel shows the best-fit model and the bottom panel shows the residuals to the best-fit model.

The best fitting models on Obs. Sn.49 and 50 contain *TKF*, while the best fitting model on Obs. Sn.51 does not contain *TKF*.

The spectral parameters of the best fitting models for Obs. Sn.49, 50 and 51 are given in Tables 3.6 and 3.7. The spectral fits for Obs. Sn.49 (having TKF) and Obs. Sn.51 (having no TKF) are shown in Fig. 3.27.

1E 1145.1–6141

1E 1145.1–6141 is a persistent HMXB pulsar located ~ 8.5 kpc away, hosting the 297 s pulsar that accretes from the wind of B-type Supergiant companion star in an eccentric ($e \sim 0.2$), 14.4 d orbit (See Ray et al. 2002, Ghising et al. 2022), and references therein.

We analysed the 3–60 keV spectrum from one *NuSTAR* observation of the source, Obs. Sn.52 in Table 3.2. Iron fluorescence line was present, which is fitted with a `gaussian`.

The best fitting model on Obs. Sn.52 does not contain *TKF*.

The spectral parameters of the best fitting models for Obs. Sn.52 is given in Tables 3.6 and 3.7. The spectral fit for the time-averaged spectrum of Obs. Sn.52 (having no TKF) is shown in Fig. 3.28.

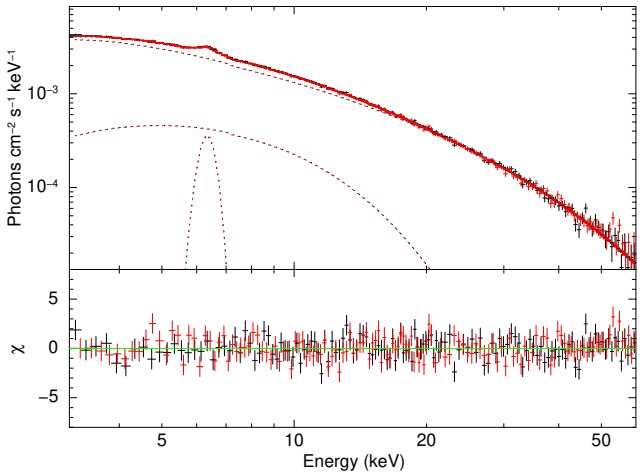

Fig. 3.28: Spectral fit using `newhcut` continuum model on 1E 1145.1–6141 Obs. Sn.52, having no *TKF*. The top panel shows the best-fit model and the bottom panel shows the residuals to the best-fit model.

OAO 1657–415

OAO 1657–415 is an HMXB pulsar located ~ 2.2 kpc away, hosting the 38 s pulsar in an eccentric orbit ($e \sim 0.1$) around the early type Ofpe/WN9 Supergiant. The binary has an orbital period of about 10.4 d (See Saavedra et al., 2022, and references therein). The spectrum of OAO 1657–415 is generally characterized by heavily absorbed powerlaw models modified by CRSF at ~ 36 keV (Orlandini, Fiume, Del Sordo, et al. 1999, Pradhan, Maitra, Paul, Islam, et al. 2014a).

We analysed the 5–70 keV spectrum from one *NuSTAR* observation of the source, Obs. Sn.53 in Table 3.2. The FPMA module was contaminated by stray light from a nearby source, because of which there was a significant deviation in spectra from FPMA and FPMB below ~ 5 keV. We tried selecting an annular background region around the source region in FPMA so that the background would include any streak of stray light contaminating the source region. Even though the residuals improved, residuals still deviated in FPMA and FPMB below 5 keV. Galactic absorption towards the source could not be constrained by the fit, therefore we fixed it to the galactic value of 1.81×10^{22} atoms cm^{-2}. Iron fluorescence line was present, which is fitted with a `gaussian`. The width of the iron emission line was not constrained by the fit and we fixed it to 10 eV.

The best fitting model on Obs. Sn.53 does not contain *TKF*.

The spectral parameters of the best fitting models for Obs. Sn.53 is given in Tables 3.6 and 3.7. The spectral fit for the time-averaged spectrum of Obs. Sn.53 (having no TKF) is shown in Fig. 3.29.

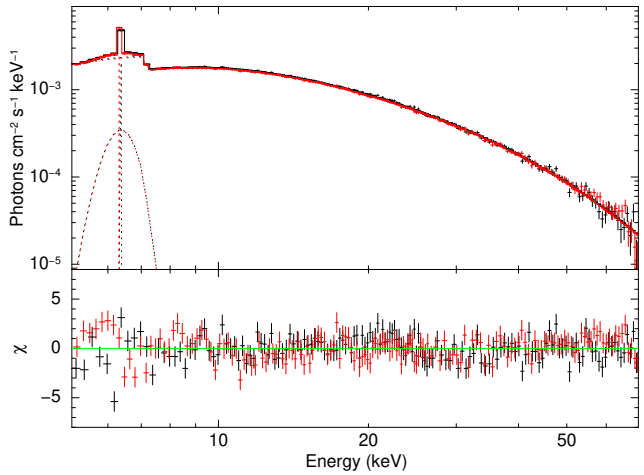

Fig. 3.29: Spectral fit using `cutoffpl` continuum model on OAO 1657–415 Obs. Sn.53. Top panel shows the best fit model and the bottom panel shows the residuals to the best fit model.

EXO 2030+375

EXO 2030+375 is a transient HMXB pulsar with $P_{spin} \sim 42$ s located about 7 kpc away, that hosts the NS and a Be-companion star in an eccentric (e∼0.36) 46 d orbit (See Parmar, White, et al. 1989 and Wilson, Finger, Coe, Laycock, et al. 2002). EXO 2030+375 is a well-studied source, and it exhibits regular Type-I outbursts during every periastron passage. Its outburst spectrum is generally modelled with an absorbed powerlaw model having an exponential cutoff at high energy, with emission lines of iron (See Reig and Coe 1999 and Naik, Maitra, et al. 2013). CRSF has not been reported in the spectrum.

We analysed the spectra from three *NuSTAR* observations, Obs. Sn.54 (3–55 keV), Obs. Sn.55 (3–79 keV) and Obs. Sn.56 (3–79 keV) (Table 3.2). Galactic absorption towards the source could not be constrained by the fit, therefore we fixed it to the galactic value of 8×10^{21} atoms cm^{-2}. Iron fluorescence line was present in all the observations, which were fitted with a `gaussian`. The width of the iron emission line was not constrained by the fit in Obs. Sn.55 and we fixed it to 10 eV.

The best fitting models on Obs. Sn.54 and 56 contain *TKF*, while the best fitting model on Obs. Sn.55 does not contain *TKF*.

The spectral parameters of the best fitting models for Obs. Sn.54, 55 and 56 are given in Tables 3.6 and 3.7. The spectral fit for the time-averaged spectrum of Obs. Sn.54 (having *TKF*) and Obs. Sn.55 (having no TKF) are shown in Fig. 3.30.

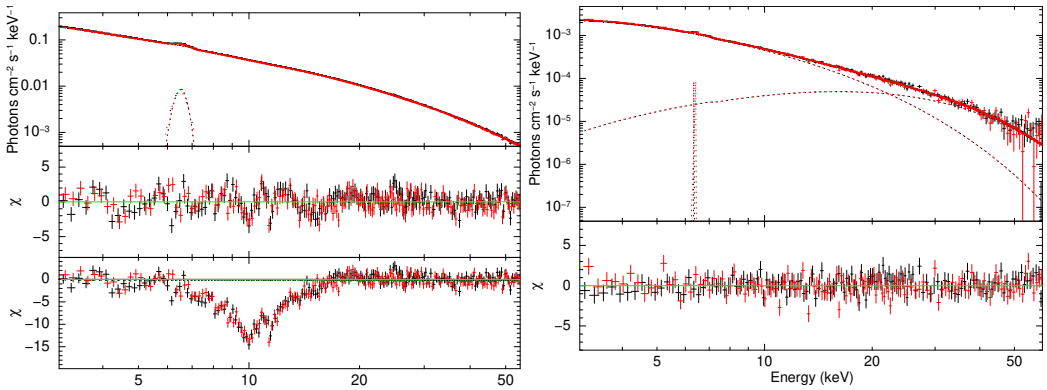

Fig. 3.30: Left: Spectral fit on EXO 2030+375 Obs. Sn.54 with `cutoffpl` continuum model, having *TKF*. The top panel shows the best-fit model, the middle panel shows the residuals to the best-fit model, and the bottom panel shows the residuals when the strength of the `gabs` component modelling *TKF* is set to 0. Right: Spectral fit on EXO 2030+375 Obs. Sn.55 with `NPEX` continuum model, having no *TKF*. The top panel shows the best-fit model and the bottom panel shows the residuals to the best-fit model.

IGR J19294+1816

IGR J19294+1816 is a transient HMXB pulsar located ~ 11 kpc away in the Perseus spiral arm of Milkyway, hosting the NS and a Be-type companion. The NS has a spin period of 12.4 s, and the binary has an orbital period of about 117 d (See Rodriguez et al. 2009, and references therein). The source spectrum is characterized by an absorbed powerlaw. Discovery of CRSF was claimed in the RXTE spectrum at ~ 35 keV by Roy et al. (2017). However, a reanalysis of the same data by Tsygankov, Doroshenko, Mushtukov, Lutovinov, et al. (2019) could not detect this CRSF. They detected the CRSF at ~ 42 keV in the *NuSTAR* data, and the same line was detected by Raman et al. (2021) in the *Astrosat* data.

We analysed the spectra from two *NuSTAR* observations, Obs. Sn.57 and Obs. Sn.58 (Table 3.2). Obs. Sn.57 and 58 were dominated by background photons above 20 keV and 50 keV respectively. Therefore 3–20 keV spectrum of Obs. Sn.57 and 3–50 keV spectrum of Obs. Sn.58 were analysed. Iron fluorescence line was present only in Obs. Sn.57, which was fitted with a `gaussian`. The spectrum of Obs. Sn.58 could be fitted without the requirement of the CRSF reported in Tsygankov, Doroshenko, Mushtukov, Lutovinov, et al. (2019).

The best models for validation were based on the top 10% AIC on the training data set of Obs. Sn.57 because only one model was in the top 5% AIC. The best fitting models on Obs. Sn.56 and 57 do not contain *TKF*.

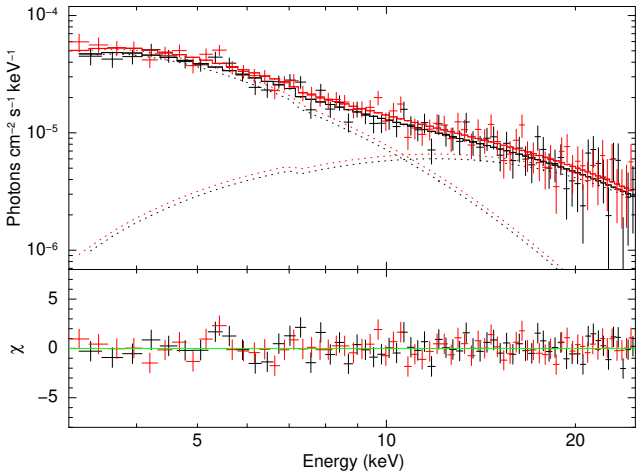

Fig. 3.31: Spectral fit using NPEX continuum model on IGR J19294+1816 Obs. Sn.57, having no *TKF*. The top panel shows the best-fit model and the bottom panel shows the residuals to the best-fit model.

The spectral parameters of the best fitting models for Obs. Sn.57 and 58 are given in Tables 3.6 and 3.7. The spectral fit for Obs. Sn.57 (having no *TKF*) is shown in Fig. 3.31.

3.1.3 Discussion

We (re)analysed the *NuSTAR* broadband spectra of 30 XRPs (Table 3.2), and 9 of them viz., Vela X–1, Her X–1, XTE J1946+274, 4U 1907+09, 4U 1538–52, Cep X–4, SMC X–1, GX 304–1 and EXO 2030+375 (See Table 3.1) have previous report(s) of *TKF*. After separating the flare and out-of-flare spectra in observations containing flares, separating the eclipse and out-of-eclipse spectra in observations containing eclipses, and by performing a systematic two-step spectral analysis of each observation given in Table 3.2 that gives importance to data in the 3–15 keV (where *TKF* is present) in the model selection, we detected *TKF* in 11 sources viz., Her X–1, Vela X–1, XTE J1946+274, 4U 1907+09, IGR J16393–4643, RX J0520.5–6932, Cen X–3, 4U 1700–37, LMC X–4, GRO J2058+42 and EXO 2030+375. This is contrary to previous reports of *TKF* in 4U 1538–52, Cep X–4, SMC X–1 and GX 304–1, and no previous reports of *TKF* in IGR J16393–4643, RX J0520.5–6932, Cen X–3, 4U 1700–37, LMC X–4 and GRO J2058+42. The centre of the gabs used to model the *TKF* varies in a very narrow range about 10 keV, while the width varies between 1-2 keV. The significance of this feature varies, which is very low in some observations (See Figs. 3.12 and 3.14), moderately significant in some (See Figs. 3.2, 3.4, 3.15) and prominent in others (See Figs. 3.3, 3.21 and 3.30).

The best fitting composite model(s) on the broadband (3–79 keV) data were identified from a set of composite models screened based on how well they fit the 3–15 keV narrower passband (10 keV range) data. The best fitting model was selected based on AIC score that considers the fit statistic but also penalizes for the model's complexity (Refer Sec. 3.1.2). The presence of *TKF* was assessed from the presence of `gabs` component modelling *TKF* in the composite model. As a consequence of this model selection methodology, different observations of the same source were sometimes fitted with different continuum models. This is however justified as the literature shows that the observations acquired at different times from the same source have often been fitted with different continuum models (See Table 3.1). Also, there are instances where the best fitting models from this work have *TKF* but individual spectral analysis of some of these observations reported by other authors do not report this feature (See for eg. Tomar et al. 2021, Bhalerao et al. 2015 and Bodaghee et al. 2016). However, it is inevitable when the selection of the best fitting model on a large set of observations happens in a systematic fashion.

Of the 58 different observations, 14 observations from 11 sources have shown the presence of this feature. Due to the presence of a CRSF at ~ 15 keV, this feature could not be checked on one observation of XTE J1829–098 (Obs. Sn.28). Because none of the mentioned models could give good fits to the spectrum, Obs. Sn.48 of 1A 0535+26 could not be checked for this feature. Therefore, the presence of *TKF* could be checked in 56 observations out of 58. Single-step validation fitting process had to be performed on 8 observations as the best-fit training models does not fit the validation data set. The two step fitting process as outlined before could be performed on 48 observations out of 58.

We screened the best fitting models on the validation set within the top 5% AIC score and have reported the best two models of two different kinds amongst them, in which one contains *TKF* and the other doesn't. In some cases, the best-fitting models on the validation set within the top 5% AIC score only contain one kind of model, in which case only one is reported. 36 out of 58 observations only had the best fitting models that do not contain *TKF*. Out of the rest, 6 out of 22 could be well fitted with two different kinds of composite models in which one contains *TKF* while the other doesn't contain *TKF*. Of the rest, 14 out of 16 include only the composite model containing *TKF* in the top 5% AIC. The two left-out observations (Obs. Sn.35 and 38) showed something peculiar; these are the two observations of LMC X–4 and have a flare in each of them. The best fitting models on the time-averaged spectra of Obs. Sn.38 contain *TKF*, while the best fitting models on the separated flaring state and out-of-flare state spectra of Obs. Sn.38 do not contain *TKF*. This is not, however, entirely true for Obs. Sn. 35. While the time-averaged spectra of 35 could only be

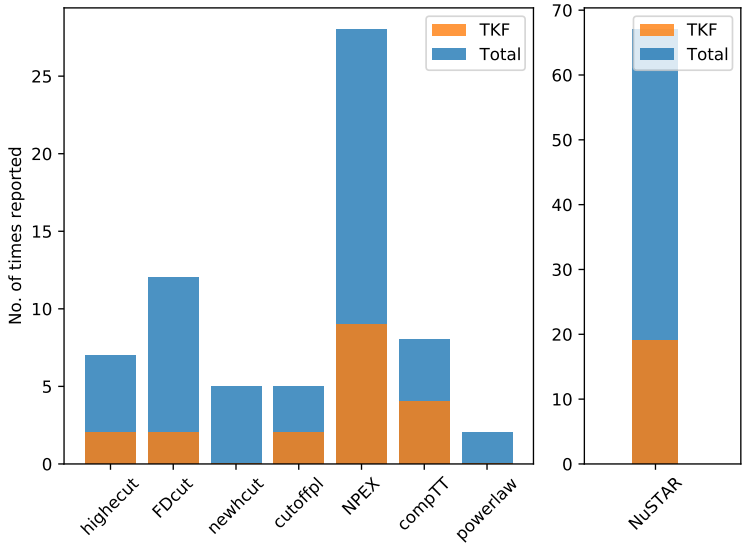

Fig. 3.32: The bar chart shows the results of our analysis of the *NuSTAR* spectral data. The distributions of *TKF* found for different continuum models are shown.

fitted with models containing *TKF* and the out-of-flare state spectrum does not need the feature, the flaring state spectrum shows the presence of it. This indicates that a combination of the flare and out-of-flare state spectrum could also mimic *TKF* like residuals. However, this was not observed in 4U 1700–37 (Obs. Sn.34), where the best fitting models to time-averaged as well as separated flare and out-of-flare state spectra contain *TKF*. A bar chart representation of the *TKF* detected with different continuum models in this work are shown in Fig. 3.32. Of the 67 spectra analysed in this work from 58 observations, `NPEX` was the continuum model that fitted the majority of the spectra (28 out of 67), of which *TKF* was detected in 19 spectra. However, the 19 *TKF* detections also include the 6 spectral sets of LMC X–4, where the presence of flare is possibly causing the presence of *TKF*. Excluding those 6, there are 13 spectral sets with a *TKF* detection.

In 4U 1907+09 (Obs. Sn.12), there were systematic absorption residuals left by almost every fit near 8 keV, and hence we re-performed the fitting by allowing the centre of the `gabs` accounting *TKF* to vary down to a lower limit of 7 keV. This is an exception to other cases of detection where the centre of *TKF* stayed within 9-11 keV. We also found that the best fitting models on none of the *NuSTAR* observations of KS 1947+300 have an absorption feature near 12 keV (Sec. 3.1.2, Fig. 3.5), whose identification as CRSF (Fürst, Pottschmidt, Wilms, Kennea, et al., 2014) or an artifact due to two-component comptonization model in low luminosity XRPs (Doroshenko, Santangelo, Doroshenko, et al., 2017) is debated.

The accretion-powered X-ray pulsars show flares and dips in their light curves, and sometimes there are spectral changes associated with the change in intensity (Pradhan, Maitra, Paul, Islam, et al., 2014b). Analysis of time-averaged spectrum, including persistent intensity, dips, flares, eclipses etc., is equivalent to fitting spectra of the sum of different powerlaw components with a single powerlaw. We have taken care of this in the current analysis. XRPs also show a significant variation in absorption column density with time (Pradhan, Maitra, Paul, Islam, et al., 2014b). We have used a partial covering absorption model to account for the column density variations at short intervals which may happen due to the clumpiness of the stellar wind of the companion. In particular, *TKF* was not observed in broadband X-ray spectra of XRPs when a partial covering absorption component was used in Maitra and Paul (2013a) and Maitra, Paul, and Naik (2012). As mentioned in Section. 3.1, analysis of the same data by different groups also have obtained different results regarding the *TKF*. In a systematic spectral study of the CRSF in XRPs using *BeppoSAX* by Doroshenko (2017), *TKF* was not required to model the spectrum in any of the sources as well. This feature being consistently at or near 10 keV, is unlikely to be related to the magnetic field of the neutron star. It was noted earlier that instead of some physical reason, the *TKF* appears from modelling the continuum below the cutoff energy with a simple model, and the `NPEX` model was moderately successful in removing this feature from the residuals in some cases (Coburn et al., 2002). Since the feature appears around the same energy in many sources regardless of changes in other source parameters like X-ray luminosity, CRSF energy, etc, it is difficult to understand the physical origin of this feature.

It is also worth noting that features that perfectly resemble *TKF* have been reported in other classes of sources like non-pulsating neutron star X-ray binaries as well, for instance, the *Ginga* observation of GX 5-1 reported in Asai et al. (1994). However, this additional feature is neither reported nor has any mention in the subsequent observations of the same source by *INTEGRAL* (Paizis et al., 2005) and *NuSTAR* (Homan et al., 2018). In the recent *NuSTAR* observations, the authors have used multi-component continuum models that have transition near 10 keV (See Fig. 2 of Homan et al. 2018). *TKF* seen in XRPs could also be similar in nature.

We also provide the parameters of the CRSF detected in the *NuSTAR* observations of XRPs analysed in this work in Table. 3.3.

Tab. 3.3: Table showing the CRSF line parameters measured from the spectral fits on the NuSTAR observations of sources used in this work. CRSF was not detected in KS 1947+300, LMC X-4, SMC X-1, GX 304-1, GRO J2058+42, 1E 1145.1-6141, OAO 1657-415, EXO 2030+375, and IGR J19294+1816. All the CRSF parameters of GRO J1008-57 reported at 78 keV could not be estimated because the CRSF line energy falls at the boundary of the 3-79 keV spectral coverage of *NuSTAR*. The errors quoted on all the parameters are their 90% confidence intervals

		Fundamental CRSF			Harmonic CRSF		
Source	Obs. Sn.	$E_{cyc,F}$ (keV)	$\sigma_{cyc,F}$ (keV)	Strength[§]	$E_{cyc,H}$ (keV)	$\sigma_{cyc,H}$ (keV)	Strength[§]
Her X–1	1 (ta)	$38.20^{+0.34}_{-0.33}$	$7.12^{+0.30}_{-0.29}$	$15.76^{+1.32}_{-1.22}$	–	–	–
	1 (oe)	$38.19^{+0.56}_{-0.53}$	$6.18^{+0.59}_{-0.53}$	$8.86^{+1.45}_{-1.23}$	–	–	–
	2	$37.31^{+0.23}_{-0.22}$	$6.67^{+0.46}_{-0.34}$	$13.91^{+2.71}_{-1.58}$	–	–	–
	3	$37.16^{+0.20}_{-0.20}$	$6.75^{+0.25}_{-0.28}$	$13.13^{+1.14}_{-1.03}$	–	–	–
Vela X–1	4	$24.79^{+0.97}_{-1.13}$	4.60⋆	$0.54^{+0.15}_{-0.12}$	$54.48^{+0.77}_{-0.67}$	$7.50^{+0.79}_{-0.65}$	$15.93^{+2.73}_{-2.09}$
	5	$26.37^{+1.24}_{-1.26}$	$3.83^{+1.15}_{-1.32}$	$0.82^{+0.49}_{-0.42}$	$57.18^{+0.83}_{-1.24}$	$9.59^{+-9.59}_{-1.23}$	$34.56^{+4.80}_{-7.16}$
	6	$27.05^{+0.58}_{-0.53}$	$5.83^{+0.57}_{-0.53}$	$3.31^{+0.80}_{-0.79}$	$52.59^{+1.07}_{-0.97}$	$8.95^{+-8.95}_{-1.16}$	$25.67^{+7.96}_{-6.93}$
	7 (f)	$27.71^{+1.26}_{-2.51}$	$3.40^{+2.12}_{-1.49}$	$1.10^{+1.29}_{-0.59}$	$56.72^{+1.93}_{-2.34}$	$9.16^{+-9.16}_{-2.27}$	$34.91^{+10.50}_{-14.07}$
XTE J1946+274	8	$38.55^{+0.87}_{-0.81}$	$5.03^{+0.71}_{-0.64}$	$3.63^{+1.06}_{-0.84}$	–	–	–
4U 1907+09	12	$17.98^{+0.08}_{-0.08}$	$2.69^{+0.12}_{-0.11}$	$3.02^{+0.21}_{-0.17}$	$36.70^{+0.42}_{-0.37}$	$3.28^{+0.35}_{-0.31}$	$7.09^{+0.93}_{-0.83}$
4U 1538-52	13 (ta)	$22.25^{+0.17}_{-0.17}$	$3.49^{+0.18}_{-0.17}$	$6.37^{+0.47}_{-0.44}$	–	–	–
	13 (ooe)	$22.35^{+0.21}_{-0.20}$	$3.39^{+0.22}_{-0.20}$	$6.18^{+0.55}_{-0.51}$	–	–	–
Cep X–4	1	$30.47^{+0.14}_{-0.14}$	$5.17^{+0.19}_{-0.20}$	$14.08^{+0.80}_{-0.71}$	–	–	–
	15	$29.35^{+0.22}_{-0.22}$	$4.60^{+0.26}_{-0.26}$	$12.95^{+1.13}_{-1.05}$	–	–	–
4U 1626-67	16	$37.30^{+0.13}_{-0.13}$	$4.76^{+0.19}_{-0.17}$	$17.28^{+1.17}_{-0.97}$	–	–	–
SMC X–2	17	$26.94^{+0.86}_{-0.71}$	$6.96^{+1.32}_{-1.39}$	$5.39^{+0.70}_{-1.97}$	–	–	–
	18	$28.92^{+2.43}_{-1.68}$	$7.20^{+2.37}_{-1.51}$	$9.23^{+10.22}_{-4.05}$	–	–	–
	19	$28.85^{+0.65}_{-0.69}$	7.1⋆	$9.42^{+1.49}_{-1.49}$	–	–	–
IGR J17544–2619	20	$17.13^{+0.60}_{-0.58}$	$1.89^{+0.73}_{-0.61}$	$1.47^{+0.70}_{-0.55}$	–	–	–
IGR J16393–4643	21	$30.75^{+1.04}_{-1.21}$	$2.44^{+0.95}_{-1.04}$	$1.87^{+0.98}_{-1.00}$	–	–	–
2S 1553–542	22	$27.13^{+0.80}_{-0.70}$	$7.75^{+1.28}_{-1.16}$	$14.92^{+14.61}_{-6.80}$	–	–	–
RX J0520.5–6932	23	$31.32^{+0.79}_{-0.70}$	$5.53^{+0.82}_{-0.67}$	$6.78^{+1.84}_{-1.38}$	–	–	–
	24	$31.92^{+0.68}_{-0.61}$	$7.43^{+0.76}_{-0.65}$	$13.45^{+3.02}_{-2.30}$	–	–	–
Cen X–3	25	$29.02^{+0.30}_{-0.29}$	$4.93^{+0.41}_{-0.35}$	$5.22^{+0.68}_{-0.56}$	–	–	–
GX 301–2	26 (ta)	$34.31^{+1.50}_{-1.04}$	$4.51^{+1.24}_{-1.23}$	$2.63^{+2.68}_{-1.43}$	$51.22^{+8.63}_{-1.87}$	$10.30^{+9.07}_{-2.54}$	$25.95^{+107.26}_{-9.60}$
	27 (ta)	$33.88^{+1.68}_{-0.84}$	$4.83^{+1.52}_{-1.16}$	$2.77^{+4.78}_{-1.31}$	$53.21^{+6.38}_{-2.37}$	$13.26^{+6.09}_{-4.14}$	$54.60^{+143.92}_{-27.02}$
	27 (f)	$32.64^{+1.26}_{-1.32}$	$4.04^{+0.81}_{-0.90}$	$1.82^{+1.00}_{-0.74}$	53.2⋆	$9.88^{+0.79}_{-0.84}$	$42.89^{+6.07}_{-4.54}$
	27 (q)	$34.30^{+0.95}_{-0.78}$	$4.74^{+0.77}_{-0.77}$	$4.20^{+2.44}_{-1.52}$	53.2⋆	$11.40^{+1.75}_{-2.02}$	$38.99^{+13.52}_{-9.70}$
XTE J1829–098	28	$14.61^{+0.10}_{-0.09}$	$2.66^{+0.19}_{-0.20}$	$3.53^{+0.64}_{-0.57}$	–	–	–
V 0332+53[†]	29	$27.82^{+0.06}_{-0.07}$	$4.98^{+0.27}_{-0.24}$	$2.21^{+0.09}_{-0.08}$	$2\times E_{cyc,F}$	$7.49^{+1.43}_{-0.87}$	$10.47^{+-10.47}_{-1.94}$
	30	$27.89^{+0.07}_{-0.07}$	$4.20^{+0.29}_{-0.26}$	$2.08^{+0.08}_{-0.08}$	$2\times E_{cyc,F}$	7.2⋆	$12.56^{+1.88}_{-1.77}$
	31	$29.43^{+0.09}_{-0.09}$	$4.04^{+0.28}_{-0.26}$	$2.32^{+0.09}_{-0.09}$	$2\times E_{cyc,F}$	$8.95^{+2.99}_{-3.69}$	$9.88^{+11.20}_{-2.69}$
	32	$29.21^{+0.10}_{-0.11}$	$4.46^{+0.46}_{-0.36}$	$2.29^{+0.15}_{-0.12}$	$2\times E_{cyc,F}$	$8.16^{+3.69}_{-4.65}$	$11.56^{+24.98}_{-3.52}$
XTE J1858+034	33	$50.52^{+3.88}_{-2.20}$	$9.74^{+2.41}_{-1.45}$	$27.80^{+18.35}_{-7.78}$	–	–	–
4U 1700–37	34 (ta)	$16.13^{+1.10}_{-0.89}$	$4.80^{+1.31}_{-1.58}$	$0.97^{+0.58}_{-0.46}$	–	–	–
	34 (f)	$16.12^{+1.11}_{-1.00}$	4.8⋆	$0.91^{+0.16}_{-0.17}$	–	–	–
	34 (q)	$16.69^{+1.07}_{-0.91}$	$3.08^{+2.00}_{-1.80}$	$0.81^{+1.16}_{-0.51}$	–	–	–
IGR J17329-2731	39	$22.43^{+0.64}_{-0.58}$	$4.35^{+0.63}_{-0.53}$	$3.49^{+0.95}_{-0.69}$	–	–	–
GRO J1008–57	44	78⋆	$9.10^{+1.68}_{-1.46}$	$12.61^{+3.02}_{-2.78}$	–	–	–
1A 0535+26	46	$44.88^{+0.82}_{-0.75}$	$7.64^{+0.92}_{-0.67}$	$10.68^{+2.59}_{-1.65}$	–	–	–
	48	$43.88^{+2.74}_{-3.49}$	7.67⋆	$27.95^{+5.83}_{-5.35}$	–	–	–

[†] `cyclabs` model parameters.

[§] Optical depth related to strength (line depth) by $\tau_{cyc} = \frac{\text{Strength}_{cyc}}{\sqrt{2\pi}\sigma_{cyc}}$.

⋆ Frozen parameter.

3.1.4 Table: Best fitting spectral parameters

The best fit spectral parameters for all the observations analyzed in this work are given in four tables.

3.1.5 Summary

In this work, we searched for the presence of the spectral feature known by the name '*10 keV feature*', which is commonly reported in XRP spectra, in the 58 archival *NuSTAR* observations of 30 different sources. We adopted a systematic two-step spectral fitting and model selection procedure based on AIC score to detect this spectral feature. The 3−79 keV spectral continua of these selected sources were fitted with a model chosen on the basis of its fitting quality in 3−15 keV and model simplicity, and then inspected for the presence of the '*10 keV feature*'. We found the presence of the '10 keV feature' in 16 out of the 58 observations (11 out of 30 sources) and it was fitted with a narrow gaussian absorption model centered around 10 keV. Our analysis also suggests that such a feature could be wrongly detected if flare data is not analyzed separately from persistent emission.

Source	Obs. Sn.	Energy range		Γ_1	norm$_1$	norm$_2$[†] / $T_0^{\ddagger}$ (keV)	E_{cut} (keV) / $kT_e^{\ddagger}$ (keV)	E_{fold} (keV) / $\tau^{\ddagger}$	E_{cyc} (keV)	σ_{cyc} (keV)	Strength[§]
Her X–1	1 (ta)	3–79	NPEX	$1.11^{+0.08}_{-0.07}$	$0.18^{+0.03}_{-0.02}$	$(3 \pm 0.1) \times 10^{-4}$	$5.75^{+0.06}_{-0.06}$	-	$38.20^{+0.30}_{-0.33}$	$7.12^{+0.30}_{-0.29}$	$15.76^{+1.32}_{-1.22}$
	1 (oe)	3–79	HEC	$0.95^{+0.01}_{-0.01}$	$0.108^{+0.001}_{-0.001}$	-	$20.51^{+0.40}_{-0.34}$	$10.13^{+0.23}_{-0.23}$	$38.19^{+0.56}_{-0.53}$	$6.18^{+0.59}_{-0.53}$	$8.86^{+1.45}_{-1.23}$
	2	3–79	FDC	$0.82^{+0.05}_{-0.05}$	$0.20^{+0.02}_{-0.02}$	-	$21.07^{+1.37}_{-1.27}$	$8.27^{+0.22}_{-0.22}$	$37.31^{+0.23}_{-0.23}$	$6.67^{+0.46}_{-0.46}$	$13.91^{+2.71}_{-2.23}$
	3	3–79	FDC	$0.77^{+0.05}_{-0.05}$	$0.24^{+0.01}_{-0.01}$	-	$15.75^{+3.34}_{-2.68}$	$8.53^{+0.10}_{-0.11}$	$37.16^{+0.20}_{-0.20}$	$6.75^{+0.34}_{-0.28}$	$13.13^{+1.14}_{-1.03}$
Vela X–1	4	3–79	compTT	-	$0.26^{+1.12}_{-0.03}$	$0.47^{+0.12}_{-0.47}$	$6.56^{+0.09}_{-0.08}$	$12.83^{+0.21}_{-0.20}$	$24.79^{+0.79}_{-1.13}$	$4.60^{+0.79}_{-0.77}$	$0.54^{+0.15}_{-0.12}$
									$54.48^{+0.67}_{-0.67}$	$7.50^{+0.65}_{-0.65}$	$15.93^{+2.73}_{-2.09}$
	5	3–79	CPL	$1.05^{+0.05}_{-0.06}$	$0.27^{+0.03}_{-0.03}$	-	$20.91^{+1.03}_{-2.02}$	-	$26.37^{+1.24}_{-1.26}$	$3.83^{+1.15}_{-1.32}$	$0.82^{+0.49}_{-0.42}$
									$57.18^{+0.83}_{-0.83}$	$9.59^{+1.33}_{-1.59}$	$34.56^{+4.80}_{-3.74}$
	6	3–79	compTT	-	$(4.2 \pm 0.2) \times 10^{-3}$	$1.01^{+0.02}_{-0.02}$	$8.41^{+0.51}_{-0.43}$	$9.72^{+0.26}_{-0.10}$	$27.05^{+0.58}_{-0.53}$	$5.83^{+0.57}_{-0.53}$	$3.31^{+0.80}_{-0.79}$
									$52.59^{+1.07}_{-0.97}$	$8.95^{+8.95}_{-1.16}$	$25.67^{+7.96}_{-6.93}$
	"	3–79	compTT	-	$0.10^{+0.40}_{-0.01}$	$0.29^{+0.11}_{-0.29}$	$7.29^{+0.19}_{-0.22}$	$10.32^{+0.33}_{-0.31}$	$24.85^{+0.76}_{-0.74}$	5.83^{*}	$2.34^{+0.29}_{-0.29}$
									$50.79^{+0.75}_{-0.66}$	$6.07^{+1.24}_{-0.84}$	$10.45^{+4.19}_{-2.26}$
	7 (f)	3–79	HEC	$1.16^{+0.04}_{-0.06}$	$0.27^{+0.03}_{-0.04}$	-	$21.80^{+0.68}_{-0.70}$	$15.04^{+1.53}_{-1.97}$	$27.71^{+2.01}_{-2.01}$	$3.40^{+2.12}_{-2.49}$	$1.10^{+1.59}_{-0.59}$
									$56.72^{+2.93}_{-2.34}$	$9.16^{+9.16}_{-2.27}$	$34.91^{+10.50}_{-6.07}$
XTE J1946+274	8	3–60	HEC	$0.99^{+0.04}_{-0.04}$	$0.07^{+0.01}_{-0.01}$	-	$18.10^{+0.19}_{-0.19}$	$9.41^{+0.26}_{-0.26}$	$38.55^{+0.87}_{-0.81}$	$5.03^{+0.71}_{-0.64}$	$3.63^{+1.06}_{-0.84}$
KS 1947+300	9	3–79	HEC	$1.17^{+0.07}_{-0.07}$	$0.23^{+0.05}_{-0.04}$	-	$7.92^{+0.27}_{-0.31}$	$25.71^{+1.26}_{-1.18}$			
	10	3–79	NPEX	$0.80^{+0.03}_{-0.03}$	$0.32^{+0.03}_{-0.04}$	$(2.1 \pm 0.3) \times 10^{-5}$	$10.70^{+0.25}_{-0.23}$	-	$36.70^{+0.42}_{-0.42}$	$3.28^{+0.35}_{-0.31}$	$7.09^{+0.93}_{-0.83}$
	11	3–79	NPEX	$0.69^{+0.04}_{-0.04}$	$0.15^{+0.02}_{-0.02}$	$(1.0 \pm 0.2) \times 10^{-5}$	$11.31^{+0.38}_{-0.31}$	-	$22.25^{+0.17}_{-0.17}$	$3.49^{+0.18}_{-0.17}$	$6.37^{+0.47}_{-0.44}$
4U 1907+09	12	3–45	CompTT	-	$0.021^{+0.013}_{-0.002}$	$0.36^{+0.11}_{-0.36}$	$4.20^{+0.03}_{-0.03}$	$19.44^{+0.39}_{-0.36}$	$22.35^{+0.21}_{-0.21}$	$3.39^{+0.22}_{-0.20}$	$6.18^{+0.55}_{-0.53}$
									$17.98^{+0.08}_{-0.08}$	$2.69^{+0.12}_{-0.11}$	$3.02^{+0.21}_{-0.17}$
4U 1538–52	13 (ta)	3–50	NPEX	$1.45^{+0.11}_{-0.11}$	$0.05^{+0.01}_{-0.01}$	$(5.0 \pm 0.3) \times 10^{-5}$	$4.77^{+0.05}_{-0.05}$	-	$19.34^{+0.84}_{-19.34}$	$2.57^{+0.84}_{-0.55}$	$0.37^{+0.31}_{-0.15}$
	13 (ooe)	3–50	NPEX	$1.11^{+0.11}_{-0.11}$	$0.07^{+0.01}_{-0.02}$	$(1.01 \pm 0.07) \times 10^{-4}$	$4.81^{+0.06}_{-0.06}$	-	$19.34^{+0.21}_{-0.19}$	$14.30^{+0.21}_{-0.19}$	$30.47^{+0.14}_{-0.14}$
Cep X–4	14	3–79	CompTT	-	$0.13^{+0.08}_{-0.01}$	$0.36^{+0.08}_{-0.36}$	$4.75^{+0.05}_{-0.06}$				$5.17^{+0.19}_{-0.20}$
											$14.08^{+0.80}_{-0.71}$
	15	3–79	NPEX	-	$1.96^{+1.70}_{-0.92}$	$0.06^{+0.13}_{-0.03}$	$(1.53 \pm 0.09) \times 10^{-4}$	$4.55^{+0.06}_{-0.06}$	$18.06^{+0.67}_{-0.56}$	$2.36^{+0.76}_{-0.67}$	$0.40^{+0.17}_{-0.26}$
									$29.35^{+0.22}_{-0.22}$	$4.60^{+0.26}_{-0.26}$	$12.95^{+1.13}_{-1.05}$
							$23.99^{+2.25}_{-2.29}$	$7.61^{+0.23}_{-0.23}$	$37.30^{+0.13}_{-0.13}$	$4.76^{+0.19}_{-0.17}$	$17.28^{+1.17}_{-1.07}$
4U 1626-67	16	3–79	FDC	$0.93^{+0.04}_{-0.05}$	$0.042^{+0.003}_{-0.003}$	-	$4.73^{+0.29}_{-0.14}$	$16.39^{+1.89}_{-2.43}$	$26.94^{+0.71}_{-0.71}$	$6.96^{+1.32}_{-1.39}$	$5.39^{+0.70}_{-1.97}$
SMC X–2	17	3–50	CompTT	-	$0.03^{+0.38}_{-0.01}$	$0.31^{+1.18}_{-0.31}$			$28.92^{+2.43}_{-2.43}$	$7.20^{+2.37}_{-1.51}$	$9.23^{+10.22}_{-4.05}$
	18	3–50	NPEX	$0.67^{+0.13}_{-0.11}$	$0.023^{+0.006}_{-0.004}$	$(1.2 \pm 0.1) \times 10^{-4}$	$4.52^{+0.26}_{-0.17}$	-	$28.85^{+0.69}_{-0.65}$	7.1^{*}	$9.42^{+1.49}_{-1.49}$
	19	3–50	NPEX	$0.96^{+0.16}_{-0.16}$	$0.02^{+0.01}_{-0.00}$	$(9.3 \pm 0.8) \times 10^{-5}$	$4.51^{+0.10}_{-0.10}$	-	$17.13^{+0.60}_{-0.58}$	$1.89^{+0.73}_{-0.61}$	$1.47^{+0.70}_{-0.55}$
IGR J17544–2619	20	3–40	NPEX	$2.97^{+0.37}_{-0.34}$	$0.09^{+0.09}_{-0.04}$	$4.75^{+0.73}_{-0.61} \times 10^{-6}$	$4.77^{+0.15}_{-0.14}$	-	$30.75^{+1.21}_{-1.04}$	$2.44^{+0.95}_{-0.91}$	$1.87^{+1.00}_{-0.68}$
IGR J16393–4643	21	3–50	NPEX	$1.19^{+0.31}_{-0.31}$	$0.014^{+0.010}_{-0.007}$	$(2.4 \pm 0.4) \times 10^{-5}$	$4.48^{+0.13}_{-0.13}$	-	$27.13^{+0.80}_{-0.80}$	$7.75^{+1.28}_{-1.16}$	$14.92^{+14.61}_{-6.80}$
2S 1553–542	22	3–50	FDC	$1.07^{+0.07}_{-0.14}$	$0.07^{+0.01}_{-0.01}$	-	$17.02^{+6.62}_{-5.85}$	$6.21^{+0.52}_{-1.15}$	$31.32^{+0.79}_{-0.70}$	$5.53^{+0.82}_{-0.82}$	$6.78^{+1.84}_{-1.73}$
RX J0520.5–6932	23	4–55	CPL	$0.42^{+0.04}_{-0.04}$	0.054 ± 0.003	-	$7.35^{+0.28}_{-0.26}$	-	$33.88^{+0.84}_{-0.84}$	$4.83^{+1.76}_{-1.52}$	$2.77^{+1.38}_{-1.03}$
	24	4–55	NPEX	$0.23^{+0.03}_{-0.03}$	0.036 ± 0.002	-	$4.93^{+0.16}_{-0.10}$	-	$31.92^{+0.68}_{-0.61}$	$7.43^{+0.76}_{-0.76}$	$13.45^{+3.02}_{-2.30}$
Cen X–3	25	3–60	HEC	$1.27^{+0.03}_{-0.03}$	$0.38^{+0.03}_{-0.03}$	-	$12.48^{+0.13}_{-0.13}$	$8.92^{+0.15}_{-0.15}$	$29.02^{+0.30}_{-0.29}$	$4.93^{+0.41}_{-0.35}$	$5.22^{+0.68}_{-0.68}$
GX 301–2	26 (ta)	3–65	NPEX	$0.78^{+0.01}_{-0.03}$	$0.09^{+0.01}_{-0.01}$	$(6.7 \pm 1.5) \times 10^{-5}$	$6.59^{+0.30}_{-0.31}$	-	$34.31^{+1.04}_{-1.04}$	$4.51^{+1.23}_{-1.23}$	$2.63^{+1.43}_{-1.43}$
									$51.22^{+8.63}_{-1.87}$	$10.30^{+9.07}_{-2.54}$	$25.95^{+107.26}_{-9.60}$
	27 (ta)	3–65	NPEX	$0.85^{+0.14}_{-0.04}$	$0.15^{+0.01}_{-0.01}$	$1.05^{+0.33}_{-0.51} \times 10^{-4}$	$6.84^{+4.09}_{-0.63}$	-	$33.88^{+0.68}_{-0.84}$	$4.83^{+1.76}_{-1.16}$	$4.83^{+1.78}_{-1.73}$
									$53.21^{+6.38}_{-6.38}$	$13.26^{+6.09}_{-4.14}$	$54.60^{+143.92}_{-27.02}$
	27 (f)	3–65	NPEX	$0.84^{+0.04}_{-0.05}$	$0.25^{+0.03}_{-0.02}$	$3.45^{+0.26}_{-0.33} \times 10^{-4}$	$5.66^{+0.15}_{-0.09}$	-	$32.64^{+1.26}_{-1.32}$	$4.04^{+0.81}_{-0.79}$	$1.82^{+1.00}_{-0.74}$
										$9.88^{+0.79}_{-0.84}$	$42.89^{+6.07}_{-4.54}$
									53.2^{*}		
	27 (q)	3–65	NPEX	$0.89^{+0.04}_{-0.04}$	$0.13^{+0.01}_{-0.01}$	$6.96 \pm 1.15) \times 10^{-5}$	$6.85^{+0.42}_{-0.31}$	-	$34.30^{+0.95}_{-0.78}$	$4.74^{+0.77}_{-0.77}$	$4.20^{+2.44}_{-1.75}$
									53.2^{*}	$11.40^{+2.02}_{-2.02}$	$38.99^{+13.52}_{-9.70}$
XTE J1829–098	28	3–40	NHC	$0.64^{+0.05}_{-0.05}$	$0.005^{+0.001}_{-0.001}$	-	$10.31^{+0.40}_{-0.47}$	$6.53^{+0.25}_{-0.28}$	$14.61^{+0.10}_{-0.09}$	$2.66^{+0.19}_{-0.20}$	$3.53^{+0.64}_{-0.57}$

[†] Normalization of `cutoffpl` model with powerlaw index -2 in `NPEX` continuum model.

[‡] Parameters for the `CompTT` continuum model.

[§] Optical depth related to strength (line depth) by $\tau_{cyc} = \frac{\text{Strength}_{cyc}}{\sqrt{2\pi}\sigma_{cyc}}$.

[*] Frozen parameter.

Tab. 3.4: The best fitting continuum model and Cyclotron resonance scattering feature model parameters from spectral fitting for Obs. Sn.1 to 28.

Obs. Sn.	tbabs	tbpcf		bbody		Atomic line			*10 keV feature*			C_{FPMB}	Fit	AIC Score
	nH_1	f	nH_2	kT_{BB}	$norm_{BB}$	E (Fe Kα)	σ (Fe Kα)	norm.	E_{gabs}	σ_{gabs}	$strength_{gabs}$		χ^2/dof	χ^2+2n_{par}
1 (ta)	0.015*	$0.45^{+0.03}_{-0.04}$	$44.45^{+5.81}_{-5.70}$	-	-	$6.41^{+0.02}_{-0.02}$	$0.15^{+0.04}_{-0.04}$	$(1 \pm 0.1) \times 10^{-3}$	-	-	-	1.035 ± 0.002	615.5/455	655.5
						$6.41^{+0.02}_{-0.02}$	$1.58^{+0.13}_{-0.14}$	$(6 \pm 0.1) \times 10^{-3}$						
1 (oe)	0.015*	-	-	-	-	$6.43^{+0.02}_{-0.02}$	$0.13^{+0.07}_{-0.09}$	$(1 \pm 0.3) \times 10^{-3}$	-	-	-	1.033 ± 0.003	500.9/433	536.9
						$6.43^{+0.02}_{-0.02}$	$0.92^{+0.17}_{-0.13}$	$(4 \pm 0.4) \times 10^{-3}$						
2	0.015*	$0.26^{+0.07}_{-0.09}$	$512.63^{+47.06}_{-83.96}$	$0.34^{+0.09}_{-0.08}$	$0.01^{+0.04}_{-0.01}$	$6.52^{+6.52}_{-6.52}$	$0.22^{+0.04}_{-0.05}$	$(3 \pm 1) \times 10^{-3}$	$11.05^{+0.23}_{-0.22}$	$0.88^{+0.32}_{-0.22}$	$0.05^{+0.03}_{-0.02}$	1.033 ± 0.001	538.3/474	595.3
						$6.52^{+0.01}_{-0.01}$	$0.67^{+0.14}_{-0.11}$	$(4 \pm 0.8) \times 10^{-3}$						
3	0.015*	$0.42^{+0.03}_{-0.03}$	$590.47^{+19.10}_{-18.52}$	$0.32^{+0.07}_{-0.05}$	$0.02^{+0.04}_{-0.01}$	$6.49^{+0.01}_{-0.01}$	$0.18^{+0.03}_{-0.03}$	$(3 \pm 0.6) \times 10^{-3}$	$10.21^{+0.12}_{-0.12}$	$0.23^{+0.13}_{-0.10}$	0.012 ± 0.004	1.016 ± 0.001	696.9/488	742.9
						$6.49^{+0.01}_{-0.01}$	$0.61^{+0.06}_{-0.07}$	$(6 \pm 0.6) \times 10^{-6}$						
4	0.37*	$0.87^{+0.01}_{-0.01}$	$33.20^{+1.63}_{-1.40}$	-	-	$6.40^{+0.01}_{-0.01}$	$0.06^{+0.06}_{-0.06}$	$(4 \pm 0.3) \times 10^{-3}$	$10.39^{+0.24}_{-0.21}$	$1.34^{+0.36}_{-0.30}$	$0.10^{+0.04}_{-0.03}$	1.044 ± 0.002	552.4/23	598.4
5	0.37*	$0.84^{+0.02}_{-0.02}$	$23.49^{+1.97}_{-1.66}$	-	-	$6.37^{+0.03}_{-0.03}$	$0.09^{+0.06}_{-0.06}$	$(1.3 \pm 0.2) \times 10^{-3}$	-	-	-	1.027 ± 0.004	531.9/435	565.9
6	0.37*	$0.71^{+0.02}_{-0.02}$	$26.10^{+1.96}_{-1.96}$	-	-	$6.37^{+0.02}_{-0.02}$	$0.05^{+0.05}_{-0.05}$	$(7.6 \pm 0.8) \times 10^{-4}$	-	-	-	1.013 ± 0.002	503.9/465	543.9
"	0.37*	$0.86^{+0.01}_{-0.01}$	$25.59^{+1.17}_{-1.03}$	-	-	$6.36^{+0.04}_{-0.02}$	$0.00^{+0.06}_{-0.00}$	$6.97^{+0.37}_{-0.62} \times 10^{-4}$	$11.97^{+0.32}_{-0.31}$	$1.96^{+0.39}_{-0.37}$	$0.20^{+0.10}_{-0.07}$	1.013 ± 0.002	540.9/463	586.9
7 (f)	0.37*	$0.88^{+0.01}_{-0.03}$	$23.45^{+0.63}_{-4.53}$	-	-	$6.35^{+0.02}_{-0.06}$	$0.22^{+0.10}_{-0.08}$	$(2.7 \pm 0.8) \times 10^{-3}$	-	-	-	1.02 ± 0.01	454.1/398	496.1
8	$0.10^{+0.21}_{-0.10}$	$0.21^{+0.04}_{-0.05}$	$79.11^{+21.83}_{-23.90}$	$2.09^{+0.10}_{-0.07}$	$(3.8 \pm 0.9) \times 10^{-3}$	$6.45^{+0.03}_{-0.03}$	$0.20^{+0.08}_{-0.08}$	$(5.2 \pm 0.1) \times 10^{-3}$	$10.25^{+0.26}_{-0.26}$	$1.11^{+0.40}_{-0.29}$	$0.07^{+0.05}_{-0.03}$	0.998 ± 0.002	506.8/23	552.8
9	$1.50^{+2.65}_{-0.60}$	$0.15^{+0.03}_{-0.03}$	$463.43^{+83.43}_{-83.47}$	$0.59^{+0.17}_{-0.17}$	$(5.4^{+7.6}_{-2.7}) \times 10^{-3}$	$6.56^{+0.03}_{-0.03}$	$0.25^{+0.06}_{-0.06}$	$(1.5 \pm 0.3) \times 10^{-3}$	-	-	-	1.017 ± 0.002	546.8/486	580.8
10	$3.39^{+1.40}_{-1.48}$	$0.26^{+0.02}_{-0.02}$	$511.99^{+52.01}_{-51.09}$	$0.53^{+0.05}_{-0.03}$	$0.02^{+0.01}_{-0.01}$	$6.51^{+0.03}_{-0.03}$	$0.23^{+0.05}_{-0.05}$	$(1.68 \pm 0.3) \times 10^{-3}$	-	-	-	1.015 ± 0.002	527.4/493	559.4
11	$4.00^{+1.27}_{-1.88}$	$0.12^{+0.02}_{-0.03}$	$564.48^{+123.68}_{-110.40}$	$0.55^{+0.04}_{-0.03}$	0.014 ± 0.002	$6.49^{+0.03}_{-0.03}$	$0.19^{+0.05}_{-0.05}$	$(9 \pm 1) \times 10^{-4}$	-	-	-	1.021 ± 0.002	583.8/503	615.8
12	$6.27^{+0.49}_{-0.47}$	-	-	-	-	$6.38^{+0.03}_{-0.04}$	$0.22^{+0.06}_{-0.07}$	$2.31^{+0.49}_{-0.44}$	$7.96^{+0.12}_{-0.14}$	$1.44^{+0.21}_{-0.17}$	$0.40^{+0.11}_{-0.07}$	1.014 ± 0.003	416.5/299	456.5
13 (ta)	0.7*	$0.87^{+0.02}_{-0.03}$	$41.77^{+4.92}_{-5.17}$	-	-	$6.43^{+0.03}_{-0.03}$	$0.16^{+0.08}_{-0.08}$	$(2.0 \pm 0.4) \times 10^{-4}$	-	-	-	$1.02^{+0.01}_{-0.01}$	363.0/306	397.0
13 (oe)	0.7*	$0.86^{+0.03}_{-0.03}$	$29.75^{+4.80}_{-4.33}$	-	-	$6.42^{+0.07}_{-0.07}$	$0.08^{+0.15}_{-0.08}$	$(1.8 \pm 0.7) \times 10^{-4}$	-	-	-	$1.01^{+0.01}_{-0.01}$	274.3/292	308.3
14	$1.53^{+0.20}_{-0.24}$	$0.33^{+0.04}_{-0.02}$	$281.64^{+40.12}_{-30.67}$	-	-	$6.45^{+0.03}_{-0.03}$	$0.17^{+0.04}_{-0.05}$	$(8.1 \pm 1.3) \times 10^{-4}$	-	-	-	1.034 ± 0.002	530.7/458	570.7
15	$0.10^{+2.65}_{-0.10}$	-	-	$1.41^{+0.08}_{-0.03}$	$(2.0 \pm 0.6) \times 10^{-3}$	$6.39^{+0.05}_{-0.05}$	$0.23^{+0.08}_{-0.08}$	$(1.9 \pm 0.5) \times 10^{-4}$	-	-	-	1.021 ± 0.004	440.8/421	478.8
16	$0.05^{+0.41}_{-0.05}$	$0.32^{+0.05}_{-0.06}$	$620.03^{+70.62}_{-71.85}$	$0.49^{+0.03}_{-0.03}$	$(2.07 \pm 0.27) \times 10^{-3}$	$6.74^{+0.05}_{-0.05}$	$0.12^{+0.07}_{-0.08}$	$(1.6 \pm 0.5) \times 10^{-4}$				$1.002^{+0.003}_{-0.003}$	691.4/444	725.4
17	$0.65^{+0.96}_{-0.65}$	-	-	$2.19^{+0.55}_{-0.28}$	$(2.1 \pm 0.3) \times 10^{-3}$	$6.33^{+0.10}_{-0.11}$	$0.62^{+0.19}_{-0.15}$	$(6.8 \pm 2.0) \times 10^{-4}$	-	-	-	1.014 ± 0.004	304.5/317	336.5
18	$0.85^{+0.07}_{-0.85}$	-	-	-	-	$6.30^{+0.08}_{-0.08}$	$0.34^{+0.09}_{-0.09}$	$(2.4 \pm 0.6) \times 10^{-4}$	-	-	-	$1.03^{+0.01}_{-0.01}$	249.4/304	277.4
19	$1.86^{+1.27}_{-1.25}$	-	-	-	-	$6.31^{+0.09}_{-0.10}$	$0.28^{+0.19}_{-0.15}$	$11.6^{+5.2}_{-3.8} \times 10^{-5}$	-	-	-	$1.03^{+0.01}_{-0.03}$	324.3/300	352.3
20	$16.36^{+3.05}_{-3.71}$	-	-	-	-	-	-	-	-	-	-	$1.09^{+0.03}_{-0.03}$	236.1/200	256.1
21	2.15*	$0.97^{+0.02}_{-0.02}$	$51.65^{+6.17}_{-6.29}$	-	-	-	-	-	$11.76^{+0.41}_{-0.45}$	$1.46^{+0.69}_{-0.47}$	$0.41^{+0.30}_{-0.16}$	$0.99^{+0.02}_{-0.02}$	371.4/267	405.4
22	$3.77^{+0.50}_{-0.84}$	$0.16^{+0.05}_{-0.03}$	$83.94^{+58.43}_{-58.67}$	-	-	$6.43^{+0.09}_{-0.09}$	$0.12^{+0.12}_{-0.07}$	$(1.4 \pm 0.7) \times 10^{-4}$	-	-	-	1.012 ± 0.003	268.6/314	298.6
23	0.2*	$0.26^{+0.03}_{-0.03}$	$266.55^{+58.67}_{-62.83}$	-	-	$6.54^{+0.05}_{-0.05}$	$0.14^{+0.08}_{-0.07}$	$(3.7 \pm 0.9) \times 10^{-4}$	$9.87^{+0.39}_{-0.24}$	$0.39^{+0.58}_{-0.38}$	$0.03^{+0.04}_{-0.02}$	1.043 ± 0.004	332.8/312	366.8
24	0.2*	-	-	-	-	$6.59^{+0.05}_{-0.05}$	$0.40^{+0.08}_{-0.08}$	$(23.3 \pm 0.1) \times 10^{-3}$	$11.69^{+0.27}_{-0.27}$	$0.37^{+0.39}_{-0.30}$	$0.02^{+0.02}_{-0.01}$	1.022 ± 0.003	381.8/339	415.8
25	$5.27^{+0.58}_{-0.63}$	$0.52^{+0.02}_{-0.02}$	$72.38^{+5.75}_{-5.64}$	-	-	$6.36^{+0.02}_{-0.02}$	$0.10^{+0.04}_{-0.04}$	$(2.03 \pm 0.23) \times 10^{-3}$	$11.22^{+0.27}_{-0.23}$	$2.52^{+0.35}_{-0.16}$	$0.98^{+0.17}_{-0.14}$	1.027 ± 0.002	422.9/381	464.9
26 (ta)	$1.62^{+7.26}_{-1.62}$	$0.90^{+0.02}_{-0.10}$	$39.30^{+2.07}_{-2.62}$	-	-	$6.36^{+0.01}_{-0.01}$	$0.01^{\star}$	$(10.0 \pm 0.6) \times 10^{-4}$	-	-	-	$1.054^{+0.004}_{-0.004}$	479.5/387	519.5
27 (ta)	$5.41^{+5.41}_{-5.41}$	$0.68^{+0.14}_{-0.14}$	$31.88^{+5.61}_{-5.61}$	-	-	$6.35^{+0.01}_{-0.01}$	$0.01^{\star}$	$1.76^{+0.26}_{-0.07} \times 10^{-3}$	-	-	-	1.065 ± 0.003	486.8/395	526.8
27 (f)	$0.10^{+5.75}_{-0.10}$	$0.82^{+0.01}_{-0.15}$	$31.62^{+2.16}_{-2.64}$	-	-	$6.33^{+0.02}_{-0.01}$	$0.01^{\star}$	$(3.04 \pm 0.15) \times 10^{-4}$	-	-	-	1.065 ± 0.005	561.1/368	601.1
27 (q)	5.12 ± 5.12	$0.71^{+0.11}_{-0.18}$	$30.65^{+6.45}_{-2.79}$	-	-	$6.35^{+0.01}_{-0.02}$	$0.01^{\star}$	$(1.27 \pm 0.07) \times 10^{-3}$	-	-	-	1.067 ± 0.004	363.9/378	403.9
28	$3.58^{+0.73}_{-0.74}$	-	-	-	-	$6.47^{+0.04}_{-0.04}$	$0.32^{+0.05}_{-0.05}$	$(4.2 \pm 0.5) \times 10^{-4}$	-	-	-	$1.00^{+0.01}_{-0.01}$	242.7/252	268.7

* Frozen parameter.

Tab. 3.5: The best fitting parameters of the absorption (`tbabs, tbpcf`), blackbody (`bbody`), iron fluorescence lines (`gaussian`) and *TKF* (`gabs`) models, along with the fit statistic and *AIC* score used for model selection. Details of Obs. Sn.1 to 28 are given in this table.

Source	Obs. Sn.	Energy range	Γ1	norm−1	norm−2† / T0 (keV)	Ecut (keV) / kTe (keV)	Efold (keV) / τ	Ecyc (keV)	σcyc (keV)	Strength
V 0332+53	29	3–55	HEC	$0.67^{+0.03}_{-0.03}$	0.054 ± 0.004	-	$13.85^{+0.41}_{-0.43}$	$19.23^{+7.20}_{-3.73}$	$27.82^{+0.06}_{-0.07}$	$4.98^{+0.27}_{-0.24}$	$2.21^{+0.09}_{-0.08}$
	"									$7.49^{+1.43}_{-1.57}$	$10.47^{+-10.47}_{-1.94}$
	30	3–55	NHC	$0.75^{+0.03}_{-0.03}$	$0.030^{+0.003}_{-0.002}$	$15.50^{+0.38}_{-0.60}$	$16.22^{+2.87}_{-2.00}$	-	$27.89^{+0.07}_{-0.07}$	$4.20^{+0.29}_{-0.26}$	$2.08^{+0.08}_{-0.08}$
	"									7.2^{*}	$12.56^{+1.88}_{-1.77}$
	30	3–55	CompTT	-	$0.031^{+0.080}_{-0.003}$	$0.45^{+0.19}_{-0.45}$	$5.87^{+0.35}_{-0.31}$	$18.68^{+0.78}_{-0.67}$	$27.67^{+0.08}_{-0.07}$	$4.44^{+0.26}_{-0.25}$	$2.06^{+0.07}_{-0.07}$
	"									$7.16^{+2.77}_{-2.09}$	$7.26^{+21.63}_{-4.44}$
	31	3–55	NHC	$0.71^{+0.04}_{-0.05}$	$0.015^{+0.002}_{-0.002}$	-	$16.49^{+0.35}_{-0.38}$	$17.85^{+3.92}_{-2.63}$	$29.43^{+0.09}_{-0.09}$	$4.04^{+0.28}_{-0.26}$	$2.32^{+0.09}_{-0.09}$
	"									$8.95^{+2.99}_{-2.09}$	$9.88^{+11.20}_{-3.29}$
	31	3–55	NPEX	$0.37^{+0.23}_{-0.07}$	$0.020^{+0.006}_{-0.001}$	$(8.4 \pm 1.9) \times 10^{-5}$	$6.14^{+0.29}_{-0.33}$	-	$29.19^{+0.08}_{-0.08}$	$4.40^{+0.28}_{-0.24}$	$2.29^{+0.07}_{-0.04}$
	"									8.95^{*}	$5.66^{+1.06}_{-1.06}$
	32	3–55	NHC	$0.66^{+0.07}_{-0.14}$	$0.011^{+0.002}_{-0.003}$	-	$16.56^{+0.57}_{-1.30}$	$19.75^{+9.31}_{-4.10}$	$29.21^{+0.10}_{-0.11}$	$4.46^{+0.46}_{-0.36}$	$2.29^{+0.15}_{-0.12}$
	"									$8.16^{+3.69}_{-2.55}$	$11.56^{+24.98}_{-5.92}$
XTE J1858+034	33	5–55	NPEX	$0.39^{+0.04}_{-0.05}$	$0.036^{+0.005}_{-0.004}$	$(1.2 \pm 0.2) \times 10^{-4}$	$5.48^{+0.27}_{-0.15}$	-	$50.52^{+3.88}_{-2.20}$	$9.74^{+2.41}_{-2.41}$	$27.80^{+18.35}_{-7.78}$
4U 1700–37	34 (ta)	3–79	NPEX	$0.82^{+0.06}_{-0.04}$	$0.10^{+0.01}_{-0.01}$	$(2.01 \pm 1.34) \times 10^{-6}$	$12.20^{+1.34}_{-1.22}$	-	$16.13^{+1.10}_{-1.09}$	$4.80^{+1.31}_{-1.58}$	$0.97^{+0.58}_{-0.46}$
	34 (f)	3–79	NPEX	$0.75^{+0.04}_{-0.04}$	$0.13^{+0.01}_{-0.01}$	$(3.79 \pm 2.05) \times 10^{-6}$	$11.68^{+1.22}_{-0.76}$	-	$16.12^{+1.01}_{-1.00}$	4.8^{*}	$0.91^{+0.17}_{-0.16}$
	34 (q)	3–79	NPEX	$1.23^{+0.08}_{-0.08}$	$0.07^{+0.01}_{-0.01}$	$6.93^{+4.97}_{-3.64} \times 10^{-7}$	$11.48^{+1.86}_{-1.46}$	-	$16.69^{+1.07}_{-0.91}$	$3.08^{+2.00}_{-1.80}$	$0.81^{+0.16}_{-0.51}$
LMC X–4	35 (ta)	3–79	NPEX	$0.60^{+0.04}_{-0.08}$	$0.05^{+0.01}_{-0.01}$	$(3.7 \pm 0.6) \times 10^{-5}$	$6.29^{+0.16}_{-0.16}$	-	-	-	-
	35 (f)	3–65	NPEX	$0.78^{+0.14}_{-0.13}$	$0.18^{+0.08}_{-0.07}$	$(1.30 \pm 0.21) \times 10^{-4}$	$5.12^{+0.13}_{-0.12}$	-	-	-	-
	35 (q)	3–79	NPEX	$0.54^{+0.11}_{-0.11}$	$0.03^{+0.01}_{-0.01}$	$(3.6 \pm 0.6) \times 10^{-5}$	$6.33^{+0.17}_{-0.12}$	-	-	-	-
	"	3–79	FDC	$0.89^{+0.04}_{-0.06}$	$0.030^{+0.004}_{-0.003}$	-	$17.70^{+3.38}_{-2.57}$	$10.10^{+0.42}_{-0.43}$	-	-	-
	36	3–60	FDC	$0.72^{+0.09}_{-0.08}$	$0.020^{+0.004}_{-0.003}$	-	$20.18^{+2.08}_{-2.05}$	$9.96^{+0.33}_{-0.31}$	-	-	-
	"	3–60	FDC	$0.62^{+0.04}_{-0.04}$	$0.021^{+0.002}_{-0.002}$	-	$15.10^{+2.93}_{-3.16}$	$10.21^{+0.30}_{-0.32}$	-	-	-
	37	3–68	FDC	$0.81^{+0.15}_{-0.18}$	$0.007^{+0.003}_{-0.003}$	-	$23.02^{+2.24}_{-2.66}$	$8.31^{+0.40}_{-0.38}$	-	-	-
	"	3–68	CompTT	-	$0.004^{+0.006}_{-0.004}$	$0.37^{+0.86}_{-0.37} \times 10^{-5}$	$5.77^{+0.09}_{-0.09}$	$24.78^{+3.58}_{-2.43}$	-	-	-
	38 (ta)	3–65	NPEX	$0.77^{+0.08}_{-0.09}$	$0.05^{+0.01}_{-0.01}$	$(2.8 \pm 0.3) \times 10^{-5}$	$6.47^{+0.13}_{-0.12}$	-	-	-	-
	38 (f)	3–65	NPEX	$0.68^{+0.07}_{-0.07}$	$0.18^{+0.02}_{-0.03}$	$1.35^{+0.37}_{-0.33} \times 10^{-4}$	$4.92^{+0.20}_{-0.17}$	-	-	-	-
	"	3–65	NPEX	$1.34^{+0.20}_{-0.18}$	$0.18^{+0.04}_{-0.04}$	-	$17.01^{+3.45}_{-3.58}$	$7.76^{+0.48}_{-0.52}$	-	-	-
	38 (q)	3–65	NPEX	$0.51^{+0.10}_{-0.10}$	$0.017^{+0.003}_{-0.003}$	$(2.7 \pm 0.4) \times 10^{-5}$	$6.52^{+0.15}_{-0.13}$	-	-	-	-
IGR J17329–2731	39	3–55	NPEX	$0.48^{+0.13}_{-0.13}$	$0.011^{+0.003}_{-0.003}$	$3.02^{+8.44}_{-3.00}$	$9.49^{+1.29}_{-1.17}$	-	$22.43^{+0.64}_{-0.58}$	$4.35^{+0.63}_{-0.53}$	$3.49^{+0.95}_{-0.69}$
SMC X–1	40	3–79	HEC	$1.32^{+0.04}_{-0.04}$	$0.08^{+0.01}_{-0.01}$	-	$19.50^{+0.70}_{-0.69}$	$11.16^{+0.29}_{-0.28}$	-	-	-
	41	3–79	FDC	$1.02^{+0.08}_{-0.08}$	$0.054^{+0.004}_{-0.005}$	-	$16.18^{+2.54}_{-2.50}$	$8.52^{+0.25}_{-0.26}$	-	-	-
	42	3–50	FDC	$1.22^{+0.23}_{-0.23}$	$0.01^{+0.01}_{-0.01}$	-	$19.79^{+1.98}_{-1.92}$	$5.80^{+0.42}_{-0.40}$	-	-	-
	43	3–65	NPEX	$0.35^{+0.01}_{-0.01}$	$0.064^{+0.001}_{-0.002}$	$(6.7 \pm 0.7) \times 10^{-5}$	$5.70^{+0.09}_{-0.08}$	-	-	-	-
	"	"	FDC	$1.01^{+0.07}_{-0.07}$	$0.09^{+0.01}_{-0.01}$	-	$13.88^{+2.39}_{-2.35}$	$8.90^{+0.21}_{-0.21}$	-	-	-
GRO J1008–57	44	3–79	NPEX	$0.48^{+0.02}_{-0.02}$	$0.46^{+0.03}_{-0.01}$	$(1.78 \pm 0.12) \times 10^{-4}$	$8.23^{+0.11}_{-0.09}$	-	78*	$9.10^{+1.68}_{-1.46}$	$12.61^{+3.02}_{-2.78}$
GX 304–1	45	3–25	PL	$1.75^{+0.20}_{-0.20}$	$(9.04 \pm 0.63) \times 10^{-4}$	-	-	-	-	-	-
1A 0535+26	46	3–79	FDC	$1.05^{+0.13}_{-0.13}$	$0.137^{+0.016}_{-0.004}$	-	$16.23^{+9.60}_{-4.55}$	$15.73^{+0.85}_{-0.91}$	$44.88^{+0.82}_{-0.75}$	$7.64^{+0.92}_{-0.67}$	$10.68^{+2.59}_{-1.65}$
	47	3–50	PL	$1.39^{+0.03}_{-0.04}$	$0.05^{+0.01}_{-0.01}$	-	-	-	-	-	-
	48	3–50	compTT+compTT	-	$(3.4 \pm 0.3) \times 10^{-4}$	$0.64^{+0.06}_{-0.56}$	$2.00^{+0.09}_{-2.00}$	$17.44^{+0.65}_{-1.20}$	$43.88^{+2.74}_{-3.49}$	7.67^{*}	$27.95^{+5.83}_{-5.35}$
					$(2.0 \pm 0.5) \times 10^{-4}$	"	$11.12^{+0.20}_{-0.42}$	"			
GRO J2058+42	49	3–79	CompTT	-	$0.041^{+0.132}_{-0.004}$	$0.40^{+0.12}_{-0.40}$	$7.99^{+0.08}_{-0.07}$	$12.83^{+0.39}_{-0.35}$	-	-	-
	50	3–79	CompTT	-	$0.043^{+0.014}_{-0.004}$	$0.41^{+0.07}_{-0.12}$	$8.11^{+0.05}_{-0.05}$	$13.26^{+0.41}_{-0.33}$	-	-	-
	51	3–79	NHC	$1.39^{+0.06}_{-0.07}$	$0.015^{+0.002}_{-0.002}$	-	$14.41^{+1.28}_{-1.31}$	$27.54^{+2.42}_{-2.10}$	-	-	-
1E 1145.1–6141	52	3–60	CPL	$0.88^{+0.06}_{-0.06}$	0.018 ± 0.002	-	-	$17.03^{+1.50}_{-0.96}$	-	-	-
OAO 1657–415	53	5–70	CPL	$0.56^{+0.05}_{-0.05}$	$0.017^{+0.002}_{-0.002}$	-	$16.27^{+0.50}_{-0.48}$	-	-	-	-
EXO 2030+375	54	3–55	CPL	$1.20^{+0.02}_{-0.02}$	$1.11^{+0.04}_{-0.04}$	-	$18.93^{+0.25}_{-0.24}$	-	-	-	-
	55	3–60	NPEX	$1.02^{+0.04}_{-0.04}$	$0.018^{+0.002}_{-0.002}$	$(1.5 \pm 0.3) \times 10^{-6}$	$7.88^{+0.40}_{-0.34}$	-	-	-	-
	56	3–79	NPEX	$0.79^{+0.02}_{-0.02}$	$0.20^{+0.01}_{-0.01}$	$(7.5 \pm 2.1) \times 10^{-6}$	$10.80^{+0.53}_{-0.43}$	-	-	-	-
IGR J19294+1816	57	3–25	NPEX	$1.35^{+0.41}_{-0.34}$	$0.001^{+0.002}_{-0.001}$	-	$5.57^{+1.93}_{-0.85}$	-	-	-	-
	58	3–50	FDC	$1.14^{+0.03}_{-0.03}$	$(8.2 \pm 0.6) \times 10^{-3}$	-	$28.23^{+0.46}_{-0.49}$	$4.80^{+0.23}_{-0.23}$	-	-	-

† Normalization of `cutoffpl` model with powerlaw index -2 in `NPEX` continuum model.

‡ Parameters for the `CompTT` continuum model.

§ Optical depth related to strength (line depth) by $\tau_{\rm cyc} = \frac{\rm Strength_{cyc}}{\sqrt{2\pi}\sigma_{\rm cyc}}$.

⋆ Frozen parameter.

Tab. 3.6: Table 3.4 contd. The best fitting continuum model and Cyclotron resonance scattering feature model parameters from spectral fitting for Obs. Sn.29 to 58.

Obs. Sn.	tbabs	tbpcf		Blackbody		Atomic line		10 keV feature			C_{FPMB}	Fit	AIC Score
	nH_1	f	nH_2	kT_{BB}	$norm_{BB}$	E (Fe Kα)	σ (Fe Kα)	norm.	E_{gabs}	σ_{gabs}	$strength_{gabs}$		χ^2/dof	$\chi^2 + 2n_{par}$
29	$0.52^{+0.38}_{-0.39}$	$0.23^{+0.04}_{-0.03}$	$266.05^{+89.25}_{-63.26}$	-	-	$6.36^{+0.06}_{-0.06}$	$0.23^{+0.10}_{-0.09}$	$(6.2 \pm 2) \times 10^{-4}$	-	-	-	$1.015^{+0.003}_{-0.003}$	420.4/340	460.4
30	$0.89^{+0.37}_{-0.37}$	$0.12^{+0.03}_{-0.03}$	$189.37^{+153.24}_{-64.02}$	-	-	$6.30^{+0.05}_{-0.05}$	$0.01^{\star}$	$(2.3 \pm 0.5) \times 10^{-4}$	-	-	-	$1.014^{+0.004}_{-0.004}$	394.1/333	430.1
"	$1.98^{+0.43}_{-0.88}$	-	-	-	-	$6.31^{+0.04}_{-0.04}$	$0.01^{\star}$	$(2.1 \pm 0.4) \times 10^{-4}$	$9.73^{+0.28}_{-0.31}$	$2.14^{+0.51}_{-0.45}$	$0.33^{+0.22}_{-0.14}$	$1.014^{+0.004}_{-0.004}$	416.4/331	454.4
31	$5.30^{+2.21}_{-1.40}$	-	$0.59^{+0.11}_{-0.05}$	$(1.02 \pm 0.32) \times 10^{-3}$	$6.28^{+0.07}_{-0.06}$	$0.01^{\star}$	$(1.03 \pm 0.5) \times 10^{-4}$	-	-	-	$1.024^{+0.004}_{-0.004}$	399.1/330	433.1
"	$0.04^{+6.03}_{-0.02}$	$0.23^{+0.06}_{-0.11}$	$158.95^{+40.23}_{-72.73}$	-	-	$6.27^{+0.07}_{-0.07}$	$0.01^{\star}$	$(9.37 \pm 3.7) \times 10^{-5}$	$11.52^{+0.35}_{-0.31}$	$0.59^{+0.43}_{-0.32}$	$0.04^{+0.03}_{-0.02}$	1.024 ± 0.004	434.5/328	478.5
32	$3.35^{+3.12}_{-3.35}$	-	-	$5.1^{+6.4}_{-2.6} \times 10^{-4}$	$6.35^{+0.06}_{-0.07}$	$0.01^{\star}$	$(9.6 \pm 2.7) \times 10^{-5}$	-	-	-	$1.04^{+0.01}_{-0.01}$	370.4/325	404.4
33	$8.45^{+2.46}_{-2.46}$	-	-	-	$6.48^{+0.03}_{-0.03}$	$0.25^{+0.05}_{-0.06}$	$(5.0 \pm 0.1) \times 10^{-3}$	-	-	-	$1.017^{+0.003}_{-0.003}$	412.4/337	440.4
34 (ta)	$0.5^{\star}$	$0.77^{+0.01}_{-0.01}$	$30.22^{+1.53}_{-1.55}$	-	$6.36^{+0.01}_{-0.01}$	$0.01^{\star}$	$(9.2 \pm 0.6) \times 10^{-4}$	$10.61^{+0.50}_{-0.42}$	$1.66^{+0.77}_{-0.63}$	$0.10^{+0.18}_{-0.06}$	$1.013^{+0.003}_{-0.003}$	481.1/467	521.1
34 (f)	$0.5^{\star}$	$0.76^{+0.01}_{-0.01}$	$30.02^{+1.64}_{-1.65}$	-	$6.36^{+0.01}_{-0.01}$	$0.01^{\star}$	$(1.40 \pm 0.08) \times 10^{-3}$	$10.54^{+0.54}_{-0.49}$	$1.83^{+0.79}_{-0.68}$	$0.11^{+0.13}_{-0.06}$	$0.928^{+0.002}_{-0.002}$	511.6/465	551.6
34 (q)	$0.5^{\star}$	$0.84^{+0.02}_{-0.02}$	$33.06^{+3.23}_{-3.22}$	-	$6.32^{+0.04}_{-0.04}$	$0.01^{\star}$	$(2.1 \pm 0.5) \times 10^{-4}$	$11.39^{+0.80}_{-0.64}$	$1.25^{+0.67}_{-0.68}$	$0.15^{+0.15}_{-0.10}$	$0.97^{+0.01}_{-0.01}$	434.7/388	474.7
35 (ta)	$0.08^{\star}$	$0.30^{+0.07}_{-0.08}$	$89.37^{+24.24}_{-17.40}$	-	$6.57^{+0.05}_{-0.05}$	$0.32^{+0.11}_{-0.10}$	$(5.62 \pm 1.8) \times 10^{-4}$	$10.70^{+0.30}_{-0.31}$	$2.21^{+0.64}_{-0.46}$	$0.56^{+0.35}_{-0.49}$	$1.021^{+0.004}_{-0.004}$	473.4/417	507.4
35 (f)	$0.08^{\star}$	$0.31^{+0.11}_{-0.12}$	$52.02^{+16.48}_{-24.08}$	-	$6.59^{+0.10}_{-0.10}$	$0.46^{+0.21}_{-0.14}$	$(1.8 \pm 0.7) \times 10^{-3}$	$10.57^{+0.46}_{-0.33}$	$1.56^{+0.47}_{-0.45}$	$0.29^{+0.20}_{-0.15}$	$1.07^{+0.01}_{-0.01}$	452.0/340	486.0
35 (q)	$0.08^{\star}$	$0.34^{+0.10}_{-0.12}$	$89.46^{+32.62}_{-24.08}$	-	$6.53^{+0.06}_{-0.07}$	$0.25^{+0.12}_{-0.16}$	$(3.3 \pm 1.5) \times 10^{-4}$	$11.14^{+0.53}_{-0.58}$	$2.03^{+0.87}_{-0.69}$	$0.34^{+0.34}_{-0.18}$	$1.00^{+0.01}_{-0.01}$	460.9/403	494.9
"	$0.08^{\star}$	$0.30^{+0.06}_{-0.06}$	$414.45^{+72.49}_{-72.53}$	-	$6.48^{+0.05}_{-0.05}$	$0.41^{+0.06}_{-0.07}$	$(8.6 \pm 1.0) \times 10^{-4}$	-	-	-	$1.00^{+0.01}_{-0.01}$	479.0/406	503.0
36	$0.08^{\star}$	$0.22^{+0.08}_{-0.06}$	$123.07^{+123.56}_{-27.86}$	-	$6.48^{+0.07}_{-0.07}$	$0.25^{+0.13}_{-0.14}$	$(2.7 \pm 0.2) \times 10^{-4}$	$10.88^{+0.49}_{-0.43}$	$1.71^{+0.46}_{-0.57}$	$0.22^{+0.10}_{-0.14}$	$1.03^{+0.01}_{-0.01}$	404.9/362	434.9
"	$0.08^{\star}$	$0.27^{+0.05}_{-0.04}$	$334.87^{+51.17}_{-51.41}$	-	$6.51^{+0.06}_{-0.06}$	$0.34^{+0.09}_{-0.07}$	$(5.05 \pm 0.82) \times 10^{-4}$	-	-	-	$1.03^{+0.01}_{-0.01}$	415.5/365	439.5
37	$0.08^{\star}$	$0.39^{+0.10}_{-0.16}$	$89.01^{+42.02}_{-19.13}$	-	$6.34^{+0.07}_{-0.07}$	$0.16^{+0.14}_{-0.16}$	$(1.3 \pm 0.7) \times 10^{-4}$	$10.42^{+0.59}_{-0.70}$	$1.89^{+0.73}_{-0.51}$	$0.37^{+0.27}_{-0.16}$	$1.02^{+0.01}_{-0.01}$	442.3/354	472.3
"	$0.08^{\star}$	-	-	$1.34^{+0.10}_{-0.15}$	$(1.8 \pm 0.8) \times 10^{-4}$	$6.35^{+0.06}_{-0.06}$	$0.45^{+0.10}_{-0.09}$	$(2.9 \pm 0.6) \times 10^{-4}$	-	-	-	$1.02^{+0.01}_{-0.01}$	446.8/357	472.8
38 (ta)	$0.08^{\star}$	$0.31^{+0.08}_{-0.11}$	$87.59^{+24.22}_{-16.32}$	-	-	$6.50^{+0.09}_{-0.10}$	$0.21^{+0.21}_{-0.17}$	$(2.2 \pm 1.6) \times 10^{-4}$	$10.45^{+0.24}_{-0.26}$	$1.60^{+0.28}_{-0.25}$	$0.40^{+0.12}_{-0.10}$	$1.02^{+0.01}_{-0.01}$	394.2/368	428.2
38 (f)	$0.08^{\star}$	-	-	-	-	$6.40^{+0.14}_{-0.13}$	$0.71^{+0.17}_{-0.18}$	$0.004^{+0.002}_{-0.001}$	$10.28^{+0.36}_{-0.33}$	$1.35^{+0.62}_{-0.52}$	$0.29^{+0.25}_{-0.17}$	$1.02^{+0.01}_{-0.01}$	321.9/322	349.9
"	$0.08^{\star}$	-	-	$1.19^{+0.13}_{-0.21}$	0.003 ± 0.002	$6.42^{+0.22}_{-0.22}$	$0.89^{+0.26}_{-0.17}$	$0.007^{+0.002}_{-0.002}$	-	-	-	$1.02^{+0.01}_{-0.01}$	336.2/323	358.2
38 (q)	$0.08^{\star}$	$0.35^{+0.07}_{-0.08}$	$124.03^{+48.95}_{-34.64}$	-	-	$6.33^{+0.06}_{-0.05}$	$0.01^{\star}$	$(1.37 \pm 0.45) \times 10^{-4}$	$10.96^{+0.47}_{-0.52}$	$1.12^{+0.55}_{-0.34}$	$0.14^{+0.08}_{-0.05}$	$1.03^{+0.01}_{-0.01}$	410.0/363	444.0
39	$0.3^{\star}$	$0.93^{+0.01}_{-0.01}$	$56.43^{+4.06}_{-4.07}$	-	-	$6.32^{+0.03}_{-0.03}$	$0.01^{\star}$	$(3.1 \pm 0.4) \times 10^{-4}$	-	-	-	$1.01^{+0.01}_{-0.01}$	372.2/318	406.2
40	$0.5^{\star}$	-	-	$2.10^{+0.08}_{-0.07}$	$(4.2 \pm 0.2) \times 10^{-3}$	$6.39^{+0.07}_{-0.08}$	$0.42^{+0.14}_{-0.11}$	$7.65^{+0.23}_{-0.17} \times 10^{-4}$	-	-	-	1.021 ± 0.004	486.2/416	514.2
41	$0.5^{\star}$	-	-	$1.87^{+0.27}_{-0.21}$	$0.001^{+0.003}_{-0.002}$	$6.30^{+0.07}_{-0.07}$	$0.45^{+0.12}_{-0.10}$	$(6.97 \pm 0.19) \times 10^{-4}$	-	-	-	$1.038^{+0.004}_{-0.004}$	479.2/408	501.2
42	$0.5^{\star}$	$0.61^{+0.10}_{-0.16}$	$66.80^{+8.98}_{-10.34}$	-	-	$6.34^{+0.04}_{-0.05}$	$0.20^{+0.10}_{-0.10}$	$(2.3 \pm 0.6) \times 10^{-4}$	-	-	-	$1.02^{+0.01}_{-0.01}$	334.1/260	358.1
43	$0.5^{\star}$	-	-	-	-	$6.39^{+0.07}_{-0.08}$	$0.51^{+0.14}_{-0.15}$	$(9.4 \pm 0.2) \times 10^{-4}$	$10.87^{+0.61}_{-0.46}$	$0.92^{+0.87}_{-0.35}$	$0.04^{+0.06}_{-0.03}$	$1.027^{+0.004}_{-0.003}$	387.6/378	415.6
"	$0.5^{\star}$	-	-	$1.83^{+0.16}_{-0.12}$	$(2.23 \pm 0.37) \times 10^{-3}$	$6.38^{+0.09}_{-0.10}$	$0.57^{+0.19}_{-0.13}$	$(1.03 \pm 0.42) \times 10^{-3}$	-	-	-	1.027 ± 0.004	396.7/379	418.7
44	$0.10^{+0.21}_{-0.10}$	$0.24^{+0.03}_{-0.03}$	$101.65^{+16.04}_{-10.70}$	-	-	$6.48^{+0.02}_{-0.02}$	$0.14^{+0.03}_{-0.04}$	$(3.7 \pm 0.5) \times 10^{-3}$	-	-	-	1.024 ± 0.001	579.4/510	619.4
							$1.95^{+0.10}_{-0.09}$	0.04 ± 0.01						
45	$0.10^{+0.26}_{-0.10}$	-	-	$1.18^{+0.02}_{-0.02}$	$(9.23 \pm 1.01) \times 10^{-5}$	-	-	-	-	-	-	$0.99^{+0.02}_{-0.02}$	1057.3/1019	1069.3
46	$0.10^{+0.71}_{-0.10}$	-	-	$1.55^{+0.31}_{-0.11}$	$(1.2 \pm 0.5) \times 10^{-3}$	$6.37^{+0.05}_{-0.05}$	$0.14^{+0.07}_{-0.08}$	$(3.8 \pm 0.8) \times 10^{-4}$	-	-	-	$0.971^{+0.003}_{-0.003}$	506.2/468	534.2
47	$0.81^{+0.50}_{-0.49}$	-	-	$1.72^{+0.44}_{-0.04}$	$(1.1 \pm 0.1) \times 10^{-3}$	$6.30^{+0.04}_{-0.15}$	$0.17^{+0.18}_{-0.17}$	$(8.9 \pm 6.2) \times 10^{-5}$	-	-	-	0.985 ± 0.004	345.5/331	369.5
48	$0.4^{\star}$	-	-	-	-	-	-	-	-	-	-	0.96 ± 0.01	313.0/278	NA
49	$0.60^{\star}$	$0.25^{+0.05}_{-0.07}$	$86.70^{+32.55}_{-25.47}$	$2.40^{+0.16}_{-0.19}$	0.005 ± 0.001	$6.39^{+0.06}_{-0.05}$	$0.11^{+0.12}_{-0.11}$	$(5.2 \pm 2.2) \times 10^{-4}$	$10.87^{+0.23}_{-0.24}$	$1.46^{+0.37}_{-0.30}$	$0.20^{+0.10}_{-0.06}$	0.986 ± 0.003	557.8/468	595.8
50	$0.60^{\star}$	$0.18^{+0.05}_{-0.08}$	$73.59^{+24.44}_{-25.37}$	$2.56^{+0.15}_{-0.10}$	0.006 ± 0.001	$6.39^{+0.04}_{-0.04}$	$0.24^{+0.12}_{-0.09}$	$(6.7 \pm 0.4) \times 10^{-4}$	$10.90^{+0.21}_{-0.22}$	$1.71^{+0.32}_{-0.28}$	$0.22^{+0.08}_{-0.07}$	0.997 ± 0.002	592.3/500	630.2
51	$0.60^{\star}$	-	-	$1.88^{+0.15}_{-0.13}$	$(5.1 \pm 0.5) \times 10^{-4}$	$6.09^{+0.32}_{-0.32}$	$0.49^{+0.34}_{-0.44}$	$7.3^{+7.2}_{-4.9} \times 10^{-5}$	-	-	-	$0.97^{+0.01}_{-0.01}$	417.8/411	441.8
52	$4.51^{+0.63}_{-0.64}$	-	-	$2.44^{+0.17}_{-0.15}$	$(6.1 \pm 0.7) \times 10^{-4}$	$6.34^{+0.04}_{-0.04}$	$0.26^{+0.04}_{-0.06}$	$(2.6 \pm 0.4) \times 10^{-4}$	-	-	-	$0.993^{+0.004}_{-0.004}$	369.3/372	389.3
53	$1.81^{\star}$	$0.79^{+0.03}_{-0.03}$	$60.99^{+5.20}_{-5.41}$	-	-	$6.33^{+0.01}_{-0.01}$	$0.01^{\star}$	$(7.13 \pm 0.58) \times 10^{-4}$	-	-	-	0.977 ± 0.003	559.8/424	587.8
54	$0.8^{\star}$	$0.14^{+0.02}_{-0.02}$	$85.04^{+5.02}_{-5.39}$	-	-	$6.51^{+0.01}_{-0.01}$	$0.24^{+0.02}_{-0.02}$	$0.058^{+0.003}_{-0.003}$	$10.86^{+0.12}_{-0.12}$	$2.06^{+0.16}_{-0.15}$	$0.25^{+0.03}_{-0.03}$	$0.984^{+0.001}_{-0.001}$	623.1/421	651.1
55	$0.8^{\star}$	$0.53^{+0.53}_{-0.10}$	$11.32^{+7.13}_{-7.02}$	-	-	$6.35^{+0.13}_{-0.13}$	$0.01^{\star}$	$(1.8 \pm 1.2) \times 10^{-5}$	-	-	-	$1.01^{+0.01}_{-0.01}$	358.5/344	386.5
56	$0.8^{\star}$	$0.19^{+0.03}_{-0.03}$	$59.13^{+19.99}_{-13.30}$	$2.01^{+0.14}_{-0.08}$	0.004 ± 0.001	$6.43^{+0.03}_{-0.03}$	$0.20^{+0.05}_{-0.05}$	$(1.2 \pm 0.2) \times 10^{-3}$	$10.57^{+0.28}_{-0.28}$	$0.99^{+0.38}_{-0.24}$	$0.06^{+0.03}_{-0.02}$	1.031 ± 0.002	535.9/483	573.9
57	$12.08^{+6.11}_{-5.61}$	-	-	-	-	-	-	-	-	-	-	$1.10^{+0.06}_{-0.06}$	107.8/128	123.8
58	$6.09^{+0.77}_{-0.77}$	-	-	-	-	$6.45^{+0.07}_{-0.07}$	$0.18^{+0.13}_{-0.18}$	$(7.5 \pm 2.5) \times 10^{-5}$	-	-	-	$1.02^{+0.01}_{-0.01}$	303.4/296	321.4

* Frozen parameter.

Tab. 3.7: Table 3.5 contd. The best fitting parameters of the absorption (`tbabs, tbpcf`), blackbody (`bbody`), iron fluorescence lines (`gaussian`) and *TKF* (`gabs`) models, along with the fit statistic and *AIC* score used for model selection. Details of Obs. Sn.29 to 58 are given in this table.

4 Accretion Disk surrounding the X-ray pulsar[a]

[a]The findings discussed in Sec. 4.1 are part of a paper submitted to the journal MNRAS

This chapter contains results from of our study of the Quasi-periodic Oscillations exhibited by XRPs and the temperature profile of the Accretion disk corona in the LMXB 4U 1822–371, both of which are associated with the accretion disk in XRPs.

4.1 Quasi-periodic Oscillations

Quasi-periodic oscillations (QPOs), exhibited as a concentration of Fourier power at frequencies of a few ten mHz in the power spectral density (PSD), are a transient phenomenon in XRPs. These mHz QPO has been reported in about twenty XRPs (See the list of sources in James et al. 2010 and Raman et al. 2021) in both transient as well as the persistent sources.

The strong magnetic field of the neutron star impedes the formation of an accretion disk inside the magnetospheric radius ($r_{\rm M}$) at about a few 1000 km from the neutron star. Therefore the radius of the inner accretion disk is expected to be of the order of $r_{\rm M}$. QPOs are usually exhibited by XRPs at frequencies of a few ten mHz, and since the Keplerian orbital frequency of matter around a canonical 1.4 $M_\odot$ neutron star at $r_{\rm M}\sim$ 5000 km is $\frac{1}{2\pi}\sqrt{\frac{GM_{\rm NS}}{r_{\rm M}^3}} \sim 200$ mHz, the QPOs are qualitatively associated with phenomena related to the inner accretion disk. The accretion disk is considered to be always present in persistent sources. In contrast, the transient sources are thought to have the phases of forming a temporary accretion disk around the neutron star during their luminous phases.

The two most commonly used models to explain QPOs in XRPs are the Magnetospheric beat-frequency model (BFM; Alpar et al. 1985) and the Keplerian frequency model (KFM; Klis 1997). BFM models the QPO as a modulation in the mass accretion rate on to the NS poles at the beat frequency between the spin frequency of NS ($\nu_{\rm NS}$) and the orbital frequency of the inner accretion disk. The matter is channelled onto

the neutron star from inhomogeneity in the inner accretion disk along the spinning magnetic field lines. According to BFM, $\nu_{\rm QPO} = \nu_{\rm k} - \nu_{\rm NS}$, where $\nu_{\rm k}$ is the Keplerian orbital frequency of the inner accretion disk and $\nu_{\rm NS}$ is the spin period of the neutron star. KFM models the QPO as an effect due to the blobs of matter in the inner accretion disk intercepting the emission from the neutron star, because of which the observer perceives a modulation in the X-ray flux. According to KFM, $\nu_{\rm QPO} = \nu_{\rm k}$. KFM puts a constraint on the observed QPO frequency based on the neutron star spin frequency that $\nu_{\rm NS} < \nu_{\rm QPO}$, based on the argument of centrifugal inhibition of the accreted matter beyond this limit. BFM, on the other hand, provides constraints on the X-ray flux maintained by accretion based on the centrifugal inhibition limit. Assuming the inner accretion disk radius to also scale by the accretion rate $\dot{M}^{-\frac{2}{7}}$ (and hence the X-ray luminosity), the Keplerian frequency of the inner accretion disk, and thereby the QPO frequency, is expected to increase with luminosity in both KFM and BFM (Finger, 1998).

QPOs exhibit variability as a function of photon energy, which puts constraints on the applicable models that explain the origin of QPO. No general characteristic trend has been recognized so far in XRPs regarding the QPO rms as a function of energy. Correlation (IGR J19294+1816; Raman et al. 2021, KS 1947+300; James et al. 2010, XTE J1858+034; Mukherjee, Bapna, et al. 2006, LMC X–4; Sharma, Jain, et al. 2023), anti-correlation (A 1118–615; Nespoli et al. 2010, V0332+53; Qu et al. 2005, Cen X–3 Liu, Wang, et al. 2022, GX 304–1; Devasia et al. 2011), and no correlation (Cen X–3; Raichur et al. 2008) have all been reported. Most of the studies mentioned above were performed using *RXTE*/PCA data, which was sensitive to photons in the 2–30 keV energy band. There are also cases where uncommon dependency is seen, for instance, the QPO detection at 80 keV and the convex-shaped relation between QPO rms and photon energy in 1A 0535+262 peaking at around 60 keV from the *Insight*/HXMT data which offers 1–250 keV spectral coverage (Ma et al., 2022).

We performed a comprehensive search for QPOs in the archival *XMM–Newton* and *NuSTAR* observations of XRPs. In the observations where QPO was detected, we measured the QPO rms as a function of photon energy and analysed the energy spectrum. We used XSPEC v12.13.1 (Arnaud, 1996) for performing the spectral analysis.

4.1.1 Observations and Data Reduction

Instruments and Data reduction

XMM–Newton: The PN-type European Photon Imaging Camera (EPIC-PN) onboard the *X-ray Multi-Mirror Mission* (*XMM–Newton*) is an array of twelve pn-CCDs coupled to focussing optics, sensitive to photons in 0.15–15 keV (Strüder et al., 2001). EPIC-PN has an effective area of around 1000 cm^2 at 1.5 keV. We followed the standard data reduction steps from *XMM–Newton* data analysis threads[1]. First, the events list for the EPIC-PN instrument was generated from Observation Data Files (ODF) with the tool epproc, using the calibration files generated with the tool cifbuild. The generated event time stamps were then corrected for the motion of the earth around the barycenter of the solar system using the tool barycen and subsequently filtered for time intervals of high background particle flaring. We also checked the observations for pile-up, following the steps mentioned in SAS Thread *epatplot*[2]. If found, piled-up data was removed by excluding the central core of the PSF in Imaging mode observations using an annular source region, and by removing the boresight columns in Timing mode observations[3].

The source and background lightcurves and spectra were extracted from the resulting events file with the tool evselect. A circular source and annular background region were used for imaging mode observations, while rectangular strips were used for timing mode observations.

NuSTAR: *NuSTAR* operating in 3–79 keV, consists of two CdZnTe detectors paired to separate hard X-ray focussing optics and have a total effective area of about 1000 cm^2 at 10 keV (Harrison et al., 2013). The two detectors are called Focal Plane Modules (FPM) A and B. We followed the standard data reduction steps from The NuSTAR Data Analysis Software Guide[4], using the NuSTAR Data Analysis Software package NuSTARDAS v2.1.1. The filtered and calibrated events files were generated with the tool nupipeline using the NuSTAR calibration database (CALDB) version 20210315. Using nuproducts, the source and background lightcurves were generated from circular regions of FPMA and FPMB modules. The lightcurves from FPMA and FPMB were summed together using the task `lcmath`.

[1] https://www.cosmos.esa.int/web/XMM--Newton/sas-threads
[2] https://www.cosmos.esa.int/web/XMM--Newton/sas-thread-epatplot
[3] http://xmm-tools.cosmos.esa.int/external/xmm_user_support/documentation/sas_usg/USG/epicpileuptiming.html
[4] https://heasarc.gsfc.nasa.gov/docs/nustar/analysis/nustar_swguide.pdf

RXTE/PCA: The Proportional Counter Array (PCA) on the *Rossi X-ray Timing Explorer* (*RXTE*) consists of five collimated large area Xenon-filled proportional counter units with a total effective area of ~ 6500 cm^2, sensitive to photons in 2–60 keV (Jahoda et al., 1996). PCA lightcurves in different energy bands were extracted from the GoodXenon Event mode data files using the tool seextrct using the photon energy to channel conversion table given here[5]. We have used only one *RXTE*/PCA observation (of 4U 1626–67) in this work.

Method of analysis

For each observation listed in Tables 4.1 and 4.2, lightcurves were generated with a bin size of 1 s. Setting the bin size to 1 s enables the construction of PSD up to 500 mHz, facilitating the ability to check for mHz QPOs. The PSD of each lightcurve was generated using the *XRONOS* tool `powspec`[8]. The lightcurves were divided into segments of length 4096 s and the power spectra obtained from each lightcurve segment were averaged to improve the signal-to-noise ratio of the PSD (Van der Klis, 1989). The resulting PSD was normalized such that it has units of (rms/mean)^2 Hz^{-1} so that integrating the PSD over frequency gives the fractional rms squared variability. An expected flat noise level of ~ 2/mean was also subtracted from the PSD (Van der Klis 1989, Belloni and Hasinger 1990).

QPOs in the PSD appeared like relatively wide asymmetric bumps and were identified through visual inspection. Apart from QPOs some of the PSDs also showed sharp narrow features (See for example Fig. 4.1 and 4.9) corresponding to the spin period of the pulsar and its harmonics). The PSD to a factor of 4 frequency range on either side of the QPO vicinity (or a factor of 8 for the low Q-factor cases) was fitted with the combination of a `powerlaw` or `lorentzian` (for the continuum), and a `lorentzian` (for the QPO). The sharp spikes in the PSD corresponding to the pulsar spin period and its harmonics were removed before performing the fit. The center ($\nu_{\rm QPO}$), width ($\Delta\nu_{\rm QPO}$) of `lorentzian` and the integrated fractional rms-squared power under the `lorentzian` ($\mathrm{P}_{rms} \pm \Delta\mathrm{P}_{rms}$) were then estimated. Fractional rms variability of the QPO was estimated as $\sqrt{\mathrm{P}_{rms}} \pm (\Delta\mathrm{P}_{rms}/2\sqrt{\mathrm{P}_{rms}})$. To assess the variation of QPO fractional rms in different energy ranges, the procedure was repeated on the PSD derived from lightcurves in different energy bands. The errors assigned to the QPO fractional rms values are their 68% (1σ) confidence intervals and all other parameters are their 90% confidence intervals unless otherwise stated.

[5] https://heasarc.gsfc.nasa.gov/docs/xte/e-c_table.html
[8] https://heasarc.gsfc.nasa.gov/lheasoft/ftools/fhelp/powspec.txt

Tab. 4.1: Observations log

Sl no.	Source	Observatory/Instrument	Obs. ID	Observation mode	Observation duration (ks)[6]
1	1A 0535+262	*XMM–Newton*/PN	0674180101	PrimeFullWindow	58
2		*NuSTAR*/FPMA,B	80001016002	-	43
3		*NuSTAR*/FPMA,B	80001016004	-	56
4		*NuSTAR*/FPMA,B	90401370001	-	118
5	2S 1553–542	*NuSTAR*/FPMA,B	90101002002	-	50
6	4U 0115+63	*NuSTAR*/FPMA,B	90102016002	-	38
7		*NuSTAR*/FPMA,B	90102016004	-	41
8	4U 1538–52	*XMM–Newton*/PN	0152780201	PrimeFullWindow	79
9		*NuSTAR*/FPMA,B	30201028002	-	85
10	4U 1626–67	*XMM–Newton*/PN	0111070201	PrimeSmallWindow	16
11		*XMM–Newton*/PN	0152620101	PrimeSmallWindow	84
12		*XMM–Newton*/PN	0764860101	FastTiming	54
13		*NuSTAR*/FPMA,B	30101029002	-	114
14	4U 1700–37	*XMM–Newton*/PN	0600950101	PrimeFullWindow	50
15		*NuSTAR*/FPMA,B	30101027002	-	74
16	4U 1901+03	*NuSTAR*/FPMA,B	90501305001	-	44
17		*NuSTAR*/FPMA,B	90501324002	-	102
18		*NuSTAR*/FPMA,B	90502307002	-	38
19		*NuSTAR*/FPMA,B	90502307004	-	55
20	4U 1907+09	*XMM–Newton*/PN	0555410101	FastTiming	21
21		*NuSTAR*/FPMA,B	30401018002	-	154
22	4U 2206+54	*XMM–Newton*/PN	0650640101	PrimeLargeWindow	75
23		*NuSTAR*/FPMA,B	30201015002	-	108
24	Cen X–3	*XMM–Newton*/PN	0111010101	PrimeSmallWindow	67
25		*XMM–Newton*/PN	0400550201	FastTiming	80
26		*NuSTAR*/FPMA,B	30101055002	-	39
27	Cep X–4	*NuSTAR*/FPMA,B	80002016002	-	79
28		*NuSTAR*/FPMA,B	80002016004	-	76
29	EXO 2030+375	*XMM–Newton*/PN	0745240201	FastTiming	31
30		*NuSTAR*/FPMA,B	90201029002	-	117
31		*NuSTAR*/FPMA,B	90701336002	-	50
32	GRO J1008–57	*NuSTAR*/FPMA,B	80001001002	-	32
33	GRO J1744–28	*XMM–Newton*/PN	0506291201	FastTiming	38
34		*XMM–Newton*/PN	0729560401	FastTiming	82
35		*NuSTAR*/FPMA,B	80002017002	-	67
36		*NuSTAR*/FPMA,B	80202027002	-	56
37	GX 301–2	*XMM–Newton*/PN	0555200301	FastTiming	59
38		*XMM–Newton*/PN	0555200401	FastTiming	47
39		*NuSTAR*/FPMA,B	30001041002	-	51
40		*NuSTAR*/FPMA,B	30101042002	-	53
41	GX 304–1	*NuSTAR*/FPMA,B	90401326002	-	108
42	IGR J16393–4643	*XMM–Newton*/PN	0206380201	PrimeLargeWindow	9
43		*XMM–Newton*/PN	0604520201	PrimeSmallWindow	19
44		*NuSTAR*/FPMA,B	30001008002	-	96
45	IGR J17329–2731	*XMM–Newton*/PN	0795711701	FastTiming	37
46		*NuSTAR*/FPMA,B	90301012002	-	38
47	IGR J17544–2619	*XMM–Newton*/PN	0679810401	PrimeSmallWindow	15
48		*XMM–Newton*/PN	0679810501	PrimeSmallWindow	15
49		*XMM–Newton*/PN	0744600101	PrimeFullWindow	135
50		*NuSTAR*/FPMA,B	30002003003	-	50
51	IGR J18027–2016	*XMM–Newton*/PN	0206380601	PrimeLargeWindow	10
52		*XMM–Newton*/PN	0745060401	PrimeFullWindow	43
53		*XMM–Newton*/PN	0745060501	PrimeFullWindow	16
54		*XMM–Newton*/PN	0745060601	PrimeFullWindow	17
55		*XMM–Newton*/PN	0745060701	PrimeFullWindow	14
56		*XMM–Newton*/PN	0745060801	PrimeFullWindow	17
57		*NuSTAR*/FPMA,B	30101049002	-	85
58	IGR J19294+1816	*XMM–Newton*/PN	0841190101	PrimeFullWindow	67
59		*NuSTAR*/FPMA,B	90401306002	-	79
60		*NuSTAR*/FPMA,B	90401306004	-	79

Tab. 4.2: Observations log continued.

Sl no.	Source	Observatory/Instrument	Obs. ID	Observation mode	Observation duration (ks)[7]
61	KS 1947+300	*XMM–Newton*/PN	0727961201	FastTiming	12
62		*NuSTAR*/FPMA,B	80002015002	-	38
63		*NuSTAR*/FPMA,B	80002015004	-	42
64		*NuSTAR*/FPMA,B	80002015006	-	56
65	RX J0520.5–6932	*XMM–Newton*/PN	0701990101	PrimeFullWindow	20
66		*XMM–Newton*/PN	0729560201	FastTiming	2
67		*XMM–Newton*/PN	0729560301	FastTiming	10
68		*NuSTAR*/FPMA,B	80001002002	-	54
69		*NuSTAR*/FPMA,B	80001002004	-	66
70	SMC X–1	*XMM–Newton*/PN	0784570201	FastTiming	19
71		*XMM–Newton*/PN	0784570301	FastTiming	19
72		*XMM–Newton*/PN	0784570401	FastTiming	21
73		*XMM–Newton*/PN	0784570501	FastTiming	19
74		*XMM–Newton*/PN	0893400101	PrimeSmallWindow	21
75		*XMM–Newton*/PN	0893400301	PrimeSmallWindow	22
76		*NuSTAR*/FPMA,B	30202004002	-	42
77		*NuSTAR*/FPMA,B	30202004004	-	42
78		*NuSTAR*/FPMA,B	30202004006	-	38
79		*NuSTAR*/FPMA,B	30202004008	-	43
80	SMC X–2	*XMM–Newton*/PN	0770580701	FastTiming	8
81		*NuSTAR*/FPMA,B	90101017002	-	48
82		*NuSTAR*/FPMA,B	90102014002	-	48
83		*NuSTAR*/FPMA,B	90102014004	-	50
84		*XMM–Newton*/PN	0770580901	PrimeSmallWindow	31
85	V 0332+53	*XMM–Newton*/PN	0506190101	PrimeFullWindow	36
86		*XMM–Newton*/PN	0763470301	FastTiming	32
87		*XMM–Newton*/PN	0763470401	FastTiming	31
88		*NuSTAR*/FPMA,B	80102002010	-	44
89		*NuSTAR*/FPMA,B	90202031002	-	44
90		*NuSTAR*/FPMA,B	90202031004	-	44
91	X Persei	*XMM–Newton*/PN	0151380101	PrimeFullWindow	30
92		*XMM–Newton*/PN	0600980101	PrimeFullWindow	124
93		*NuSTAR*/FPMA,B			
94	XTE J1829–098	*XMM–Newton*/PN	0135746701	PrimeFullWindow	1
95		*NuSTAR*/FPMA,B	90401332002	-	55

We analysed energy-resolved lightcurves for a total of 97 observations of 29 X-ray pulsars and QPOs were identified in nine of them.

4.1.2 Sources and Results

4U 1626–67

4U 1626–67 is a persistent Low mass Ultra-compact X-ray binary in which a 130 mHz spinning strongly magnetized ($\sim 3 \times 10^{12}$ G) neutron star (Coburn et al. 2002, and references therein) is accreting Oxygen and Neon rich matter from a companion by Roche lobe overflow, that is assessed from the presence of Oxygen/Neon emission complex at 1 keV in its energy spectrum (Schulz et al., 2001). The X-ray spectrum of the persistent accreting pulsar 4U 1626–67 has been extensively studied, and it usually exhibits a soft blackbody component along with the powerlaw (Camero-Arranz et al., 2012). A QPO at 48 mHz is well established in the source at multiple wavelengths, in the Optical band with 3% rms amplitude (Chakrabarty, 1998), UV band with 3% rms amplitude in the near-UV to 15% in the far-UV (Chakrabarty

Tab. 4.3: Observations catalogue for timing and spectral analysis, of sources with QPO detection.

Source	Observatory/Instrument	Obs. ID	Observing mode	Start date (Duration in ks)	Avg. count rate[†] (cts s^{-1})	Piled-up	Avg. count rate[‡] (cts s^{-1})
4U 1626–67	*XMM–Newton*/PN	0111070201	PrimeSmallWindow	24-08-2001 (16)	33.20 ± 0.06	-	-
		0152620101	PrimeSmallWindow	20-08-2003 (84)	27.63 ± 0.02	XRL[§]	-
	RXTE/PCA	P10101	Good Xenon	10-02-1996 (395)	306.9 ± 0.05[¶]	-	-
IGR J19294+1816	*XMM–Newton*/PN	0841190101	PrimeFullWindow	13-10-2019 (67)	20.57±0.03	PU	2.74 ± 0.09
V 0332+53	*XMM–Newton*/PN	0763470301	FastTiming	09-10-2015 (32)	423.68±0.19	PU	194.7 ± 0.1
		0763470401	FastTiming	16-09-2015 (31)	280.12±0.12	PU	162.0 ± 0.1
	NuSTAR/FPM	90202031002	N/A	30-07-2016 (44)	24.52 ± 0.02[‖]	-	-
		90202031004	N/A	31-07-2016 (44)	19.64 ± 0.02[‖]	-	-
Cen X–3	*XMM–Newton*/PN	0400550201	FastTiming	27-01-2001 (80)	452.1 ± 0.07	No	-
XTE J1858+034	*NuSTAR*/FPM	90501348002	N/A	03-11-2019 (90)	17.27 ± 0.02[‖]	-	-

[†] Before pile-up correction.
[‡] After pile-up correction.
[§] This *XMM–Newton* observation is affected by X-ray loading.
[¶] Across all five PCUs of *RXTE* that were ON during this observation.
[‖] In FPMA module.

et al., 2001) and X-ray band with 15% rms (Shinoda et al. 1990, Kaur et al. 2008). The 48 mHz QPO is observed in 4U 1626–67 when the pulsar is spinning down, and lower frequency QPOs (36 and 40 mHz) are observed when the source is spinning up (See Jain et al., 2010, and references therein).

The 48 mHz QPO is present in two *XMM–Newton* observations (Table 4.9 and Fig. 4.1) (Beri, Jain, et al., 2014). To extend the QPO variation to higher energy bands, we also selected an *RXTE*/PCA observation having $\sim$ 147 ks on-source exposure in which 48 mHZ QPO was reported by Kaur et al. (2008). We determined the energy-resolved variation of QPO in the 0.5–60 keV energy band (Fig. 4.2). It shows that the fractional rms amplitude of QPO is high in the 1–3 keV at around 20% rms and the 0.5–1 keV at around 18% rms. In 3–60 keV, the QPO rms show a steady rising trend, increasing from about 15% to 28%.

We analysed spectra from both *XMM–Newton* observations. A power law could fit the continuum, and the strong Neon emission complex at $\sim$ 1 keV is fitted with a gaussian profile (See Beri, Paul, et al. 2018). The spectrum also showed the presence of soft excess, which is modelled with a black body component of $kT_{\rm BB} \sim 0.3$ keV (Fig. 4.4).

IGR J19294+1816

IGR J19294+1816 is a transient High mass X-ray binary in which a spinning ($\nu_{\rm spin}\sim$83 mHz) strongly magnetized ($\sim 4 \times 10^{12}$ G) neutron star (Tsygankov, Doroshenko, Mushtukov, Lutovinov, et al., 2019) accretes matter from a Be-type companion star (Rodes-Roca et al., 2018) in a 117 d orbit (Rodriguez et al., 2009).

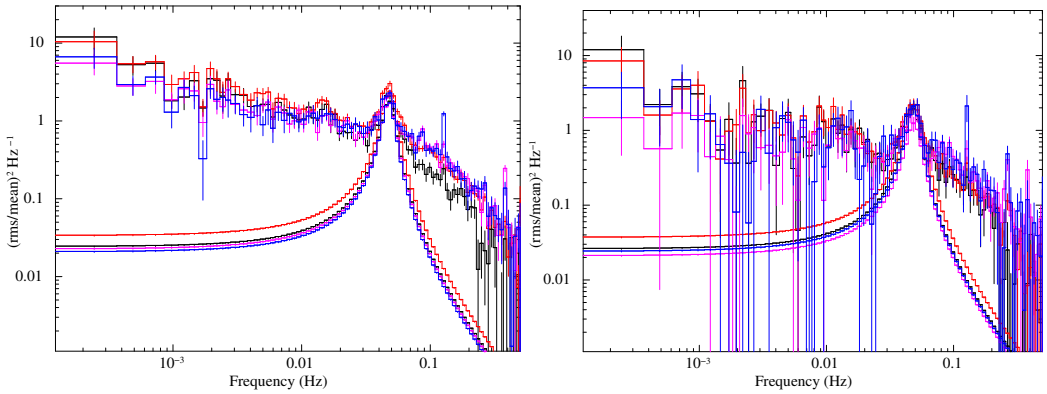

Fig. 4.1: The *XMM–Newton*/PN PSD of 4U 1626–67 in different energy bands (0.5-1 keV in black, 1–3 keV in red, 3–5.7 keV in blue, 5.7–10 keV in magenta) of OID 0152620101 (Left) and OID 111070201 (Right). QPO at 40 mHz is fitted with lorentzian profile. The sharp features in the PSDs correspond to the NS pulsations at 130 mHz and its harmonics.

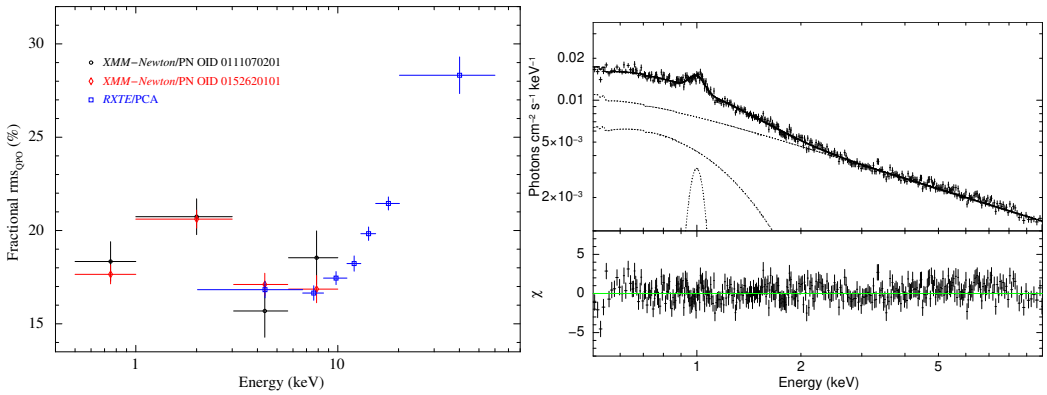

Fig. 4.2: Left: 4U 1626–67 QPO rms energy dependence from *XMM–Newton*-PN (red, black) and *RXTE*-PCA (blue). Right: The 0.5–10 keV unfolded spectrum and residuals to the best fit model (`tbabs * (powerlaw + gauss + bbody)`) on the *XMM–Newton* Obs. ID 0111070201. Soft excess is modelled with a black body component of $kT \sim 0.3$ keV.

Tab. 4.4: The results of spectral fit performed on two observations of 4U 1626–67 having QPO. The best fit model parameter values and their errors are given. The errors quoted on all the parameters are their 90% confidence ranges.

Obs. ID	0111070201	0152620101
nH†	0.05 ± 0.01	0.07 ± 0.01
PhoIndex (Γ)	0.81 ± 0.02	0.80 ± 0.01
N_{PL}‡	$(8.1 \pm 0.2) \times 10^{-4}$	$(6.8 \pm 0.1) \times 10^{-4}$
kT_{bbody} (keV)	0.27 ± 0.01	0.24 ± 0.01
N_{bbody}§	$(1.2 \pm 0.1) \times 10^{-4}$	$(1.10 \pm 0.04) \times 10^{-4}$
E_{Gauss}	1.00 ± 0.01	1.01 ± 0.01
σ_{Gauss}	0.04 ± 0.01	$0.02^{+0.01}_{-0.02}$
N_{Gauss}¶	$(3.9 \pm 0.5) \times 10^{-4}$	$(2.1 \pm 0.2) \times 10^{-4}$
$Flux_{2\text{-}20\ keV}$ (10^{-10} erg s^{-1} cm^{-2})	2.90 ± 0.01	2.31 ± 0.004
χ^2 (dof)	1823 (1642)	2153 (1896)
χ^2_{red}	1.11	1.14

† in units of 10^{22} atoms cm^{-2}.
‡ Normalization in units of photons s^{-1} cm^{-2} keV^{-1} at 1 keV.
§ Normalization in units of 10^{37} ergs s^{-1} kpc^{-2}.
¶ Total photons s^{-1} cm^{-2} in the gaussian line.

QPO was reported in the *AstroSat*/LAXPC observation at 32 mHz during an outburst of the source during the periastron passage in 2019 (Raman et al., 2021).

We detected QPO in an *XMM–Newton* observation at 30 mHz (Table 4.9, Fig. 4.3), and the fractional rms amplitude of QPO shows an increasing trend in the 0.5–10 keV range (See Table 4.9 and Fig. 4.4), in agreement with the results of Raman et al. (2021).

The 0.5–10 keV *XMM–Newton*/PN spectrum could be well-fitted with a power law having a high energy cutoff. Residuals left by the iron fluorescence line were modelled with a `gaussian` emission profile (Table 4.5, Fig. 4.5). Since the width of the `gaussian` line was not constrained by the fit, we fixed it to 10 eV.

V0332+53

V 0332+53 is a transient High mass X-ray binary in which a 227 mHz pulsar accretes matter from a Be-type companion star in a 34 d eccentric ($e \sim 0.3$) orbit (Stella, White, et al., 1985). QPO was discovered in the source during an outburst from *Ginga*/LAC observations by Takeshima, Dotani, et al. (1994) at 51 mHz with about 5% rms in the 2.3–37.2 keV energy band. The 51 mHz QPO and another 220 mHz QPO (centred at the NS spin frequency) were found in a later observation taken

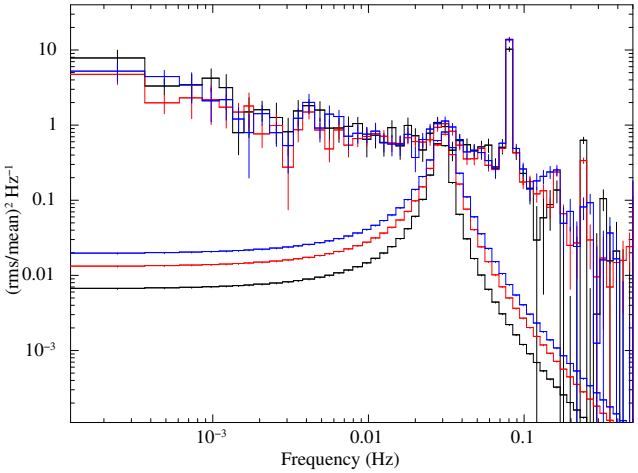

Fig. 4.3: The *XMM–Newton*/PN PSD of IGR J19296+1816 in different energy bands (0.5–3 keV in black, 3–5.7 keV in red, 5.7–10 keV in blue) and QPOs fitted with lorentzian profiles. The sharp features in the PSDs correspond to the NS pulsations at 83 mHz and its harmonics.

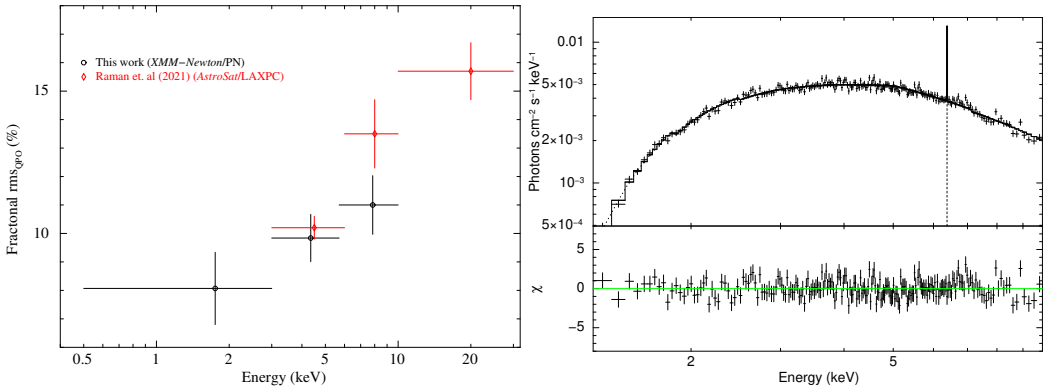

Fig. 4.4: Left: IGR J19294+1816 QPO rms energy dependence from *XMM–Newton* (this work) (black) and *Astrosat*/LAXPC (red) (Raman et al., 2021). Right: The 0.5–10 keV unfolded *XMM–Newton*/PN spectrum and residuals to the best fit model `tbabs * (powerlaw * highecut + gaussian)`.

Tab. 4.5: The results of spectral fit performed on one observation of IGR J19294+1816 having QPO. The best fit model parameter values and their errors are given. The errors quoted on all the parameters are their 90% confidence ranges.

Obs. ID	0841190101
nH†	3.62 ± 0.17
PhoIndex (Γ)	0.41 ± 0.07
N_{PL}‡	0.010 ± 0.001
cutoffE (keV)	4.96 ± 0.30
foldE (keV)	7.03 ± 0.50
E_{Gauss}	6.39 ± 0.01
σ_{Gauss}	0.01*
N_{Gauss}¶	$(2.9 \pm 0.4) \times 10^{-4}$
$Flux_{2\text{-}20\ keV}$ (10^{-10} erg s^{-1} cm^{-2})	4.04 ± 0.02
χ^2 (dof)	679 (669)
χ^2_{red}	1.02

* Frozen.
† in units of 10^{22} atoms cm^{-2}.
‡ Normalization in units of photons s^{-1} cm^{-2} keV^{-1} at 1 keV.
¶ Total photons s^{-1} cm^{-2} in the gaussian line.

during the outburst decay phase by *RXTE*/PCA (Qu et al., 2005), and *INTEGRAL*/JEM-X and IBIS (Mowlavi et al., 2006) observations. Takeshima, Dotani, et al. (1994) also observed that the QPO central frequency does not vary with flux and that the QPO rms stays constant as a function of photon energy till 10 keV and drops beyond 10 keV.

Two observations from *XMM–Newton*/PN show the presence of a QPO at about 40 mHz (Table 4.9, Fig. 4.5), and two observations from *NuSTAR* show twin QPOs at 2.5 mHz and 18 mHz (Table 4.9, Fig. 4.6). The 40 mHz QPO shows a slightly increasing trend of the QPO rms as a function of photon energy, while the 2 mHz and 18 mHz QPO rms show no trend in the QPO rms as a function of energy (Fig. 4.7). The quality factor of QPO detected in *XMM–Newton* is also a factor of ~ 4 lower than *NuSTAR*. *NuSTAR* PSD of both the observations also show the presence of a faint QPO-like structure at about 100 mHz (See Fig. 4.6).

The 1–10 keV *XMM–Newton* spectrum could be modelled well with a partially covered powerlaw model or a `bbody + compTT` model. The 3–55 keV *NuSTAR* spectrum could be well modelled with `bbody + powerlaw*newhcut*cyclabs` (Table 4.6, Fig. 4.7).

Tab. 4.6: The results of spectral fit performed on four observations of V 0332+53 having a QPO. The best fit model parameter values and their errors are given. The errors quoted on all the parameters are their 90% confidence ranges.

	XMM–Newton				*NuSTAR*‖	
Obs. ID	0763470301		0763470401		90202031002	90202031004
Continuum	`tbpcf*powerlaw`	`bbody+comptt`	`tbpcf*powerlaw`	`bbody+comptt`		
Energy range	1–10 keV	1–10 keV	1–10 keV	1–10 keV	3–55 keV	3–55 keV
nH_1†	0.69⋆	1.00 ± 0.02	0.69⋆	$1.05^{0.02}_{-0.02}$	$4.49^{+2.04}_{-3.80}$	$1.09^{+4.28}_{-1.11}$
nH_2†	1.33 ± 0.23	-	0.74 ± 0.04	-	-	-
Cvr. fraction	0.67 ± 0.02	-	0.87 ± 0.02	-	-	-
PhoIndex (Γ)	0.46 ± 0.01	-	0.44 ± 0.01	-	$0.69^{+0.04}_{-0.06}$	$0.59^{+0.14}_{-0.09}$
N_{PL}‡	0.06 ± 0.001	-	0.04 ± 0.001	-	0.014 ± 0.002	0.008 ± 0.002
kT	-	3.13 ± 0.09	-	$3.27^{0.10}_{-0.12}$	-	-
τ	-	$73.05^{-73.03}_{-21.59}$	-	$60.05^{-60.07}_{-13.96}$	-	-
N_{compTT}	-	0.10 ± 0.01	-	0.08 ± 0.004	-	-
E_{cut}	-	-	-	-	16.39 ± 0.40	15.94 ± 0.72
E_{fold}	-	-	-		18.08 ± 3.20	22.44 ± 7.25
$E_{Gauss,Fe}$	6.67 ± 0.01	6.64 ± 0.01	6.63 ± 0.01	$6.64^{+0.01}_{-0.01}$	$6.28^{+0.09}_{-0.08}$	$6.36^{+0.07}_{-0.07}$
$\sigma_{Gauss,Fe,1}$	0.23 ± 0.03	0.32 ± 0.02	0.20 ± 0.02	$0.24^{+0.02}_{-0.02}$	$0.15^{+-0.15}_{-0.15}$	$0.15^{+0.13}_{-0.15}$
$N_{Gauss,Fe,1}$¶	$(1.4 \pm 0.1) \times 10^{-3}$	$(2.0 \pm 0.1) \times 10^{-4}$	$(1.0 \pm 0.1) \times 10^{-3}$	$(1.3 \pm 0.1) \times 10^{-3}$	$(1.0 \pm 0.1) \times 10^{-4}$	$(1.2 \pm 0.4) \times 10^{-5}$
$\sigma_{Gauss,Fe,2}$	1.43 ± 0.24	-	1.37 ± 0.14	-	-	-
$N_{Gauss,Fe,2}$¶	0.01 ± 0.002	-	0.01 ± 0.001	$(8 \pm 1) \times 10^{-4}$	-	-
$E_{Gauss,2}$	1.77 ± 0.24	$1.86^{0.03}_{-0.07}$	1.92 ± 0.04	$1.85^{+0.02}_{-0.02}$	-	-
$\sigma_{Gauss,2}$	0.61 ± 0.13	0.13 ± 0.03	0.51 ± 0.04	$0.19^{0.03}_{-0.03}$	-	-
$N_{Gauss,2}$¶	0.01 ± 0.0001	$(8 \pm 1) \times 10^{-4}$	0.01 ± 0.001	$(9 \pm 2) \times 10^{-4}$	-	-
kT_{bbody} (keV)	-	0.79 ± 0.04	-	$0.77^{0.04}_{-0.04}$	$0.62^{+0.30}_{-0.06}$	$0.91^{+0.19}_{-0.31}$
N_{bbody}§	-	0.004 ± 0.001	-	0.003 ± 0.001	$(1.0 \pm 0.5) \times 10^{-3}$	$(3.0 \pm 0.2) \times 10^{-4}$
$Flux_{2\text{-}20\ keV}$ (10^{-10} erg s^{-1} cm^{-2})	41 ± 0.03	34 ± 0.03	33 ± 0.03	28 ± 0.03	7.51 ± 0.02	6.10 ± 0.02
Unabsorbed $flux_{2\text{-}20\ keV}$	42 ± 0.03	34.93 ± 0.03	34.13 ± 0.03	28.99 ± 0.02	7.62 ± 0.02	6.14 ± 0.02
χ^2 (dof)	1939 (1791)	1992.43 (17871)	2253 (1851)	2066.24(1787)	400(329)	369(324)
χ^2_{red}	1.08	1.11	1.22	1.16	1.22	1.14

⋆ Frozen.
† in units of 10^{22} atoms cm^{-2}.
‡ Normalization in units of photons s^{-1} cm^{-2} keV^{-1} at 1 keV.
§ Normalization in units of 10^{37} ergs s^{-1} kpc^{-2}.
¶ Total photons s^{-1} cm^{-2} in the gaussian line.
‖ A CRSF at 29 keV and its harmonic is modelled with `cyclabs` model, the parameters of which are not given in this table.

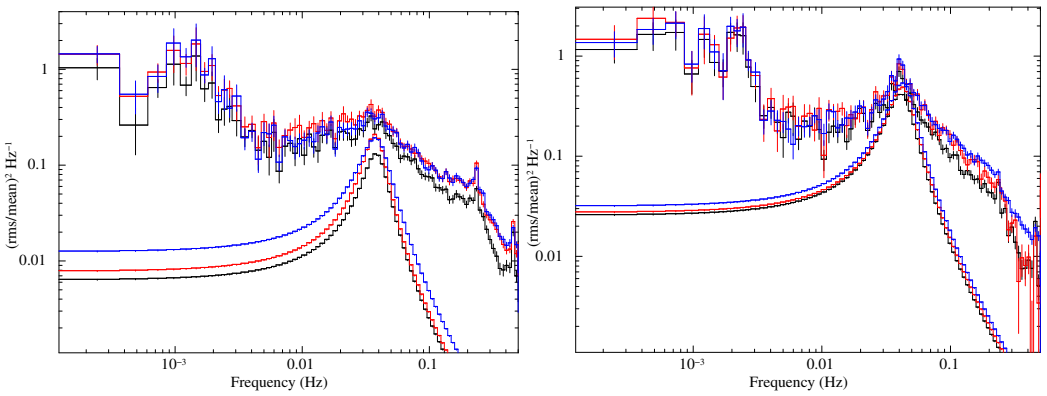

Fig. 4.5: The *XMM–Newton*/PN PSD of V 0332+53 in different energy bands (0.5–3 keV in black, 3–5.7 keV in red, 5.7–10 keV in blue) of OID 0763470301 (Left) and OID 0763470401 (Right). QPO at 40 mHz is fitted with lorentzian profile. The sharp features in the PSDs correspond to the NS pulsations at 227 mHz and its harmonics.

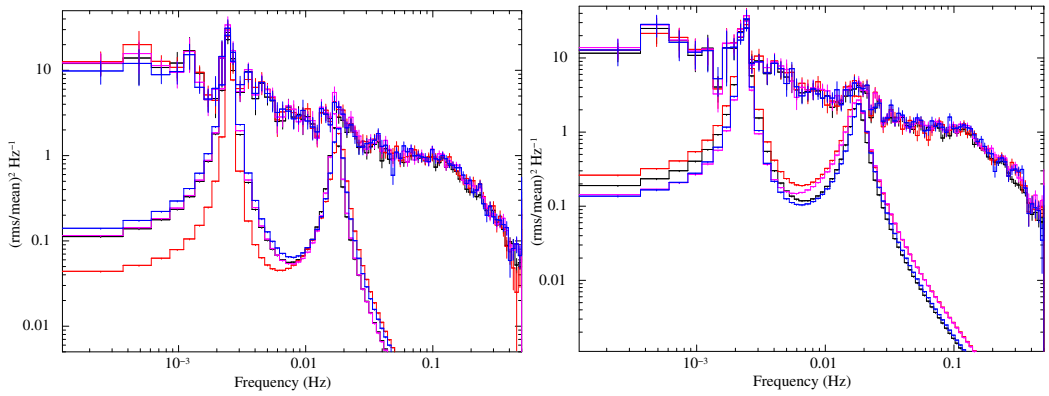

Fig. 4.6: The *NuSTAR* PSD of V 0332+53 in different energy bands (3–8 keV in black, 8–10 keV in red, 10–15 keV in blue, 15–25 keV in magenta) of OID 90202031002 (Left) and OID 90202031004 (Right). Twin QPOs at 2.5 mHz and 18 mHz fitted with lorentzian profiles.

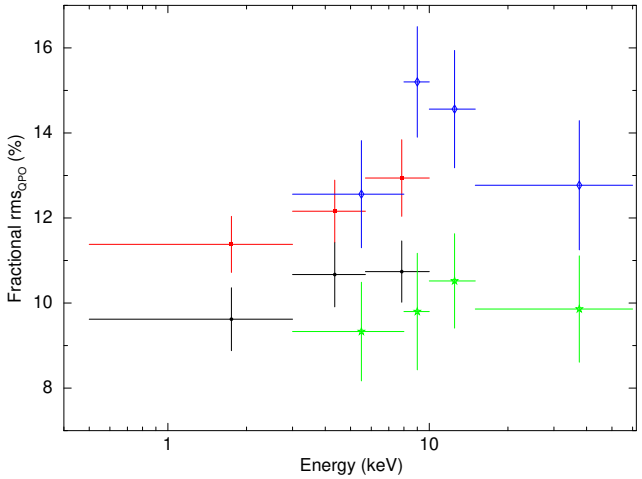

Fig. 4.7: Energy dependence of QPO rms of V 0332+53 from *XMM–Newton* (black, red) at 40 mHz and *NuSTAR* (blue, green) observations at 18 mHz.

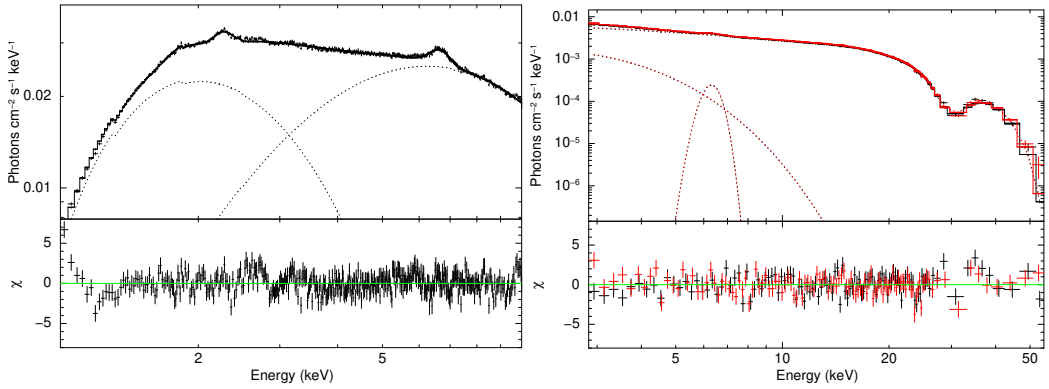

Fig. 4.8: Spectral fit to *XMM–Newton* observation 0763470301 (Left) and *NuSTAR* observation 90202031002 (Right) with the model described in Table. 4.6.

Cen X–3

Cen X–3 is a persistent 208 mHz X-ray pulsar accreting matter from a massive O-type 20 $M_{\odot}$ supergiant companion star in a compact, nearly circular 2.2-day orbit (See Suchy, Pottschmidt, et al. 2008, and references therein). The accretion is expected to be partly from stellar wind and partly from the accretion disk due to the overall spin-up trend of the pulsar (Petterson, 1978). Cen X–3 shows QPO at different frequencies ranging from 30 mHz (this work) to 90 mHz (Raichur et al., 2008), and Raichur et al. (2008) and Liu, Wang, et al. (2022) have shown that the QPO frequency or rms showed no dependence on the X-ray luminosity. Even though in Raichur et al. (2008) and this work, the QPO rms does not show any dependence on photon energy, recently Liu, Wang, et al. (2022) showed that the 40 mHz QPO rms decrease from 13% at 2 keV to about 9% at 17 keV. They further argue that the QPO frequency and rms have an orbital dependence and that the QPO photons show an overall soft lag.

We detected the presence of a QPO at around 30 mHz in one *XMM–Newton* observation. The QPO rms shows a weak increasing trend with photon energy. The QPO rms increases from about 4% in 0.5–3 keV to about 6% in 5.7–10 keV (Table 4.9, Fig. 4.10).

The spectral continuum could be modelled well using a partially absorbed `cutoffpl`. Multiple emission lines were present at 0.95 keV and around 6.5 keV. The iron line emission region is complex, which is modelled with a combination of a narrow `gaussian` at 6.55 keV and a broad `gaussian` at 6.77 keV. The complex iron region is possibly due to three distinct iron lines at 6.4, 6.7 and 7 keV (Naik and Paul, 2012). Even though the continuum and individual emission lines were well-modelled, the high SNR data left sharp residuals all over the spectrum that impacted the fit statistic. We, therefore, included a systematic error at 0.5% to the data (Table 4.7, Fig. 4.10).

XTE J1858+034

XTE J1858+034 is a transient X-ray pulsar spinning at 4.5 mHz. The binary is thought to be a Be-type HMXB due to its transient nature (Takeshima, Corbet, et al., 1998) and nature of the optical companion (Reig, Negueruela, et al., 2005). However, a recent study by Tsygankov, Lutovinov, Molkov, et al. (2021) proposed that the system is a Symbiotic binary hosting a K/M-type stellar companion. QPO was first reported in the source from an *RXTE*/PCA observation by Paul and Rao

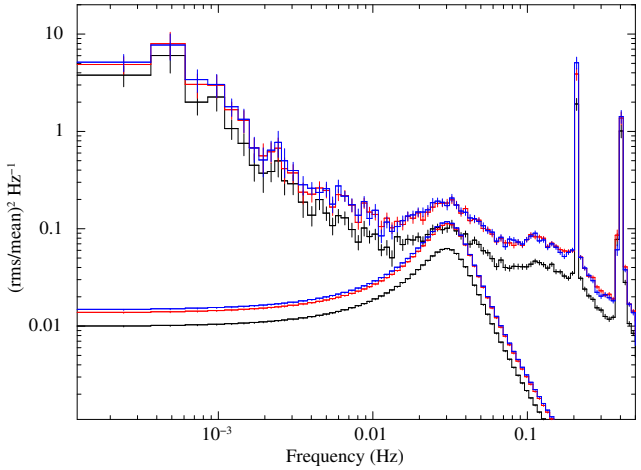

Fig. 4.9: The *XMM–Newton*/PN Cen X–3 PSD in three different energy bands (0.5–3 keV in black, 3–5.7 keV in red, 5.7–10 keV in blue) and QPOs fitted with lorentzian profiles. The sharp features in the PSDs correspond to the NS pulsations at 208 mHz and its harmonics.

Tab. 4.7: The results of spectral fit performed on the *XMM–Newton* observation of Cen X–3 having a QPO. The best fit model parameter values and their errors are given. The errors quoted on all the parameters are their 90% confidence ranges.

Obs. ID	040550201[§]
nH_1[†]	$0.23^{+0.08}_{-0.09}$
nH_2[†]	$1.29^{+0.017}_{-0.05}$
Cvr. fraction	$0.96^{+0.02}_{-0.02}$
PhoIndex (Γ)	$0.48^{+0.02}_{-0.02}$
foldE	7.01 ± 0.16
N_{PL}[‡]	0.06 ± 0.001
$E_{Gauss,1}$	6.55 ± 0.01
$\sigma_{Gauss,1}$	0.21 ± 0.01
$E_{Gauss,2}$	6.77 ± 0.05
$\sigma_{Gauss,2}$	0.82 ± 0.07
$E_{Gauss,3}$	0.95 ± 0.03
$\sigma_{Gauss,3}$	0.15 ± 0.01
χ^2 (dof)	2338.5/1883
χ^2_{red}	1.24

[§] We have introduced a 0.5% systematic error to the data to avoid systematic residuals to a certain extent in the high photon statistics spectrum.
[†] in units of 10^{22} atoms cm^{-2}.
[‡] Normalization in units of photons s^{-1} cm^{-2} keV^{-1} at 1 keV.
[¶] Total photons s^{-1} cm^{-2} in the gaussian line.

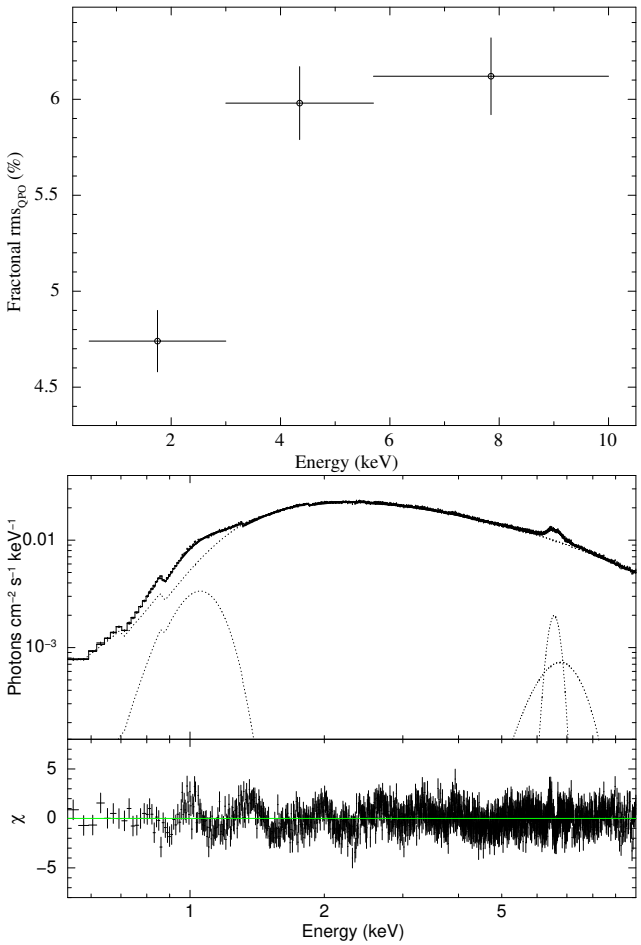

Fig. 4.10: Top: Cen X–3 QPO rms energy dependence from *XMM–Newton*. Bottom: The 0.5–10 keV unfolded *XMM–Newton*/PN spectrum and residuals to the best fit model `tbabs * tbpcf * (cutoffpl + gaussian)`.

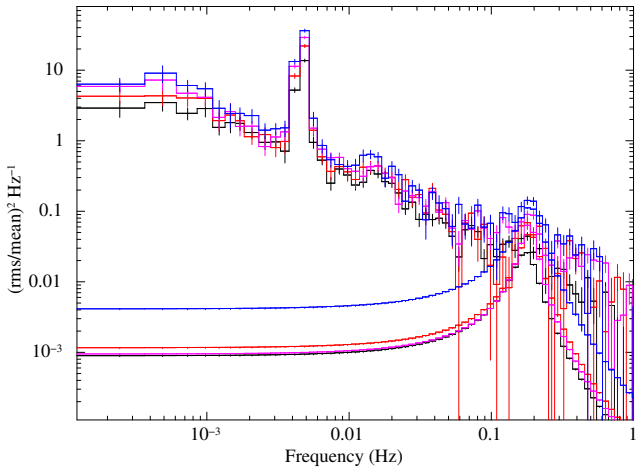

Fig. 4.11: The *NuSTAR* PSD of XTE J1858+034 in four different energy bands (3–8 keV in black, 8–10 keV in red, 10–15 keV in blue, 15–25 keV in magenta). QPO at 196 mHz is fitted with lorentzian profile. The sharp peak in the PSDs corresponds to the NS pulsations at 4.5 mHz.

(1998) at 110 mHz. In subsequent outbursts, Mukherjee, Bapna, et al. (2006) found the centroid frequency of the QPO being variable from 140 to 185 mHz and that rms amplitude of QPO has a strong correlation with photon energy. QPO was again reported in the *NuSTAR* observation at 196 mHz by Mandal et al. (2021).

We generated the energy-dependent variation of the QPO detected at 196 mHz (Table 4.9, Fig. 4.11), the same one reported by Mandal et al. (2021). The QPO is detected only till 25 keV. The QPO rms increases from about 6% in 3–8 keV to about 14% in 15–25 keV (Fig. 4.12).

The 5–55 keV *NuSTAR* spectrum could be fitted with a powerlaw with a high energy cutoff. Iron emission line and CRSF were present, which were modelled with a `gaussian` and `gabs` respectively (Table. 4.8, Fig. 4.12).

4.1.3 Discussions

Our search for QPOs in the archival *XMM–Newton* and *NuSTAR* observations resulted in the detection of QPO in nine observations of five sources viz., 4U 1626–67 (*XMM–Newton/PN*) (Fig. 4.1), IGR J19294+1816 (*XMM–Newton/PN*) (Fig. 4.3), V0332+53 (*XMM–Newton/PN*, *NuSTAR*) ((Fig. 4.5), Fig. 4.6), Cen X–3 (*XMM–Newton/PN*) (Fig. 4.9) and XTE J1858+034 (*NuSTAR*) (Fig. 4.11). The variation of QPO rms as a function of photon energy was constructed (Table 4.9). We discuss the observed QPO characteristics in various contexts below.

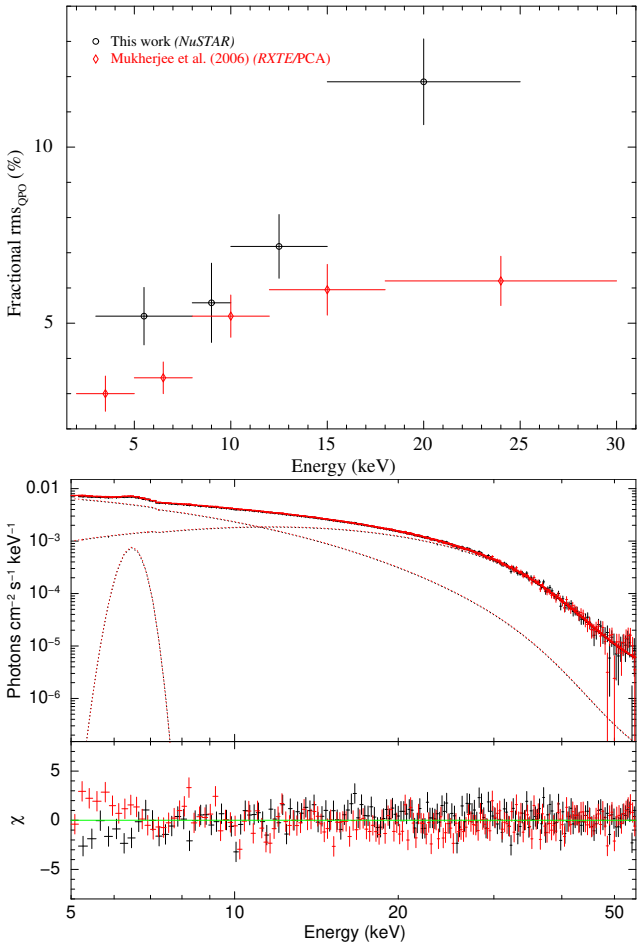

Fig. 4.12: Top: XTE J1858+034 QPO rms energy dependence from *NuSTAR* (black) and *RXTE*-PCA (red). Bottom: The 3–60 keV unfolded spectrum and residuals to the best fit model (`tbabs * (NPEX * gabs + gaussian)`) on the *NuSTAR* Obs. ID 90501348002.

Tab. 4.8: The results of spectral fit performed on the *NuSTAR* observation of XTE J1858+034 having QPO. The best fit model parameter values and their errors are given. The errors quoted on all the parameters are their 90% confidence ranges.

Obs. ID	90501348002
nH†	8.44 ± 2.5
PhoIndex (Γ_1)	0.39 ± 0.05
$N_{PL,1}{}^{\ddagger}$	$1.2e{-4} \pm 2e\text{-}5$
E_{cut}	5.48 ± 0.20
$N_{PL,2}{}^{\ddagger}$	0.036 ± 0.004
E_{CRSF}	50.52 ± 2.4
σ_{CRSF}	9.73 ± 7.9
τ_{CRSF}	1.14 ± 0.33
$E_{FeK\alpha}$	6.48 ± 0.03
$\sigma_{FeK\alpha}$	0.25 ± 0.05
$N_{FeK\alpha}{}^{\P}$	$(5 \pm 1) \times 10^{-4}$
$Flux_{2\text{-}20\ keV}$ (10^{-10} erg s^{-1} cm^{-2})	10.35 ± 0.02
χ^2(dof)	412.43/337
χ^2_{red}	1.22

† in units of 10^{22} atoms cm^{-2}.
‡ Normalization in units of photons s^{-1} cm^{-2} keV^{-1} at 1 keV.
¶ Total photons s^{-1} cm^{-2} in the gaussian line.

Twin QPOs in V0332+53

The QPOs we detected in V0332+53 at 2.5 mHz, 18 mHz and 40 mHz in the *XMM–Newton* and *NuSTAR* observations have different frequencies compared to the ones reported earlier. We also noticed that the PSDs of the two *XMM–Newton* observations have a different overall shape when compared to the *NuSTAR* PSDs (this work) and the previously reported PSDs from *Ginga* (Takeshima, Dotani, et al., 1994) and *RXTE* (Qu et al. 2005, Caballero-Garcìa et al. 2016). This variable nature of the PSD directly indicates that the factors contributing towards aperiodic variability in the source vary over time. *XMM–Newton* observations show a QPO at 40 mHz (Fig. 4.5) while the *NuSTAR* observations show twin QPOs at 2.5 mHz and 18 mHz (Fig. 4.6). Twin QPOs have been reported in GX 304–1 (Devasia et al., 2011) but the second QPO was a harmonic of the first, which is not the case here. Spectra from both observatories could be modelled with a soft-black body component and a powerlaw-based comptonization component (Table 4.6). Even though the spectral shape does not differ significantly (Fig. 4.7), the *XMM–Newton* observations were performed when the source was ≥ 5 time brighter than during the *NuSTAR* observations. The higher QPO frequency during a high X-ray flux state favours the inner accretion disk origin of QPO, which might move closer to the

Tab. 4.9: Summary of the QPO fits. The continuum is fitted with either or a combination of *powerlaw*, *lorentzian* and the QPO is fitted with a *lorentzian*. The centre and width of the *lorentzian* are considered the centroid and width of the QPO respectively. Errors assigned to the centroid and width of the QPO are their 90% confidence intervals, while error assigned to the rms powers are their 68% confidence intervals.

Source	Obs. ID	Energy range (keV)	Avg. count rate[¶]	ν_{QPO} (mHz)	$width_{QPO}$ (mHz)	$Power_{rms}$ (%)	Q-factor
4U 1626–67	0111070201	0.5–1	5.53 ± 0.03	48 ± 1	12 ± 3	18.34 ± 1.06	4.0
		1–3	13.35 ± 0.04	49 ± 1	13 ± 3	20.74 ± 0.96	3.8
		3–5.7	6.19 ± 0.03	49 ± 2	14 ± 7	15.69 ± 1.41	3.5
		5.7–10	4.08 ± 0.02	49 ± 1	11 ± 4	18.54 ± 1.44	4.5
	0152620101	0.5–1	4.63 ± 0.01	48 ± 1	11 ± 2	17.65 ± 0.51	4.3
		1–3	10.96 ± 0.02	48 ± 1	11 ± 1	20.61 ± 0.48	4.2
		3–5.7	5.24 ± 0.01	47 ± 1	11 ± 2	17.11 ± 0.60	4.3
		5.7–10	3.53 ± 0.10	48 ± 1	10 ± 2	16.86 ± 0.73	4.5
	P10101	2.02–6.7	61.23 ± 0.02	48.2 ± 0.3	11 ± 1	16.83 ± 0.44	4.3
		6.7–8.5	31.75 ± 0.02	48.3 ± 0.3	10 ± 1	16.65 ± 0.39	4.8
		8.5–11.1	35.33 ± 0.02	48.4 ± 0.3	11 ± 1	17.45 ± 0.35	4.4
		11.1–13	19.40 ± 0.01	48.2 ± 0.3	10 ± 1	18.23 ± 0.41	4.8
		13–15.4	16.31 ± 0.01	48.3 ± 0.3	11 ± 1	19.83 ± 0.36	4.4
		15.4–20.2	19.67 ± 0.01	48.4 ± 0.3	11 ± 1	21.45 ± 0.35	4.4
		20.2–60.0	11.38 ± 0.02	48.7 ± 0.5	9 ± 1	28.32 ± 0.98	5.4
IGR J19294+1816	0841190101	0.5–3	4.38 ± 0.02	29 ± 1	8 ± 5	8.07 ± 1.27	7.8
		3–5.7	8.95 ± 0.02	31 ± 1	9 ± 3	9.84 ± 0.83	3.6
		5.7–10	7.70 ± 0.03	31 ± 1	10 ± 5	11.00 ± 1.03	3.0
V 0332+53	0763470301	0.5–3	123.77 ± 0.11	38 ± 3	38 ± 8	9.62 ± 0.74	1.0
		3–5.7	153.56 ± 0.18	39 ± 2	33 ± 7	10.67 ± 0.76	1.2
		5.7–10	147.28 ± 0.12	38 ± 2	38 ± 7	10.74 ± 0.72	1.8
	0763470401	0.5–3	84.54 ± 0.07	41 ± 1	22 ± 6	11.38 ± 0.66	1.9
		3–5.7	100.66 ± 0.13	42 ± 1	21 ± 5	12.16 ± 0.73	2.0
		5.7–10	95.23 ± 0.07	42 ± 1	22 ± 5	12.94 ± 0.90	2.0
	90202031002	3–8	14.69 ± 0.03	17 ± 1	3 ± 1	9.33 ± 1.16	6.3
		8–10	6.00 ± 0.02	18 ± 1	3 ± 1	9.80 ± 1.37	5.5
		10–15	9.15 ± 0.03	17 ± 1	2 ± 1	10.52 ± 1.11	8.7
		15–60	6.29 ± 0.02	18 ± 1	3 ± 1	9.86 ± 1.25	6.4
		3–8	14.69 ± 0.03	2.48 ± 0.05	0.27 ± 0.13	10.91 ± 1.38	9.2
		8–10	6.00 ± 0.02	2.51 ± 0.05	0.11 ± 0.11	9.61 ± 1.43	>11.4
		10–15	9.15 ± 0.03	2.49 ± 0.05	0.23 ± 0.11	11.95 ± 1.43	10.8
		15–60	6.29 ± 0.02	2.49 ± 0.05	0.29 ± 0.13	11.92 ± 1.44	8.6
	90202031004	3–8	12.05 ± 0.03	18 ± 1	4 ± 2	12.56 ± 1.26	4.1
		8–10	4.88 ± 0.02	18 ± 1	5 ± 2	15.20 ± 1.30	3.6
		10–15	7.46 ± 0.02	18 ± 1	5 ± 2	14.56 ± 1.38	3.2
		15–60	5.14 ± 0.02	18 ± 1	5 ± 2	12.77 ± 1.52	4.0
		3–8	12.05 ± 0.03	2.33 ± 0.08	0.36 ± 0.26	12.55 ± 1.33	6.5
		8–10	4.88 ± 0.02	2.33 ± 0.08	0.40 ± 0.27	13.64 ± 1.41	5.8
		10–15	7.46 ± 0.02	2.35 ± 0.05	0.18 ± 0.15	12.36 ± 1.26	>10.2
		15–60	5.14 ± 0.02	2.30 ± 0.12	0.40 ± 0.36	11.73 ± 1.49	5.8
Cen X–3	040550201	0.5–3	187.88 ± 0.06	30 ± 1	23 ± 5	4.74 ± 0.16	1.2
		3–5.7	186.94 ± 0.06	31 ± 1	23 ± 4	5.98 ± 0.19	1.4
		5.7–10	118.63 ± 0.05	30 ± 1	23 ± 3	6.12 ± 0.20	1.3
XTE J1858+034	90501348002	3–8	23.03 ± 0.03	178 ± 9	70 ± 30	5.20 ± 0.69	2.5
		8–10	9.08 ± 0.02	185 ± 8	37 ± 22	6.02 ± 0.87	5.0
		10–15	12.45 ± 0.02	183 ± 7	56 ± 20	7.07 ± 0.69	3.3
		15–25	3.69 ± 0.01	186 ± 7	84 ± 27	11.73 ± 1.03	2.2

[¶] Across all PCUs (*RXTE*) or FPMs (*NuSTAR*).

neutron star, resulting in an enhanced Keplerian orbital frequency. Following the relations $r \propto \dot{M}^{-2/7}$ and Keplerian relation of $\nu \propto r^{-3/2}$, we get $\nu \propto \dot{M}^{3/7}$. Under this argument, an increase in QPO frequency to a factor of ∼2 (from 18 mHz to 40 mHz) requires $\dot{M}$ (L_X) to scale up to a factor of ~ 5, which agrees with the measured X-ray flux from the spectral analysis. However, a similar argument for an increase in QPO frequency from 2.5 mHz to 40 mHz would require a factor of ≥ 600 increase in $\dot{M}$. Thus, the 40 mHz QPO observed in *XMM–Newton* and 18 mHz QPO observed in *NuSTAR* are likely of similar origin, while the 2.5 mHz QPO is likely of a different origin. The *Q*-factor of 18 mHz QPO present at low flux is also about twice that of the 40 mHz QPO present at a high flux (Table 4.9). A similar increment in the *Q*-factor with decreasing flux has also been observed for the 220 mHz QPO by Qu et al. (2005). However, this interpretation contrasts with the observation of Takeshima, Dotani, et al. (1994), where it was shown that the QPO frequency does not evolve with source flux.

Association of QPO with the soft excess

XRPs sufficiently away from the galactic plane are known to exhibit soft excess in their energy spectrum and is usually associated with the X-ray emission from the NS reprocessed by the inner accretion disk (Paul, Nagase, et al. 2002, Hickox et al. 2004). It is usually modelled with a low temperature ($kT \sim 100 - 200$ eV) blackbody component. The idea that both soft excess and QPOs in XRPs are considered to originate from the inner accretion disk motivated us to look for patterns in the QPO strength in the soft-excess energy band. *XMM–Newton*/PN is the most suitable detector for such a study, as it has low energy coverage till 0.5 keV to detect the soft excess and a relatively good effective area for high significance detection of QPO. However, sources that exhibit both QPO in the lightcurve and soft excess in the spectrum were needed to perform such a study. Out of the five sources in which we detected *XMM–Newton* observations, only 4U 1626–67 satisfies this criterion. We modelled the soft excess in 4U 1626–67 with a blackbody component of $kT_{BB} \sim 0.3$ keV. The black body contribution is expected to peak around 0.8 keV ($\sim 2.8\ kT_{BB}$). Incidentally, QPO also shows high rms values of about 20% in the 0.5–3 keV spectral band in 4U 1626–67. An alternate interpretation is that the QPO rms is consistently high in the 0.5–10 keV with an abrupt drop in 3–5.7 keV, which seems unlikely when looking at it together with QPO rms from other wavelengths (See Sec. 4.1.2) and the *RXTE*/PCA observation (Fig .4.1). However, apart from the soft excess, 1–3 keV also contains the Ne emission complex (See Fig. 4.4), the origin of which is believed to be the O/Ne rich accretion disk of 4U 1626–67 (Schulz et al., 2001). To check

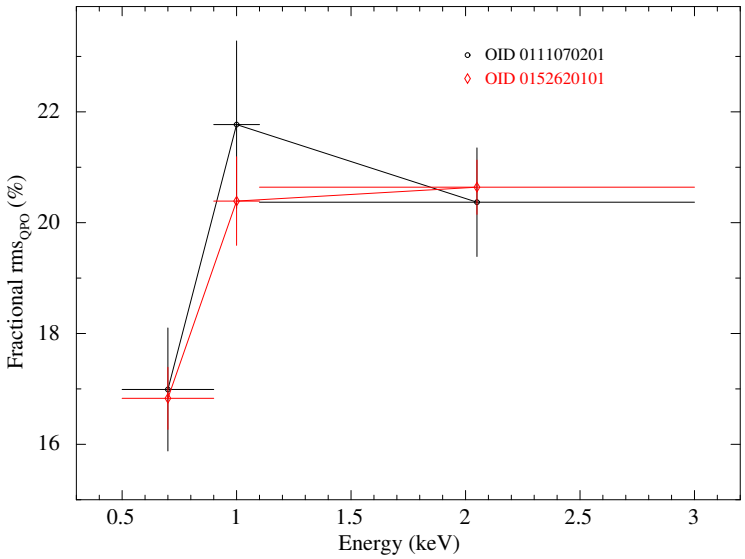

Fig. 4.13: QPO rms in three different energy ranges of two observations of 4U 1626–67. The QPO rms shows a rise throughout the 0.9–3.0 keV band in both observations.

if the QPO rms show any anomaly in the energy range corresponding to the Neon emission complex, we calculated the QPO rms in 0.5–0.9 keV, 0.9–1.1 keV and 1.1–3 keV energy bands. There seems to be no significant rise in the QPO rms peculiar to the Neon spectral range (Figure 4.13). Regardless, the QPO rms is still high in 0.5–0.9 and 0.9–1.1 keV bands with values $\gtrapprox 18\%$. Therefore, it could be argued that the QPO rms show an increase in the soft-excess band in 4U 1626–67. However, the sample size of two observations of 4U 1626–67 is arguably too low, and more observations with the presence of QPO and soft excess are required to establish any conclusive claim on the association between the origins of QPO and soft excess.

Applicability of KFM and BFM

The KFM treats QPO as the NS emission modulated by the inhomogeneous matter orbiting at Keplerian orbit in the inner accretion disk. KFM imposes the condition $\nu_{\rm NS} < \nu_{\rm QPO}$, and based on this the applicability of KFM is invalid on four of the five QPOs we detected (See Table 4.10). It could be applicable in XTE J1858+034, which gives the inner accretion disk orbital frequency as 196 mHz. But considering that soft X-rays are vulnerable to absorption from cold matter compared to hard X-rays, the QPO rms is expected to peak at lower energies, i.e., exhibiting anti-correlation with energy. However, a strong positive correlation is exhibited by XTE J1858+034 between QPO rms and photon energy in both the *NuSTAR* (this work) and *RXTE*/PCA

Tab. 4.10: Characterisitcs of the observed QPOs and applicability of Keplerian and Beat frequency models.

Source	Type	E-relation	ν_{QPO}	ν_{orb} (inner acc. disk) KFM[†]	BFM[§]
4U 1626–67	Persistent	+ve	48 mHz	N.A	178 mHz
Cen X–3	Persistent	+ve	32 mHz	N.A	240 mHz
IGR J19294+1816	Transient	+ve	30 mHz	N.A	103 mHz
V 0332+53	Transient	+ve	2-42 mHz	N.A	210-267 mHz
XTE J1858+034	Transient	+ve	196 mHz	196 mHz	201 mHz

[†] $\nu_{orb} = \nu_{QPO}$. KFM is not applicable if $\nu_{QPO} < \nu_{NS}$ (denoted by N.A).
[§] $\nu_{orb} = \nu_{QPO} + \nu_{NS}$.

(Mukherjee, Bapna, et al., 2006), with the QPO rms reaching about 10% in 15–25 keV in the *NuSTAR* observation.

BFM is therefore more apt to explain the QPOs we observed. From the observed QPO frequency and the pulsar spin frequency, we estimated the orbital frequency of the inner accretion disk in each case (Table 4.10). Both KFM and BFM also predict the QPO centroid frequency to vary with the X-ray luminosity, which is not generally observed in XRPs (Finger, 1998; Raichur et al., 2008). Exceptions are A 0535+262 (Finger et al., 1996; Finger, 1998) and XTE J1858+034 (Mukherjee, Bapna, et al., 2006), where, a positive correlation of the QPO frequency with X-ray flux was observed. We found such a variation in V0332+53, where the QPO centroid frequency is almost doubled when the X-ray flux increased ∼5 times (See the discussion in Sec. 4.1.3). This increase in QPO frequency was also accompanied by the *Q*-factor reducing by a factor of two.

QPOs in other accretion-powered X-ray sources

Besides XRPs, black hole binaries (BHBs) and low magnetic field (10^8–10^9 G) neutron stars in Low mass X-ray binaries (NSBs) are two other classes of accretion-powered X-ray binaries containing primary compact stellar objects with mass of the order of $M_\odot$, that exhibits QPOs which has been well studied. The QPOs exhibited by BHBs are broadly classified into two types based on their centroid frequency, namely the low-frequency LFQPOs (0.1–30 Hz) and the high-frequency HFQPOs (> 30 Hz). HFQPOs in BHBs like the QPOs exhibited by XRP are also a transient phenomena (Belloni, Sanna, et al., 2012). NSBs exhibit QPOs at kHz frequencies, known as kHz QPOs (they sometimes appear in pairs, and are then known as twin kHz QPOs). Due to the centroid frequency being close to the Keplerian frequency of their inner accretion disks, the kHz QPOs in NSBs and HFQPOs in BHBs are generally associated with the

accretion disk (Remillard et al., 2006). Moreover, BHBs and NHBs usually exhibit different spectral states like high-soft state (high luminosity and soft spectrum), low-hard state and intermediate state. The kHz QPOs in NSBs and HFQPOs in BHBs are usually observed during the soft states (Motta et al., 2017), which are generally associated with the accretion disk. Considering their connection with the accretion disk, the mHz QPOs in XRPs, kHz QPOs in NHBs and HFQPOs in BHBs could be discussed in the same context.

The twin kHz QPOs in NSBs are usually explained by two models; the sonic point beat-frequency model (Miller et al., 1998) and the relativistic precession model (Stella and Vietri, 1997). The relativistic precession model interprets the HF kHz QPO from the inner accretion disk and LF kHz QPO as relativistic precession modes at that orbit. The sonic point beat-frequency model interprets the high-frequency kHz QPO to be related to the clumps in the innermost accretion disk and the LF kHz QPO as the beat frequency between neutron star spin and the HF kHz QPO. The sonic point model is a combination of the KFM and BFM employed in XRPs. If the sonic point model is employed to explain the twin QPOs (2,18 mHz) observed in two *NuSTAR* observations of V0332+53, the model predicts a spin frequency of NS around 20 mHz, while the true value stands at 220 mHz.

In general, QPOs in XRPs (this work), HFQPOs (Morgan et al. 1997, Klis 2000) and kHz QPOs (Strohmayer et al. 1996, Zhang et al. 1996, Berger et al. 1996, Wijnands et al. 1997) exhibit a positive correlation of QPO rms with photon energy. A key aspect that sets the QPOs in XRPs apart is their QPO rms that regularly goes over 10% up to 30% (this work) when compared to $< 20\%$ in kHz QPOs (Zhang et al. 1996, Wijnands et al. 1997) and even lower values for the rarely detected transient HFQPOs (Belloni, Sanna, et al., 2012). The kHz QPOs exhibit hard lags, usually explained by inverse Compton scattering of soft photons in the comptonizing corona, or soft lags, explained by oscillations in the temperature of the corona and its feedback to the soft disk (Peirano et al. 2022, Karpouzas et al. 2020). QPO lags have also been reported in XRPs (eg., Liu, Wang, et al. 2022). In XRPs, however, the comptonized emission is expected to appear from the accretion column of the neutron star, and the accretion disk corona is rarely observed (eg., LMXB 4U 1822–371). Therefore, the physical interpretation of the QPO lag in the context of disk and coronal emission is not very appropriate in XRPs.

4.1.4 Summary

In this work, we presented the results from an investigation of the energy dependence of Quasi-Periodic Oscillations (QPOs) exhibited by accreting X-ray pulsars using data from archival *XMM–Newton*, *NuSTAR* and *RXTE* observations. In a search for the QPOs in 97 *XMM–Newton* and *NuSTAR* observations, we detected QPOs in nine observations from five sources, viz., 4U 1626–67, IGR J19294+1816, V0332+53, Cen X–3 and XTE J1858+034. A positive correlation of QPO rms with energy is exhibited by 4U 1626–67, IGR J19294+1816, Cen X–3 and XTE J1858+034, while no correlation is visible in V0332+53. In 4U 1626–67, the QPO rms is high in the soft-excess energy range, but no evidence is found to associate the origins of the soft-excess and the QPOs. The *NuSTAR* PSD of V 0332+53 shows the presence of twin QPOs at 2.5 mHz and 18 mHz, while the *XMM–Newton* observations show a QPO at 40 mHz. We reviewed the observed QPO properties in the context of QPOs found in other types of accreting sources and the applicability of KFM and BFM models usually used to explain the QPOs in accreting X-ray pulsars.

4.2 Accretion Disk Corona of 4U 1822–371

4U 1822–371 (alias 2A 1822–371 or 2S 1822–371 or X 1822–371) is a prototypical Accretion Disk Corona (ADC) source hosting an accreting X-ray pulsar and Roche-lobe filling low mass companion (Harlaftis et al., 1997). The binary is highly inclined with respect to the line of sight, viewed almost edge-on (Hellier, 1990, and references therein), and the thick accretion disk obstructs most of the X-rays from central NS emission site (Milgrom, 1978).

A 5.5 hr modulation and V-shaped minimum in the source lightcurve was discovered by Seitzer et al. (1979). Optical (Mason, Middleditch, et al., 1980), UV (Mason and Córdova, 1982) and X-ray (White, Becker, et al., 1981) flux also modulates with period 5.57 hr, which is the binary orbital period of the system. Broad He emission lines suggested the possibility of an accretion disk around the degenerate companion (Charles et al., 1980), which was later confirmed by Optical observations (Mason, Murdin, et al., 1982). Analysis of orbit and eclipse parameters gave evidence for Roche lobe overflown LMXB system (CRAMPTONI et al., 1982). UV spectro-photometry of the source revealed a bulge at the accretion disk rim (Mason and Córdova, 1982), which was reasserted by high-resolution X-ray spectroscopy (Cottam et al., 2001). The mass of the donor star is estimated to be $0.44 - 0.56$ $M_{\odot}$, and

that of NS is $1.61 - 2.32$ $M_{\odot}$ (Munoz-Darias et al., 2005). The binary system is at a distance of 2–3 kpc from the earth (Mason and Cordova, 1982).

The presence of accretion disk corona in 4U 1822–371 was proposed by White, Becker, et al. (1981) from HEAO and Einstein observations, and from EXOSAT observation by Hellier and Mason (1989) by analysing periodic partial eclipses, modelling the system as an almost edge-on ADC source partially obscured by an accretion disk. 4U 1822–371 is one of the very few LMXBs exhibiting partial eclipses, the others being S 0921–630, XTE 2123–056, 4U 2129+12 and 4U 2129+47(Chou, 2014). White, Becker, et al. (1981) also proposed that the accretion disc may have azimuthal variation in height near the accretion disc rim, later confirmed by Hellier and Mason (1989) (EXOSAT) and Heinz et al. (2001) (*RXTE*/ASCA). The introduction of ADC also solved the discrepancy of a rarity in the number of observed eclipsing LMXBs, sanctioning the thick accretion disk model by (Milgrom, 1978; Lewin et al., 1997).

In high-inclination ADC sources viewed close to the accretion disk plane, the central compact source is cut off from the observer by the thick accretion disk, and the observed flux are the photons scattered off the ADC. During the eclipse phase, the companion obscures part of the ADC. Still, residual flux due to photons scattered off the extended ADC gas cloud reaches the observer making the eclipse appear partial (Frank, King, and Lasota, 1987). A simple model assumes the Accretion Disc corona as an ionised gas cloud around the NS which acts like a mirror (or lampshade), scattering the original NS and accretion disk radiation into LOS (Hellier, 1990; White and Holt, 1982). Spectral modelling also supports the picture of photons from a central engine scattered off an extended gas cloud (White, Becker, et al. (1981) and Fabian et al. (1982)). Such an ADC may be produced by X-Ray heating of the accretion disk by the Neutron star photons (Begelman et al., 1983).

Low amplitude periodic pulsations were discovered in 4U 1822–371 with period 0.59 s in the *RXTE*/PCA observations (Jonker et al., 2001), and from pulse arrival time analysis, the binary orbit is estimated to be compact ($a_x \sin i \sim 1.006$ lt-sec) and circular (e<0.03). Observed coherent pulsations due to rotating beamed radiation from the spinning NS can get destroyed (due to light travel time delays from scattering), depending on the optical depth and size of the scattering medium (ADC) (See Bussard et al. (1988) and Göğüş et al. (2007), and references therein). The observed pulse fraction is low and increases with energy, but the detection of pulsation indicates that at least some portion of the ADC is optically thin (Jonker et al., 2001).

Analysing the eclipse profiles in lightcurve in different energy bands can provide information on the thermal structure and size of ADC (Church et al., 2004). Such studies have been performed on $\sim$ 48 ks of *Ginga* 1–20 keV spectrum (Hellier, Mason, and Williams, 1992) and simultaneous $\sim$ 25 ks *RXTE/ASCA* 0.6–15 keV observations (Heinz et al., 2001). The studies indicated that partial eclipse width and fractional eclipse depth increase as a function of energy. We try to extend the study of energy-dependent characteristics of the partial eclipse profile in this work, exploiting the broadband high energy coverage from non-simultaneous *NuSTAR* and XMM archival observations in 0.1–79 keV energy band. We also inspected the long-term lightcurves from *RXTE*/ASM, *Swift*/BAT and *MAXI* jointly spanning almost 30 years.

Instruments, Observations and Data Reduction

Nuclear Spectroscopic Telescope Array (*NuSTAR*) is a NASA small explorer mission (SMEX) and is the first hard X-ray focusing telescope in the 3–79 keV spectral band. Standard data reduction steps are followed from *NuSTAR* data analysis software guide [9] for generating lightcurves and spectrum from *NuSTAR* event files. Calibrated event files are generated using task `nupipeline` v0.4.8 with CALDB 20191008. Source product files are extracted from 85" circular region and background from 120" circular region away from the source and regions are defined using DS9. lightcurves and spectra from these regions are generated using the task `nuproducts` v0.3.2.

X-ray Multi-Mirror Mission (XMM–Newton) is an X-ray space observatory of ESA[10]. It consists of three Wolter-I telescopes focusing X-rays into three X-ray CCD cameras (called European Photon Imaging Camera or EPIC); a pair of Metal Oxide Semiconductor (MOS)-CCD cameras (Each camera having seven CCDs) called EPIC-MOS and a PN-CCD camera (twelve CCDs) called EPIC-PN. It also has an RGS grating spectrometer to which half of the flux is diverted from the two telescopes, while the MOS-CCDs get the other half of the flux. On the other hand, PN-CCD gets unobstructed flux from the third telescope, because of which it has a better effective area. Standard data reduction steps are followed from Science Analysis Software(SAS) Data Analysis threads [11] for generating lightcurves from *XMM–Newton* event files. Event files are first screened for background flaring events, and source

[9] https://heasarc.gsfc.nasa.gov/docs/NuSTAR/analysis/NuSTAR_swguide.pdf
[10] https://www.cosmos.esa.int/web/XMM--Newton/technical-details
[11] https://www.cosmos.esa.int/web/XMM--Newton/sas-threads

Observatory	Instrument	Obs.ID	Year	Exposure (ks)
NuSTAR	FPM A,B	30301009002	2018	28.7
XMM–Newton	EPIC-PN	0111230101	2001	36.6
		0784820101	2017	28.6

Tab. 4.11: List of Observation IDs used for analysis. Both the lightcurves and spectra from *NuSTAR* are used. Only the lightcurves from EPIC-PN camera of *XMM–Newton* are used. Data from the *XMM–Newton* observation IDs are used for analysis in Iaria et al. (2015) and Mazzola et al. (2019)

and background regions are selected from circular or rectangular regions for Imaging or Timing mode data, respectively. Lightcurves are then generated from these regions.

Long-term lightcurves from All-Sky Monitor on-board *Rossi X-Ray Timing Explorer* (*RXTE*/ASM)[12], Burst Alert Telescope on-board Neil Gehrels *Swift* Observatory (*Swift*/BAT)[13] and *The Monitor of All-sky X-Ray Image* (*MAXI*)[14] are also used.

Errors on all the estimated parameter values are quoted at 2.706σ confidence level unless stated otherwise.

Eclipse profile analysis

We combined the *NuSTAR* FPMA and FPMB background corrected lightcurves, along with the XMM EPIC-PN background-corrected lightcurves from two different observations are folded with the binary orbital period 20054.26644192 s and period derivative 1.475×10^{-10} s s^{-1} into 128 phase bins at the reference epoch MJD 50353.08733 (ephemeris from Mazzola et al., 2019) as shown in Fig. 4.14. Mid-eclipse falls at orbital phase ~ 1.0. Folded lightcurves were generated in multiple energy bands (*NuSTAR* 3–5, 5–7, 7–10, 10–15, 15–25 keV; *XMM*–Newton/PN 1–2, 2–3, 3–4, 4–6, 6–8, 8–10 keV).

We fitted eclipse profiles in the folded lightcurves (region in-between dashed lines in Fig. 4.14, orbital phase 0.9 to 1.1) with two models as described by equations 4.1 and 4.2. The first model (equation 4.1) represents pre-ingress counts and post-egress counts with two constants, eclipse region with a combination of two straight lines, one with a positive and one with a negative slope (making a V-shape). The second model (equation 4.2) is an inverted Gaussian super-imposed over a straight line with a positive slope, this model is adopted from Hellier, Mason, and Williams (1992).

[12] http://xte.mit.edu/asmlc/ASM.html
[13] https://swift.gsfc.nasa.gov/results/transients/
[14] http://maxi.riken.jp/top/lc.html

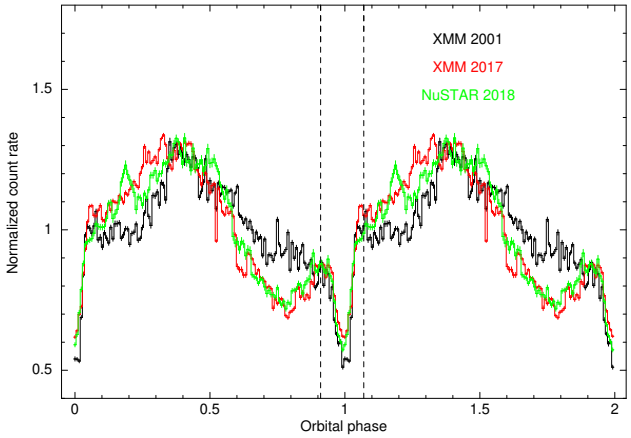

Fig. 4.14: Figure showing lightcurves of 4U 1822–371 from three observation IDs mentioned in 4.11 folded with orbital period 20054.26644192s at the reference epoch 50353.08733. The region between the dashed line shows the partial eclipse phase.

Sample fits using both models performed on *NuSTAR* 5–7 keV band folded lightcurve eclipse region are shown in Figs. 4.15 and 4.16. The functional forms of the two models are given below:

$$\mathrm{mod1}(\phi) = \begin{cases} M_1\phi_{HW} + A_{\mathrm{mid}} & \phi < \phi_{\mathrm{mid}} - \phi_{HW} \\ M_1(\phi_{\mathrm{mid}} - \phi) + A_{\mathrm{mid}} & \phi_{\mathrm{mid}} - \phi_{HW} < \phi > \phi_{\mathrm{mid}} \\ M_2(\phi - \phi_{\mathrm{mid}}) + A_{\mathrm{mid}} & \phi_{\mathrm{mid}} < \phi > \phi_{\mathrm{mid}} + \phi_{HW} \\ M_2\phi_{HW} + A_{\mathrm{mid}} & \phi > \phi_{\mathrm{mid}} \end{cases} \tag{4.1}$$

where, ϕ_{mid} is the mid-eclipse orbital phase; ϕ_{HW} is the eclipse half-width; M_1 and M_2 are the slopes of two lines; $\mathrm{A}_{\mathrm{mid}}$ is the count rate at mid-eclipse phase ϕ_{mid}.

$$\mathrm{mod2}(\phi) = (M\phi + B) + \left(\frac{A_G}{2\pi\sigma^2}\exp - \frac{(\phi - \phi_{\mathrm{mid}})^2}{2\sigma^2}\right) \tag{4.2}$$

where, $\mathrm{M}\phi + \mathrm{B}$ represents a straight-line with positive slope M and intercept B; second term defines a Gaussian profile with negative amplitude A_{G} and full-width half maximum (FWHM) of 2.355σ.

After fitting the eclipse with both the models, best fit parameters and their 1σ errors were then noted down. Eclipse half-width (ϕ_{HW} in equation 4.1), FWHM of

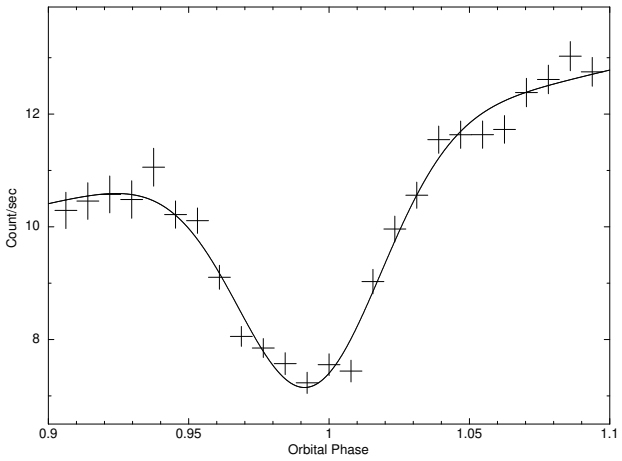

Fig. 4.15: Figure showing Gaussian model described by equation (4.2) fitted on the eclipse region (orbital phase 0.9–1.1) of folded *NuSTAR* 5–7 keV lightcurve.

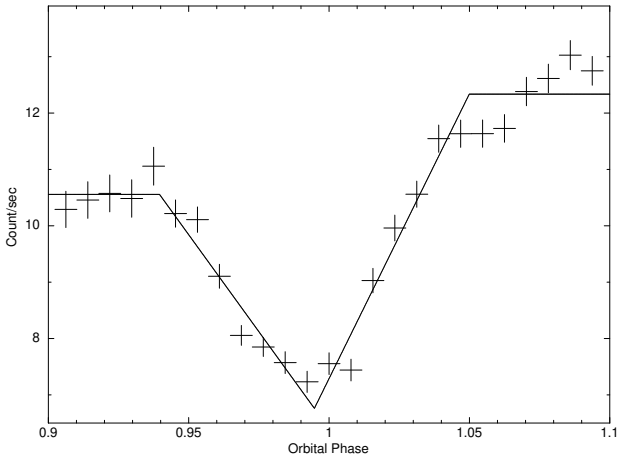

Fig. 4.16: Figure showing fit performed using V-shaped model described by equation (4.1) on the eclipse region (orbital phase 0.9–1.1) of folded *NuSTAR* 5–7 keV lightcurve.

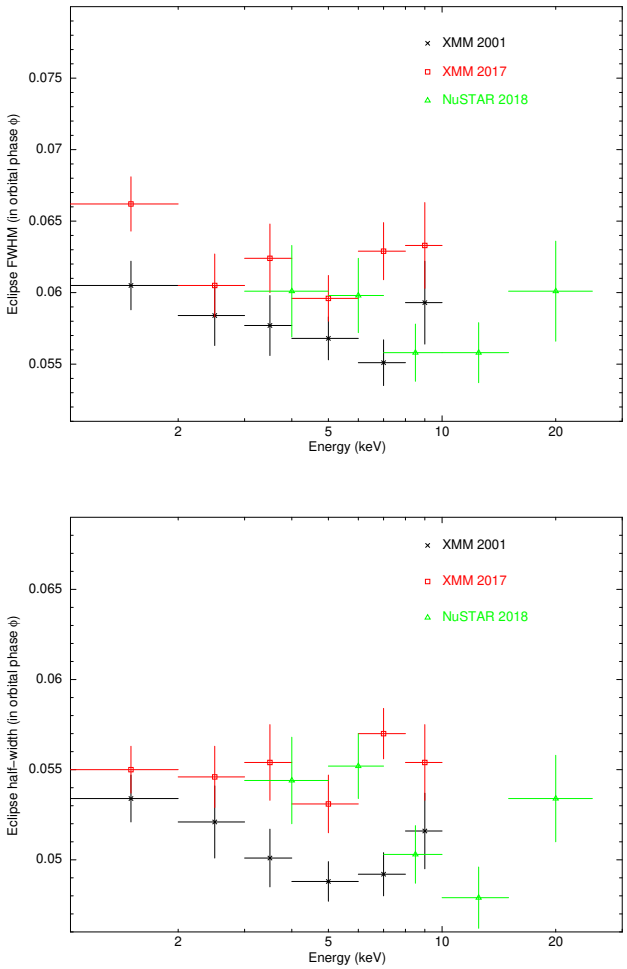

Fig. 4.17: Plots showing eclipse width as a function of energy. Top figure shows results from Gaussian shaped eclipse profile model and bottom figure shows results from V-shaped eclipse profile model. The results from two models do not show significant variation.

Gaussian in equation 4.2 and relative eclipse depth (fractional Gaussian amplitude) were then plotted as functions of energy (See Figs. 4.17 and 4.18).

Overall, the eclipse width shows a decreasing trend as a function of energy till 15 keV compared to previous reports. However, poor photon statistics limit the data to establish any clear trend on eclipse depth.

Long-term lightcurves

Long-term X-ray lightcurves of the source from multiple observatories spanning ~ 25 years *RXTE*/ASM (2–10keV) (1996–2010), *Swift*/BAT (15–50keV) (2005–2021) and

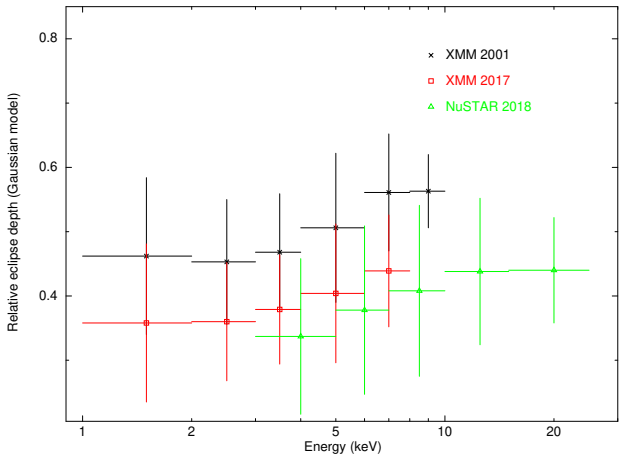

Fig. 4.18: Plot showing eclipse depth as a function of energy. Eclipse depth is defined as $A_G/(M\phi_{\rm mid} + B)$, parameters from equation 4.2.

MAXI/GSC (2–20keV) (2009–2021) are available. *RXTE*/ASM lightcurve shows decaying flux at the rate of -1.1×10^{-4} counts sec^{-1} day^{-1} (See Fig. 4.19 panel 1). This decay was also reported by Bayless et al. (2009). To check for possible instrumental origin, we examined the long-term lightcurve of Crab nebula from *RXTE*/ASM in the same duration and fitted it with a straight line having a negative slope. The best-fit decay rate is only a fraction (10 %) of the decay rate present in 4U 1822–371 lightcurve. This rules out the instrumental origin. Moreover, *RXTE*/ASM is also calibrated against the observed flux of Crab nebula (Levine, Bradt, et al., 1996).

Swift/BAT and *MAXI* long-term lightcurves in none of the (2–4, 4–10, 10–20 keV) energy bands show the similar flux decay present in *RXTE*/ASM lightcurve. However, interestingly, a prominent long-term pseudo-sinusoidal modulation is visible in the *Swift*/BAT lightcurve. To check if such modulation is blinded in ASM lightcurve by the dominant flux decay, we subtracted a straight line model (with slope equal to the observed ASM flux decay rate) from the ASM lightcurve (Fig. 4.20). The process revealed similar modulation in the ASM lightcurve. To assess the suspected long-term periodicity, we initially fitted a sinusoidal function of the form

$$const + A\,\sin([2\pi(t-\phi)/P]) \tag{4.3}$$

on the long-term lightcurves from three observatories. Best fit parameters with 1σ error are quoted in the upper half of table 4.12. The best fit period of the sine is around 1700 d in all three lightcurves, and it is most prominent in the BAT lightcurve(10% sine amplitude swing), followed by *MAXI* (6%) and ASM (3%).

	RXTE/ASM	*Swift*/BAT	MAXI
E(keV)	2–10	15–50	2–20
const.[15]	2.75 ± 0.01	0.008 ± 0.00002	0.1 ± 0.0003
P	1778.06 ± 52	1779.1 ± 17	1896.5 ± 30
$\frac{A_{sin}}{const}\%$	2.6	10.1	5.9
P_{LS}(d)	868.64	1758.6	1705.4
$Power_{LS}$	123.7±3	1.1×10^{-2}	4.31×10^{-2}

Tab. 4.12: Results of best fit parameters for the sine model (equation 4.3) on long-term X-ray lightcurves (bin size 180d) is given in top half of the table. Bottom half of the table shows the results of the Lomb-Scargle periodogram performed to search for periodicity greater than 1 year. Quoted uncertainties are of 1σ confidence level.

We used the Lomb-Scargle periodogram (*Astropy*) to search for periodicity in the three lightcurves for periods greater than one year. Results of the LS periodogram are shown in Fig. 4.21. The most prominent period detected along with the LS power (amplitude) is given in the bottom half of table 4.12. *Swift*/BAT and *MAXI* have prominent periodicities at ~ 1759 d and ~ 1705 d respectively. But the periodicity detected in *RXTE*/ASM is ~ 868 d, which is roughly half of the period value obtained by sinusoidal fit. *MAXI* also shows a period detected at ~ 610 d.

4.2.1 Discussion

Analysing the *NuSTAR* and *XMM–Newton* lightcurve in different energy bands indicates the presence of eclipse in all energy ranges (Parmar, Oosterbroek, et al., 2000), which implies that the detected hard X-Ray photons also emerge from the extended coronal region. Energy resolved variation of eclipse profile has been studied in the 1–30 keV range from *Ginga*/LAC data (Hellier and Mason, 1989) and in 0.4–11 keV range from *RXTE/ASCA* observatory data (Heinz et al., 2001). Both studies reported increasing eclipse width and depth as a function of energy. The trend in the eclipse depth favours the model of hard X-ray photons emerging close to the accretion disk plane, but the trend of eclipse width does not. The authors proposed two possible scenarios as follows; 1. A non-spherical ADC structure where hard X-ray emission region is wide but short; 2. an-isotropic illumination of the optically thin ADC by the NS. Unlike the previous findings, our results of the eclipse width from *NuSTAR* and *XMM–Newton* observations do not show a definite increasing trend as a function of energy at 1σ significance level. We found that the eclipse is narrow in the hard energy band and broad in lower energies, which indicates that the harder photons emerge near the accretion disk plane while softer photons

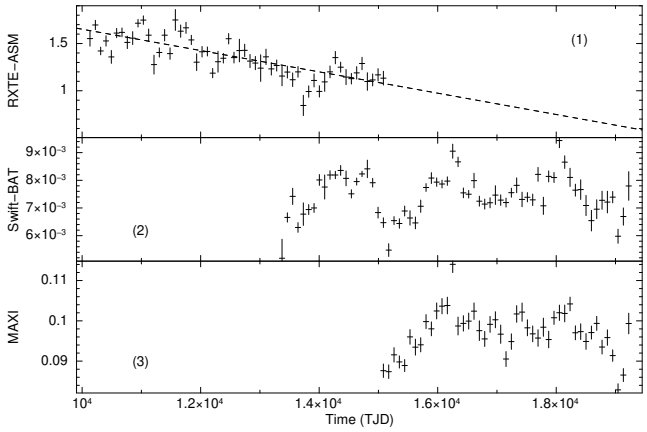

Fig. 4.19: 4U 1822–371 long-term lightcurves (in counts s^{-1}) from *RXTE*/ASM (panel 1), *Swift*/BAT (panel 2) and MAXI(panel 3). ASM lightcurve clearly shows flux decay, which is fitted with the dotted straight line having a negative slope. In the *Swift*/BAT lightcurve, a pseudo-sinusoidal modulation is visible. All the lightcurves are time binned to 90 d and all the data points having relatively high error bars are removed.

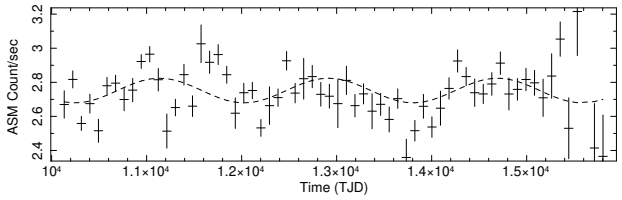

Fig. 4.20: Figure shows 4U 1822–371 long-term lightcurve from *RXTE*/ASM after removing the observed long-term flux decay. A sinusoidal model fit with a period of ~ 1800d is shown with the dotted line.

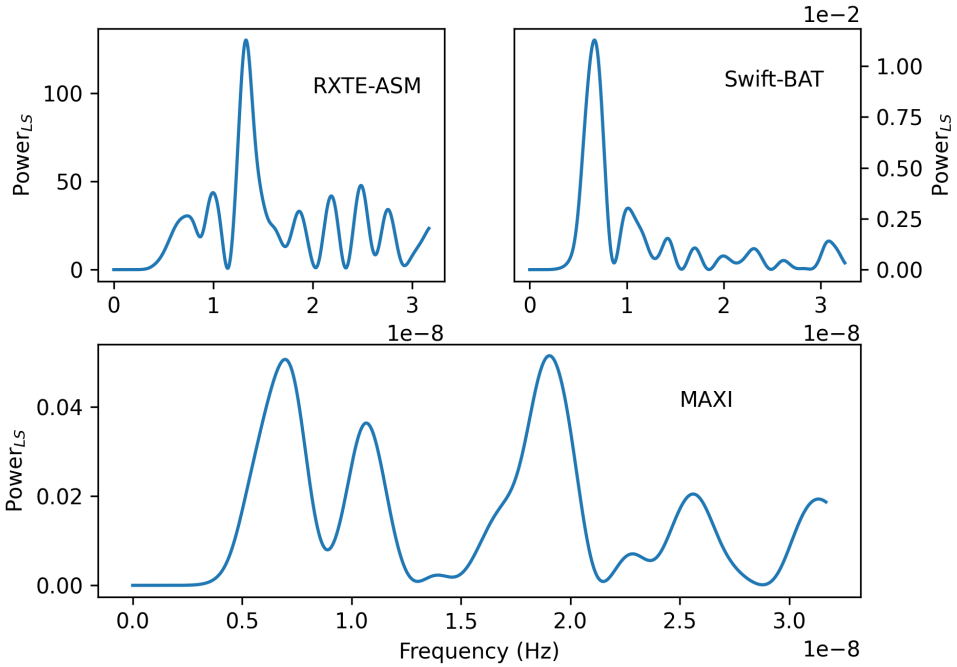

Fig. 4.21: Lomb-Scargle periodicity search performed on long-term lightcurves from *RXTE*/ASM, *Swift*/BAT and *MAXI* for periods greater than 1 year. Peak power in ASM corresponds to the period of 870 d, with a false alarm probability (FAP) of 0.002. The peak in BAT corresponds to a period of 1734 d (FAP 2×10^{-12}), and *MAXI* shows two peaks; one at period of 608 d (FAP 0.003) and the other at a period of 1661 d (FAP 0.003).

away from the disk. The eclipse depth doesn't reveal any specific trend at 1σ level, possibly due to inadequate data statistics. Nevertheless, the eclipse widths show an overall decreasing trend with energy, which contrasts with the previous findings from *Ginga* and *ASCA* observations. Deeper and narrower eclipses at hard X-rays favour an ADC temperature profile that is radially decreasing from the central region. In the source's *RXTE*/ASM long-term lightcurve, it is evident that 2–10 keV flux is slowly declining till ∼MJD 53000. Subsequent data is not available from *RXTE*, but long-term lightcurves from ∼MJD 54000 by *Swift*/BAT and *MAXI* don't show such a flux decay in any energy band. To check if the variation in ADC energy structure is accompanied by a change in the source flux, we compared the 2–10 keV source flux from *NuSTAR* and *XMM–Newton* observations with the earlier *Ginga* and *RXTE/ASCA* observations. There is no disparity in the source flux between observations.

Additionally, the Lomb-Scargle periodogram search revealed the presence of flux modulation with period ∼5 years in the long-term X-ray lightcurves of the source. The presence of a super-orbital period in the X-ray lightcurve, apart from binary orbit and NS spin periods, has been observed in X-ray binaries but is relatively rare in LMXBs (Cyg X–2, 4U 1820–30 and 4U 1916–05) (Lewin et al., 1997). The origin of the third period may be attributed to the precession of the accretion disc, NS magnetic axis or accretion hotspot location, intrinsic period variability of the donor star, or the presence of a third stellar object affecting the accretion flow dynamics of the binary system (Durant et al., 2010). Precessing accretion disk will manifest as energy-dependent super-orbital modulation in the source flux, and donor star variations will be visible in the optical lightcurve (Farrell et al., 2006). For LMXBs, the reprocessed emission from the accretion disk in the optical band dominates over the observed flux from the donor star which impacts the study of variability in the donor. The precessing accretion disk modulates the soft X-rays while hard X-rays generally pass through, making the modulation deeper for soft X-rays. However, we saw prominent modulation on the hard band 15–50 keV *Swift*/BAT lightcurve compared to soft band *RXTE*/ASM and *MAXI* lightcurves. This can occur due to the high inclination of the source and presence of ADC, where soft X-rays emerge away from the accretion disk plane in the extended ADC, and hence may not be obscured by the precessing accretion disk. Mazeh et al. (1979) proposed that a distant third stellar companion can disturb the inner binary orbit, thereby inducing long-term modulations on the binary separation and eccentricity of even an evolved binary system with very small eccentricity. If the binary orbital parameter(s) of 4U 1822–371 are modulated by such a third companion at period $\mathrm{P_{long}}$ and if the binary

orbital period is $\mathrm{P_{inner}}$, then adopting the triple-system model of Mazeh et al. (1979) the orbital period of the third companion can be estimated by

$$P_{outer} = \sqrt{K P_{long} P_{inner}} \tag{4.4}$$

where, is K is a constant of order unity which depends on mass ratios and relative inclinations (Refer Chou and Grindlay, 2001, for similar calculation of 4U 1820–30). For $\mathrm{P_{long}}$=1700 d and $\mathrm{P_{inner}}$=0.23 d, we get from equation (4.4) the orbital period of third body $\mathrm{P_{outer}} \sim 20$ d. The observed super-orbital period has to be investigated in a detailed manner for establishing the exact mechanism.

4.2.2 Summary

4U 1822-371 is a low mass X-ray binary and a prototypical accretion disc corona (ADC) source partially eclipsed by the companion. In this work, we have analysed the archival *NuSTAR*, and *XMM-Newton* pointed observations of the source. We performed an energy-resolved study of the partial eclipse profile in the 0.2–45 keV energy range using non-simultaneous *NuSTAR* and *XMM*-Newton observations. Our study of the partial eclipse profile revealed short(narrow) eclipses at high energies in contrast with the previously reported trend of increasing eclipse width with energy. The slow long term flux decay of the source ($\sim 10^{-4}$ counts $\mathrm{s^{-1}}$ $\mathrm{d^{-1}}$) visible in the 2-12 keV band in RXTE-ASM long term lightcurve from MJD ~ 50088 to ~ 54000 does not continue in the MAXI-GSC 2–10 keV band lightcurve from MJD 55054 to 59247. We also report the presence of a ~ 5 year super-orbital periodic variability in long-term X-ray lightcurve.

5

Evolution of binary environment and binary orbit of the HMXB GX 301-2[a]

[a]The findings discussed in this chapter are part of two papers published in the journal MNRAS.

GX 301-2 is an X-ray pulsar that accretes matter from an early-type Supergiant Wray 15-977 in the 41.5 days long wide eccentric ($e \sim 0.47$) binary orbit with $a_x \sin i$ of ~ 160 lt-s. In Sec. 5.1 this chapter, we explore the evolution of the binary environment of GX 301-2, which is contaminated by the companion wind, during an 80 d long spin-up episode of the pulsar in 2020. In Sec. 5.2 of this chapter, we used the All-sky monitor long-term X-ray lightcurves spanning over three decades to estimate the orbital evolution of GX 301-2.

5.1 Evolution of the X-ray reprocessing environment of GX 301-2 during a spin-up episode

A peculiar characteristic of the HMXB pulsar GX 301-2 is that it regularly exhibits a significant increase in the X-ray intensity ~ 1.4 days before every periastron passage of the pulsar (Fig. 5.1). The presence of characteristic emission lines of iron at 6.4 keV (Fe Kα) and a prominent Compton shoulder of the iron line in the observed spectrum indicates X-ray reprocessing in the pulsar neighbourhood, suggesting the presence of dense stellar wind from the companion (See Watanabe et al., 2003, and references therein). However, the commonly regarded spherically symmetric stellar wind from the companion could explain only an X-ray flare during or after the periastron passage of the NS. Several models have been proposed to explain the unusual pre-periastron flaring nature of the source, the two most promising ones being discussed in Pravdo et al. (2001) and Leahy and Kostka (2008). The model by Leahy and Kostka (2008) proposed a dense equatorial gas stream from Wray 15-977 in addition to the strong, symmetric, high-velocity stellar wind from the massive companion star. The model by Pravdo et al. (2001) suggested the

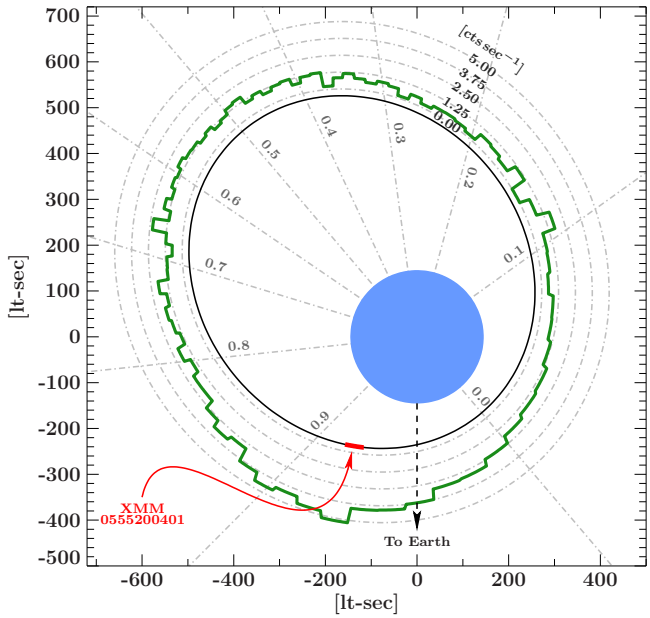

Fig. 5.1: A sketch of the binary orbit of GX 301–2 and variation of X-ray intensity across the orbital phases. (Fig. credits: Fürst, Suchy, et al., 2011)

presence of an enhanced circumstellar disc around Wray 15-977. The X-ray pulsar intercepting either the gas stream or the circumbinary disk of Wray 15-977 at an orbital phase before the periastron could explain the observed pre-periastron flare in GX 301-2. Both models predict the orbital variation of the observed X-ray flux and the equivalent hydrogen column density, which helps one verify the model against observations. Along with the observed column density, the equivalent width of the iron fluorescence line at different orbital phases is another diagnostic tool for probing the neutron star's accretion/reprocessing/circum-binary environment. The orbital profile of the intensity, absorption column density and equivalent width were measured with the first few years of data obtained with *MAXI*/GSC (Islam and Paul, 2014) and the results, however, were found to deviate from the predictions made by these two models.

GX 301-2 is peculiar in its spinning nature as well, that it exhibits rapid spin-up episodes, which is an observed characteristic of accreting X-ray pulsars (XRPs) in Be high mass X-ray binaries (Be HMXBs), but it also exhibits transient spin-ups and spin-downs, which is a characteristic of XRPs in Sg HMXBs (See Bildsten et al., 1997). During a rapid spin-up episode in 2019, the spin frequency of the pulsar in GX 301-2 increased by about 2% in about 80 days (See Nabizadeh, Armin et al. 2019, Abarr et al. 2020, Liu 2020, Liu, Ji, et al. 2021 and Fig. 5.2 in this chapter), accompanied by an overall increase in the X-ray luminosity. The pulsar exhibited an enhanced X-ray flux in both low (2-30 keV) as well as high (15-50 keV) energies

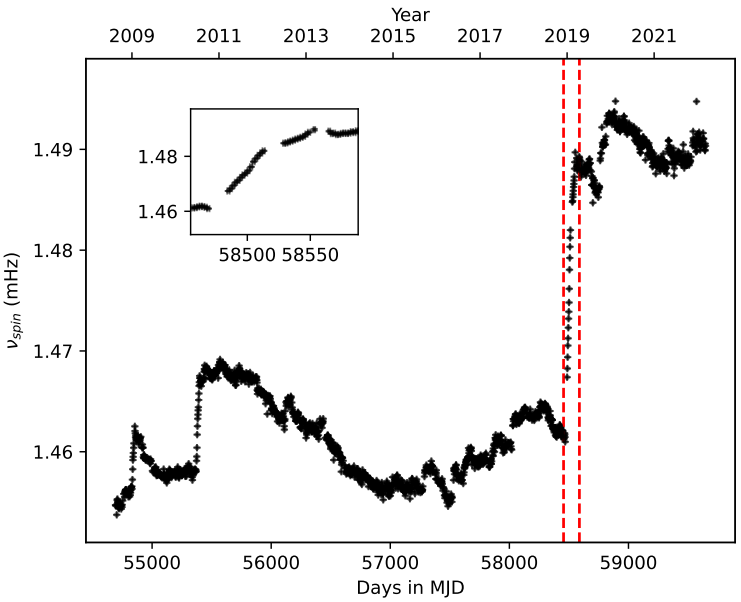

Fig. 5.2: Figure showing the pulse frequency history of GX 301-2 obtained with *Fermi*/GBM. The red dashed line indicates the 2019 spin-up episode of GX 301-2. The spin-up episode roughly spans 80 days between MJD 58480 to MJD 58560 and is shown in the inset.

evident from *MAXI* and *Swift*/BAT lightcurves respectively. While Nabizadeh, Armin et al. (2019) and Liu, Ji, et al. (2021) used the pointed observations of *NuSTAR* and *Insight-HXMT* respectively during the 2019 spin-up episode and outside the spin-up episode to probe the differences in the spectral properties, Abarr et al. (2020) reported constraints on the hard X-ray polarization using *X-Calibur*, and Liu (2020) used the *Fermi*/GBM and *Swift*/BAT data to suggest the presence of a transient accretion disk during the spin-up.

5.1.1 Methods

Probing the strength of the photoelectric absorption (the absorption column density) and the iron fluorescence line (the equivalent width) in the spectra is a useful tool to understand the X-ray reprocessing environment of the pulsar (See Islam and Paul, 2014, and references therein). Both of these parameters can be estimated by analysing the X-ray spectra of the source.

In order to estimate the orbital variation of spectral parameters, it is desirable to have pointed observations of the source covering an entire orbit of the source. However, the binary orbital period of GX 301-2 is long at about 41.5 days (Sato et al., 1986) and pointed observations at the source spanning complete binary orbit(s) are

not feasible. *MAXI* on the other hand being an All-sky monitor scans the entire sky every day, and its spectral coverage at low energies helps constrain the photoelectric absorption parameter. The orbital variation of spectral parameters of GX 301-2 using ~ 4 years of data accumulated by *MAXI*/GSC was reported earlier in Islam and Paul in 2014. As of now, *MAXI* have acquired almost two times more data (~ 12 years since MJD 55058). Hence, one should be able to constrain the orbital phase-resolved spectral parameters to a greater degree by using the three times longer exposure.

Like the similar wind accreting pulsar OAO 1657-415 (Jenke et al., 2012), GX 301-2 has also exhibited several rapid spin-up episodes throughout the time it was monitored by the all-sky monitors *CGRO*/BATSE and *Fermi*/GBM. Burst and Transient Source Experiment (BATSE) instrument onboard the Compton Gamma Ray Observatory (CGRO) discovered two such episodes between 1991 to 1995 (Koh et al., 1997). *Fermi*/GBM between 2008 to 2022 has detected four such episodes (Liu, 2020) as shown in the Fig. 5.2. The longest spin-up episode of the source was the one in 2019 (vertical dashed lines in Fig. 5.2), during which there were no pointed observations of the source with any of the current X-ray telescopes. We have therefore used data from the *MAXI*/GSC to probe the evolution of spectral parameters over time considering the bright nature of the source. The spectrum accumulated in one day though, has very limited photon statistics to perform such an analysis. We, therefore, used the *MAXI*/GSC spectra accumulated from 6-day sliding windows during the spin-up episode, to search for the temporal variation of the spectral parameters of interest.

All the spectral analyses were performed in XSPEC v12.11.1 (Arnaud, 1996). Interstellar photoelectric absorption is modelled using `tbabs`, with elemental abundances from Wilms et al. (2000) and photoelectric absorption cross-sections from Verner et al. (1996).

5.1.2 Instrument and Data Reduction

The Monitor of All-sky X-ray Image (*MAXI*) [1] is an X-ray scanning sky monitor installed on the Japanese Experiment Module Exposed Facility (Kibo-EF) onboard the International Space Station (ISS). *MAXI* (Matsuoka et al., 2009) is equipped with two different kinds of X-ray detectors; A pair of Gas Slit Camera (GSC) (Mihara, Nakajima, et al., 2011) which are position-sensitive gas proportional counters detecting events in 2-30 keV and Solid-state Slit Camera (SSC) (Tomida, Tsunemi, Kimura, Kitayama, Matsuoka, Ueno, Kawasaki, Katayama, Miyaguchi, Maeda, et al.,

[1] https://iss.jaxa.jp/en/kiboexp/ef/maxi/

2011a), the CCDs detecting events in 0.5-12 keV. The GSC detectors are paired to two Slit-camera optics scanning the sky in the Earth-horizon and zenith directions with the ISS motion. The 96-minute orbit of ISS around the earth facilitates GSC and SSC to scan the entire sky during one orbit.

The *MAXI*/GSC consists of 12 position-sensitive proportional counter detectors with a total geometric area of about 5300 cm^2, has a FOV of $1.5° \times 160°$ and provides an energy resolution of 18% FWHM at 5.9 keV. In this work, we have used the GSC data for performing the spectral analysis owing to its larger effective area over SSC. The spectra and response files were obtained from MAXI on-demand process[2].

The Gamma-ray Burst Monitor (GBM) is the secondary instrument onboard the Fermi Gamma-ray Space Telescope (Meegan, Lichti, et al., 2009). GBM comprises 12 Sodium Iodide (NaI) scintillation detectors and 2 Bismuth Germanate (BGO) Scintillation detectors covering the energy ranges of 8 keV to 1 MeV and 150 keV to 40 MeV respectively. The data acquired by the GBM NaI detectors in CTIME data mode with 0.256 s time resolution in the 12-50 keV energy band is used by the GBM Accreting Pulsars Program to measure the spin frequency of accreting X-ray pulsars. Typically, the integration times ranging from 1 to 4 days are searched for pulse frequency using the epoch folding technique and corrected for the solar system barycenter and for the known binary orbit of the source. A review of the GBM Accreting Pulsars Program is present in Malacaria, Jenke, et al. (2020). The spin history of GX 301-2 was obtained from GBM Accreting Pulsar Histories[3].

The Burst Alert Telescope (BAT) on the Neil Gehrels Swift Observatory (Barthelmy et al., 2005) is a hard X-ray All-sky monitor operating in the 15-150 keV energy band. *Swift*/BAT consists of a combination of an array of Cadmium Zinc Telluride detectors (CdZnTe) with a total detection area of 5200 cm^2 and a Coded Aperture mask made of Lead tiles to image the X-ray sky in its 1.4 str field of view. Since the *Swift*/BAT provides almost 88% coverage of the sky every day (Krimm et al., 2013), long-term lightcurves of many X-ray sources have been made which are publicly available[4]. We have used the *Swift*/BAT long-term lightcurve of GX 301-2 in this work.

[2] http://maxi.riken.jp/mxondem/index.html
[3] https://gammaray.nsstc.nasa.gov/gbm/science/pulsars.html
[4] https://swift.gsfc.nasa.gov/results/transients/

5.1.3 Long-term averaged spectrum and average spectrum during the spin-up episode

We fitted the 3.5-20 keV *MAXI*/GSC spectrum of GX 301-2 with different models, all of them including an iron line and: i) a powerlaw, ii) powerlaw with a high energy cutoff, and iii) powerlaw with a partial covering absorption and iv) powerlaw with a high energy cutoff, with a partial covering absorption.

Though short observations of GX 301-2 are known to exhibit partially covered powerlaw with cutoff at high energies, with fluorescent emission lines of iron (Mukherjee and Paul, 2004), the long-term average *MAXI*/GSC spectrum does not require a partial covering absorption. We obtained a good fit with a model consisting of an absorption column, powerlaw with a high energy cutoff and a gaussian emission line of iron. The best fit spectral parameters are given in Table. 5.1 and the spectrum along with the residuals to the best fit is shown in Fig. 5.3.

The long-term averaged spectrum is dominated by the relatively bright main peak of the X-ray orbital intensity profile (Near orbital phase 0.95 shown in the top panel of Fig. 5.4). The iron line has an equivalent width ($\mathrm{eqw_{Fe}}$) of 708 ± 1 eV, one of the highest values among HMXB systems, and the absorption column density is 16.22 ± 1.22 in units of 10^{22} atoms $\mathrm{cm^{-2}}$. The best fit spectral parameters are given in Table. 5.1 and shown in Fig. 5.3.

We fitted the overall *MAXI*/GSC spectra of the source in MJD 58480-58560 during the spin-up episode and found that the model `tbabs(powerlaw+gaus)` gives a good fit. All the parameters except the gaussian width were constrained by the fit, and the best fit spectral parameters are listed in the Table. 5.1. The spectra, the best fit model and residuals to the best fit model are shown in Fig. 5.3.

5.1.4 Orbital phase-resolved spectral analysis

We folded the 2-20 keV *MAXI* long-term lightcurve with the binary orbital period (3583034 s) derived using the tool efsearch from the same lightcurve at epoch MJD 55025.77 so that the pre-periastron peak appears at orbital phase 0.95 (aligning with Koh et al. 1997). The folded lightcurve (Top panel of Fig. 5.4) was then split into 19 phase segments such that each phase segment has equal number of photon counts. We then generated the Good Time Intervals corresponding to these 19 orbital phase ranges within the duration of operation of *MAXI*, and retrieved the spectral files corresponding to each GTI so that each of the spectra has similar photon statistics.

Tab. 5.1: The table lists the best fit spectral fit parameters for the long-term average spectrum and the spectrum during the 2019 sin-up episode. The errors quoted on all the spectral parameters are their 90% confidence ranges.

Model	Parameter	Units	long-term average	Spin-up episode
tbabs	N_H	10^{22} atoms cm^{-2}	16.2 ± 1.2	30.9 ± 6
powerlaw	Γ		0.41 ± 0.04	0.94 ± 0.12
	Norm.	photons keV^{-1} cm^{-2} s^{-1} at 1 keV	0.024 ± 0.003	0.16 ± 0.05
highecut	E_{cut}	keV	13.95 ± 0.41	-
	E_{fold}	keV	15.61 ± 1.8	-
gaussian	E_{line}	keV	$6.29 \pm 0.01^{\dagger}$	6.34 ± 0.11
	σ_{line}	keV	0.26 ± 0.03	0.008 ± 0.008
	Norm.	photons cm^{-2} s^{-1}	0.008 ± 0.0003	0.008 ± 0.002
	Eq. width	eV	708 ± 1	295 ± 77
$Flux_{2\text{-}20\ keV}$		10^{-9} ergs cm^{-2} s^{-1}	2.22 ± 0.001	3.77 ± 0.09
χ^2/dof			372.2/322	308.8/303

† The slightly lower than expected measured value of E_{line} is possibly due to the presence of iron Kα Compton shoulder and the limited energy resolution of the *MAXI*/GSC detectors.

The effective exposure durations for the spectra in each phase range are given in Table. 5.2.

We found that the phase resolved spectra in individual phase segments were not good enough to constrain all the spectral parameters which were well constrained in the orbital phase averaged spectroscopy. We, therefore, chose to freeze the high energy cutoff (`highecut`) parameters E_{cut} and E_{fold}, and the iron line parameters E_{line} and σ_{line} to the best fit value obtained from orbital phase averaged spectrum while performing the orbital phase resolved spectral analysis. The results of orbital phase resolved spectral analysis using powerlaw with a high energy cutoff are shown in the Fig. 5.4. The first panel from the top shows the folded *MAXI* 2-20 keV lightcurve, and the second, third and fourth panels show the orbital variation of 2-20 keV flux, absorption column density and iron line equivalent width respectively, obtained from phase resolved spectroscopy.

As seen in Fig. 5.4, the column density N_H and eqw_{Fe} peaks at the orbital phase corresponding to pre-periastron flare with N_H reaching $\sim 50 \times 10^{22}$ atoms cm^{-2} and $eqw_{Fe} \sim 1500$ eV. At around the orbital phase 0.2, eqw_{Fe} is still high, but N_H is low. Around phase 0.4, the value of N_H again shows an increase to $\sim 30 \times 10^{22}$ atoms cm^{-2}. These results are in agreement with Islam and Paul (2014) obtained using the early *MAXI*/GSC data from 2009 to 2013. However, the improved photon statistics in this study also indicate that the absorption column density is highest not during the peak of the pre-periastron flare but 1.9 ± 1 days later, during the decay phase of the pre-periastron flare.

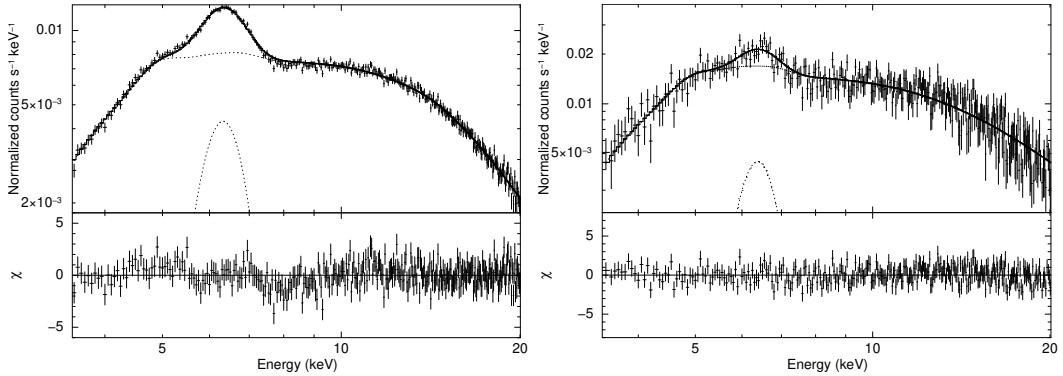

Fig. 5.3: The figure on the left shows the *MAXI*/GSC spectrum and the best fit spectral model `tabs(powerla*highecut+gauss)` for the long-term average spectrum of GX 301-2. The figure on the right shows the *MAXI*/GSC spectrum and the best fit model `tabs(powerla+gauss)` during the spin-up episode in MJD 58480-58560. In both the figures, the top panel shows the spectrum and the best fit model, while the bottom panel shows the residuals to the best fit model.

Tab. 5.2: The effective exposures and spectral count rates of the *MAXI*/GSC spectra in each orbital phase range used in orbital phase resolved spectroscopy.

Orbital phase range	Effective exposure (ks)	Count rate (Cts s^{-1})
0.0-0.03	358	0.16 ± 0.001
0.03-0.09	723	0.09 ± 0.001
0.09-0.21	1271	0.04 ± 0.001
0.21-0.32	1216	0.04 ± 0.001
0.32-0.40	860	0.07 ± 0.001
0.40-0.47	775	0.07 ± 0.001
0.47-0.53	730	0.08 ± 0.001
0.53-0.59	703	0.09 ± 0.001
0.59-0.66	780	0.08 ± 0.001
0.66-0.73	682	0.08 ± 0.001
0.73-0.79	667	0.09 ± 0.001
0.79-0.84	609	0.11 ± 0.001
0.84-0.88	423	0.16 ± 0.001
0.88-0.91	248	0.24 ± 0.002
0.91-0.93	258	0.34 ± 0.002
0.93-0.95	179	0.38 ± 0.002
0.95-0.96	173	0.38 ± 0.002
0.96-0.98	260	0.32 ± 0.002
0.98-1.0	176	0.22 ± 0.002

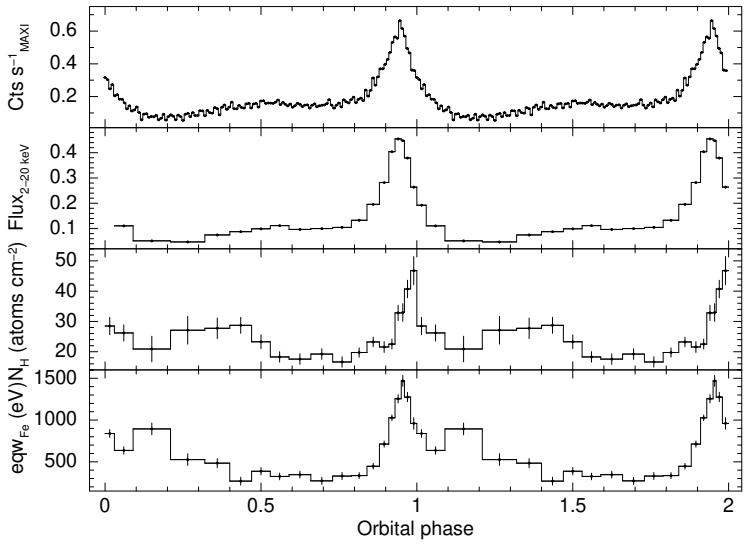

Fig. 5.4: The top panel in the figure shows the *MAXI* long-term X-ray lightcurve of GX 301-2 in the 2-20 keV energy band folded with the orbital period, and the next three panels show the variation of the best fit spectral parameters over orbital phase. The 3.5-20 keV spectra in each orbital phase were fitted with the model `tbabs*(powerlaw*highecut+gaus)` and the best fit values for absorption column density and iron line equivalent width are plotted against the orbital phase. Error bars assigned to each data point are their 90% confidence ranges. $Flux_{2\text{-}20\ keV}$ is derived from the spectral fit and has units of photons cm^{-2} s^{-1}.

5.1.5 Time resolved spectral analysis during the spin-up episode

Even though it is desirable to analyze the day-by-day spectrum of *MAXI*/GSC to study the time-resolved spectral parameters during the spin-up episode, one-day *MAXI*/GSC spectrum is limited by photon statistics. Therefore we chose multi-day sliding window spectra to fulfil the task and selected six-day windows; the window length is much less than the orbital period of the system such that orbital variation in parameters is not averaged out. Therefore we made a total of 135 sliding windows having a width of 6 days and a stride of 1 day, from MJD 58450 to 58590. This interval fully covers three orbits of the binary, including one periastron passage before the spin-up episode and two periastron passages during the spin-up episode. However, there is gap in the data especially 1) near the pre-periastron flare before the spin-up begins, and 2) just before the start of the spin-up.

The 3.5-20 keV spectra obtained from each of these sliding windows were then fitted with the model `tbabs(powerlaw+gaus)`. The center and width of the gaussian could not be constrained well in all the windows, and therefore center of the gaussian was fixed to the value obtained from the fit to the spectra in MJD 58480-58560, while the width of the gaussian was fixed to the value obtained from fit to the long-term

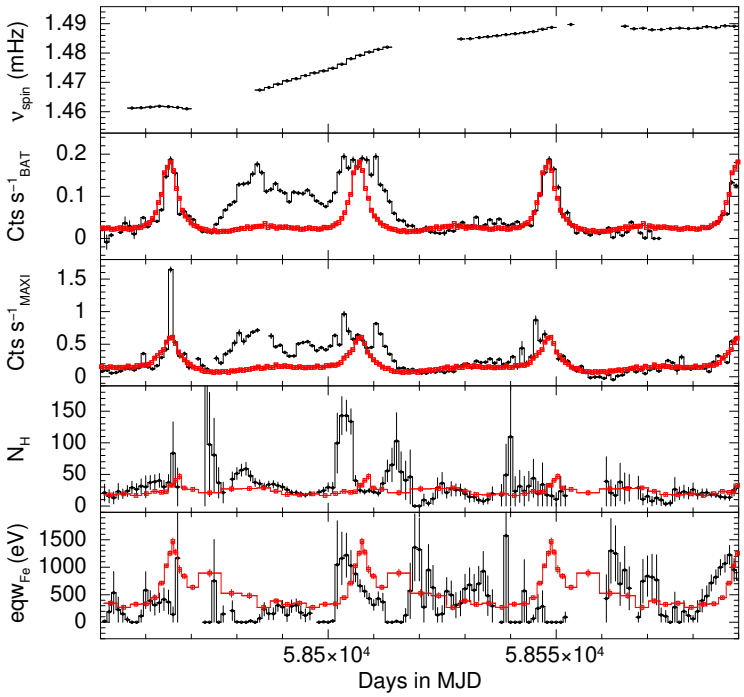

Fig. 5.5: The data points in black shows the daily evolution of parameters while the data points in red show the long-term average orbital parameters. The first panel from the top shows the *Fermi*/GBM pulsar spin history, and the next two panels show the long-term X-ray lightcurves from *Swift*/BAT and *MAXI* and their folded profiles. Two panels from the bottom of the plot show the comparison of the spectral parameters N_H (in 10^{22} atoms cm^{-2}) and eqw_{Fe} during an average orbit to that during the spin-up episode.

average spectra (See Table. 5.1). The best fit values of the spectral parameters absorption column density N_H and equivalent width of the iron line eqw_{Fe} obtained from the analysis of each window are assigned to the MJD corresponding to the center of the window. The results of spectral analysis during the sliding window are shown in the Fig. 5.5. There are three particular regions: i) high N_H and low eqw_{Fe} during MJD $\sim$ 58480-58490, ii) high N_H and high eqw_{Fe} during MJD $\sim$ 58500-58510, and iii) low N_H and high eqw_{Fe} during MJD $\sim$ 58528-58538. The *MAXI*/GSC spectra in these three regions are shown in the Fig. 5.6.

5.1.6 Discussion: Evolution of the circum-binary environment during the spin-up episode

The mean values and variation of the equivalent hydrogen column density and iron line equivalent width over orbital phases (Fig. 5.4) are in agreement with Islam and Paul (2014), except for the secondary peak in column density near the apastron

passage. We also found that the column density peaks during the decay of the pre-periastron flare and not during its maximum. Maximum absorption column density is observed ~ 1 day after the peak of pre-periastron flare, at/near the periastron passage of the neutron star. With the improved statistics, we could also achieve considerably smaller errors on the estimates of N_H and eqw_{Fe} compared to Islam and Paul (2014). The reported discrepancy between the observations of absorption column density and the predictions from the models in Pravdo et al. (2001) and Leahy and Kostka (2008) is very clear.

Though the *Fermi*/GBM pulsar spin history has a data gap when the spin-up episode began, extrapolating the trend indicates it should have started at $\sim$ MJD 58475, about 10 days after the pre-periastron passage at $\sim$ MJD 58465. The *Swift*/BAT (15-50 keV) and *MAXI* (2-20 keV) lightcurves also indicate an associated increase in the flux a few days after the pre-periastron flare at the same epoch (See panel 1, 2 and 3 from the top of the Fig. 5.5). The two other spin-up episodes of GX 301-2 probed by *Fermi*/GBM and *Swift*/BAT also show a similar delay after the pre-periastron flare before the spin-up begins (Also see Abarr et al. 2020 and Liu 2020). The 2019 spin-up episode differs from the other spin-up episodes in the sense that it lasted for almost two binary orbits compared to less than one binary orbit for the other episodes. However, the increase in X-ray flux compared to the long-term average is seen throughout the first orbit and again during the pre-periastron flare of the second orbit. We also point out that the increase in spin-up rate happened for a luminosity comparable to the pre-periastron flare seen in every orbit of this source. GX 301-2 does not show a spin-up episode along with the increase in X-ray flux at the pre-periastron flare in every orbit. It is, therefore, likely that GX 301-2 usually has direct wind accretion, and the large spin-up episodes are instances when an accretion disk is formed around the NS. The time resolved spectral analysis presented here using the *MAXI*/GSC data shows that the formation of the accretion disk is driven by some process that also causes significant changes in the X-ray reprocessing environment in the binary system.

Using pointed observations, Nabizadeh, Armin et al. (2019) (*NuSTAR*) and Liu, Ji, et al. (2021) (*Insight-HXMT*) reported contrasting results on the difference in the nature of reprocessing environment during and outside the 2019 spin-up episode. The latter reported relatively low N_H during the spin-up episode (disk-fed state) when compared to outside the spin-up (wind-fed state), but the former reported no major differences in the spectral parameters. However, it has to be noted that each of the pointed observations only probes a tiny fraction of the orbital phase, and GX 301-2 is known to exhibit significant changes across the binary orbit (Islam and Paul, 2014). Therefore it is preferable to compare the

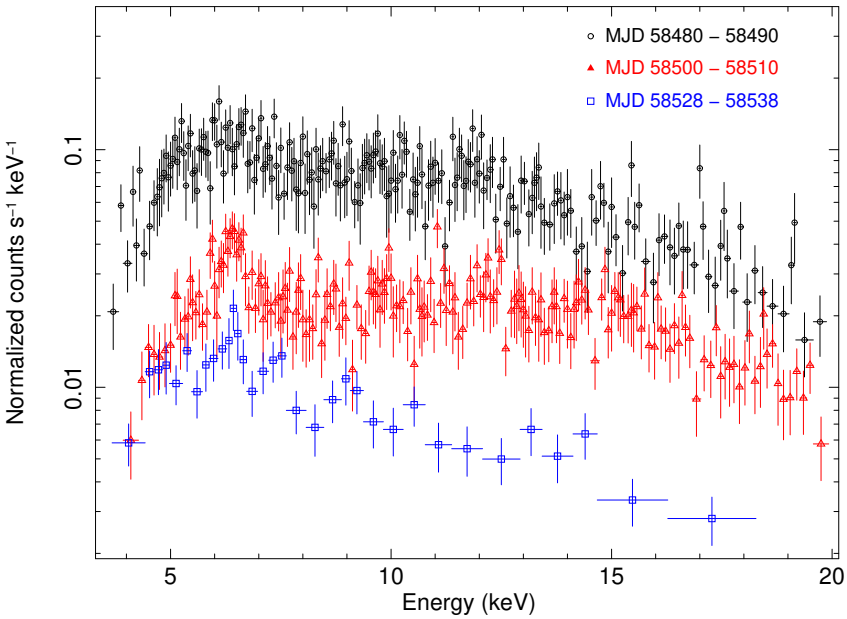

Fig. 5.6: The figure shows the *MAXI*/GSC spectra of GX 301-2 during three instances of the spin-up episode classified based on the strengths of N_H and eqw_{Fe}. The spectra during MJD 58528 to 58538 is shown in black (○) and scaled by a factor of 3 for better visibility. The spectra during MJD 58480 to 58490 is shown in red (△) and MJD 58500 to 58510 in blue (□), and both are shown in original scales.

reprocessing environment of the pulsar using observations that probe similar orbital phase of the binary. Moreover, our analysis shows that the reprocessing environment underwent significant variation during the spin-up episode itself (See Fig. 5.6 and 5.5). Following are our observations about GX 301-2 during the spin-up episode:

- Usually the spin-up episodes are accompanied by an increase in the flux, indicating an increase in the accreted matter due to the formation of a transient accretion disk around the NS (Ghosh et al., 1979). The spin-up rate (the time derivative of spin frequency obtained by fitting straight line segments on the Fig. 5.2) is relatively higher during the first orbit at about 6.5×10^{-12} Hz s^{-1}, incidentally where the X-ray flux is also high. During the second orbit, where the X-ray flux has not increased as such and the spin-up rate is also lower at about 2.3×10^{-12} Hz s^{-1} (Also see Fig. 1 of Liu, 2020).

- The onset of spin-up happened at the orbital phase where N_H would have been low, and iron equivalent width would have been high in an average orbit. But at the onset of spin-up, the eqw_{Fe} is low, and N_H is high.

- In an average orbit, both N_H and eqw_{Fe} peaks at/near the pre-periastron flare. However, during the rapid phase of the spin-up episode, this happens ~ 5 days prior to the phase of pre-periastron flare (observed at $\sim$ MJD 58502). This

is accompanied by an increase in the X-ray flux which is clearly seen in the *Swift*/BAT lightcurve. At the phase of the pre-periastron flare, the values of N_H and iron equivalent are lower than what is expected from an average orbit.

- Soon after the unusual increase in absorption and luminosity observed at $\sim$ MJD 58502 during the rapid phase of the spin-up episode and the subsequent pre-periastron flare, the pulsar went into the slow spin-up state with an associated decrease in the luminosity.
- After the apastron passage towards the end of the spin-up episode, at around 58530 MJD, the iron line equivalent width has shown an abrupt increase to values of ~ 1000 eV, which is not observed during an average orbit.
- During the entire spin-up episode the values of peak N_H ($\sim 100 \times 10^{22}$ atoms cm^{-2}) are relatively higher than that during the average orbits ($\sim 50 \times 10^{22}$ atoms cm^{-2}). However, the average equivalent width of the iron line during the spin-up episode is less than half of the long-term average value of the same. This is perhaps due to the fact that, during the spin-up episode, the source was bright throughout a binary orbit, while in the long-term averaged data, the spectrum is dominated by the emission during the pre-periastron flare.

5.1.7 Summary

In this work, we utilized the spectroscopic capability of the All-sky monitor *MAXI*/GSC to probe the changes in the X-ray reprocessing environment of the HMXB pulsar GX 301-2 during a rapid spin-up episode of the pulsar in 2019. We probed the variation in equivalent hydrogen column density and equivalent width of the iron fluorescence emission line during the two-orbits long spin-up episode and compared them with the long-term average orbit-resolved values. We found significant changes in these parameters during the spin-up episode from that of the long-term average. This indicates a significant change in the X-ray reprocessing environment of the pulsar during the spin-up episode.

5.2 Evolution of the binary orbit of GX 301-2

Accreting High Mass X-ray Binary (HMXB) pulsars that host a rotating neutron star accreting matter from a companion star are hypothesised to be born from the supernova explosion of the more massive star in a preliminary binary stellar system

hosting two relatively massive components (>12 M$\odot$) (Tauris et al. 2006, and references therein). When the mass of the companion star is over 10 M$\odot$, and it is of OB spectral type, they are called Supergiant HMXBs (SGXBs), which account for about one-third of the known HMXBs (Tauris et al., 2006). The binary orbit of SGXBs is postulated to evolve due to (i) tidal interactions, which also causes circularization of the eccentric orbit, (ii) mass transfer from companion to the neutron star by accretion, (iii) loss of mass from the binary by the stellar wind from the companion, and (iv) radiation by gravitational waves (Paul and Naik 2011, and references therein). The most accurate estimation of the orbital parameters and, thereby, the orbital evolution of accreting X-ray pulsars are obtained by measuring the time of arrival of the stable X-ray pulses from the X-ray pulsar due to the motion of the pulsar in the binary orbit. This technique is called the pulse time of arrival (TOA) analysis. The pulse TOA technique optimizes a parameter space comprising intrinsic pulse emission time stamps from the pulsar (accounting for inherent pulse period derivatives) and the binary orbit-induced arrival time delays in order to obtain the observed time of arrivals of each X-ray pulse (Nagase, Hayakawa, et al., 1982). Pulse timing analysis has been extensively used to accurately estimate the orbital evolution of SGXBs like Cen X–3, SMC X–1, LMC X–4, OAO 1657–415 and 4U 1538–52 (See Paul, 2017, and references therein.). Orbital decay (shrinking orbit) was observed in all the HMXBs hosting a pulsar, and the estimated decay time scale $|P_{\rm orb}/\dot{P}_{\rm orb}|$ varies from $\sim 10^6$ yr in SMC X–1, Cen X–3, LMC X–4 and 4U 1538–52 to about $\sim 10^7$ yr in OAO 1657–415 and 4U 1700–37 (Table 5.6).

GX 301–2 is a rare galactic SGXB because of the unusually eccentric (e ~0.47) binary orbit (Sato et al., 1986), which is a peculiarity of Be-HMXBs (Paul and Naik 2011), and the only SGXB known to have a Hypergiant companion (Kaper et al., 1995). GX 301–2 is located ~ 5.3 kpc away on the galactic plane and hosts a $\sim 50 M_\odot$ Hypergiant stellar companion Wray 15-977 (BP Crucis) (Kaper et al., 1995) in a ~ 41.5 d long binary orbit (Sato et al., 1986). From the Hα absorption profile in the optical spectrum, Kaper et al. (1995) estimated the mass loss rate from Wray 15-977 by the stellar wind to be $\lesssim 10^{-5} M_\odot$ yr^{-1}. A peculiar feature of GX 301–2 is its pre-periastron flaring nature, which is usually explained either by enhanced accretion of matter either from a dense gas stream from the companion star (Haberl 1991, Leahy and Kostka 2008) or an equatorial gas disc circumscribing Wray 15-977 (Pravdo et al., 2001). Because of the pre-periastron flare, GX 301–2 exhibits variable X-ray intensity within each orbit, and the extent of the variation is energy dependent. The intensity varies by a factor of ~ 5 in 4–10 keV and ~ 12 in 15–50 keV. The pre-periastron flaring nature and binary ephemeris of GX 301–2 were first estimated by Sato et al. (1986) by pulse TOA analysis from *SAS 3*, *Hakucho*, and

Ariel 5 observations. A similar analysis was performed by Koh et al. (1997) on the *CGRO*/BATSE data, and the reported orbital elements were consistent with Sato et al. (1986). However, the orbital solution estimated by Sato et al. (1986) and Koh et al. (1997) did not show any evidence of the decay of the orbital period. Evidence for orbital decay of the binary with $\dot{P}_{\rm orb} = -(3.7 \pm 0.5) \times 10^{-6}$ s s^{-1} was later discovered by Doroshenko, Santangelo, Suleimanov, et al. (2010) using pulse TOA analysis from a long *INTEGRAL* observation (covering about 60% of a binary orbit), under the assumption of a constant spin-up/down rate ($\dot{P}_{\rm spin}$). This is the smallest orbital decay timescale observed in any HMXB. However, the large luminosity change of GX 301–2 along its orbital phase is most likely due to a variable mass accretion rate, and an important implication of the variable luminosity of GX 301–2 within each orbit is its effect on the spin-up rate of the pulsar. The spin-up rate of GX 301–2 is known to be correlated with the X-ray luminosity (Koh et al., 1997). Previous estimations of orbital parameters and orbital evolution (Koh et al. 1997, Doroshenko, Santangelo, Suleimanov, et al. 2010), however, did not consider a luminosity-dependent period derivative (Mönkkönen et al., 2020).

In this work, we use the long-term X-ray lightcurves of GX 301–2 available from the X-ray All-sky monitors *RXTE*/ASM, *Swift*/BAT and *MAXI* and the pulsed flux histories available from *CGRO*/BATSE and *Fermi*/GBM to investigate the orbital decay, which has previously been reported from pulse TOA analysis. Instead of the pulsar time stamps, which are used in the pulse TOA analysis, we make use of the similarity in the shapes of recurring orbital intensity profiles and the timing signature of the recurring flare peaks of GX 301–2. Assuming the orbital intensity profile of GX 301–2 to preserve an overall shape over the long term, epoch folding the long-term lightcurves and pulsed-flux histories could be used to estimate the orbital period and period derivative. Assuming that the physical mechanism responsible for the pre-periastron flares remains stable over the long term, we also utilize the changes in the arrival times of pre-periastron flares over an extended period to estimate the rate of change of the orbital period.

5.2.1 Instrument and Observations

The orbital period of GX 301–2 is relatively long, spanning 41.5 days (3586 ks), which makes conducting pointed observations throughout the entire orbit of GX 301–2 infeasible. However, being one of the brightest sources in the X-ray sky, GX 301–2 is monitored by all of the X-ray all-sky monitor observatories. The long-term lightcurves or pulsed flux histories from these observatories are available for over three decades.

The Burst and Transient Source Alert (BATSE) instrument onboard the *Comption Gamma Ray Observatory (CGRO)* (Meegan, Fishman, et al., 1992) consisted of eight inorganic NaI-based Scintillation detectors detecting hard X-ray photons from different parts of the sky in 20 keV – 2 MeV. *CGRO*/BATSE was operational from 1991 to 2000. The pulse periods of several X-ray pulsars were measured by epoch folding technique, and their pulse period and pulsed flux histories are available for download at BATSE Pulsars webpage[5].

The All-sky monitor (ASM) onboard the *Rossi X-ray Timing Explorer* (RXTE) (Levine, Bradt, et al. 1996; Jahoda et al. 1996) consisted of three position-sensitive Xenon proportional counters coupled to three coded-aperture masks respectively, and it operated in the 1.5–12 keV energy band. It had a total collecting area of 90 cm^2 and covered almost 80% of the entire sky during each 90 min orbit, and it provided continuous data coverage of bright X-ray sources from 1996 to 2011.

The Burst Alert Telescope (BAT) onboard the Neil Gehrels Swift Observatory (Barthelmy et al. 2005; Gehrels et al. 2004) is a hard X-ray all-sky monitor operating in the 15–50 keV band. BAT consists of Cadmium Zinc Telluride (CZT) detectors (total detector area of about 5200 cm^2) coupled to a two-dimensional coded-aperture mask. This facilitates imaging of the X-ray sky with a large instantaneous field of view of 1.4 std. *Swift*/BAT is operational from 2004 until now.

The Gamma Burst Monitor (GBM) onboard the *Fermi Gamma-ray Space Telescope* is a hard X-ray monitor operating in 8 keV to 40 MeV. It consists of 12 Thallium activated Sodium Iodide (NaI(Tl)) scintillation detectors operating in 8 keV – 1 MeV range and two Bismuth Gemanate (BGO) scintillation detectors operating in 200 keV - 40 MeV range. The GBM Accreting Pulsars Program (GAPP) provides the pulsed flux histories of bright X-ray pulsars (See Malacaria, Jenke, et al. 2020 for a review). It is operational since 2008.

The Gas Slit Camera (GSC) onboard the *Monitor of All-sky X-ray Image* (*MAXI*) observatory (Mihara, Nakajima, et al. 2011; Matsuoka et al. 2009) is an All-sky monitor onboard the International Space Station (ISS) operating in the range 2–30 keV. GSC comprises twelve large-area position-sensitive proportional counters, each coupled to a slit-slat collimator. They have an instantaneous FOV of $160° \times 3°$ and scan the whole sky during each orbit of the ISS. The narrow FOV and position-sensitive proportional counters facilitate imaging of the X-ray sky. The long-term lightcurves of X-ray sources from *MAXI* are available since 2008.

[5] https://gammaray.nsstc.nasa.gov/batse/pulsar/

We downloaded the orbit-by-orbit (dwell) long-term lightcurves from *RXTE*/ASM (1.5–12 keV), *Swift*/BAT (15–50 keV) and *MAXI* (2-4, 4–10, 10–20 keV). The dwell lightcurves have a bin size of about 90 minutes (0.0625 days). However, the pulsed flux histories from *CGRO*/BATSE and *Fermi*/GBM were available with a bin size of 1 day and 2 days, respectively. The *Swift*/BAT lightcurve was screened such that the data points having a value of error greater than 500 times the lowest error were removed from the data.

5.2.2 Analysis

We performed three independent analyses to search for the orbital period decay in GX 301–2. In the first approach, epoch folding search (Leahy, 1987) was run on each long-term lightcurve without $\dot{P}$, and the slope of the best-fitting straight line fitting the best periods derived from each of them as a function of time was derived. In the second approach, epoch folding search was run on each long-term lightcurves for a prospective range of $\dot{P}_{\rm orb}$ from -3×10^{-5} to $+3 \times 10^{-5}$ s s^{-1} to check if there is improved detection of periodicity corresponding to any $\dot{P}_{\rm orb}$. This would indicate the presence of any period evolution in the long-term lightcurves. In the third approach, we use the times of the periodic pre-periastron flares to estimate the orbital period decay. The first two approaches depend on the long-term consistency of the orbital intensity profile of GX 301–2, which is dominated by the pre-periastron flare. The third approach depends on precisely locating the peak of the pre-periastron flares and the long-term stability of the time of arrival of pre-periastron flares. This means that the most significant factor affecting both analyses is the accuracy of the shape of the flare. Since the flare is about 2 days long, the lightcurves used for analysis should preferably have a finer time resolution to construct the shape of the flare accurately. For this purpose, the 0.0625 d bin size dwell lightcurves are used for the analysis. However, the pulsed histories from BATSE and GBM were only available with a bin size of 1 d and 2 d, respectively, impacting the estimation accuracy from these two light curves.

Epoch folding search

We ran the epoch folding search over the entire duration of all five long-term lightcurves (Tables 5.3, 5.4) using the *heasoft* tool *efsearch*[6]. We searched for periods in the vicinity of 3583780 s (41.5 d), which is the known binary orbital period.

[6] https://heasarc.gsfc.nasa.gov/ftools/fhelp/efsearch.txt

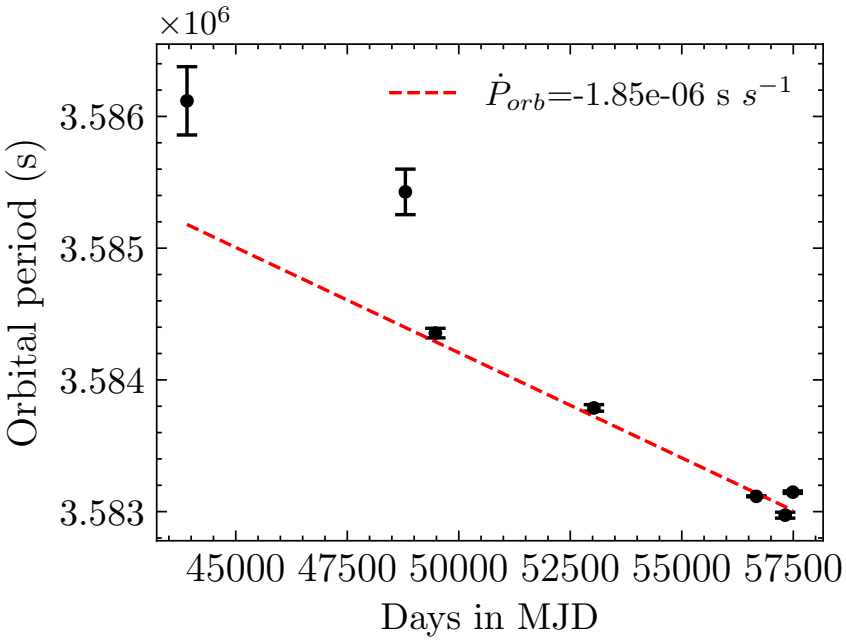

Fig. 5.7: Estimates of the orbital periods from the long-term lightcurves and pulsed flux histories. $\dot{P}$ from fitting a linear model is $-(1.85 \pm 0.34) \times 10^{-6}$ s s^{-1}.

For estimating the error in the best period returned by *efsearch* in a lightcurve, we simulated 1000 instances of that particular lightcurve and ran *efsearch* on each one of them, and the variance of the distribution of the best periods returned from 1000 lightcurves was used to estimate the 1σ error in the period (See Appendix 5.2.4 for details). The best period returned from each lightcurve was then assigned to the middle of the respective lightcurve duration and then plotted (Fig 5.7, Table 5.3). There is a clear trend of decreasing period, and a linear fit returns a best-fit orbital decay rate of $-(1.85 \pm 0.34) \times 10^{-6}$ s s^{-1}.

Epoch folding search with a period derivative

To search for the presence of such an orbital period decay within the duration of each lightcurve, we ran *efsearch* in a range of sample period derivatives ranging from -3×10^{-5} to $+3 \times 10^{-5}$ s s^{-1} in each of the lightcurves. The results are shown in Fig. 5.8. *Swift*/BAT, *Fermi*/GBM and *MAXI* clearly shows the presence of an orbital decay rate of around -10^{-6} s/s and *RXTE*/ASM is consistent with this value (See the caption of Fig. 5.8). However, such an orbital decay is not detected with *CGRO*/BATSE.

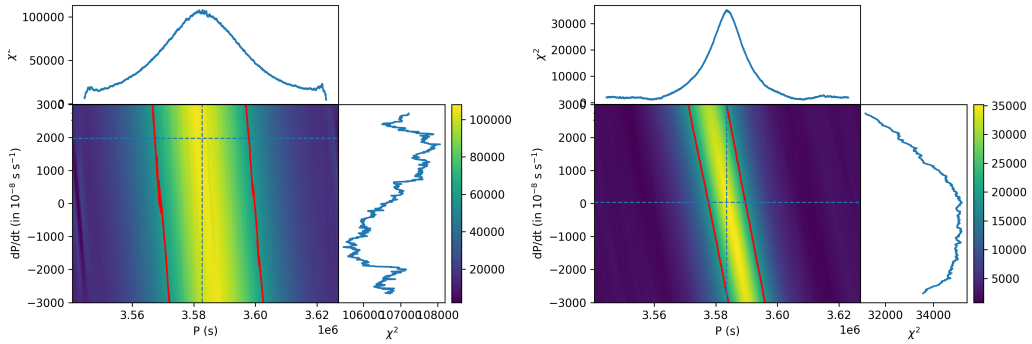

(a) *CGRO*/BATSE

(b) *RXTE*/ASM

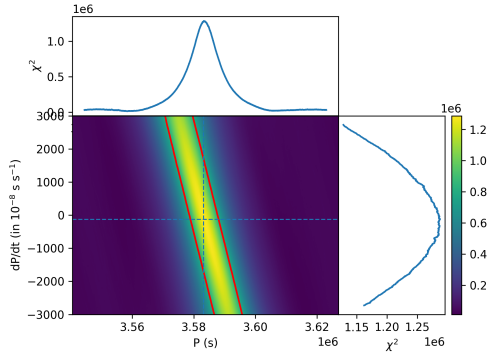

(c) *Swift*/BAT

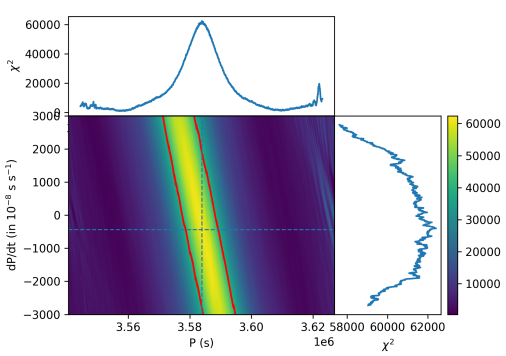

(d) *Fermi*/GBM

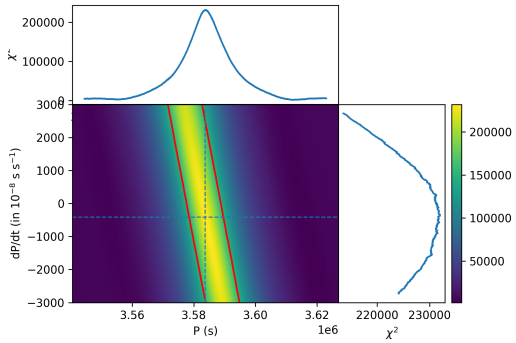

(e) *MAXI*

Fig. 5.8: Figure shows the results of *efsearch* for different $\dot{P}$ values when run on three long-term orbit light curves and two pulsed flux histories. The epoch used for the period search for each lightcurve is the start of the respective lightcurve. Each plot has three panels, and the middle panel has $\chi^2 - P$ horizontal plots stacked vertically for different $\dot{P}$, with χ^2 colour-coded. The top plot shows the $\chi^2 - P$ plot returned for the best $\dot{P}$ ($\chi^2 - P$ with the highest ${\chi^2}_{\rm peak}$), and the right panel shows the ${\chi^2}_{\rm peak}$ obtained from each *efsearch* run. The pair of horizontal and vertical dashed lines in the middle panel denotes $(P, \dot{P})$ corresponding to the highest ${\chi^2}_{\rm peak}$ along each axes. *Swift*/BAT, *MAXI* and *Fermi*-GBM show the presence of a secular $\dot{P}_{\rm orb}$ of the order of 10^{-6} s s^{-1}, and *RXTE*/ASM is consistent with such a value, but such a trend is not evident in *CGRO*/BATSE.

Tab. 5.3: Estimates of the orbital period from the long term All sky monitor daily lightcurves and pulsed flux history lightcurves with associated 1σ error bars.

Observatory	Epoch (MJD)	Best period	Reference
SAS-3, *Hakucho*, *Ariel-5* ‡	43906.06	3586291.2 ± 604.8	Sato et al. (1986)
INTEGRAL ‡	43906.06	3586118.4 ± 259.2	Doroshenko, Santangelo, Suleimanov, et al. (2010)
CGRO/BATSE ‡	48802.79	3585427.2 ± 172.8	Koh et al. (1997)
CGRO/BATSE	49475.00	3584355.24 ± 36.34	This work.
RXTE/ASM†	53030.0	3583787.19 ± 24.95	This work.
Swift/BAT	56671.32	3583115.88 ± 3.92	This work.
Fermi-GBM	57318.77	3582973.00 ± 22.67	This work.
MAXI	57489.84	3583147.78 ± 9.45	This work.

† 1.5–12 keV band.
‡ From pulse TOA analysis.
The long-term lightcurves from *RXTE*/ASM, *Swift*/BAT and *MAXI* have bin size of 0.0625 d. The pulsed flux history from *CGRO*/BATSE and *Fermi*/GBM have bin sizes of 1.0 d and 2.0 days, respectively.

O-C curves using the pre-periastron flares

The recurring pre-periastron flares at regular intervals are a peculiarity of GX 301–2, and the time stamps ($T_{\rm flare}$) of pre-periastron flare peaks are useful markers to track the evolution of the binary orbital period. For a stable binary orbital period without temporal evolution, if the timestamp of flare in $0^{\rm th}$ orbit (T_0) is known, the time stamp of flare in $n^{\rm th}$ orbit will follow the linear function $T_0 + nP_{\rm orb}$. Any deviation from linearity in the observed time stamps of the flares indicates orbital period evolution. The difference between the observed and computed time of flares as a function of time is called the O-C curve. This technique was utilized for the estimation of orbital evolution by monitoring the time of arrivals of minima in the orbital intensity profile of Cyg X–3 (Singh et al. 2002) and by tracking the mid-eclipse times of eclipsing binaries Cen X–3, SMC X–1 (Raichur et al., 2010b) and LMC X–4 (Naik and Paul, 2004b). We use the same technique, with the orbital-intensity minima or mid-eclipse time substituted by pre-periastron flare peak (essentially the orbital-intensity maxima).

Since the photon statistics do not allow an accurate estimation of flare times for every orbital cycle from the long-term lightcurves, we constructed a representative flare peak time for short-duration segments of the long-term lightcurves. We divided each of the five lightcurves into three segments of equal duration and determined a representative time of arrival of the flare in each of those time segments. The time of arrival of the flare on $n^{\rm th}$ orbital cycle can be expressed as a Taylor polynomial function of n:

$$T_n = T_0 + \frac{n}{1!}P_{\rm orb} + \frac{n^2}{2!}P_{\rm orb}\dot{P}_{\rm orb} + \ldots \tag{5.1}$$

Tab. 5.4: Peak flare times from overlapping duration of the long-term lightcurves in different energy bands.

Observatory/Instrument	Energy range (keV)	LC duration (MJD)	No. of orbits during overlap	$\Delta T_{\rm flare}$ (d)
CGRO-BATSE	20-50 keV	48370-50579	Reference LC	
RXTE/ASM	1.5–12 keV	50133-55927	10	-0.57 ± 0.09
Swift/BAT	15–50 keV	53416-59927	Reference LC	
RXTE/ASM	1.5–12 keV	50133-55927	60	-0.96 ± 0.06
Fermi/GBM	12–50 keV	54691-59947	126	-0.23 ± 0.04
MAXI	2–20 keV	55053-59927	116	-0.36 ± 0.02
	4–10 keV	"	"	-0.88 ± 0.03
	10–20 keV	"	"	-0.08 ± 0.02

T_n is the time stamp of the n$^{\rm th}$ pre-periastron flare peak, T_0 is the time stamp of the reference pre-periastron flare peak, $P_{\rm orb}$ is the orbital period, and $\dot{P}_{\rm orb}$ is the rate of change of orbital period. Assuming $\dot{P}_{\rm orb}$ is present and ignoring the higher order derivatives, equation 5.1 can be used to verify the presence and get an estimate of $\dot{P}_{\rm orb}$ if it exists (See Klis and Bonnet-Bidaud 1984; Raichur et al. 2010b).

However, the five long-term lightcurves are from different energy ranges, and the periodic pre-periastron flares of GX 301–2 are known to exhibit a hard X-ray lag of about a day (Liu, 2020). Therefore, we checked the simultaneity of the flare peaks in the long-term lightcurves before proceeding with the $\dot{P}_{\rm orb}$ estimation. The long-term lightcurves and pulsed histories have overlapping data duration (See Table 5.4 and the vertical dashed lines in Fig. 5.9). We checked the flares in BATSE (20–50 keV), ASM (1.5–12 keV), BAT (15–50 keV), GBM (12–50 keV) and *MAXI* (4–10, 10–20 keV). The long-term lightcurve from *Swift*/BAT have considerable overlapping data duration with *RXTE*/ASM, *Fermi*/GBM and *MAXI* lightcurves and *CGRO*/BATSE has overlap with *RXTE*/ASM to perform this study. We estimated the difference in flare times ($\Delta T_{\rm flare}$) between lightcurves in the overlapping durations using the technique described in Appendix 5.2.4. These $\Delta T_{\rm flare}$s Except for *BATSE* and GBM, we found a very clear hard X-ray lag of $\sim$ 0.9 d (Table 5.4). As the *BATSE* and GBM pulse flux histories are generated by integrating the pulsed flux over one day and two days, respectively, which is of the same order as the flare duration, it may impact the accurate construction of the flare shape and, subsequently, our estimation of the flare peak. This inadequacy of the data most likely causes the contrasting results from *BATSE* and GBM. We derived error scaling factors for the flare times T_n from *BATSE* (4.3), GBM (5.8) and *MAXI* 10–20 keV (4), and a time shift for ASM ($+0.96$ d) so that the energy dependence of flare arrival times are eliminated and all the flare times are consistent with BAT.

The time stamps of the pre-periastron flares T_ns derived from the long-term lightcurves were corrected for the energy dependence mentioned before and the energy inde-

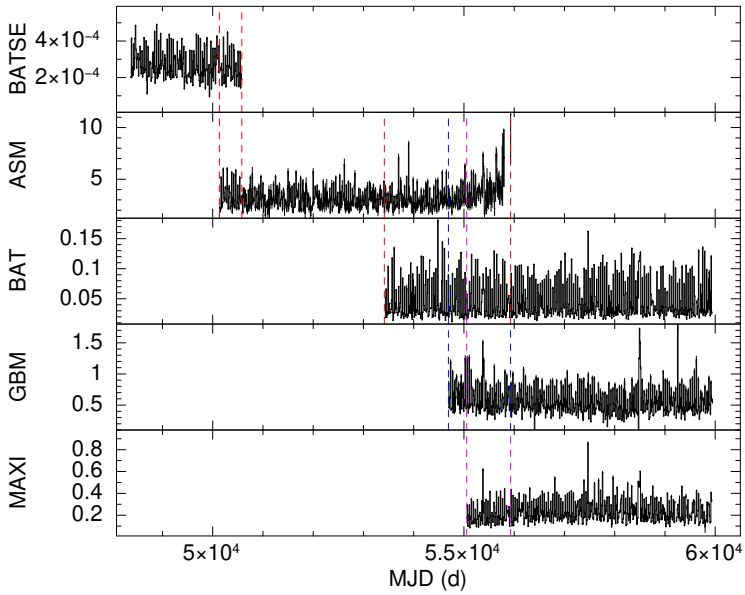

Fig. 5.9: The long term lightcurves and pulsed flux histories from different All-sky monitors plotted with a bin size of 10 d. The overlapping duration for BATSE-ASM, BAT-ASM, BAT-GBM and BAT-*MAXI* are shown in vertical dashed lines. The simultaneous data allowed a check for the energy dependence of flares, and there is a clear hard lag (Table 5.4).

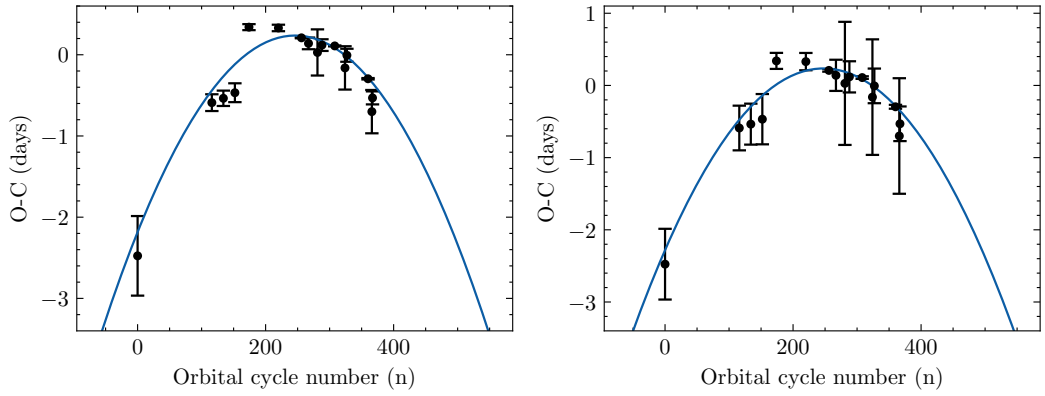

Fig. 5.10: O-C curve from pre-periastron flare peak times derived from BATSE, ASM, BAT, GBM and *MAXI*. The first data point is taken from Sato et al. (1986). Error in GBM data points are scaled by a factor of 8.3, and ASM data points are shifted by +0.7 days to account for the energy dependence of flare times (See text). Top figure shows $\dot{P}_{\rm orb} = -(1.93 \pm 0.11) \times 10^{-6}$ s $^{-1}$. However, the weighted variance (`wvar`) of fit is poor at 145 for 14 $(16 - 3 + 1)$ d.o.f, which impacts the parameter error estimation. The large variance is contributed by the low error bar of the data points $(\sum_{i=1}^{15}(\frac{d_i - m_i}{e_i})^2 \sim 145)$. To make the wvar≈d.o.f, we scaled up each error e_i with a scaling factor of $\sqrt{145/15} \sim 3$. This reduced the `wvar` to ~ 16 (14 d.o.f). The bottom figure shows the best-fit quadratic model on the error re-scaled data. Best fit $\dot{P}_{\rm orb}$ is $-(1.98 \pm 0.28) \times 10^{-6}$ s s^{-1}. The quoted errors on all the parameters are their 2.7σ confidence ranges.

pendent flare times were used for further analysis. In addition to these data points, we used the flare time from Sato et al. (1986), which was derived from *Ariel-V* (2–15 keV), *SAS–3* (8–18 keV), *Hakucho* (9–22 keV) and *HEAO–1* (15–175 keV). The T_n vs n was then fitted with a linear function in n (mimicking $T_0 + nP_{\rm orb}$), and the residuals to the linear fit (δT_n or O-C vs n) were plotted. A clear negative parabolic trend was visible in the residuals, indicating the orbital decay (Fig. 5.10 top). Fitting a function of the form $T_0 + nP_0 + 0.5n^2 P_{\rm orb}\dot{P}_{\rm orb}$ gave the best fit $\dot{P}_{\rm orb}$ as $-(1.93 \pm 0.11) \times 10^{-6}$ s s^{-1} (Fig. 5.10 bottom). However, the fit statistic was large, and we, therefore, scaled the errors in flare times by a factor of 3. This is justified because, along with the regular pre-periastron flares, GX 301–2 is also known to exhibit short-term variability, which could contribute to additional systematic error in the determination of pr-periastron flare times. Scaling of errors improved the fit statistic and the subsequently obtained best fit $\dot{P}_{\rm orb}$ is $-(1.98 \pm 0.28) \times 10^{-6}$ s s^{-1}.

5.2.3 Discussions

Estimation of decay in orbital period

The rapid orbital decay rate of GX 301–2 was estimated by Doroshenko, Santangelo, Suleimanov, et al. (2010) from multiple *INTEGRAL* pointed observations by timing the X-ray pulses. A constant $\dot{P}_{\rm spin}$ of the pulsar is assumed in the calculation. However, GX 301–2 exhibits an intensity variation by a factor of 15 within the orbit (evident from folded *Swift*/BAT orbital intensity profile) and even a factor of 3 during the out-of-flare states (Fürst, Falkner, et al., 2018). The torque-state of the X-ray pulsar is also known to be dependent on its luminosity Pravdo et al. (2001). These factors adversely impact the assumption of a constant $\dot{P}_{\rm spin}$ and subsequently the estimation of $\dot{P}_{\rm orb}$ (Mönkkönen et al., 2020).

Our estimate of the orbital period decay from an independent method using the flare timing signatures in long-term X-ray lightcurves is not affected by the uncertainty of $\dot{P}_{\rm spin}$. Assuming the individual flare peaks are accurate to $\delta t \sim 0.0625$ d, for a time interval of $\Delta t \sim 10^4$ d, an orbital evolution timescale $|t_p| = |P/\dot{P}| \sim$ can be estimated to a precision of $t_p \delta t / \Delta t^2 \times 100 \sim 2\%$ (Eggleton, 2006). However, this technique of $\dot{P}_{\rm orb}$ estimation will depend on the shape of the orbital intensity profile, which has the major contribution from the pre-periastron flare and will be the main contributor to the uncertainty of this technique. Even though not entirely understood, the orbital profile of GX 301–2 is generally explained on the basis of two common models by (i) Pravdo et al. (2001) based on an equatorial circumstellar disc of gas around the companion star and (ii) Haberl (1991) and Leahy and Kostka

(2008) based on a dense stream of matter from the companion following the pulsar. Changes in the properties of the circumstellar disk or the accretion stream can therefore change the shape of the orbital intensity profile. Our analysis is the most accurate if the orbital intensity profile stays the same throughout the long-term data used for the analysis.

Our analysis also suggests the presence of rapid orbital decay. The estimate of orbital period decay is $\dot{P}_{\rm orb} - (1.98 \pm 0.28) \times 10^{-6}$ s s^{-1} corresponding to an orbital evolution time scale of $|P_{\rm orb}/\dot{P}_{\rm orb}| \approx 0.6 \times 10^5$ yr. Our estimate of $\dot{P}_{\rm orb}$ is different from the value reported by Doroshenko, Santangelo, Suleimanov, et al. (2010), which is $-(3.7 \pm 0.5) \times 10^{-6}$ s s^{-1}, by a factor of ~ 2.

Possible reasons for the rapid orbital decay

The observed orbital evolution time scale of $|P_{\rm orb}/\dot{P}_{\rm orb}| \sim 10^5$ years in GX 301–2 is an order of magnitude shorter than the mass loss time scale of the companion of $|M_c/\dot{M}_c| \sim 10^6$ years. Until now, this is the fastest orbital decay ever observed in an HMXB (See Table 5.6). Even though there was a recent report by Shirke et al. (2021) of a much larger orbital decay rate of $|\dot{P}_{\rm orb}/P_{\rm orb}| \sim 10^{-4}$ yr^{-1} in the HMXB Cen X–3, which contradicts previous measurements (Table 5.6), it should be noted that for the pulse time-of-arrival (TOA) analysis, these authors utilized data from only a portion (half) of one orbit, and any intrinsic variations in the pulsar spin rate may have contributed to this disparate result. Disregarding this report, GX 301–2 has exhibited the fastest observed orbital decay among HMXBs, and we are examining potential causes for the observed orbital decay.

The orbital evolution of a binary star system can be described by the changes in its orbital angular momentum and mass transfer (Tauris et al., 2006; Bachetti et al., 2022) as follows

$$\frac{2}{3}\frac{\dot{P}_{\rm orb}}{P_{\rm orb}} = 2\frac{\dot{J}_{\rm orb}}{J_{\rm orb}} - 2\frac{\dot{M}_c}{M_c} - 2\frac{\dot{M}_x}{M_x} + \frac{\dot{M}_c + \dot{M}_x}{M_c + M_x} - 2e\dot{e} \tag{5.2}$$

In equation 5.2, the binary orbital period $P_{\rm orb}$ and its rate of change $\dot{P}_{\rm orb}$ are expressed in terms of the evolution of other binary parameters. $J_{\rm orb}$ and $\dot{J}_{\rm orb}$ are the orbital angular momentum of the binary and its rate of change, respectively, M_c and $\dot{M}_c$ are the companion mass and its rate of change, respectively, and M_x and $\dot{M}_x$ are the NS mass and its rate of change, respectively.

Some of these parameters are known for GX 301–2 (Table 5.5). The observed orbital decay ($\dot{P}_{\rm orb} < 0$) in GX 301–2 could be investigated through equation 5.2, which implies that $\dot{J}_{\rm orb} < 0$, $\dot{e} > 0$ and certain combinations of $\dot{M}_c$, $\dot{M}_x$, M_x and M_c has the potential to cause $\dot{P}_{\rm orb} < 0$. Furthermore, some of these parameters may exert a greater influence on $\dot{P}_{\rm orb}$ compared to the others. A case in point is, although equation 5.2 suggests that $\dot{e} < 0$ can lead to the expansion of the orbit, in HMXBs the opposite happens. This reason could be $\dot{e} < 0$ in HMXBs arises from tidal interactions, which also results in $\dot{J}_{\rm orb} < 0$ which dominates over the $\dot{e}$ term, and causes the orbit to decay instead of expanding.

Our aim is to evaluate three feasible factors that can produce the observed orbital decay in GX 301–2, which are mass transfer from the companion to the NS, mass loss from the binary, and tidal interaction between NS and the companion. The conservation of $J_{\rm orb}$ characterizes the former mechanism, in which the decay of the orbit is driven by mass redistribution. On the other hand, the latter two mechanisms are characterized by loss of $J_{\rm orb}$, leading to the decay of the orbit. Recent simulations of GX 301–2 by Bunzel et al. (2022) do not predict this rapid orbital decay before the Common Envelope phase, but not all of the aforementioned mechanisms were included in their simulations. Although the loss of $J_{\rm orb}$ is possible due to gravitational wave radiation and magnetic braking, they only dominate for orbits that are sufficiently compact, as stated by Heuvel (1994), and hence we do not discuss it further.

Conservative mass transfer

The simplest case is the conservative mass transfer from companion to the NS, where the orbital angular momentum is conserved ($\dot{J}_{\rm orb} = 0$), and eccentricity stays constant ($\dot{e} = 0$). In the scenario of conservative mass transfer, the entire mass lost by the companion is accreted by the neutron star ($-\dot{M}_c = M_x$), and there is no significant alteration of the orbital angular momentum ($\dot{J}_{\rm orb} = 0$).

Substituting the values from Table 5.5 in equation 5.1, the required mass transfer rate (accretion rate) to the NS for attaining the observed orbital decay rate is $\dot{M}_x \sim 8 \times 10^{-6}$ $\mathrm{M}_\odot$ yr^{-1}. This is roughly the mass loss rate from the companion (Table 5.5). However, the Eddington accretion limit for spherical accretion of Hydrogen-rich matter to a canonical 1.4 $\mathrm{M}_\odot$ 10 km radius NS is about 10^{-8} $\mathrm{M}_\odot$ yr^{-1} (Heuvel, 1994), implying only a maximum of 1% of the mass lost by Wray 15-977 could be accreted by the NS even if it is accreting at the Eddington limit. Therefore, conservative mass transfer can't be the primary mechanism driving the observed $\dot{P}_{\rm orb}$ in GX 301–2.

Tab. 5.5: Some reported estimates of GX 301–2 parameters. We use these values to assess various possibilities of the observed orbital decay in Sec. 5.2.3.

Parameter	Value	Reference
$P_{\rm orb}$	41.5 d	Sato et al. (1986)
$\lvert\dot{P}_{\rm orb}/P_{\rm orb}\rvert$	5.52×10^{-13} s^{-1}	This work
	1.74×10^{-5} yr^{-1}	
M_x	1.4 $M_\odot$	Canonical
M_c	50 $M_\odot$	Kaper et al. (1995)
R_c	87 $R_\odot$	Kaper et al. (1995)
i	$\leq 64°$	Kaper et al. (1995)
$a_x \sin i$	159 ± 1.5 $R_\odot$	Sato et al. (1986)
a_x	177 $R\odot$	
e	0.47	Sato et al. (1986)
$\dot{M}_c$	$-(3$ to $10) \times 10^{-6}$ $M_\odot$ yr^{-1}	Parkes et al. (1980); Kaper et al. (1995)
$v_{\rm wind}$	400 km s^{-1}	Parkes et al. (1980)
$v_e \sin i$	55 km s^{-1}	Clark, Najarro, et al. (2012)
v_e	61 km s^{-1}	
$P_c^\dagger$	72 d	

† $P_c = 2\pi R_c / v_e$.

Mass loss from the binary

The efficiency of wind accretion in GX 301–2 could be calculated using the equations $e_{\rm wind} = \pi r_{\rm acc}^2 / 4\pi a_x^2$ and $r_{\rm acc} = GM_x/v_w^2$. Here $e_{\rm wind}$ is the efficiency of wind accretion, v_w is the velocity of stellar wind from companion, and accretion radius $r_{\rm acc}$ is the distance from the NS at which the stellar wind is gravitationally captured. Substituting values for GX 301–2 from Table 5.5 gives the efficiency of wind accretion $e_{\rm wind} \sim 3 \times 10^{-5}$. The unaccreted matter will likely be lost from the binary and contribute to $\dot{J}_{\rm orb}$. A complete consideration of mass loss from the binary makes the estimation of binary evolution a three-body problem (M_x, M_c and the lost mass δM), rendering a general solution difficult. Therefore, certain physically motivated scenarios for loss of mass from the binary (mass loss modes) causing $\dot{J}_{\rm orb}$ viz., Jeans' mode, Isotropic re-emission mode and Intermediate mode (See HUANG 1963 and Heuvel 1994) are usually explored. If the mass loss is the most dominant factor contributing to $\dot{J}_{\rm orb}$, assuming a mass loss to proceed in any of these three mentioned modes, $\dot{J}$ can be expressed as (equation 16.18 in Tauris et al. 2006):

$$\frac{\dot{J}}{J} = \frac{\alpha + \beta q^2 + \delta\gamma(1+q^2)}{1+q} \frac{\dot{M}_c}{M_c} \tag{5.3}$$

$$\dot{M}_x = -(1 - \alpha - \beta - \delta)\dot{M}_c \tag{5.4}$$

where α, β and δ denote the fractions of mass lost from the companion by (i) direct isotropic wind without gravitationally interacting with the NS (Jean's mode), (ii) isotropic ejection after being captured by NS' gravitational field (Isotropic re-emission), and (iii) lost mass overcoming the individual gravitational attractions of companion and NS, and escape through the lagrangian points L_2 or L_3 to form an extended circumbinary ring revolving around the common mass $(M_c + M_x)$ of binary at a radius of $\gamma^2 a_x$ (Intermediate mode), respectively. $q = M_c/M_x$ is the mass ratio and $\epsilon = 1 - \alpha - \beta - \delta$ denotes the fraction of mass accreted.

Individual contributions to orbital evolution due to these three different modes of mass loss could be explored by assigning values for $\alpha, \beta$and δ and using the equations 5.2,5.3 and 5.4, assuming $\dot{e} = 0$.

A direct isotropic wind loss from the companion could be defined by $(\alpha = 1, \beta = \delta = 0)$. If the lost mass has an outward velocity greater than escape velocity, it emulates an instant reduction of the total mass in the binary and hence the gravitational attraction between two stellar components. This leads to expansion of the orbit $(+\dot{P}_{\rm orb})$ instead of the observed orbital decay. Simulations of the wind loss from Wray 15-977 indeed show this physical scenario causing expansion of the orbit in GX 301–2 (Fig. 5 of Bunzel et al. 2022).

Isotropic re-emission from the vicinity of the primary could be defined by $(\alpha = 0, \beta = 1, \delta = 0)$. In this case, the mass lost by the stellar wind from Wray 15-977 is first conservatively captured by the gravitational force of NS and then re-ejected isotropically from the vicinity of NS. The re-emission of matter could occur due to radiation/magnetically driven wind from the neutron star as pointed out by Doroshenko, Santangelo, Suleimanov, et al. (2010). This scenario can lead to orbital decay. Substituting known values from Table 5.5 demonstrates that the observed orbital decay can occur for $\dot{M}_c \sim 9 \times 10^{-6}\ M_\odot$ yr^{-1}. Despite the scenario being considered, it cannot fully account for the observed orbital evolution in GX 301–2 because of the companion's inability to undergo a conservative mass transfer to the NS vicinity due to the poor wind capture efficiency ($e_{\rm wind} << 1$).

Anisotropic mass loss from the companion through L_2 or L_3 resulting in the formation of an extended toroidal ring around the common mass $(M_c + M_x)$ at a distance $\gamma^2 a_x$ from the centre of mass could be defined by $(\alpha = 0, \beta = 0, \delta = 1)$. For $\gamma \gtrapprox 1$, $\dot{M}_c \leq 9 \times 10^{-6}\ M_\odot$ yr^{-1} have the potential to produce the observed orbital decay in GX 301–2.

Although each mass loss mode alone could not be responsible for the observed orbital decay, it is possible that the actual mass ejection mode could be a composite of these idealized modes, and thereby produce the observed orbital decay.

Tidal interaction

Apart from mass-loss from the binary, another dominant mechanism that can contribute to $\dot{J}_{\rm orb}$ is tidal interaction between the NS and the rotating deformable companion in an eccentric binary (Darwin 1879; Lecar et al. 1976). The compact object raises a tide on the surface of the companion. The tide facilitates angular momentum exchange between the rotating companion and the binary orbit and the dissipation of rotational and orbital energies. This results in synchronising the rotation of the companion and binary orbit (tidal synchronization) and circularizing the binary orbit (tidal circularization). If the companion rotation frequency (Ω_c) is less than the binary orbital frequency ($\Omega_{\rm orb}$), the retarding force of tide at the periastron is expected to circularize the orbit and cause orbital decay in the process[7]. The spin angular momentum of the companion will increase at the expense of orbital angular momentum.

A general form of tidal evolution in an HMXB is rather complex which includes invoking dynamical tides that cause oscillating tidal response from the companion (Witte et al., 2001). However, a fairly simple approximation is the weak friction model of the tide which does not include the non-linear tidal dissipation processes (Hut, 1981). Our objective is to comprehend the swift orbital evolution witnessed in GX 301–2 concerning tidal dissipation through the weak friction model. Calculations based on Lecar et al. (1976) and Hut (1981) under the assumption of weak friction model shows that tidal dissipation in the outer convective envelope of Wray 15-977 having a characteristic $\lambda\eta v_{\rm conv} = 2 \times 10^{-4}$ km s^{-1} (λ is the fractional depth of the convective layer of the companion, η is the fractional mass of the convective layer, and $v_{\rm conv}$ is the convective velocity) can cause the observed orbital decay in GX 301–2 (See Appendix 5.2.4 for detailed calculation). Considering the significant mass loss rate of the companion which can cause expansion of the binary orbit, the calculated convective envelope parameters would be a lower limit if tidal dissipation is the lone factor driving orbital decay in GX 301–2.

A complete consideration of the effect of tidal interaction invoking the dynamical tides to estimate the tidal parameters required to produce the observed rapid orbital evolution of GX 301–2 is beyond the scope of this work. However, we refer to the work Lai (1996) which discusses the orbital decay of the young eccentric binary radio

[7] One could grasp in a general sense the tide induced orbital decay, based on the principle of Hohmann orbit for satellite transfer (Hohmann, 1960), even though both phenomena are unrelated

pulsar PSR J0045-7319 having similar binary parameters as GX 301–2 ($P_{\rm orb}\sim 52$ d, $e\sim 0.8$, B-type $M_c\sim 9M_\odot$, $a_x\sim 12R_\odot$) and exhibits a rapid orbital decay of $|P_{\rm orb}/\dot{P}_{\rm orb}|\sim 5\times10^5$ years. Lai (1996) had shown that tidal interaction between the pulsar and a retrograde spinning companion may cause such a rapid orbital decay by invoking dynamical tides.

In binary systems such as GX 301–2, where there exists a significant difference in the mass of the components, with the mass ratio $M_c/M_x\sim 35$, it is possible for the system to undergo a Common Envelope (CE) phase during the later stages of evolution, due to either tidally induced orbital decay or significant Roche lobe overflow. Tidal interactions work towards synchronizing the slow rotation of the star with the fast binary orbit. However, in situations where the companion star is significantly more massive than the neutron star, the latter finds it difficult to spin up the former. An intriguing outcome occurs when $J_{\rm orb}\lesssim 3J_{\rm c}$ (equations 102 and 99 in Heuvel 1994), where the binary orbit continues to shrink, gradually achieving synchronization with the slowly spinning, massive companion, culminating in 'tidal catastrophe' where the neutron star spirals towards the core of the companion and merges.

Assuming an optimal scenario in which the binary orbit synchronises with the companion by the time of circularization, i.e., $\Omega_c=\Omega_{\rm orb}=\Omega$. The relation $3J_{\rm c}/J_{\rm orb}>1$ can be simplified to $3I_{\rm c}/I_{\rm orb}>1$ (See Lecar et al. 1976), where $I_{\rm c}$ and $I_{\rm orb}$ represents the moment of inertia of the companion and binary orbit, respectively, at the later circularized phase. Since the orbital separation is expected to shrink by this time, $I_{\rm orb}\lesssim M_x a_x^2\lesssim 4.4\times10^4\ M_\odot R_\odot^2$. Meanwhile, the companion star is expected to evolve, resulting in an increase in its radius and a decrease in mass due to stellar wind. Assuming $I_{\rm c}\approx M_c R_c^2\approx 40\times10^4\ M_\odot R_\odot^2$. The ratio $3I_{\rm c}/I_{\rm orb}$ is $\gtrsim 30$, indicating unstable orbit post orbit circularization and the possibility of tidal catastrophe.

In the Roche lobe overflow phase, if the NS cannot accept the Roche lobe overflown matter from the companion beyond the Eddington accretion rate, it forms a Common Envelope (CE) surrounding both stars. This CE phase can also result in the spiral in of NS due to frictional drag in the companion's stellar envelope, as proposed by Bunzel et al. (2022) for GX 301–2. The aftereffect of the CE phase could be the ejection of the common envelope and subsequent formation of a binary comprising the already existing neutron star and the companion's He-rich core. However, if the orbital energy lost during spiralling-in is not efficiently converted into mechanical energy and transferred to the envelope for CE ejection, it may instead result in the NS merging with the core of the companion. The resulting unique object has a NS core surrounded by H/He envelope (Heuvel, 1994) and is called Thorne-Żytkow Object

Tab. 5.6: Previous reports of the orbital decay reported for HMXBs in the order of increasing $|\dot{P}_{\rm orb}/P_{\rm orb}|$. The evolution time scale is of the order of the inverse of the second column. The shortest evolution timescale corresponds to GX 301–2 ($\sim 10^5$ yr), and the longest evolution timescale corresponds to OAO 1657–415 ($\sim 10^7$) yr.

Source	$\dot{P}_{\rm orb}/P_{\rm orb}$ (in 10^{-6} yr^{-1})	Reference
OAO 1657–415	-0.0974 ± 0.0078	Jenke et al. (2012)
4U 1700–37	-0.47 ± 0.19	Islam and Paul (2016)
4U 1538–52	-0.95 ± 0.37	Hemphill, Rothschild, Cheatham, et al. (2019)
Cyg X–3	-1.05 ± 0.04	Singh et al. (2002)
LMC X–4	-0.989 ± 0.005	Naik and Paul (2004b)
Cen X–3	-1.799 ± 0.002	Raichur et al. (2010b)
SMC X–1	-3.414 ± 0.003	Raichur et al. (2010b)
GX 301–2	-32.5 ± 4.4	Doroshenko, Santangelo, Suleimanov, et al. (2010)
	-17.4 ± 2.5	This work

(TZO) (Thorne et al., 1977). The same may happen with the Tidal catastrophe as well. GX 301–2 is thus a prospective future TZO candidate.

5.2.4 Appendix

Error estimation by Bootstrap

- In each of the dwell lightcurves used, count-rate in the $i^{\rm th}$ temporal bin c_i was replaced with $c_i + x\sigma_i$, where x is independently randomly sampled from the uniform distribution $\mathcal{U}(-1, 1)$ (See Lutovinov, Tsygankov, and Chernyakova 2012, Boldin et al. 2013 and Raman et al. 2021).
- Using this technique, 1000 sample lightcurves were simulated for each long-term lightcurve and pulsed flux history.
- The best period from each simulated lightcurve was estimated by fitting a `gaussian` to the χ^2 vs $P_{\rm orb}$ plot and retrieving the best-fit `gaussian` centre.
- The mean (μ) and standard deviation (σ) of the distribution of best-fit `gaussian` centres for 1000 simulations from each lightcurve were assigned its $P_{\rm orb}$ and $\Delta P_{\rm orb}$, respectively.

Energy dependence of flares

To assess the energy dependence of the arrival time of pre-periastron flares, we used the overlapping duration of *Swift*/BAT (15–50 keV) lightcurve with *RXTE*/ASM

(1.5–12 keV), *MAXI* (2–20 keV, 2-4 keV, 4–10 keV, 10–20 keV) and *Fermi*/GBM (12–50 keV) (Fig. 5.9), and the overlapping duration of *RXTE*/ASM with *CGRO*/BATSE. BAT and BATSE were selected as reference lightcurves, and the below steps were performed individually for both.

- The overlapping duration between lc_{ref} and each lc_{oth}s were first identified, where lc_{ref} is the refernce lightcurve (BAT or BATSE) and lc_{oth} is the other lightcurve having an overlap with lc_{ref}.

- *xronos* compatible window files were created using the *heasoft* tool *xronwin* to restrict data to the overlap duration.

- In the overlap duration, lc_{ref} and lc_{oth} were folded at an arbitrary reference epoch (T_{fold}) with the average of the orbital periods (P_{orb}) derived from the two lightcurves (Table 5.3).

- The vicinity of the flare in each folded orbital intensity profile was modelled with a `constant+lorentzian` and the centre of `lorentzian` was estimated along with its 2.7σ error. The centre of `lorentzian` is assigned as the phase of flare peak (ϕ_{flare}).

- Number of orbits elapsed since T_{fold} to the middle of each window was estimated by *floor*$((\mathrm{T_{window\text{-}mid}} - 48370.5)/\mathrm{P_{orb}})$. Flare time for i^{th} lightcurve was estimated by $T_{\mathrm{flare,i}} = T_{\mathrm{fold}} + NP_{\mathrm{orb,i}} + P_{\mathrm{orb,i}}\phi_{\mathrm{peak,i}}$.

- The delay ($\Delta T_{\mathrm{flare}}$) between the flare times of reference lightcurve and the other lightcurve was calculated (Table 5.4).

Orbital period derivative from timing signature of the pre-periastron flares

The pulsed histories from BATSE (20–50 keV) and GBM (12–50 keV), and the long-term lightcuves from ASM (1.5–12 keV), BAT (15–50 keV), and MAXI (10–20 keV) were used to estimate the time signature of flare peaks. The steps were followed in the order in which they are listed below:

- Each lightcurve was split into three equal slices (windows) and is folded with the the respective orbital period (Table 5.3) at an the epoch corresponding to the beginning of the window. The idea is to find three representative flare-peak times per lightcurve.

- The maximum SNR for orbital intensity profile was obtained from BAT, where it was also found that `lorentzian` is a better fit to the flare compared to `gaussian` based on weighted variance. Therefore, a `constant+lorentzian` was fit on the folded lightcurve in the vicinity of flare ($\phi_{\rm orb}$), and the centre of the best fit `lorentzian` was assigned the phase of flare peak $\phi_{\rm flare} \pm \Delta\phi_{\rm flare}$.

- Orbital cycles n elapsed since start of the window to the flare peak ($T_{\rm flare}$) in each slice of the lightcurve was estimated by *floor*(($\rm T_{slice\text{-}mid} - 48370.5$)/$\rm P_{orb}$). The flare time was then estimated by $T_{\rm flare} = T_{\rm win\text{-}begin} + nP_{\rm orb} + \phi_{\rm peak}P_{\rm orb}$.

- The data $T_{\rm flare}$ vs n was fitted with a linear function, and the residuals to the best fit linear function were then checked for a quadratic trend indicative of orbital evolution.

Tidal evolution

Under the weak friction model approximation, due to internal frictional properties of companion, the formation of a tidal bulge occurs τ s after the compact object exerts gravitational force to raise it. τ is called the tidal time lag and by this duration, the compact object would have moved a relative angular displacement of $\delta = \tau\sigma$ about the tidal bulge, called the tidal lag angle. This displacement of the tidal bulge relative to the line connecting two stars results in a tidal torque that affects the binary orbit. The tidal time lag (τ) is related to the properties of stellar structure. The degree of response of the binary orbit to the tidal forces is represented by the apsidal motion constant k. $\sigma \approx \Omega_c - \Omega_{\rm orb}$ is the apparent angular velocity of NS relative to the sufrace of companion.

The rate of change of the semi-major axis due to tidal circularization of the binary is given by Hut (1981) as the following equation 5.5

$$\frac{\dot{a}}{a} = \frac{2\dot{P}_{\rm orb}}{3P_{\rm orb}} = -6\frac{k}{T}\dot{q}(1+\dot{q})\left(\frac{R_c}{a}\right)^8 \frac{1}{(1-e^2)^{7.5}}\left[f_1(e^2) - (1-e^2)^{1.5}f_2(e^2)\frac{\Omega_c}{n}\right] \quad (5.5)$$

where,
a and $P_{\rm orb}$ are the semi-major axis and orbital period, and $\dot{a}$ and $\dot{P}_{\rm orb}$ their rate of changes, R_c is the companion radius, e is the binary eccentricity, Ω_c is the rotation frequency of the companion. After substituting the known parameters of GX 301–2 from (Table 5.5),

$$f_1(e^2) = 1 + \frac{31}{2}e^2 + \frac{255}{8}e^4 + \frac{185}{16}e^6 + \frac{25}{64}e^8 \sim 6.1$$

$$f_2(e^2) = 1 + \frac{15}{2}e^2 + \frac{45}{8}e^4 + \frac{5}{16}e^6 \sim 2.9$$

$$n = \sqrt{\frac{G(M_x + M_c)}{a_x^3}} \sim 1.9 \times 10^{-6} \text{ rad s}^{-1}$$

$$\Omega_c = \frac{2\pi}{P_c} \sim 1.01 \times 10^{-6} \text{ rad s}^{-1}$$

$$\grave{q} = \frac{M_x}{M_c} \sim 0.03$$

$$T = \frac{R_c^3}{GM_c\tau} \sim \frac{3.3 \times 10^{10}}{\tau} \text{ s}$$

Substituting in equation 5.5

$$-\frac{2 \times 5.52 \times 10^{-13}}{3} \approx -6\frac{k\tau}{3.3 \times 10^{10}} \times 0.029 \times 0.003 \times 6.5 \times 5.05$$

$$k\tau \approx 0.64 \text{ s}$$

If tidal dissipation is assumed to be facilitated by an outer convective layer around the stellar core of Wray 15-977, equation A1 in Lecar et al. (1976) gives the relation of $k\tau$ to the characteristics of such a convection layer as

$$k\tau \approx 25\ s\frac{\lambda\eta v_{\text{conv}}(\text{km s}^{-1})}{(g/g_\odot)} \tag{5.6}$$

where, λ (fractional depth of convective layer), η (fractional mass of the convective zone) and v_{conv} (convective velocity) define the property of the convective envelope, and

$$\frac{g}{g_\odot} = \frac{(M_c/M_\odot)}{(R_c/R_\odot)^2} \approx 0.007$$

Substituting $k\tau = 0.71$ s in equation 5.6 gives

$$\lambda\eta v_{\text{conv}} \approx 1.68 \times 10^{-4} \text{ km s}^{-1}$$

5.2.5 Summary

In this study, we utilized the recurring pre-periastron flares observed in the long-term X-ray lightcurves of GX 301–2 to measure its orbital period evolution. Our analysis yielded a measured orbital decay timescale of $|\dot{P}_{\text{orb}}/P_{\text{orb}}| \sim 2 \times 10^{-5}$ yr^{-1}, which is currently the shortest known evolution timescale for a high-mass X-ray binary (HMXB). Previous estimates of this decay timescale were based on pulse time-of-arrival (TOA) analysis, which is influenced by the large orbital intensity

variations and spin-up/down fluctuations of the pulsar. Our analysis of the long-term lightcurves, however, relies on the recurring orbital intensity profile, which is independent of the pulse TOA methods. There is a difference of about a factor of two between our estimate and the previous estimate based on pulse TOA analysis. Our estimate is limited by the repeatability of pre-periastron flares and is dependent on the stability and recurrence of the process causing these flares, which is still uncertain. We argue that a combination of distinct mechanisms, such as unique mass loss pathways and/or tidal interaction could be driving this rapid orbital decay.

6 Development of an X-ray Polarimeter

X-ray polarimetry deals with measuring the net linear polarization in the photons emitted by a target astronomical source. An astronomical source is said to be polarized in X-rays with N% degree of polarization if N% of the total photons detected from that source have a net linear polarization direction. The observation technique is to expose a polarization detector to the target source and identify if there is a net polarization direction in the accumulated set of source photons after removing the contribution from background photons. Therefore, X-ray polarimetry requires a large number of source photons to be collected, because of which X-ray polarimetry instruments are often not flown with observatories carrying spectroscopy or timing instruments as the primary payload. Even though observational X-ray astronomy began in the 1960s and the space observatories have consistently improved their spectral, timing and imaging performance, X-ray polarimetry is still in its infancy.

The linear X-ray polarization of Crab Nebula measured at two narrow energy bands centred at 2.6 keV and 5.2 keV, respectively, using a pair of Bragg-reflection-based Stellar X-ray polarimeter instruments onboard the *OSO–8* (The Eighth Orbiting Solar Observatory; Novick, Weisskopf, et al., 1978) marked the beginning of X-ray polarimetry by confirming the Crab nebula to be equally polarized in X-rays (Weisskopf, Cohen, et al., 1976) as it is in Optical and Radio bands from previous observations. Since *OSO–8*, no dedicated satellite-borne polarimetry instrument was flown for about five decades until the recent launch of *Imaging X-ray Timing Explorer (IXPE)* (Weisskopf, Soffitta, et al., 2022) in 2021. *IXPE* commenced its science observations in early 2022 and has been providing interesting results on various astrophysical sources in the wide 2–8 keV band using the onboard Gas Pixel Detectors (GPDs), viz., accreting X-ray pulsars, Blackhole binaries, Supernova remnants, Magnetars, etc. *IXPE* observations revealed energy dependence of polarization in several sources (for e.g., Forsblom et al., 2023, Mushtukov, Tsygankov, et al., 2023, Doroshenko, Poutanen, et al., 2022), signaling the requirement of polarimeters having coverage at energies beyond 2–8 keV. *X-ray Polarimetry Satellite* (*XPoSat*) (Paul, 2022) is an upcoming satellite mission of the Indian Space Research Organization (ISRO) dedicated for X-ray polarimetry in the 8–30 keV spectral band with the onboard

X-ray polarimeter POLIX, and the polarization sensitivity extending up to 50 keV for the brightest sources.

In this chapter, some aspects of the development and assembly of the proportional counter detectors used in POLIX and the tests performed on the Qualification model of the detectors are discussed.

6.1 Formalism and Statistics

X-ray polarimetry could be performed when incoming polarized X-ray photons modulate either the response of a passive element coupled to an X-ray detector or the X-ray detector itself. The output of any X-ray polarimeter is photon counts (C) as a function of azimuthal angle (φ) given by,

$$C(\varphi) = A + B\ cos^2(\varphi - \phi) \tag{6.1}$$

where, $\frac{B}{2A+B}$ is the fractional modulation amplitude and ϕ is the net liner polarization direction of the incident photons (See left panel of Fig. 6.1).

The key factor deciding the sensitivity of an X-ray polarimeter is the strength of this modulation for 100% polarized incident photons, called the modulation factor μ, given by

$$\mu = \left(\frac{C(\varphi)_{max} - C(\varphi)_{min}}{C(\varphi)_{max} + C(\varphi)_{min}}\right)_{100\%\ pol} = \left(\frac{B}{2A+B}\right)_{100\%\ pol} \tag{6.2}$$

An ideal polarimeter will have $\mu = 1$, while a polarimeter insensitive to polarized photons will have $\mu = 0$. A practical polarimeter will have $0 < \mu < 1$. If photons with a fractional polarization (degree of polarization) a_s/μ is incident on a polarimeter having modulation factor μ, it will produce a modulation with fractional modulation amplitude $\frac{B}{2A+B} = a_s$ (Fig. 6.1).

The sensitivity of a polarimeter is expressed based on its ability to distinguish an unpolarized source from a polarized source, called the Minimum Detectable Polarization (MDP). It is expressed as the probability that a polarimeter produces a modulated output when exposed to unpolarized photons. MDP signifies the lowest sensitive degree of polarization that could be reliably measured from a polarimeter. MDP could be motivated in the following way.

If N is the total number of photons incident on the X-ray detector, assuming Poisson counting statistics, the probability of detecting a modulation amplitude $\hat{a}$ and phase angle ϕ from the polarimeter, for a true amplitude a_0 and a true phase $\hat{\phi}$ is given by (Weisskopf, Elsner, et al., 2010),

$$p(a, \phi|\hat{a}, \hat{\phi}) = \frac{a}{\pi\sigma^2} exp\left[-\frac{a^2 + \hat{a}^2 - 2a\hat{a}cos(\phi - \hat{\phi})}{\sigma^2}\right] \tag{6.3}$$

where, $\sigma = \frac{2}{\sqrt{N}}$

If one is interested only in the fractional modulation amplitude a, integrating this bi-variate distribution in a and ϕ over the azimuthal angle ϕ gives the probability of measuring a fractional modulation amplitude a, given the true fractional modulation amplitude $\hat{a}$.

Additionally, a could be contributed by (C_S number of) source photons and (C_B number of) background photons. Therefore, a fractional modulation amplitude only due to source photons (a_s) is defined. a is scaled by a factor of $C_S/(C_S + C_B)$ so that $a_s = a \times (C_S + C_B)/C_S$.

This two-step process of scaling and integration of eq. 6.3 gives the probability distribution of the modulation amplitude (a_s) measured by the polarimeter due to source photons, given a true modulation amplitude from source photons $\hat{a}_s$. The resulting probability distribution takes the form of *Rice distribution* (Elsner et al., 2012) given by,

$$p(a_s|\hat{a}_s) = \frac{a_s}{\sigma_{a_s}^2} exp\left[-\frac{a_s^2 + \hat{a}_s^2}{2\sigma_{a_s}^2}\right] I_0\left[\frac{a_s\hat{a}_s}{\sigma_{a_s}^2}\right] \tag{6.4}$$

where, I_0 is a modified Bessel function of the first kind and order 0, and $\sigma_{a_S} = \sqrt{2(C_s + C_B)}/C_S$.

Substituting $\hat{a}_s = 0$ (unpolarized source) in eq. 6.4 gives the probability distribution of fractional modulation amplitude produced in the polarimeter due to photons from an unpolarized source. This distribution takes the the form of a *Rayleigh distribution* (Elsner et al., 2012) given by

$$p(a_s|\hat{a}_s = 0) \approx \frac{a_s}{\sigma_{a_s}^2} exp\left[-\frac{a_s^2}{2\sigma_{a_s}^2}\right] \tag{6.5}$$

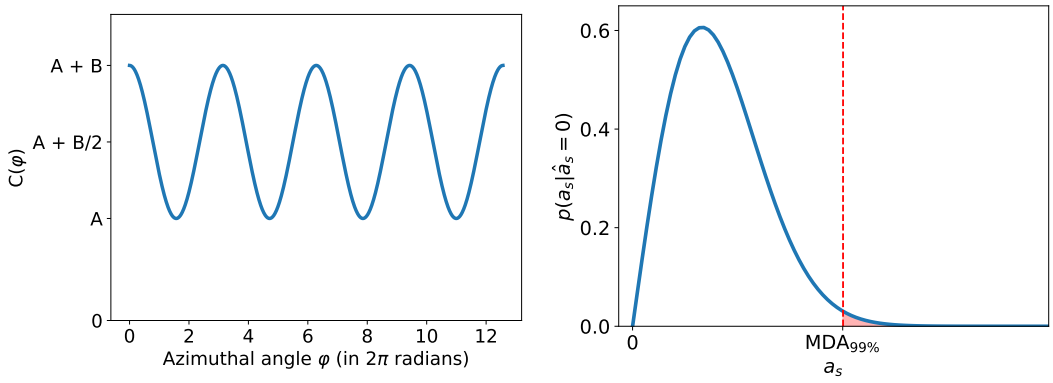

Fig. 6.1: Left: The response of a polarimeter to polarized photons. Right: The probability distribution of modulation amplitude generated in a polarimeter for incident unpolarized source photons. There is always a non-zero chance of getting a modulation for an unpolarized source. The vertical dashed line indicates the observed amplitude (MDA) that has only 1% chance of exceeding. The shaded region indicates 1% probability.

From eq. 6.5 (Fig. 6.1), it is evident that there always exists a non-zero probability for an X-ray polarimeter to produce a non-zero modulation amplitude a_s even for an unpolarized source ($\hat{a}_s = 0$). In such a case, the probability of a_s exceeding a fractional amplitude *MDA* could be given by $\int_{MDA}^{\infty} p(a_s|\hat{a}_s = 0)\, da_s$.

For example, for a polarimeter exposed to unpolarized photons, an amplitude $a_{1\%}$ could be defined such that $\int_{a_{1\%}}^{\infty} p(a_s|\hat{a}_s = 0)\, da_s = 1/100$. This means there exists a 1% probability that the polarimeter produces a modulation amplitude exceeding $a_{1\%}$ for an unpolarized source. Such a polarimeter is said to have a Minimum Detectable (fractional) Amplitude (MDA) of $a_{1\%}$ at $(100 - 1) = 99\%$ confidence level. Inverting this integral with the desired confidence level would give the MDA corresponding to that confidence level. The MDA at 99% ($\sim 3\sigma$) confidence level is given by (Elsner et al., 2012) ,

$$\text{MDA}_{99\%} = \sqrt{-2\ln(1 - 0.99)}\sigma_{a_S} = 3.03\sigma_{a_S} = 4.29\sqrt{C_S + C_B}/C_S \tag{6.6}$$

Subsequently, normalizing MDA by the instrument's modulation factor gives the instrument independent Minimum Detectable Polarization MDP as,

$$\text{MDP}_{99\%} = \text{MDA}_{99\%}/\mu = 4.29\frac{\sqrt{C_S + C_B}}{\mu C_S} \tag{6.7}$$

If the source being observed has a flux of S counts s^{-1} cm^{-2}, and is observed by the instrument having an effective area of A_{eff} cm^2 and efficiency ϵ for a duration of T s, the substitution of parameters in eq. 6.7 yields,

$$MDP_{99\%} = \frac{4.29}{\mu\sqrt{\epsilon S T A_{\text{eff}}}} \tag{6.8}$$

Hence, $MDA_{99\%}$ is the minimum modulation amplitude a polarimeter should produce to claim an $MDP_{99\%}$ degree of polarization in the source at 99% confidence level. This is the figure of merit of an X-ray polarimeter.

The construction of the modulation curve is, therefore, crucial for any polarimeter. The modulation generally takes the cos^2 form (eq. 6.1) (Muleri, 2014), the fractional amplitude ($\frac{B}{2A+B}$) of which gives the information of the degree of polarization and the phase of which (ϕ) gives the information of direction of polarization. The fractional amplitude a is generally proportional to the degree of polarization. The phase (ϕ) could be equal to the angle of polarization for a photoelectron polarimeter but offset by 90° for a Thomson or Compton scattering polarimeter. The parameters A, B, and ϕ are estimated by fitting the observed azimuthal distribution of photons with a function of the form of eq. 6.1, where the noise (background) is expected to be χ^2 distributed with two degrees of freedom (*Rayleigh* distribution) as seen in eq. 6.5. An approach alternate to the construction of modulation curve is also sometimes employed, wherein Stokes parameters I, Q, and U of each event are constructed (Kislat et al., 2015).

6.2 Polarization Detection Techniques

There are different kinds of X-ray polarization detection instruments whose detection technique varies based on the photon energies it is sensitive to (Hubbell, 2003 and Fig. 6.2). The dominant interaction mechanism of photons with the detector material varies from the photo-electric effect in the low energy bands (2–8 keV) to Thomson scattering in the intermediate energy bands (5–50 keV), and Compton scattering in the high energy bands (50–500 keV).

Bragg reflection is a result of the combined effect of coherent scattering processes (individually subdued by the photoelectric effect) at energies below ~ 10 keV. When a photon of wavelength λ is incident on the crystal lattice plane with lattice separation d at an angle θ with respect to the plane, the wavelengths that satisfy $2dsin\theta = n\lambda$ (*Bragg condition*) will get reflected. Bragg reflectors act as good polarimeters because

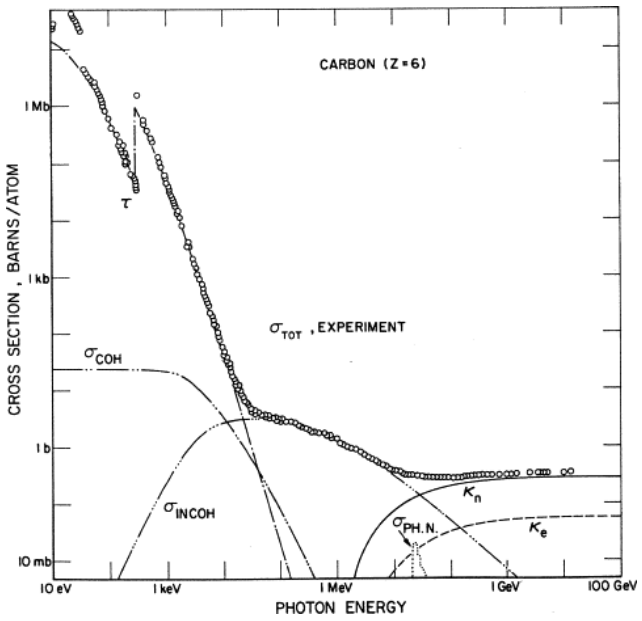

Fig. 6.2: Constituents of photon interaction cross-section on Carbon. The lowest energies are dominated by photo-electric absorption and a little contribution from coherent scattering (Rayleigh), the middle energies are dominated by Compton scattering and higher energies by pair production. (Fig. credits: Hubbell, 2003)

P-polarized X-ray photons incident at Brewster's angle are not reflected by the crystal, while the S-polarized photons are reflected by the crystal. Bragg polarimeters are constructed such that the angle of the X-ray photons that satisfies the *Bragg condition* on the crystal is close to Brewster's angle ($\sim 45°$) (Kaaret, 2021). The first successful X-ray polarimeter for observing non-solar objects was a Bragg polarimeter onboard a sounding rocket (Weisskopf, Berthelsdorf, et al., 1972), which hosted four Graphite crystals inclined at $45°$ to the pointing axis. The scattered photons were detected by the Xenon-filled multi-wire proportional counter at the centre and the instrument was rotated about the viewing axis. This polarimeter successfully measured the polarization from the Crab Nebula, establishing the Synchrotron origin of its X-ray emission. Two orthogonal Graphite crystal polarimeters were flown onboard the *Eighth Orbitting Solar Observatory* (*OSO–8*) (Novick, Weisskopf, et al., 1978), which operated at two energies of 2.6 keV and 5.2 keV. Graphite crystals with parabolic reflection surfaces were used on them, which resulted in the Bragg angle varying between 30-40° and μ to a slightly lower value of $\sim 93\%$. The reflected photons were registered by a gas-proportional counter X-ray detector, and rotation of the crystal-detector assembly about the viewing axis to the source gave the modulation curve (eq. 6.1). The benefit of Bragg X-ray polarimeters are the large modulation factors (μ) (eq. 6.2) that they provide, which goes beyond 90%. However, they

suffer from the drawback that they only operate with monochromatic photons of energies $nhc/2dsin\ \theta$ and their efficiency of scattering is usually less than 50%.

The most dominant photon interaction mechanism below 10 keV is the photoelectric effect. In photo-electric polarimeters, the absorption of a photon in the X-ray detector causes a photo-electron to be ejected along the direction of the polarization vector of the interacting photon. In photo-electric interaction, an electron from the innermost shell is ejected along the electric field direction with a kinetic energy equal to the difference between the incident photon energy and binding energy of the electron. The inner shell electron is ejected at an angle θ with a velocity $c\beta$ and azimuthal angle ϕ between the electron direction and polarization vector with a probability given by the photoelectric cross section (Costa et al., 2001) given by

$$\frac{d\sigma}{d\Omega} \propto \frac{\sin^2\theta\cos^2\phi}{(1-\beta\cos\theta)^4} \tag{6.9}$$

The photoelectron is most likely to be ejected along $\phi = 0°$ (eq. 6.9), i.e., in the direction of the polarization vector. Identifying the direction of the ejected photo-electron is therefore useful to identify the polarization vector of the incident photon, and this is performed by imaging the photoelectron track. The photoelectrons should make sufficiently long tracks to construct the modulation curve but longer paths also suffer diffusion due to multiple scatterings, reducing the modulation factor. The photoelectron generally dumps little energy at the initial interaction point and the majority of the energy at the final termination point. The photoelectron track should be longer than the pixel size of the detector, because of which gas detectors like GPD are preferred over solid-state detectors. A high Z gas gives more quantum efficiency, but to trigger the innermost shell, the K-shell binding energy should be greater than the lower limit of operation (~ 2 keV), which limits the Z. The Gas Electron Multiplier is a gas detector in which the electrons forming the track are drifted to the collecting anode pixels by applying electric fields parallel to the incident photons (Costa et al., 2001) or perpendicular to the incident photons (Black et al., 2004). Due to their broadband operability, photoelectric polarimeters are preferred in the 2–8 keV band, however, the modulation factor is affected by Auger electrons that are released from the photoelectron origin site. The modulation factor μ of photoelectric polarimeters is $< 50\%$, while it is close to unity for Bragg polarimeters. The three Gas Pixel Detector (GPD) (Soffitta et al., 2021) instruments onboard the *Imaging X-ray Polarimeter Explorer* (Weisskopf, Ramsey, et al., 2016) operating in 2–8 keV, uses three X-ray telescopes of Wolter-I geometry with focal length 4 m to focus X-rays into the GPDs and image the photo-electron tracks to extract the polarization information.

The dominant photon interaction mechanism in ~ 50 keV to ~ 1 MeV (hard X-rays and soft γ-rays) is Compton Scattering and Compton polarimeters are therefore preferred in this energy band. The Compton scattering cross-section for a free electron is given by the Klein-Nishina formula

$$\frac{d\sigma}{d\Omega} \propto \left(\frac{E}{E'}\right)\left(\frac{E}{E'} + \frac{E'}{E} - 2\sin^2\theta\cos^2\phi\right) \tag{6.10}$$

The Compton scattered photons have a higher probability of being scattered in a direction perpendicular to the polarization vector ($\phi = 90°$ in eq. 6.10). Therefore, identifying the direction of the scattered photons provides information on the incident photon polarization. However, Compton scattering is inelastic and some energy of the incident photon of energy E_γ is transferred to the interacting election after scattering. Therefore, it is important to measure the energy lost by the incident photon to the interacting electron. The energy lost by a photon after scattered by an angle θ is given by

$$\delta E = E_\gamma \left(\frac{\frac{E_\gamma}{m_e c^2}(1 - cos\ \theta)}{1\ +\ \frac{E_\gamma}{m_e c^2}(1 - cos\ \theta)}\right)$$

For instance, for an incident photon of energy E_γ 100 keV scattering at an angle of 20°, the energy loss δE is ~ 1.2 keV.

Compton polarimeters work with dual events: a Compton scattering event in which some energy of the photon is dumped and a detection event in which the scattered photon is absorbed by the detector (Del Monte et al., 2023). The direction of polarization is assessed from the direction of the photon assessed from the Compton interaction point and detection point of the scattered photon. Even though no dedicated polarimetry satellite missions exploiting Compton scattering have been flown until now, some Solid-state detectors developed for imaging purposes have been successfully utilized to extract polarization information for some bright sources with the Compton scattering technique. The *INTEGRAL*/IBIS (Stephen et al., 2001) used CdTe Solid-state ISGRI detectors to Compton scatter and PiCsIT CsI Scintillation detectors to detect the scattered photons. *Astrosat*/CZTI (Chattopadhyay et al., 2014) made with pixelated CdZnTe detectors employed the technique of using a set of neighboring pixels to capture the double event and detect the polarization. *INTEGRAL*/IBIS and *Astrosat*/CZTI detected the polarization of the Crab pulsar above 200 keV and 100 keV respectively (See Forot et al., 2008 and Vadawale et al., 2018).

In the limit of $E_\gamma \ll m_e c^2$ (511 keV), the energy lost in the Compton interaction δE is almost equal to 0 (eq. 6.11), and it is called Thomson scattering. The requirement of Thomson polarimeters is to record the distribution of Thomson scattered photons. Thomson scattering polarimeters are similar to Compton scattering polarimeters but without the additional requirement of an active scattering element, as it is an elastic scattering approximation. Thomson scattering polarimeters employ a passive scattering element (low Z material to suppress photoelectric absorption) that scatters the photons and exploits the characteristic that Thomson scattering is preferentially in a direction orthogonal to the polarization ($\phi = 90°$ in eq. 6.10). The first ever X-ray polarimeter for a non-solar source was flown on a sounding rocket, and it was a Lithium scattering Thomson polarimeter (Novick and Wolff, 1971), however, it was unsuccessful in detecting polarization from Sco X-1. Another Thomson scattering polarimeter Stellar X-ray Polarimeter (SXRP) (Kaaret et al., 1990) was developed for a Soviet Union mission that was later cancelled. *X-ray Polarimetry Satellite* (*XPoSat*) (Paul, 2022) is an upcoming satellite mission of the Indian Space Research Organization (ISRO) dedicated for X-ray polarimetry. The primary scientific instrument onboard *XPoSat* is the Thomson scattering-based X-ray polarimeter called the **I**ndian **X**-ray **Pol**arimeter (POLIX) operating in the 8–30 keV energy band. Thomson scattering polarimeters suffer from the drawback of loss of photons due to photoelectric absorption at low energies. Also, since the original Thomson scattering interaction is lost due to the passive scattering element, imaging could not be achieved with Thomson polarimeters, limiting their sensitivity to only bright sources. An artistic rendering of *XPoSat* is shown in Fig. 6.3. In addition to POLIX, *XPoSat* hosts a timing and spectroscopy capable Swept-charge CCD-based instrument called X-ray Spectroscopy and Timing (XSPECT). XPECT will view the same source as POLIX and capture the timing and spectral properties of the source photons throughout the relatively long exposures of POLIX.

6.3 Indian X-ray Polarimter (POLIX)

POLIX is the Thomson scattering X-ray polarimeter instrument onboard *XPoSat*. POLIX uses the combination of a collimator that restricts the field of view of the instrument to $3° \times 3°$, a passive Beryllium scattering block that facilitates Thomson scattering, and four proportional counters surrounding the scattering block to measure the degree and direction of linear polarization of the incident photon beam. The low Z Beryllium scatter suppresses photo-electric absorption, thereby fostering Thomson scattering. The azimuthal distribution of scattered photons $C(\varphi)$ measured

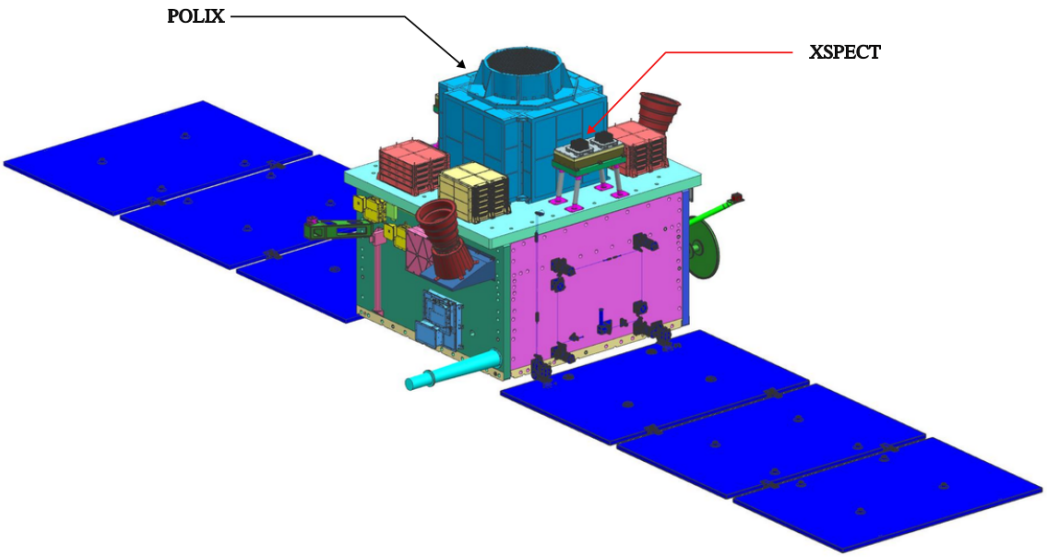

Fig. 6.3: An artistic rendering of the *X-ray Polarimetry Satellite* (*XPoSat*) (Figure credits: ISRO)

by POLIX for a photon beam having $B/(2A+B)$ fraction of polarized photons with a net polarization angle ϕ takes the form

$$C(\varphi) = A \ + \ B \ sin^2(\varphi - \phi) \tag{6.11}$$

The satellite is spun about the viewing axis of POLIX at a nominal rotation rate of 0.2 rpm so that each detector samples the entire azimuth span. The azimuthal distribution of photons could be reconstructed if the time of arrival of each scattered photon on the detector and satellite spin state is known. An illustration of the operation of POLIX is shown in Fig. 6.5. The relevant technical specifications of POLIX are given in Table 6.1. The assembled POLIX instrument is shown in Fig. 6.4. In this thesis, the fabrication and assembly of the proportional counters, and some functionality and environmental tests that were performed on the *Qualification model* (*QM*) gas-filled proportional counters of POLIX are described in detail.

6.4 X-ray detectors of POLIX

A quad-proportional counters setup forms the photon counting unit of azimuthal distribution C(φ) of the scattered photons around the Beryllium scatterer. The large photon collection areas offered by the proportional counters make them suitable to intercept a good fraction of the scattered photons. A proportional counter is a

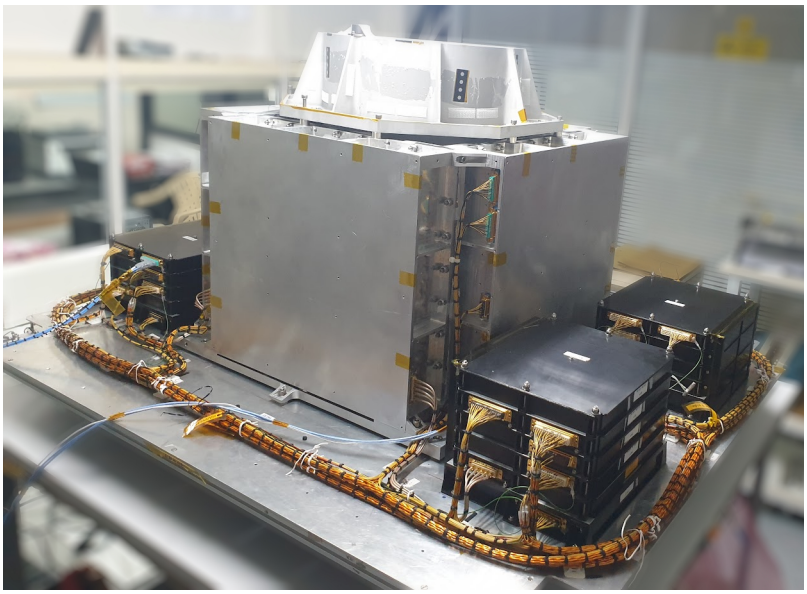

Fig. 6.4: Assembled POLIX instrument at the laboratory. At the top is the Aluminium Collimator, a Beryllium Scatterer is placed below the collimator (not visible), and surrounded by four Gas-filled Proportional counters (two of them visible). Four Back-end electronics packages are placed on the sides (three visible).

Paramter	Value/Description
Type	Thomson Polarimter
Energy range	8–30 keV
Field of View	$3^\circ \times 3^\circ$
Scattering element	Beryllium
Scattering efficiency	<3 %
Photon collection area[a]	640 cm^2
Detector type	Proportional counters
Detector gas mixture	90% Xenon + 9% Argon + 1% Methane
Detector gas pressure	800 Torr
Modulation factor[b] (μ)	~ 0.4
Satellite spin rate	0.2 rpm
Duty cycle	< 30

[a] Considering both the Collimator and Scattering elements.
[b] For 100% polarized source.

Tab. 6.1: Technical specifications of POLIX.

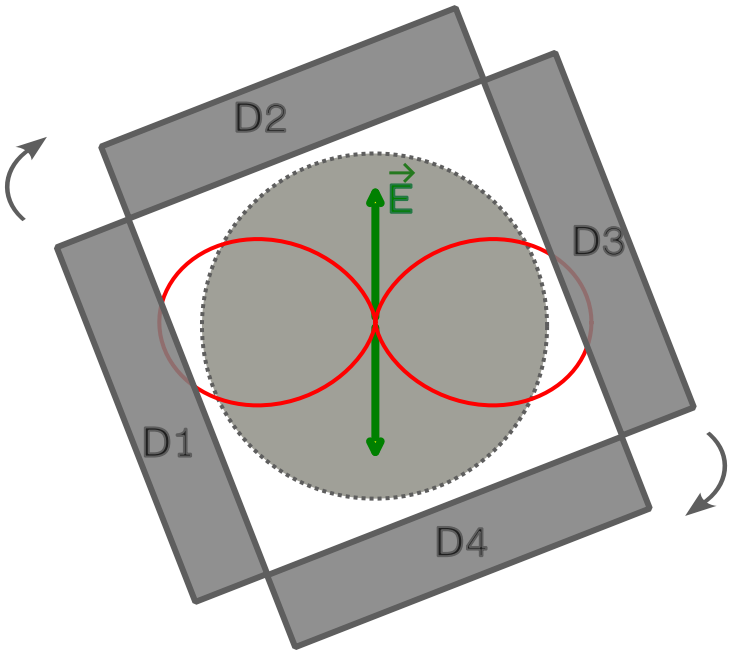

Fig. 6.5: Figure showing the principle of operation of POLIX. Shown is the top view of POLIX along *XPoSat*'s viewing axis. Polarized photons having electric field $\vec{E}$ in two opposite directions, indicated by the green arrows, is incident on the dotted circular shaded Beryllium scattering element. The resulting distribution of scattered photons is shown with the red dipole envelope. Four proportional counters (D1, D2, D3 and D4) individually measure the azimuthal distribution of the scattered photons when the satellite is spun about the viewing axis of POLIX.

sealed grounded box of inert gas having thin anode wires that carry high voltages. X-ray/γ-ray photons and charged particles that carry enough energy to ionize the atoms are absorbed in the gas, resulting in the generation of electron-ion pairs. The generated electrons are drifted towards the anode wires by applying electric fields, causing *Townsend avalanche* and the formation of secondary electrons (providing an in-built signal amplification), which are then converted to a voltage pulse. The voltage pulse is processed to assess the time of arrival of the event and the energy of the incident photon.

6.4.1 Design of POLIX's proportional counters

POLIX uses four single-layer multi-wire proportional counters and each of them has four major mechanical parts. It has a uni-body five-wall cuboid Aluminium housing forming five sides of the gas-containing volume. A high tensile strength 50 μm thick polyester film, made of the Polyethylene Terephthalate (PET) material, called Mylar® is fixed on the sixth side of the cuboid housing. One side of the Mylar®

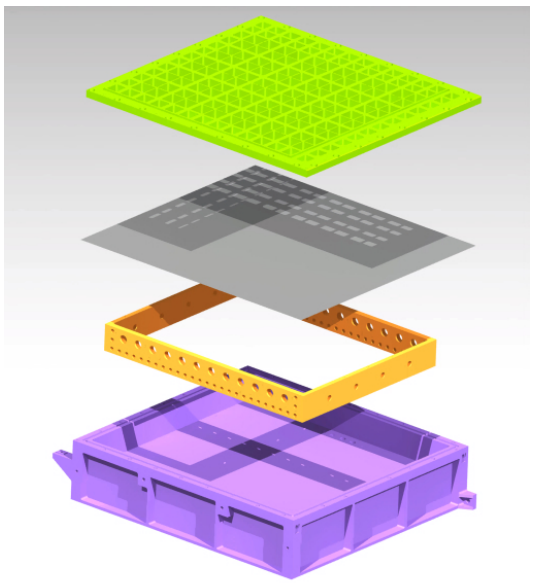

Fig. 6.6: Exploded view of a POLIX proportional counter showing its main mechanical components. From bottom to top is the proportional counter housing, Wireframe, Mylar® window, and the window support plate. (Fig. credits: Rishin PV)

is vapour deposited with a very thin layer of Aluminium. The Mylar® is fixed to the Aluminum housing such that the Aluminized side of Mylar® window faces the housing. A solid aluminium top plate having openings for entry of X-ray photons is also attached to provide mechanical support to the Mylar® window against the gas pressure. The Mylar® window is sandwiched between two Viton™ O-rings; one attached to housing and one to the top plate to make it air-tight. This creates an airtight enclosure of dimensions $45 \times 42 \times 4.5$ cm^3 with six conductive inner walls to contain the required inert gas mixture. The Mylar® facilitates an entry window of X-ray photons into the gas chamber, thereby deciding the low energy threshold of the X-ray detectors. The wireframe that holds the high voltage carrying main anode wires and grounded cathode wires is fixed to the wall of the Aluminium housing opposite to the Mylar window. An exploded view of the proportional counter used in POLIX, indicating its mechanical parts, is shown in Fig. 6.6. The proportional counter volume consists of twelve main anode cells and fifty veto anode cells as a consequence of the design of the wireframe (Fig. 6.7).

The proportional counters were filled with a gas mixture of 90% Xe, 9% Ar, and 1% CH_4 at 800 Torr (1.05 atm) pressure. The proportional counter has to hold the gas mixture for several years, starting right after filling to the launch and the subsequent post-launch period. The proportional counters were therefore validated for any leak below a threshold. The threshold was decided such that the gas gain (eq. 6.14) remains reasonable during the operation of POLIX. We, therefore, performed a

three-step leak test on each proportional counter comprising of a Helium-based mass spectrometer leak detector leak test, a positive pressure exposing proportional counter walls to the pressure gradient in space vacuum conditions, and finally by monitoring the gas gain (Refer Secion 6.4.5). The detectors were qualified for flight after successfully passing all three tests for gas leak.

6.4.2 Photon interaction in the Gas Mixture

The principal interaction mechanism of X-rays within the gas mixture of proportional counters is photoelectric absorption. In this type of interaction, the incident photon of energy E_γ interacts with a bounded electron of the absorber atom, ionizing the atom by ejecting the bound electron. The photon disappears in the process, and the ejected photoelectron carries an energy of $E_{\rm PE} = E_\gamma - E_b$, where E_b is the binding energy of the bound electron. The rough expression for the probability of photoelectric absorption of a photon with energy E_γ by an atom with the atomic number Z is given by (Knoll, 2010)

$$\tau \propto \frac{Z^4}{E_\gamma^{3.5}} \tag{6.12}$$

The photoelectric absorption mechanism is enhanced for soft photons (low E_γ) and absorbers with higher atomic numbers (Z). For this reason, proportional counter photon detection chambers are generally filled with high Z inert gases, Xenon ($Z = 54$) in the case of POLIX. If the photons are energetic enough, it is most likely to interact with the innermost K-shell electron, and if not, they may interact with the L-shell electron, etc.

Even though an X-ray photon interacting with the detector gas creates a photo electron via photoelectric absorption which subsequently creates many electron-ion pairs by ionization, the entire kinetic energy of the photoelectron is not utilized for further ionization, some energy is also lost to other processes like excitation and scattering. It is found from experiments that, on average, an electron-ion pair is generated in the gas for the energy of about 25-35 eV dumped by the photon in the gas (called the W-value), irrespective of the used gas mixture. Therefore, a photon of energy E_γ, on average, produces ($\sim E_\gamma/W$-value) numbers of 'primary' electron-ion pairs.

Registering these 'primary' charge carriers is the key requirement for an X-ray photon detector, as their number is proportional to the photon energy. An electric field

is applied to drift these charged particles to a collection electrode. Due to their higher mobility (about 1000 times that of an ion), the electrons acquire larger drift velocities and could be collected in a short time scale (about 10000 times smaller than that of an ion, a few μs for a few cms distance). The electrons accelerate to very high kinetic energies when the electric field is maintained sufficiently high ($\sim 10^6$ V/m) such that the subsequent electron-atom collisions are sufficient to ionize the colliding atom. This multiplication of charge continues in cascade and is called *Townsend Avalanche* multiplication, effectively amplifying the signal. In order for the electrons to gain sufficient kinetic energy between the collisions, a long mean free path is maintained by mixing low Z gases (Argon in POLIX) with the primary high Z (Xe in POLIX) noble gas.

To maintain the proportionality between E_γ and the total charge collected by the anode, the proportional counters are specially designed such that all the primary electrons are uniformly multiplied. An electric field is applied with cylindrical geometry so that the electric field decreases as a function of radial distance from the anode wire. The electric field at a radial distance r from the anode wire of thickness b units and the grounded cathode layer a distance away is given by Knoll (2010)

$$E(r) = \frac{V}{r \ln(b/a)} \tag{6.13}$$

This ensures that the electrons experience electric fields (10^6 V/m) suitable for multiplication only within the vicinity (within a few b) of the anode wire. Additionally, by using a thin anode wire ($b/a \sim 10^{-3}$), an applied voltage of the order of 10^3 V could provide high electric fields (10^6 V/m) required for multiplication, thus eliminating the need for unfeasible high voltages.

The gas multiplication achieved in a proportional counter is expressed as '*gas multiplication factor*' or '*gas gain*'. The *gas multiplication factor (M)* for a proportional counter with cylindrical geometry could be expressed as a function of the physical conditions. The assumed conditions are an applied anode voltage V, gas pressure p, thickness of anode wire a, anode cell size b, the required E/p threshold for gas multiplication K, and that an electron moves through an average potential difference of ΔV between successive ionizations. Assuming the avalanche only proceeds through collisions by electrons and the generated ions are less in number to not alter the applied electric field, M is given by (Knoll, 2010)

$$M = \exp\left[\frac{V}{\ln(b/a)} \frac{\ln 2}{\Delta V}\left(\ln\frac{V}{pa \ln(b/a)} - \ln K\right)\right] \tag{6.14}$$

The electron multiplication is quenched when all the electrons are finally collected by the anode, but the less mobile ions gradually reach the cathode and neutralize by gaining electrons, which can result in the emission of UV photons. Such stray emissions could cause further ionizations and subsequent avalanches, resulting in stray detections and instrument dead time. Organic poly-atomic 'quench' gases are included in the gas mixture to prevent this. Quench gas molecules have weaker electron affinity and they either collisionally de-excite the ions or absorb the re-combination photons, and dissociate into Carbon in the process, quenching further generation of electron-ion pairs. 1% v/v of Methane (CH_4) is used as a quenching gas in the proportional counters of POLIX.

6.4.3 Exploiting Charge Division for Position Sensitivity

The wireframe is designed such that twelve different anode wires are separated by the boundary of grounded cathode wires, and fifty anti-anode wires surround the main anodes (Fig. 6.7). The aluminized wall of the Mylar® and the aluminium housing are also grounded. The wireframe, aluminized Mylar® window, and the aluminum housing divide the gas-containing volume into twelve main anode cells for photon detection and fifty veto cells for rejection of charged particle background. Six main anodes in the wireframe are serially wired such that each detector contains two separate *detector channels* (*Ch*0 and *Ch*1), each constituted by six main anode cells (Fig. 6.7). Two event processing electronics units (Charge Sensitive Pre-Amplifier (CSPA) and a Peak Detector) are located at either end of each *detector channel* and high voltage is applied to each *detector channel*. A Mylar® window side view of the proportional counter illustrating the six anode cells of a *detector channel* is shown in Fig. 6.8. The detectors are arranged around the Beryllium scatter such that each main anode cell in a proportional counter sits vertically with respect to the scatterer azimuth plane and spans about a 7.5° azimuth bin. Spinning the satellite at 0.2 rpm ensures that each anode cell of the proportional counter covers the whole 360° azimuth in 5 minutes. Provided the anode cell in which the photon has been detected is known, using the timestamps of each event and the rotational status of the satellite, one could construct the entire azimuthal distribution of Thomson scattered photons from each anode cell. By appropriately phase-shifting and adding the distributions from multiple anode cells, the net azimuthal distribution of scattered photons $C(\varphi)$ having the functional form eq. 6.11 could be constructed with improved quality.

The key functional requirement for the POLIX proportional counters other than the time of arrival and energy of scattered photons is therefore, the determination of the

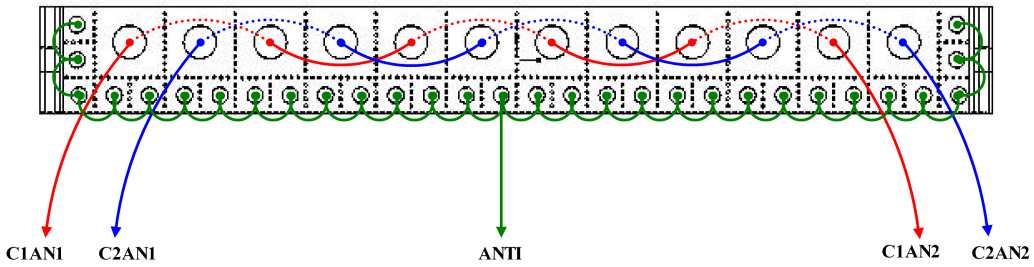

Fig. 6.7: Schematic diagram of the wireframe showing its front view. Twelve anode cells are divided into two channels, and each channel is made by connecting six alternate anode cells in series (two separate channels are shown in red and blue colors). Fifty anode cells are connected in series (green). (Fig. credits: Rishin PV)

anode cell on which the photon was incident, called the position resolving capability. Position resolution is achieved by a technique called *'charge division'*.

A photon scattered from the Beryllium disk towards the anode cell passes through the Mylar® window and dumps its energy E_γ in an anode cell (Sec. 6.4.1) by photoelectric absorption (Sec. 6.4.2). The primary electrons released in the gas are accelerated towards the HV-supplied anode wire, resulting in gas multiplication en route. The multiplied electrons amounting to a total charge of Q units ($\propto E_\gamma$) are collected at a tiny length of the anode wire. Since the anode wire makes one part of a detector channel comprising six anode wires, the total charge Q splits up and travels to either end of the *detector channel*. A fraction of the total charge q_1 reaches one end, while the other fraction $q_2 = Q - q_1$ reaches the other end depending on the electrical resistance experienced along the path. For a detector channel made of six wires having uniform resistivity, this means that the fractional charge reaching either end of the channel depends on the lengths it has to travel, l_1 and l_2 (See the illustration in Fig. 6.9).

Therefore, the anode cell of X-ray photon incidence could be estimated by assessing the fractional charge q_1 or q_2 reaching either end of the detector channel, giving POLIX the required position sensitivity. The CSPA connected to either end of each *detector channel* takes charge q_1 and q_2 as input and outputs a voltage pulse, the amplitude of which is proportional to q_1 and q_2, respectively. The CSPA is followed by an electronic peak detector at either end to extract the peak value of the voltage pulse V_1 and V_2. The voltage peak is digitized by a 12-bit Analog-to-Digital converter (ADC) to one out of 0-4095 discrete pulse height amplitude levels (PHA). The discrete PHA from one end of the *detector channel* is named PAN_1 ($\propto V_1 \propto q_1$), the other end is named PAN_2 ($\propto V_2 \propto q_2$). The sum $\text{PAN}_1 + \text{PAN}_2 = \text{PAN}_{12}$ signifies the energy of the absorbed photon ($\propto V_1 + V_2 \propto Q \propto E_\gamma$). The fractional charge $q2/Q$

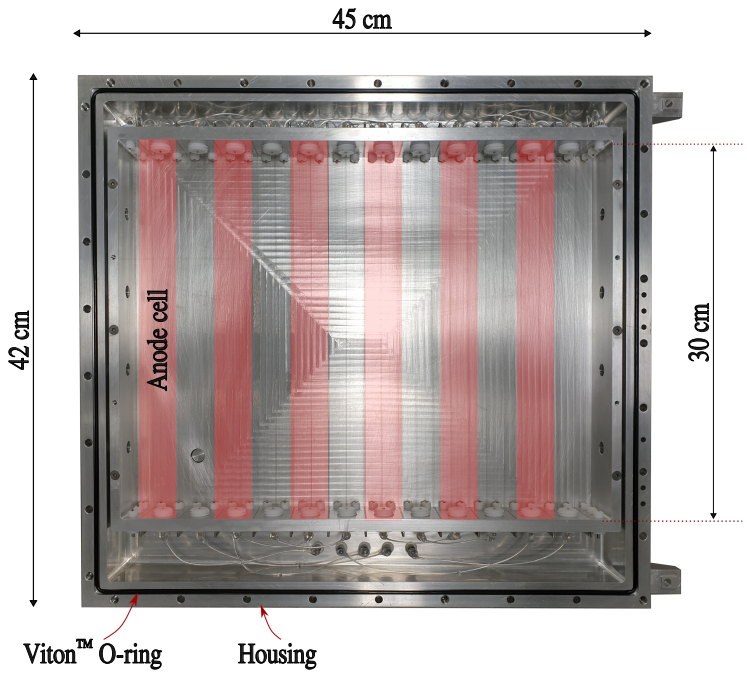

Fig. 6.8: A wireframe fixed inside the proportional counter housing. The six vertical anode cells highlighted in red colour form one detector channel. To close the detector, the Mylar® window and window support plate are attached on this side.

indicative of the position of photon incidence is assessed through the ratio given by

$$r = \frac{\mathrm{PAN}_2}{\mathrm{PAN}_{12}} = \frac{\mathrm{PAN}_2}{\mathrm{PAN}_1 \ + \ \mathrm{PAN}_2} \tag{6.15}$$

Calibrating the ratio r against known locations on the detector is the key principle behind position sensitivity. Since estimating the charges q_1 and q_2 are crucial for the operation, the anode wires used in the wireframes are made of high resistivity Nichrome alloy material, providing a resistance of $600 - 700\Omega$ for each unit of an anode cell (30 cms). The resistive wires minimize thermal noise on the readout, improving the estimation of $q1$ and $q2$ and consequently improving the position sensitivity.

Surrounding the anode cells on all sides except the Mylar® side are 30 anti-anode cells, acting as an active anti-coincidence shield for rejection of charged particle background. The principle of operation of anti-coincidence cells is the same as that of the photon-detecting anode cells, without the requirement of position sensitivity. All 30 anti-coincidence cells are connected in series, working as a single detector channel. Unlike photons, the charged particles that enter the gas chamber are

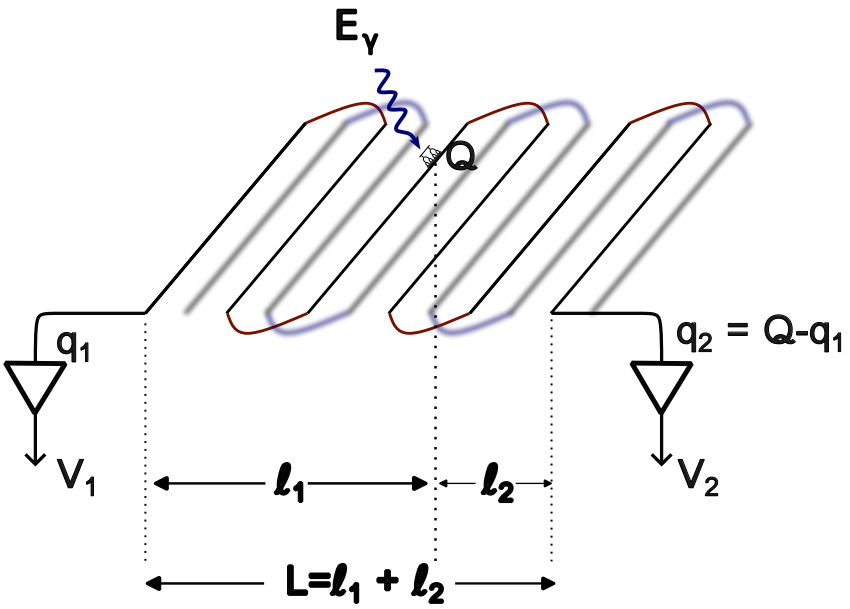

Fig. 6.9: The figure illustrates the principle of charge division which is exploited to achieve position sensitivity in the proportional counters of POLIX. A photon of energy $h\nu$ deposits its energy in one anode cell of the proportional counter, which is a part of one detector channel, and the subsequent gas multiplied electrons amounting to a total charge of Q units are collected by the high voltage anode wire. The charge collected by the anode travels to either end of the channel, and the total charge reaching either end of the wire is inversely proportional to the distance it travels to either end l_1 and l_2. The charge is converted to a voltage pulse by a CSPA, and the height of the voltage pulse is identified.

expected to produce long ionization tracks, triggering both the anode and anti-coincidence cells simultaneously. A simultaneous signal trigger in the anode and anti-anode cell is leveraged to reject charged particle backgrounds using event selection logic implemented in an onboard Field Programmable Gate Array (FPGA). Gold-coated stainless steel wires (resistance of $\sim 50\Omega$ per 30 cm long anti-anode cell) are used as anti-anodes, and they are not capable of position-sensitivity

6.4.4 Gas gain stability tests

Monitoring the gas gain (eq. 6.14) is a way of assessing the performance of the proportional counters. Gas gain is deduced by recording the spectral response of proportional counter to known mono-energetic photons. Any anomalous shift in the gas gain is indicative of the poor performance of the detector.

We used two radioactive sources ^{55}Fe and ^{109}Cd for the *gas gain* stability tests of the proportional counters of POLIX. ^{55}Fe is a radioactive isotope of iron, manufactured by bombarding ^{56}Fe or ^{54}Fe with neutrons. ^{55}Fe has a half-life of 2.7 years and it decays into ^{55}Mn by electron capture. During the decay, the nucleus of ^{55}Fe captures an electron from its innermost K-shell, converting a proton into a neutron in the process. The vacancy left in the K-shell is filled by the de-excitation of an outer shell electron, and the energy difference is liberated either as an Auger electron or an X-ray photon. The most probable photons emitted are the $K\alpha 1$ and $K\alpha 2$ X-ray photons, both having energies very near to 5.9 keV. ^{109}Cd is a radioactive isotope of cadmium which decays by electron capture to ^{109}Ag, emitting a 22.1 keV photon in the process. ^{109}Cd has a half-life of 1.3 years.

One of the applications of the *gas gain* stability test was to test the performance of a flexible sealant called Room-temperature vulcanizing (RTV) Silicon, which is required to reinforce the solder joints of the wireframe. The RTV Silicone (DOWSIL™ 732) is a runny viscous semi-solid material, which, when applied to a metallic surface and exposed to sufficient humidity, cures and adheres to the metallic surface, transforming into a high tensile strength (resistant to ~ 300 psi) sealant. The RTV sealant, however, was known to produce a small amount of acetic acid as a byproduct upon curing. Any extra compound or out-gassing produced by the sealant during its application or curing may deteriorate the gas mixture used in the proportional counter, thereby affecting the gas gain. The RTV sealant was therefore tested for any impact on the gas gain by applying it on a test wireframe and monitoring the gas gain of the assembled detector for a few weeks.

The ^{55}Fe source was shined at the detector for a preset duration, and the distribution of pulse heights (PAN_{12}) of the recorded events was generated. The sum $PAN_1+PAN_2=PAN_{12}$ of each event is proportional to the energy of the incident photon (See Sec. 6.4.3). For a large number of photons, the histogram of PAN_{12} is expected to peak around a value corresponding to 5.9 keV. The peak of the distribution of PAN_{12} was estimated by simple curve fitting with a `gaussian` model (Fig. 6.10a). The gas gain is tracked by monitoring the change in response of the detector ($PAN_{12-55Fe}$) to these 5.9 keV photons. The spectral response of the detector was monitored for eight days, and the peak PAN_{12} was observed to decrease over time, indicative of a reduction in the gas gain (Fig. 6.10b). However, the entire detector was exposed to atmospheric conditions throughout the exercise, resulting in water vapour molecules, which have electron affinity, in the atmosphere diffusing into the detector chamber through the Mylar® window, and the reduction in gas gain could be caused by water vapour contamination rather than RTV outgassing. This is because the Mylar® window is permeable to water vapour molecules, even though it holds the filled gas inside the chamber without leaking out. Exposing the Mylar® window to an extended period of vacuum could retrieve the initial gas gain by drawing the water vapour out, establishing that the reduction in gas gain was caused by water vapour contamination. We found that within seven days, the peak PAN_{12} corresponding to the 5.9 keV X-ray line started approaching the initial value (See Fig. 6.10). This exercise confirmed that the proposed RTV material has no noticeable impact on the gas gain. The DOWSIL™ 732 Multi-Purpose Sealant was used to fabricate all the Qualification and Flight model wireframes. The solder joints were found durable when all the detectors later underwent multiple environmental tests.

6.4.5 Detector functionality test

The performance of the gas-filled proportional counter detectors was verified by validating the spectral response to mono-energetic sources and verifying the position sensitivity. The response to ^{55}Fe line at 5.9 keV and ^{109}Cd line at 22.1 keV (See Sec. 6.4.4) were used to validate the detector's spectral response functionality (Fig. 6.11a).

The major validation is, however, the position-resolving capability of the detectors. The detectors were made to acquire the background (charged particles or photons from cosmic/γ-ray air shower) for extended durations. The background data was then processed and a histogram of the ratios (eq. 6.15) of the detected events was constructed. The background is expected to illuminate all the anode cells uniformly,

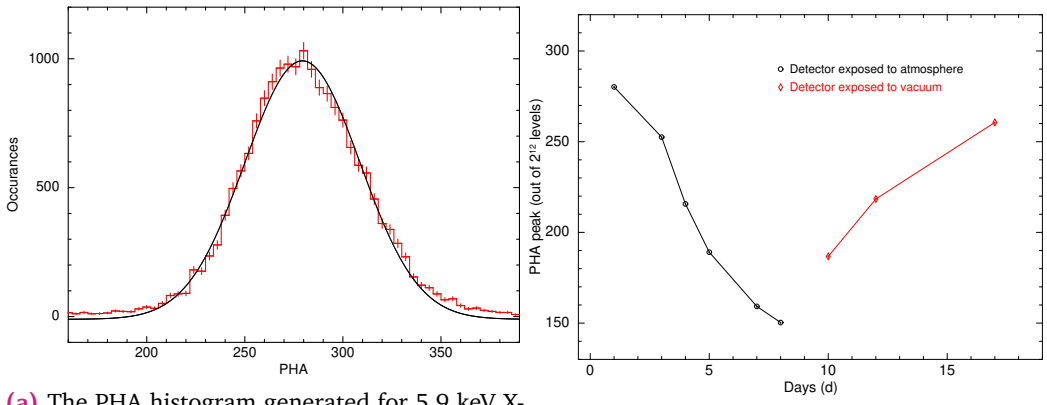

(a) The PHA histogram generated for 5.9 keV X-rays.

(b) Evolution of gas gain.

Fig. 6.10: Impact assessment of RTV material on the gas gain. A test proportional counter having an RTV-applied wire frame is checked and periodically shined with radioactive ^{55}Fe isotope. The pulse height amplitude (PHA) recorded by the proportional counter corresponding to the 5.9 keV X-ray photons is monitored. Change in the gas gain manifests as a change in the PHA. A reduction in gas gain was observed due to contamination by water vapour which could be retrieved creating an external vacuum. The RTV material has no noticeable impact on the gas gain.

and the six distinct lengths of wires in each detector channel should therefore be apparent when the histogram of ratios for each detector channel is constructed (Fig. 6.11b). The six distinct wide peaks in the ratio histogram indicate that the photons falling on each of the six anode wires in that detector channel could be distinguished. The width of each peak indicates the position resolving capability along the corresponding anode cell.

Post-data acquisition, the detector is kept in a vacuum chamber to prevent water vapour contamination through the Mylar® window and any subsequent gain deterioration.

6.5 Environmental Tests of the Qualification Model Detectors

The detectors and other subsystems of POLIX were tested to assess the endurance of the payload during the launch and in-space conditions. The vibration and thermal vacuum tests replicate the mechanical vibrations during the launch and temperature variations in space conditions. This section discusses the performance of the Qualification model proportional counter detectors of POLIX during the environmental tests.

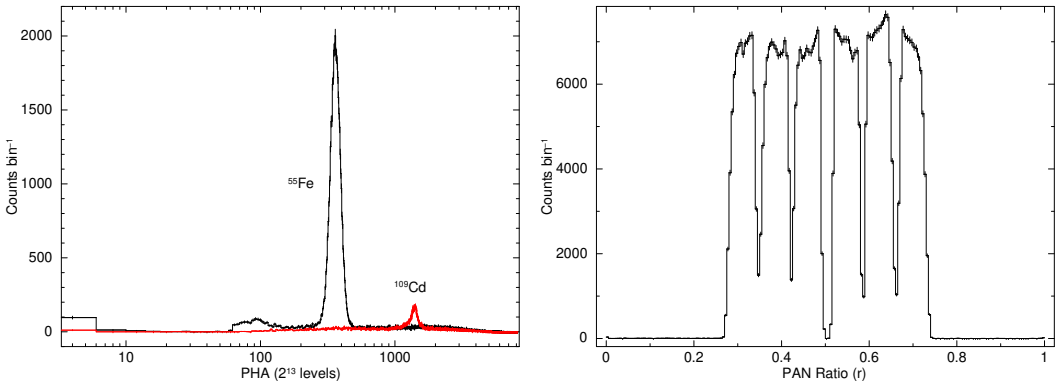

(a) Histogram of PAN_{12} showing the spectral response of the gas-filled detector to the radioactive sources ^{55}Fe and ^{109}Cd.

(b) Histogram of the ratios (eq. 6.15) illustrating the position sensitivity of the gas-filled detector.

Fig. 6.11: Figure showing the spectral and position response of one detector channel of a QM model detector. The spectral response is validated using radioactive sources, while the position sensitivity is validated from background data acquisition.

Two detectors were assembled for the Qualification tests, called the Qualification Model (QM) detectors. In vibration tests and thermal-vacuum tests, two dummy mass models were used along with the two QM detectors and to make the POLIX QM prototype. This was attached to the qualification model Beryllium scattering element and electronics. The detectors were validated by comparing and verifying the spectral response and position calibration before and after the environmental tests.

6.5.1 Vibration Test

The vibration test is performed to check the mechanical integrity of the payload to qualify it for the launch. Each proportional counter is an assembled unit, with thin wires attached to the wireframe, wireframe attached to the housing, interconnecting wires between feed-through pins and the wireframe, Mylar® window, and the top plate attached to the housing. Mechanical vibration tests are crucial to test their integrity. Breakage of the wires carrying the HV can result in a short circuit, making the entire detector nonfunctional.

The payload was subjected to two kinds of vibration tests in three mutually orthogonal directions (lateral axes X, Y and longitudinal axis Z). The first is the random vibration test which supplies a broad range of vibration frequencies simultaneously. The second is the swept sine vibration test, which performs vibration in the form of a sweep sine wave with a narrow frequency range. While the random vibration test

helps identify the potential mechanical resonances, the swept sine wave replicates the mechanical oscillations encountered during the launch conditions.

Before vibration tests, the proportional counters were connected to the electronics and laboratory DAQ system, and pre-vibration calibration data were acquired using radioactive ^{55}Fe and ^{109}Cd. The radioactive sources were shined at known locations on the detector using a thick stainless steel masking top plate (See Fig. 6.12b). Data was acquired at two HV levels 0x880 and 0x900 near 2200 V, for both the radioactive sources. The histograms of PHA and the ratio of PHAs (eq. 6.15) were constructed, giving the energy response and position response. The data was again acquired post-vibration tests. By comparing the PHA histograms and PHA ratio histograms before and after vibration tests, the performance of QM detectors against vibration was validated.

Each anode cell has a 30 cm length and is made of one thin continuous Nichrome wire. Six anode cells making one detector channel are built by serially connecting the cells with a looping wire. Along the thin Nichrome wire (hence the anode cell), the proportionality is maintained because the resistivity of the wire is uniform. On each wire, the radioactive source is shined at three different locations. The ratio vs length is constructed, and a linear fitting is performed on the three data points corresponding to each wire. The best fit linear function on each wire is shown in Fig. 6.14c. A change in the slope of the best fit linear function between two anode cells indicates an extra resistance between the two cells. Such resistance is expected to be caused by the junction between the thin anode wire and loop wire, hence called the junction resistance. By subtracting the slopes of the best-fit linear function between successive anodes in a channel, the junction resistance between each anode cell could be estimated. This is shown in the bottom panel of Fig. 6.14d. Mechanically unstable junction is vulnerable to vibration tests, and it can produce electrical discontinuity between anode cells, consequently compromising the position sensitivity of a *detector channel*. The position sensitivity is harmed because the increase in the electrical resistance within the detector channel impacts the charge division (Sec. 6.4.3).

POLIX payload with two QM detectors and two dummy detectors (to replicate the mechanical structure) was mounted to an Electrodynamic Shaker (Fig. 6.13). Both random and swept charge vibration was performed. The first QM vibration tests were performed in 2019, the results of which necessitated the need for RTV reinforcement of the solder joints and feed-through joints (Sec. 6.4.4). After re-fabricating all the detectors using the RTV, the QM vibration tests were performed in February 2021 after the COVID-19 pandemic-induced delays. The qualification model vibration

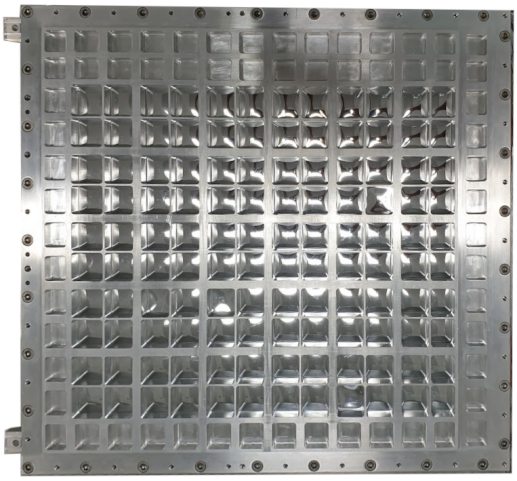

(a) Top view of the assembled detector from Mylar® window side.

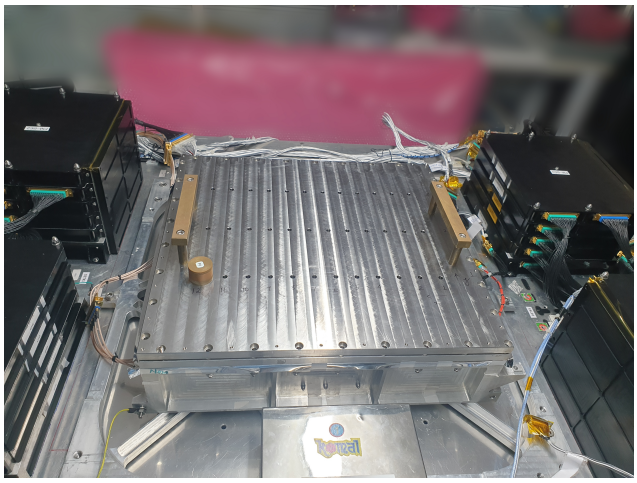

(b) Stainless Steel plate for location restricted data acquisition.

Fig. 6.12: The pre-vibration tests data acquisition using radioactive sources. Radioactive sources are shined above the Mylar® window pockets at known locations. The data acquisition is repeated after the vibration tests and the data are compared.

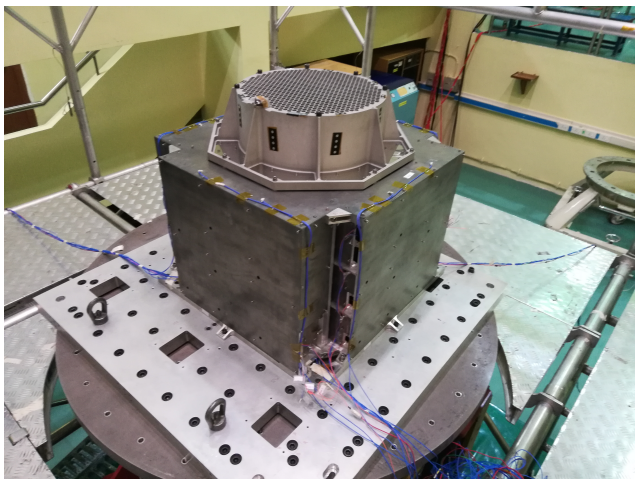

Fig. 6.13: POLIX QM unit mounted on vibration facility. Picture credits: Vikram Rana

tests were performed at the UR Rao Satellite Center (URSC), Bengaluru. The results of the comparison of the calibration data collected with ^{55}Fe at HV 0x900, before and after vibration are shown in Fig. 6.14. Since the detectors were exposed to the atmosphere for several weeks during transportation and setup at the vibration tests facility, the gas gain was found to be reduced from the comparison of pre-vibration with post-vibration spectral response. The position sensitivity calibration data stayed within margins with little to no impact from the vibration tests. POLIX passed the qualification model vibration tests.

6.5.2 Thermal-Vacuum Test

The Thermal-Vacuum tests of POLIX QM Detectors were performed at the Thermovac facility of URSC in 2021. During this test, the payload was kept under extreme vacuum levels of $\sim 10^{-6}$ mBar, and the payload temperature was cycled between different temperature levels. Thermostats installed at various locations on the payload were used to monitor the temperature at different locations. Shown in Fig. 6.15 is the temperature graph of POLIX Backend Electronics (BE) packages during the activity. The temperature at the package area was cycled six times between -15 °C and +60 °C, and sustained at each extreme temperature for some duration to carry out the tests on payload functionality. The validation of QM detector performance during thermal-vacuum tests is discussed in this section.

An X-ray generator with a Silver target was mounted on the ceiling of the Thermovac chamber for detector validation at various temperature levels. We used the Amptek® Mini-X X-ray generator, which produces a bremsstrahlung continuum with the

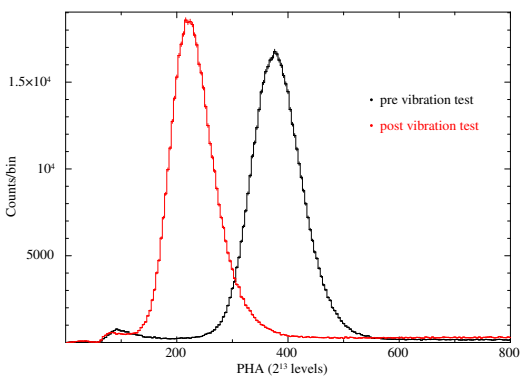

(a) Overall PHA histogram in CH1 from 18 known locations.

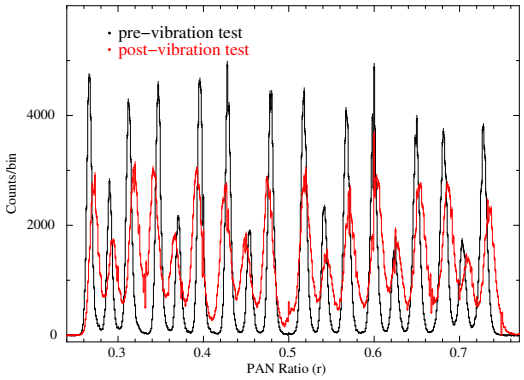

(b) Ratio histogram in CH1 from 18 known locations.

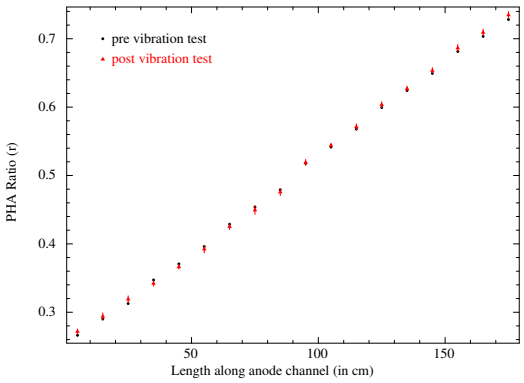

(c) The ratios plotted as a function of known locations.

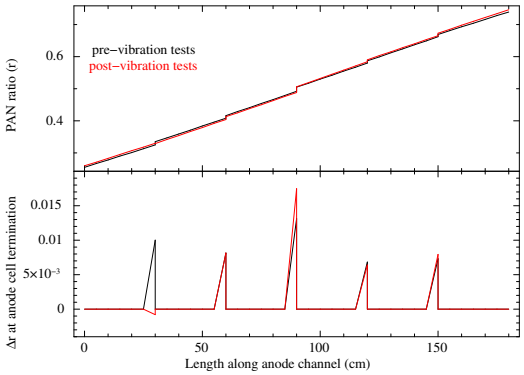

(d) Junction resistance assessed linear fits on individual anode cells.

Fig. 6.14: Results from vibration test of the POLIX QM proportional counter TPV2D2. Shown are the results of one of the detector channels (CH1) shined with radioactive ^{55}Fe source at 18 known locations (3 locations on each anode cell). The data acquired before the vibration tests are shown in black color and data acquired after the vibration tests are shown in red. Figs. (a) and (b) show the spectral and position (ratio) responses respectively. Fig. (c) shows the peaks of the ratio histograms plotted as a function of length along the wire. The top panel of Fig. (d) shows the best fit linear function on the ratios along each anode cell, and the bottom panel shows the difference between the linear fits at the junction between successive anode cells.

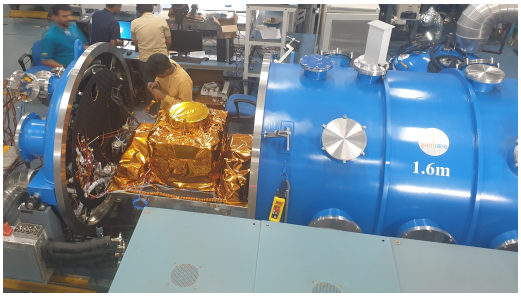

(a) POLIX loaded into Vacuum Chamber.

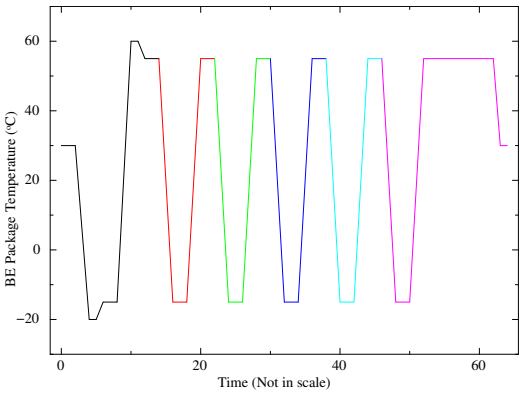

(b) Thermovac temperature cycle of the QM.

Fig. 6.15: Figure showing details of POLIX Thermal-vacuum tests.

characteristic line of Ag at 22 keV (Kα) as a result of firing energetic electrons against a Silver target. The generator having a 120° conical opening was pointed towards the Be scatterer and blocked with a Copper plug at the generator opening to restrict the number of photons. This was to ensure that the detectors did not encounter an overload of photons. The generator was operated at 30 kV and 20 μA. The generator shining at the central Be scattering block ensured that both the active QM proportional counters got enough scattered photons. The final expected spectrum from the generator operating at 30 kV voltage was verified by shining the generator on the Beryllium scatterer and recording the energy spectrum of the scattered photons using an Amptek® XR-100-CdTe detector (Fig. 6.16). It showed a low energy continuum cutoff below $\sim$ 10 keV (due to the Cu plug) and a high energy continuum cutoff above $\sim$ 30 keV, with characteristic emission lines of Ag at $\sim$ 22 keV and Cu at $\sim$ 8 keV.

When the temperature was maintained at each extreme temperature level, the detectors were tested by turning on the X-ray generator and acquiring data with all the detectors (Fig. 6.17). The spectral response and position sensitivity of the detectors were validated by constructing the histogram of PHAs (Fig. 6.18) and PHA ratios (Fig. 6.17) in individual detector channels in the same way as discussed in Sec. 6.5.1. During the temperature transition phases, both the detectors were set to continuously acquire background data and the histograms of ratio were frequently monitored for anomalies.

POLIX passed the Qualification Thermovac tests in 2021.

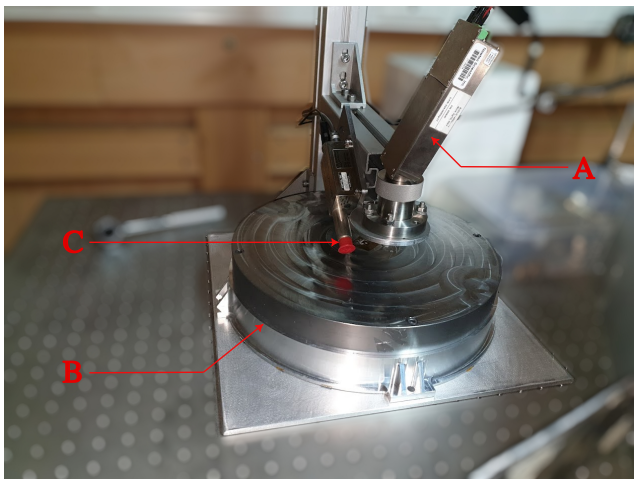

Fig. 6.16: The laboratory setup to record spectral response of the X-ray generator prior to Thermovac tests. Shown are (A) the X-ray generator, (B) the Beryllium scattering block, and (C) the CdTe X-ray detector.

6.6 Conclusions

The Thomson scattering X-ray polarimeter instrument POLIX onboard the *XPoSat* satellite mission is scheduled to launch in the second half of 2023. POLIX will detect the linear polarization of astrophysical X-ray sources in the unexplored energy range of 8–30 keV. In this Chapter, the design, assembly, and some tests performed on the qualification model proportional counters used in POLIX are explained. The Flight Model detectors were also assembled and tested following the same procedure.

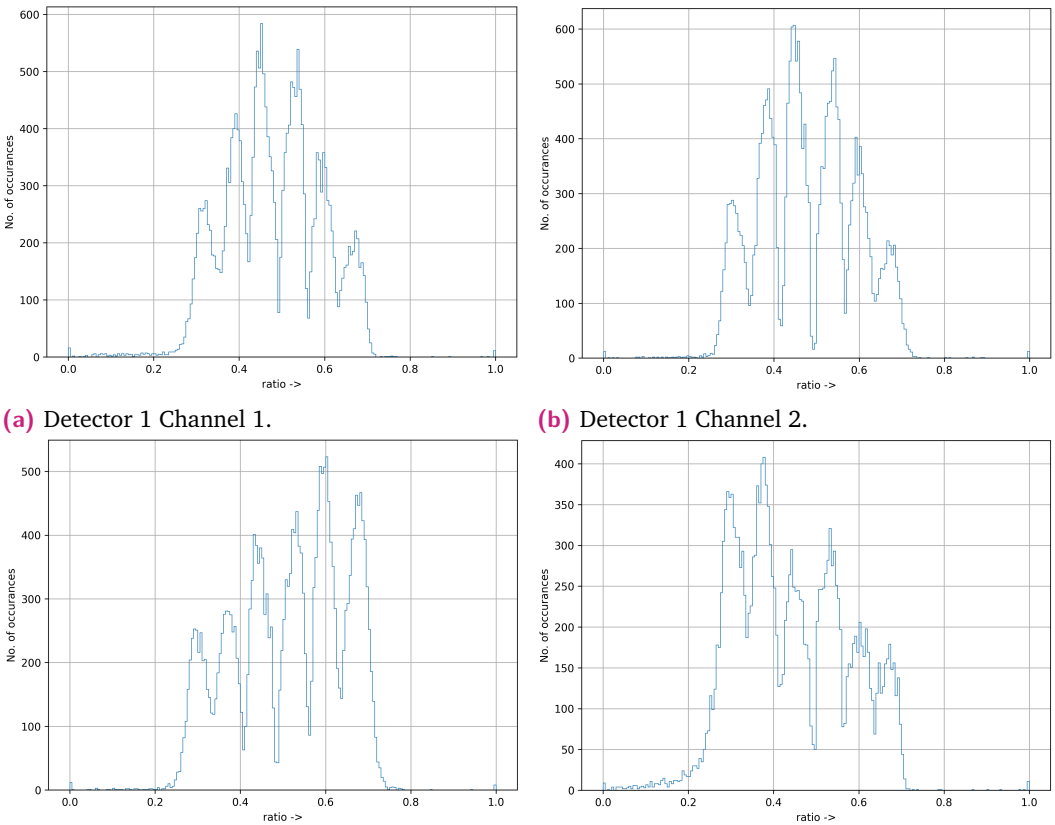

(a) Detector 1 Channel 1.

(b) Detector 1 Channel 2.

(c) Detector 2 Channel 1.

(d) Detector 2 Channel 2.

Fig. 6.17: The ratio histograms generated from two detectors when the X-ray generator operated during Thermovac Cycle 0 Stage 2. The difference in symmetry of the ratio histograms between the proportional counter Detectors 1 and 2 is due to the difference in the design of wireframes installed on the two detectors. A wireframe with the inter-leaved wiring scheme (alternate anode cells are connected in series to make one channel as shown in Fig. 6.7) was used in Detector 1 while a wireframe with the block wiring scheme (six successive anode cells are connected in series to make one channel) was used in Detector 2.

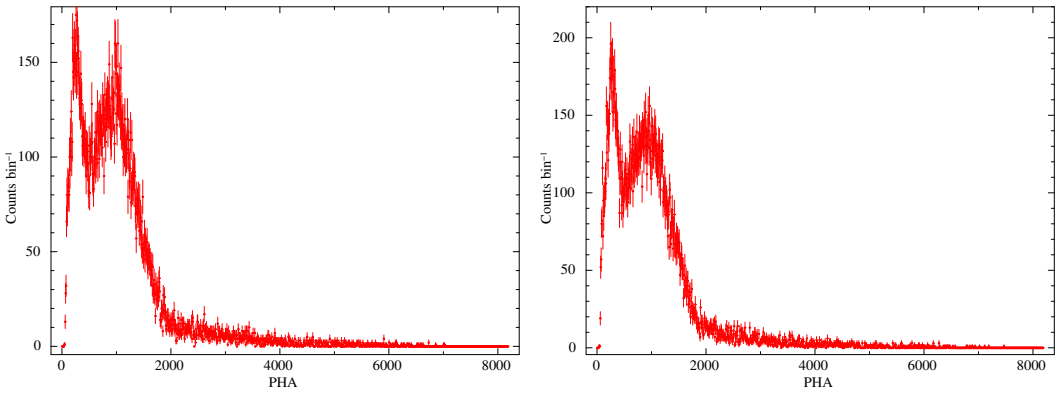

(a) Detector 1 Channel 1.

(b) Detector 1 Channel 2.

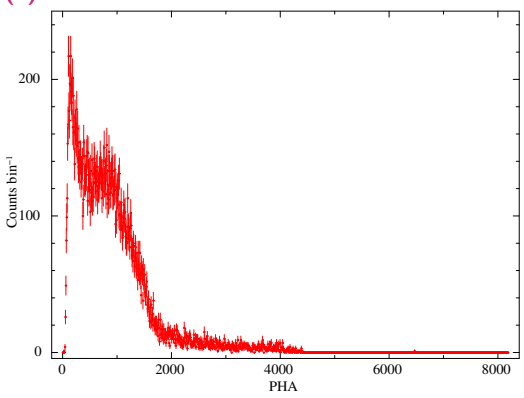

(c) Detector 2 Channel 1.

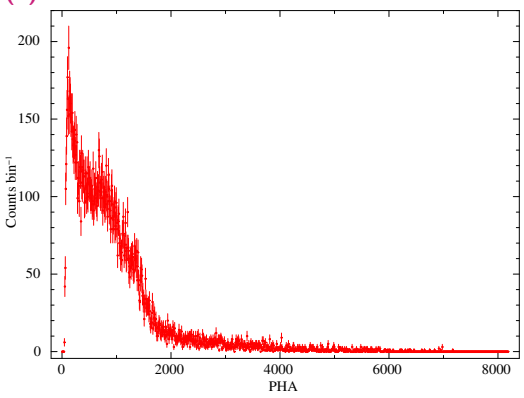

(d) Detector 2 Channel 2.

Fig. 6.18: The spectral response of two detectors when the X-ray generator operated during Thermovac Cycle 0 Stage 2.

7 Summary and Forward Outlook

7.1 Summary of the works

Chapter 3 discusses our search for the presence of '*10 keV feature*' in the *NuSTAR* spectra of XRPs. The '*10 keV feature*' has been frequently reported in the spectrum of XRPs since the *RXTE* era. *NuSTAR* is the most ideal X-ray observatory as of now which can study '*10 keV feature*', and we performed a systematic search for the '*10 keV feature*' in archival *NuSTAR* observations of XRPs. We found the '*10 keV feature*' in 16 out of 58 *NuSTAR* observations of XRPs. It could be fitted with a gaussian absorption model centred around 10 keV in 15 out of 16 observations (exception 4U 1907+09). We also found that out of these 16 observations, two of them could have an appearance of this feature due to the presence of flare in the observations. Considering that the '*10 keV feature*' is abundant in *NuSTAR*, the most suitable instrument to detect it, future theoretical investigations must be undertaken to uncover the origin of this feature.

The first portion of Chapter 4 discusses the timing analysis of 97 *XMM-Newton* and *NuSTAR* archival observations of 29 accreting X-ray pulsars to search for the presence of mHz Quasi-periodic oscillations in them. We detected QPOs in six *XMM-Newton* observations and three *NuSTAR* observations and estimated the variation of QPO properties with photon energy. The Magnetospheric beat frequency model (BFM) is favourable over the Keplerian frequency model (KFM) in all nine QPO detections. We also detected twin QPOs in the *NuSTAR* observation of V 0332+53.

The second portion of Chapter 4 discusses our findings of the analysis of the archival *NuSTAR*, and *XMM-Newton* pointed observations of the prototypical accretion disc corona (ADC) source 4U 1822–37, which exhibits partial eclipses. In this work, we performed an energy-resolved study of the partial eclipse profile in the 0.2–45 keV energy range using non-simultaneous *NuSTAR* and XMM observations. We found short (narrow) eclipses at high energies in contrast with the previously reported trend of increasing eclipse width with energy. We also found a gradual long-term flux decay of the source ($\sim 10^{-4}$ counts s^{-1} day^{-1}) in the 2–12 keV band in RXTE-ASM

long term light curve from MJD ~ 50088 to ~ 54000, but it does not continue in the later MAXI-GSC 2–10 keV band light curve from MJD 55054 to 59247. We also report the presence of a ~ 5 year super-orbital periodic variability in long-term X-ray lightcurves.

The first part of Chapter 5 discusses our investigation of the changes in the accretion environment of the pulsar GX 301–2 during its 80 days long spin-up episode in 2019. During this spin-up episode, the spin frequency of the pulsar increased by ∼2% over two orbits of the binary. By performing time-resolved spectroscopy with the *MAXI*/GSC spectra of the source, we estimated the equivalent hydrogen column density and equivalent width of the iron fluorescence line during the spin-up episode and compared them with the long-term average values estimated by orbital-phase resolved spectroscopy. We found that the measured absorption column density during the spin-up episode is about twice that of an average orbit, while the equivalent width of the iron line is less than half of an average orbit and that the absorption column density and iron line equivalent width vary throughout the spin-up episode. The orbital variation of these parameters during the spin-up episode is distinct from an average orbit, which indicates a significant change in the accretion and reprocessing environment in GX 301–2 during the spin-up episode.

In the second part of Chapter 5, the long-term orbital period evolution of GX 301–2 deduced by utilising the recurring pre-periastron flares is described. Our analysis yielded a measured orbital decay timescale of $|\dot{P}_{\rm orb}/P_{\rm orb}| \sim 10^{-5}$ yr^{-1}, which is currently the shortest known evolution timescale for a high-mass X-ray binary (HMXB). Previous estimates of this decay timescale were based on pulse time-of-arrival (TOA) analysis, which is influenced by the large orbital intensity variations and spin-up/down fluctuations of the pulsar. Our analysis of the long-term lightcurves, however, relies on the recurring orbital intensity profile, which is independent of the pulse TOA methods. There is a difference of a factor of three between our estimate and the previous estimate based on pulse TOA analysis.

Chapter 6 discusses some of the developmental activities and tests performed on the X-ray polarimeter instrument POLIX that will fly onboard the first dedicated X-ray polarimetry satellite mission of India called *XPoSat*. The X-ray polarization detection techniques, the operating principle of POLIX, the details of fabrication, assembly and some tests of the proportional counter detectors of POLIX are explained. The performance of the POLIX proportional counters during the Qualification Environmental tests is also described.

7.2 Forward Outlook

The spectroscopic capability of *MAXI*/GSC provides a unique opportunity to study the orbital dependence of spectral parameters in long-period binaries. One such study was performed on GX 301–2, which is reported in Chapter 5 of this thesis. In the future, similar studies could be performed on other bright sources with long orbital periods like EXO 2030+375. EXO 2030+375 is a transient Be-HMXB X-ray pulsar with a spin period of 42 s, located at a distance of 2-7 kpc (Motch et al., 1987). The binary has an eccentric ($e \sim 0.41$) binary orbit ($a_x \sin i$ ~246 lt-s) with a long orbital period of ~ 46 d (Wilson, Finger, and Camero-Arranz, 2008a). This source exhibits regular outbursts during each periastron passage of the neutron star. Even though orbital phase-resolved spectroscopy is a very useful tool to probe the characteristics of the overall circum-binary environment of X-ray pulsars (See for example Mukherjee, Raichur, et al. 2006), performing orbital phase-resolved spectroscopy of sources like EXO 2030+375 is unfeasible due to long orbital period. We plan to use *MAXI* All-sky monitor to perform the orbital phase-resolved spectroscopy during the long ~ 46 d orbital period, using a similar technique as in Chapter 5.

With *XPoSat* planned to launch in the coming months, we will have the opportunity to perform X-ray polarimetry in the unexplored 8–30 keV energy band. Coupled with the *IXPE* sensitivity in 2–8 keV, *XPoSat–IXPE* simultaneous data would enable one to perform broadband polarimetry in 2-30 keV broadband. In Chapter 6 of this thesis, my contribution to some of the developmental aspects and testing of POLIX detectors are described. I plan to perform the broadband polarimetric analysis of some of the bright X-ray pulsars.

Bibliography

Abarr Q. et al. (2020). “Observations of a GX 301–2 Apastron Flare with the X-Calibur Hard X-Ray Polarimeter Supported by NICER, the Swift XRT and BAT, and Fermi GBM”. In: *The Astrophysical Journal* 891.1, p. 70.

Aftab N., Paul B., and Kretschmar P. (2019). “X-Ray Reprocessing: Through the Eclipse Spectra of High-mass X-Ray Binaries with XMM-Newton”. In: *The Astrophysical Journal Supplement Series* 243.2, p. 29.

Akaike H. (1998). “Information theory and an extension of the maximum likelihood principle”. In: *Selected papers of hirotugu akaike*, pp. 199–213.

Alpar M. A. and Shaham J. (1985). “Is GX5–1 a millisecond pulsar?” In: *Nature* 316.6025, pp. 239–241.

Antia H. et al. (2017). “Calibration of the large area X-ray proportional counter (LAXPC) instrument on board AstroSat”. In: *The Astrophysical Journal Supplement Series* 231.1, p. 10.

Arnaud K. (1996). “XSPEC: the first ten years”. In: *Astronomical Data Analysis Software and Systems V, ASP Conference Series, Vol. 101, 1996, George H. Jacoby and Jeannette Barnes, eds., p. 17*. Vol. 101, p. 17.

Asai K. et al. (1994). “Spectral Variations along the Branches in GX 5-1”. In: *Publications of the Astronomical Society of Japan* 46, pp. 479–491.

Bachetti M. et al. (2022). “Orbital decay in M82 X-2”. In: *The Astrophysical Journal* 937.2, p. 125.

Bala S., Bhattacharya D., Staubert R., and Maitra C. (2020). “Time evolution of cyclotron line of Her X-1: a detailed statistical analysis including new AstroSat data”. In: *Monthly Notices of the Royal Astronomical Society* 497.1, pp. 1029–1042.

Bala S., Roy J., and Bhattacharya D. (2020). “Possible detection of a new cyclotron feature in 4U 1700–37”. In: *Monthly Notices of the Royal Astronomical Society* 493.2, pp. 3045–3053.

Ballhausen R. et al. (2017). “Looking at A 0535+ 26 at low luminosities with NuSTAR”. In: *Astronomy & Astrophysics* 608, A105.

Ballhausen, Ralf et al. (2016). “Suzaku observations of the 2013 outburst of KS 1947+300”. In: *A&A* 591, A65. DOI: 10.1051/0004-6361/201527193. URL: https://doi.org/10.1051/0004-6361/201527193.

Barnstedt, J. et al. (2008). “INTEGRAL observations of the variability of OAO 1657-415*”. In: *A&A* 486.1, pp. 293–302. DOI: 10.1051/0004-6361:20078707. URL: https://doi.org/10.1051/0004-6361:20078707.

Barthelmy S. D. et al. (2005). “The burst alert telescope (BAT) on the SWIFT midex mission”. In: *Space Science Reviews* 120.3, pp. 143–164.

Baum Z. A., Cherry M. L., and Rodi J. (2017). “Observations of V0332+ 53 during the 2015 outburst using Fermi/GBM, MAXI, Swift and INTEGRAL”. In: *Monthly Notices of the Royal Astronomical Society* 467.4, pp. 4424–4430.

Bayless A. J., Robinson E. L., Hynes R. I., Ashcraft T. A., and Cornell M. E. (2009). “THE STRUCTURE OF THE ACCRETION DISK IN THE ACCRETION DISK CORONA X-RAY BINARY 4U 1822- 371 AT OPTICAL AND ULTRAVIOLET WAVELENGTHS”. In: *The Astrophysical Journal* 709.1, p. 251.

Becker P. A. and Wolff M. T. (2007). “Thermal and bulk comptonization in accretion-powered X-ray pulsars”. In: *The Astrophysical Journal* 654.1, p. 435.

Begelman M. C., McKee C. F., and Shields G. A. (1983). “Compton heated winds and coronae above accretion disks. I Dynamics”. In: *Astrophysical Journal, Part 1 (ISSN 0004-637X), vol. 271, Aug. 1, 1983, p. 70-88. Research supported by the Science Research Council of England.* 271, pp. 70–88.

Bellm E. C. et al. (2014). “Confirmation of a high magnetic field in GRO J1008–57”. In: *The Astrophysical Journal* 792.2, p. 108.

Belloni T. and Hasinger G. (1990). “An atlas of aperiodic variability in HMXB”. In: *Astronomy and Astrophysics (ISSN 0004-6361), vol. 230, no. 1, April 1990, p. 103-119. Research supported by the Della Riccia Foundations.* 230, pp. 103–119.

Belloni T. M., Sanna A., and Mendez M. (2012). “High-frequency quasi-periodic oscillations in black hole binaries”. In: *Monthly Notices of the Royal Astronomical Society* 426.3, pp. 1701–1709.

Berger M. et al. (Sept. 1996). “Discovery of 800 Hz Quasi-periodic Oscillations in 4U 1608–52”. In: *The Astrophysical Journal* 469.1, p. L13. DOI: 10.1086/310256. URL: https://dx.doi.org/10.1086/310256.

Beri A., Jain C., Paul B., and Raichur H. (2014). “Torque reversals and pulse profile of the pulsar 4U 1626- 67”. In: *Monthly Notices of the Royal Astronomical Society* 439.2, pp. 1940–1947.

Beri A., Paul B., and Dewangan G. C. (2018). “Changes in the pulse phase dependence of X-ray emission lines in 4U 1626- 67 with a torque reversal”. In: *Monthly Notices of the Royal Astronomical Society* 475.1, pp. 999–1009.

Bhalerao V. et al. (2015). “NuSTAR detection of a cyclotron line in the supergiant fast X-ray transient IGR J17544- 2619”. In: *Monthly Notices of the Royal Astronomical Society* 447.3, pp. 2274–2281.

Bhargava Y. et al. (2019). “Explaining the asymmetric line profile in Cepheus X-4 with spectral variation across pulse phase”. In: *Monthly Notices of the Royal Astronomical Society* 482.3, pp. 2902–2912.

Bildsten L. et al. (1997). “Observations of accreting pulsars”. In: *The Astrophysical Journal Supplement Series* 113.2, p. 367.

Black J. K., Deines-Jones P., Jahoda K., Ready S. E., and Street R. A. (2004). “High-sensitivity x-ray polarimetry with amorphous-silicon active-matrix pixel proportional counters”. In: *X-Ray and Gamma-Ray Instrumentation for Astronomy XIII*. Vol. 5165. SPIE, pp. 346–353.

Bodaghee A. et al. (2016). “NuSTAR discovery of a cyclotron line in the accreting X-ray pulsar IGR J16393-4643”. In: *The Astrophysical Journal* 823.2, p. 146.

Boella G. et al. (1997). “BeppoSAX, the wide band mission for X-ray astronomy”. In: *Astronomy and Astrophysics Supplement Series* 122.2, pp. 299–307.

Boldin P., Tsygankov S., and Lutovinov A. (2013). “On timing and spectral characteristics of the x-ray pulsar 4U 0115+ 63: evolution of the pulsation period and the cyclotron line energy”. In: *Astronomy Letters* 39, pp. 375–388.

Bonnet-Bidaud J.-M. and Mouchet M. (1998). “The identification of the transient X-ray pulsar Cepheus X-4 with a Be/X-ray binary”. In: *Arxiv preprint astro-ph/9801215*.

Bozzo E. et al. (2018). “IGR J17329-2731: The birth of a symbiotic X-ray binary”. In: *Astronomy & Astrophysics* 613, A22.

Brumback M. C. et al. (2020). “Modeling the precession of the warped inner accretion disk in the pulsars LMC X-4 and SMC X-1 with NuSTAR and XMM-Newton”. In: *The Astrophysical Journal* 888.2, p. 125.

Bunzel A. S., Garcìa F., Combi J. A., and Chaty S. (2022). “Evolution of eccentric high-mass X-ray binaries. The case of GX 301-2”. In: *arXiv preprint arXiv:2212.11881*.

Burderi L., Di Salvo T., Robba N., La Barbera A., and Guainazzi M. (2000). “The 0.1-100 keV spectrum of Centaurus X-3: pulse phase spectroscopy of the cyclotron line and magnetic field structure”. In: *The Astrophysical Journal* 530.1, p. 429.

Bussard R., Weisskopf M. C., Elsner R., and Shibazaki N. (1988). “The effect of a hot, spherical scattering cloud on quasi-periodic oscillation behavior”. In: *Astrophysical Journal, Part 1 (ISSN 0004-637X), vol. 327, April 1, 1988, p. 284-293.* 327, pp. 284–293.

Bykov S. et al. (2021). “Pulsating iron spectral features in the emission of X-ray pulsar V 0332+ 53”. In: *Monthly Notices of the Royal Astronomical Society* 506.2, pp. 2156–2169.

Caballero I., Kretschmar P., et al. (2007). “A 0535+ 26 in the August/September 2005 outburst observed by RXTE and INTEGRAL”. In: *Astronomy & Astrophysics* 465.2, pp. L21–L24.

Caballero I., Pottschmidt K., et al. (2013). “A Double-peaked Outburst of A 0535+ 26 Observed with INTEGRAL, RXTE, and Suzaku”. In: *The Astrophysical journal letters* 764.2, p. L23.

Caballero I. and Wilms J. (2012). “X-ray pulsars: a review”. In: *arXiv preprint arXiv:1206.3124*.

Caballero-Garcìa M. D. et al. (2016). “Activity from the Be/X-ray binary system V0332+ 53 during its intermediate-luminosity outburst in 2008”. In: *Astronomy & Astrophysics* 589, A9.

Camero Arranz, A. et al. (2005). “INTEGRAL observations of the Be/X-ray binary EXO 2030+375 during outburst”. In: *A&A* 441.1, pp. 261–269. DOI: 10.1051/0004-6361:20053335. URL: https://doi.org/10.1051/0004-6361:20053335.

Camero-Arranz A. et al. (2012). “4U 1626–67 as seen by Suzaku before and after the 2008 torque reversal”. In: *Astronomy & Astrophysics* 546, A40.

Chakrabarty D. (1998). “High-Speed Optical Photometry of the Ultracompact X-Ray Binary 4U 1626–67”. In: *The Astrophysical Journal* 492.1, p. 342.

Chakrabarty D., Homer L., Charles P. A., and O’Donoghue D. (2001). “Millihertz Optical/Ultraviolet Oscillations in 4U 1626–67: Evidence for a Warped Accretion Disk”. In: *The Astrophysical Journal* 562.2, p. 985.

Charles P., Thorstensen J. R., and Barr P. (1980). “Optical and X-ray studies of 2A 1822-371”. In: *Astrophysical Journal, Part 1, vol. 241, Nov. 1, 1980, p. 1148-1152. Research supported by the Science Research Council of England* 241, pp. 1148–1152.

Chattopadhyay T., Vadawale S., Rao A., Sreekumar S., and Bhattacharya D. (2014). “Prospects of hard X-ray polarimetry with Astrosat-CZTI”. In: *Experimental Astronomy* 37, pp. 555–577.

Choi C., Dotani T., Day C., and Nagase F. (1996). “Pulse Phase-Dependent Spectroscopic Study of Vela X-1”. In: *The Astrophysical Journal* 471.1, p. 447.

Chou Y. (2014). “Measuring the orbital periods of low mass X-ray binaries in the X-ray band”. In: *Research in Astronomy and Astrophysics* 14.11, p. 1367.

Chou Y. and Grindlay J. (2001). “Binary and Long-Term (Triple?) Modulations of 4U 1820–30 in NGC 6624”. In: *The Astrophysical Journal* 563.2, p. 934.

Church M. and Bałucińska-Church M. (2004). “Measurements of accretion disc corona size in LMXB: consequences for Comptonization and LMXB models”. In: *Monthly Notices of the Royal Astronomical Society* 348.3, pp. 955–963.

Clark D. J., Hill A. B., et al. (2009). “Discovery of the orbital period in the supergiant fast X-ray transient IGR J17544–2619”. In: *Monthly Notices of the Royal Astronomical Society: Letters* 399.1, pp. L113–L117.

Clark G. W., Woo J. W., Nagase F., Makishima K., and Sakao T. (1990). “Discovery of a cyclotron absorption line in the spectrum of the binary X-ray pulsar 4U 1538-52 observed by GINGA”. In: *Astrophysical Journal, Part 1 (ISSN 0004-637X), vol. 353, April 10, 1990, p. 274-280. Research supported by MOESC.* 353, pp. 274–280.

Clark J. S., Najarro F., et al. (2012). “On the nature of the galactic early-B hypergiants”. In: *Astronomy & Astrophysics* 541, A145.

Coburn W. et al. (2002). “Magnetic fields of accreting X-ray pulsars with the Rossi X-ray timing explorer”. In: *The Astrophysical Journal* 580.1, p. 394.

Coe M., Negueruela I., Buckley D., Haigh N., and Laycock S. (2001). “Optical studies of two Large Magellanic Cloud X-ray transients: RX J0544. 1–7100 and RX J0520. 5–6932”. In: *Monthly Notices of the Royal Astronomical Society* 324.3, pp. 623–627.

Corbet R., Marshall F., Coe M., Laycock S., and Handler G. (2001). "The Discovery of an Outburst and Pulsed X-Ray Flux from SMC X-2 Using the Rossi X-Ray Timing Explorer". In: *The Astrophysical Journal* 548.1, p. L41.

Costa E. et al. (2001). "An efficient photoelectric X-ray polarimeter for the study of black holes and neutron stars". In: *Nature* 411.6838, pp. 662–665.

Cottam J., Sako M., Kahn S. M., Paerels F., and Liedahl D. A. (2001). "High-Resolution X-Ray Spectroscopy of the Accretion Disk Corona Source 4U 1822–37". In: *The Astrophysical Journal* 557.2, p. L101.

Cox N., Kaper L., and Mokiem M. (2005). "VLT/UVES spectroscopy of the O supergiant companion to 4U 1907+ 09 (7)". In: *Astronomy & Astrophysics* 436.2, pp. 661–669.

Crampton D., Hutchings J., and Cowley A. (1978). "The optical counterparts of SMC X-2 and SMC X-3". In: *The Astrophysical Journal* 223, pp. L79–L81.

CRAMPTONI D. and HUTCHINGSI J. (1982). "AP COWLEY ". In: *THE ASTROPHYSICAL JOURNAL* 255, pp. 596–602.

Cusumano G. et al. (2000). "Bepposax observation of 4U1907+ 09: Detection of a cyclotron line and its second harmonic". In: *Advances in Space Research* 25.3-4, pp. 409–412.

D'Aí A., Cusumano G., Del Santo M., La Parola V., and Segreto A. (2017). "A broad-band self-consistent modelling of the X-ray spectrum of 4U 1626- 67". In: *Monthly Notices of the Royal Astronomical Society* 470.2, pp. 2457–2468.

Darwin G. (1879). "A tidal theory of the evolution of satellites". In: *The Observatory, Vol. 3, p. 79-84 (1879)* 3, pp. 79–84.

Davidson K. and Ostriker J. P. (1973). "Neutron-star accretion in a stellar wind: model for a pulsed X-ray source". In: *The Astrophysical Journal* 179, pp. 585–598.

Del Monte E., Fabiani S., and Pearce M. (2023). "Compton Polarimetry". In: *arXiv preprint arXiv:2301.09934*.

Devaraj A. and Paul B. (2022). "Phase-dependent cyclotron line feature in XTE J1946+ 274: a NuSTAR view". In: *Monthly Notices of the Royal Astronomical Society* 517.2, pp. 2599–2609.

Devasia J., James M., Paul B., and Indulekha K. (2011). "Timing and spectral studies of the transient X-ray pulsar GX 304- 1 during an outburst". In: *Monthly Notices of the Royal Astronomical Society* 417.1, pp. 348–358.

Diez C. et al. (2022). "Continuum, cyclotron line, and absorption variability in the high-mass X-ray binary Vela X-1". In: *Astronomy & Astrophysics* 660, A19.

Doroshenko R., Piraino S., Doroshenko V., and Santangelo A. (2020). "Revisiting BeppoSAX and NuSTAR observations of KS 1947+ 300 and the missing cyclotron line". In: *Monthly Notices of the Royal Astronomical Society* 493.3, pp. 3442–3448.

Doroshenko R., Santangelo A., Doroshenko V., and Piraino S. (2017). "BeppoSAX observations of XTE J1946+274". In: *A&A* 600, A52. DOI: 10.1051/0004-6361/201630137. URL: https://doi.org/10.1051/0004-6361/201630137.

Doroshenko R. (2017). “A Systematic Study of the X-ray Cyclotron-Line Sources Observed by BeppoSAX”. PhD thesis. Universitätsbibliothek Tübingen.

Doroshenko V., Santangelo A., Suleimanov V., et al. (2010). “Is there a highly magnetized neutron star in GX 301–2?” In: *Astronomy & Astrophysics* 515, A10.

Doroshenko V., Doroshenko R., Postnov K., Cherepashchuk A., and Tsygankov S. (2008). “A study of the X-ray pulsars X1845-024 and XTE J1858+ 034 based on INTEGRAL observations”. In: *Astronomy reports* 52, pp. 138–151.

Doroshenko V., Poutanen J., et al. (2022). “Determination of X-ray pulsar geometry with IXPE polarimetry”. In: *Nature Astronomy* 6.12, pp. 1433–1443.

Doroshenko V., Tsygankov S. S., et al. (2017). “Luminosity dependence of the cyclotron line and evidence for the accretion regime transition in V 0332+ 53”. In: *Monthly Notices of the Royal Astronomical Society* 466.2, pp. 2143–2150.

Doroshenko, V. et al. (2010). “Is there a highly magnetized neutron star in GX 301-2?” In: *A&A* 515, A10. DOI: 10.1051/0004-6361/200912951. URL: https://doi.org/10.1051/0004-6361/200912951.

Drave S., Bird A., Sidoli L., et al. (2014). “New insights on accretion in supergiant fast X-ray transients from XMM–Newton and INTEGRAL observations of IGR J17544- 2619”. In: *Monthly Notices of the Royal Astronomical Society* 439.2, pp. 2175–2185.

Drave S., Bird A., Townsend L., et al. (2012). “X-ray pulsations from the region of the supergiant fast X-ray transient IGR J17544- 2619”. In: *Astronomy & Astrophysics* 539, A21.

Durant M., Cornelisse R., Remillard R., and Levine A. (2010). “Decade time-scale modulation of low-mass X-ray binaries”. In: *Monthly Notices of the Royal Astronomical Society* 401.1, pp. 355–361.

Eggleton P. (2006). *Evolutionary processes in binary and multiple stars*. Vol. 40. Cambridge University Press.

Eggleton P. P. (1983). “Approximations to the radii of Roche lobes”. In: *Astrophysical Journal, Part 1 (ISSN 0004-637X), vol. 268, May 1, 1983, p. 368, 369.* 268, p. 368.

Elsner R., O’Dell S., and Weisskopf M. C. (2012). “Measuring x-ray polarization in the presence of systematic effects: known background”. In: *Space Telescopes and Instrumentation 2012: Ultraviolet to Gamma Ray*. Vol. 8443. SPIE, pp. 1339–1350.

Enoto T. et al. (2008). “Suzaku observations of Hercules X-1: Measurements of the two cyclotron harmonics”. In: *Publications of the Astronomical Society of Japan* 60.sp1, S57–S68.

Epili P., Naik S., Jaisawal G. K., and Gupta S. (2017). “Decade long RXTE monitoring observations of Be/X-ray binary pulsar EXO 2030+ 375”. In: *Monthly Notices of the Royal Astronomical Society* 472.3, pp. 3455–3466.

Fabian A., Guilbert P., and Ross R. (1982). “An interpretation of the X-ray spectrum of 4U 1822–37”. In: *Monthly Notices of the Royal Astronomical Society* 199.4, pp. 1045–1051.

Farrell S., Sood R., and O'Neill P. (2006). "Super-orbital period in the high-mass X-ray binary 2S 0114+ 650". In: *Monthly Notices of the Royal Astronomical Society* 367.4, pp. 1457–1462.

Ferrigno C., Segreto A., Mineo T., Santangelo A., and Staubert R. (2008). "INTEGRAL observation of the accreting pulsar 1E1145. 1-6141". In: *Astronomy & Astrophysics* 479.2, pp. 533–539.

Ferrigno, Carlo et al. (2016). "Two giant outbursts of V0332+53 observed with INTEGRAL". In: *A&A* 595, A17. DOI: 10.1051/0004-6361/201628865. URL: https://doi.org/10.1051/0004-6361/201628865.

Filippova E., Tsygankov S., Lutovinov A., and Sunyaev R. (2005). "Hard spectra of X-ray pulsars from INTEGRAL data". In: *Astronomy Letters* 31, pp. 729–747.

Finger M. H. (1998). "QPO in transient pulsars". In: *Advances in Space Research* 22.7, pp. 1007–1016.

Finger M., Wilson R., and Harmon B. (1996). "Quasi-periodic Oscillations during a Giant Outburst of A0535+ 262". In: *Astrophysical Journal v. 459, p. 288* 459, p. 288.

Fiume D. D. et al. (1998). "The broad-band (0.1-200 kev) spectrum of her x-1 observed with bepposax". In: *Astron. Astrophys.* 329, p. L41. arXiv: astro-ph/9711295.

Forot M., Laurent P., Grenier I., Gouiffes C., and Lebrun F. (2008). "Polarization of the Crab pulsar and nebula as observed by the Integral/IBIS telescope". In: *The Astrophysical Journal* 688.1, p. L29.

Forsblom S. V. et al. (2023). "IXPE observations of the quintessential wind-accreting X-ray pulsar Vela X-1". In: *The Astrophysical Journal Letters* 947.2, p. L20.

Frank J., King A., and Lasota J.-P. (1987). "The light curves of low-mass X-ray binaries". In: *Astronomy and Astrophysics* 178, pp. 137–142.

Frank J., King A., and Raine D. (2002). *Accretion power in astrophysics*. Cambridge university press.

Frontera F. et al. (1997). "The high energy instrument PDS on-board the BeppoSAX X–ray astronomy satellite". In: *Astronomy and Astrophysics Supplement Series* 122.2, pp. 357–369.

Fuerst F. et al. (2013). "The smooth cyclotron line in Her X-1 as seen with nuclear spectroscopic telescope array". In: *The Astrophysical Journal* 779.1, p. 69.

Fürst F., Falkner S., et al. (2018). "Multiple cyclotron line-forming regions in GX 301- 2". In: *Astronomy & Astrophysics* 620, A153.

Fürst F., Kretschmar P., et al. (2017). "Studying the accretion geometry of EXO 2030+ 375 at luminosities close to the propeller regime". In: *Astronomy & Astrophysics* 606, A89.

Fürst F., Pottschmidt K., Miyasaka H., et al. (2015). "Distorted cyclotron line profile in Cep X-4 as observed by NuSTAR". In: *The Astrophysical Journal Letters* 806.2, p. L24.

Fürst F., Suchy S., et al. (2011). "Study of the many fluorescent lines and the absorption variability in GX 301- 2 with XMM-Newton". In: *Astronomy & Astrophysics* 535, A9.

Fürst F., Pottschmidt K., Wilms J., Kennea J., et al. (2014). “NuSTAR discovery of a cyclotron line in KS 1947+ 300”. In: *The Astrophysical Journal Letters* 784.2, p. L40.

Fürst F., Pottschmidt K., Wilms J., Tomsick J. A., et al. (2013). “NuSTAR discovery of a luminosity dependent cyclotron line energy in Vela X-1”. In: *The Astrophysical Journal* 780.2, p. 133.

Galloway D. K., Morgan E. H., and Levine A. (2004). “A frequency glitch in an accreting pulsar”. In: *The Astrophysical Journal* 613.2, p. 1164.

Gehrels N. et al. (Aug. 2004). “The Swift Gamma-Ray Burst Mission”. In: *The Astrophysical Journal* 611.2, p. 1005. DOI: 10.1086/422091. URL: https://dx.doi.org/10.1086/422091.

Ghising M., Tobrej M., Rai B., Tamang R., and Paul B. C. (2022). “NuSTAR observation of X-ray pulsar 1E 1145.1- 6141”. In: *Monthly Notices of the Royal Astronomical Society* 517.3, pp. 4132–4137.

Ghosh P. and Lamb F. (1979). “Accretion by rotating magnetic neutron stars. III-Accretion torques and period changes in pulsating X-ray sources”. In: *Astrophysical Journal, Part 1, vol. 234, Nov. 15, 1979, p. 296-316.* 234, pp. 296–316.

Giacconi R., Gursky H., Kellogg E., Levinson R., et al. (1973). “Further X-ray observations of Hercules X-1 from Uhuru.” In: *Astrophysical Journal, Vol. 184, p. 227-236* 184, pp. 227–236.

Giacconi R., Gursky H., Kellogg E., Schreier E., and Tananbaum H. (1971). “Discovery of periodic X-ray pulsations in Centaurus X-3 from Uhuru”. In: *Astrophysical Journal, vol. 167, p. L67* 167, p. L67.

Göğüş E., Alpar M. A., and Gilfanov M. (2007). “Is the lack of pulsations in low-mass X-ray binaries due to comptonizing coronae?” In: *The Astrophysical Journal* 659.1, p. 580.

Gordon C. and Arnaud K. (2021). “PyXspec: Python interface to XSPEC spectral-fitting program”. In: *Astrophysics Source Code Library*, ascl–2101.

Gruber D. et al. (2001). “Stability of the cyclotron resonance scattering feature in Hercules X-1 with RXTE”. In: *The Astrophysical Journal* 562.1, p. 499.

Haberl F. (1991). “The X-ray properties of GX 301-2 (4U 1223-62)”. In: *Astrophysical Journal, Part 1 (ISSN 0004-637X), vol. 376, July 20, 1991, p. 245-255.* 376, pp. 245–255.

Haberl F. and Day C. (1992). “A GINGA observation of the supergiant X-ray binary system 4U 1700-37/HD 153919”. In: *Astronomy and Astrophysics* 263, pp. 241–248.

Halpern J. and Gotthelf E. (2007). “X-Ray Observations and Infrared Identification of the Transient 7.8 s X-Ray Binary Pulsar XTE J1829–098”. In: *The Astrophysical Journal* 669.1, p. 579.

Harding A. K. (2003). “Physical processes in strong magnetic fields of neutron stars”. In: *arXiv preprint astro-ph/0304120*.

Harding A. K. and Lai D. (2006). “Physics of strongly magnetized neutron stars”. In: *Reports on Progress in Physics* 69.9, p. 2631.

Harlaftis E., Charles P., and Home K. (1997). “Detection of the X-ray-heated companion of X1822—371”. In: *Monthly Notices of the Royal Astronomical Society* 285.4, pp. 673–682.

Harrison F. A. et al. (2013). “The nuclear spectroscopic telescope array (NuSTAR) high-energy X-ray mission”. In: *The Astrophysical Journal* 770.2, p. 103.

Heindl W. et al. (2001). “Discovery of a cyclotron resonance scattering feature in the X-ray spectrum of XTE J1946+ 274”. In: *The Astrophysical Journal* 563.1, p. L35.

Heinz S. and Nowak M. (2001). “The Flared Disc Project: RXTE and ASCA observations of X 1822—371”. In: *Monthly Notices of the Royal Astronomical Society* 320.2, pp. 249–260.

Hellier C. (Jan. 1990). “Accretion flows in compact binary stars”. PhD thesis. University of London, University College London (United Kingdom).

Hellier C. and Mason K. O. (1989). “EXOSAT observations of X 1822–371: modelling of the accretion disc rim”. In: *Monthly Notices of the Royal Astronomical Society* 239.3, pp. 715–732.

Hellier C., Mason K. O., and Williams O. R. (1992). “Energy structure of the accretion disc corona in X 1822–371”. In: *Monthly Notices of the Royal Astronomical Society* 258.3, pp. 457–460.

Hemphill P. B., Rothschild R. E., Caballero I., et al. (2013). “Measurements of Cyclotron Features and Pulse Periods in the High-mass X-Ray Binaries 4U 1538- 522 and 4U 1907+ 09 with the International Gamma-Ray Astrophysics Laboratory”. In: *The Astrophysical Journal* 777.1, p. 61.

Hemphill P. B., Rothschild R. E., Cheatham D. M., et al. (2019). “The First NuSTAR Observation of 4U 1538–522: Updated Orbital Ephemeris and a Strengthened Case for an Evolving Cyclotron Line Energy”. In: *The Astrophysical Journal* 873.1, p. 62.

Heuvel E. P. J. van den (1994). “Interacting binaries: topics in close binary evolution.” In: *Saas-Fee Advanced Course 22: Interacting Binaries*, pp. 263–474.

Hickox R. C., Narayan R., and Kallman T. R. (2004). “Origin of the soft excess in X-ray pulsars”. In: *The Astrophysical Journal* 614.2, p. 881.

Hohmann W. (1960). *The attainability of heavenly bodies*. 44. National Aeronautics and Space Administration.

Homan J. et al. (Feb. 2018). “Absence of Reflection Features in $NuSTAR$ Spectra of the Luminous Neutron Star X-Ray Binary GX 5–1”. In: *The Astrophysical Journal* 853.2, p. 157. DOI: 10.3847/1538-4357/aaa439. URL: https://doi.org/10.3847/1538-4357/aaa439.

HUANG S. (1963). “Modes of mass ejection by binary stars and the effect on their orbital periods”. In: *Publications of Goddard Space Flight Center*, p. 63.

Hubbell J. H. (2003). “Radiation Physics”. In: *Encyclopedia of Physical Science and Technology (Third Edition)*. Ed. by R. A. Meyers. Third Edition. New York: Academic Press, pp. 561–580. ISBN: 978-0-12-227410-7. DOI: https://doi.org/10.1016/B0-12-227410-5/00634-7. URL: https://www.sciencedirect.com/science/article/pii/B0122274105006347.

Hung L.-W., Hickox R. C., Boroson B. S., and Vrtilek S. D. (2010). “Suzaku X-ray Spectra and Pulse Profile Variations During the Superorbital Cycle of LMC X-4”. In: *The Astrophysical Journal* 720.2, p. 1202.

Hut P. (1981). “Tidal evolution in close binary systems”. In: *Astronomy and Astrophysics, vol. 99, no. 1, June 1981, p. 126-140.* 99, pp. 126–140.

Iaria R. et al. (2015). “A possible cyclotron resonance scattering feature near 0.7 keV in X1822-371”. In: *Astronomy & Astrophysics* 577, A63.

Inam S., Baykal A., and Beklen E. (2010). “Analysis of RXTE-PCA Observations of SMC X-1”. In: *Monthly Notices of the Royal Astronomical Society* 403.1, pp. 378–386.

Isenberg M., Lamb D., and Wang J. C. (1998). “Effects of the geometry of the line-forming region on the properties of cyclotron resonant scattering lines”. In: *The Astrophysical Journal* 505.2, p. 688.

Islam N., Maitra C., Pradhan P., and Paul B. (2015). “A Suzaku view of IGR J16393–4643”. In: *Monthly Notices of the Royal Astronomical Society* 446.4, pp. 4148–4154.

Islam N. and Paul B. (2014). “Orbital phase resolved spectroscopy of GX 301-2 with MAXI”. In: *Monthly Notices of the Royal Astronomical Society* 441.3, pp. 2539–2545.

– (2016). “Orbital evolution and search for eccentricity and apsidal motion in the eclipsing HMXB 4U 1700- 37”. In: *Monthly Notices of the Royal Astronomical Society* 461.1, pp. 816–824.

Iwakiri W. B., Pottschmidt K., et al. (2019). “Spectral and Timing Analysis of the Accretion-powered Pulsar 4U 1626–67 Observed with Suzaku and NuSTAR”. In: *The Astrophysical Journal* 878.2, p. 121.

Iwakiri W., Terada Y., et al. (2012). “POSSIBLE DETECTION OF AN EMISSION CYCLOTRON RESONANCE SCATTERING FEATURE FROM THE ACCRETION-POWERED PULSAR 4U 1626- 67”. In: *The Astrophysical Journal* 751.1, p. 35.

Jahoda K. et al. (1996). “In-orbit performance and calibration of the Rossi X-ray Timing Explorer (RXTE) Proportional Counter Array (PCA)”. In: *Euv, x-ray, and gamma-ray instrumentation for astronomy vii*. Vol. 2808. SPIE, pp. 59–70.

Jain C., Paul B., and Dutta A. (2010). “New measurement of orbital and spin period evolution of the accretion disc corona source 4U 1822- 37”. In: *Monthly Notices of the Royal Astronomical Society* 409.2, pp. 755–762.

Jaisawal G. K. and Naik S. (2015a). “Broad-band spectroscopy of the eclipsing high-mass X-ray binary 4U 1700- 37 with Suzaku”. In: *Monthly Notices of the Royal Astronomical Society* 448.1, pp. 620–628.

– (2015b). “Detection of fundamental and first harmonic cyclotron line in X-ray pulsar Cep X-4”. In: *Monthly Notices of the Royal Astronomical Society: Letters* 453.1, pp. L21–L25.

– (2016a). “Detection of cyclotron resonance scattering feature in high-mass X-ray binary pulsar SMC X-2”. In: *Monthly Notices of the Royal Astronomical Society: Letters* 461.1, pp. L97–L101.

– (2016b). “Investigation of iron emission lines in the eclipsing high mass X-ray binary pulsar OAO 1657-415”. In: *arXiv preprint arXiv:1601.02345*.

Jaisawal G. K., Naik S., and Epili P. (2016). “Suzaku view of the Be/X-ray binary pulsar GX 304-1 during Type I X-ray outbursts”. In: *Monthly Notices of the Royal Astronomical Society* 457.3, pp. 2749–2760.

Jaisawal G. K., Naik S., Epili P. R., et al. (2021). “AstroSat observations of eclipsing high mass X-ray binary pulsar OAO 1657-415”. In: *Journal of Astrophysics and Astronomy* 42.2, p. 72.

Jaisawal G. K., Naik S., Gupta S., et al. (2021). “Detection of X-ray pulsations at the lowest observed luminosity of Be/X-ray binary pulsar EXO 2030+ 375 with AstroSat”. In: *Journal of Astrophysics and Astronomy* 42.2, p. 33.

James M., Paul B., Devasia J., and Indulekha K. (2010). “Discovery of a 0.02 Hz QPO feature in the transient X-ray pulsar KS 1947+ 300”. In: *Monthly Notices of the Royal Astronomical Society* 407.1, pp. 285–290.

Jansen F. et al. (2001). “XMM-Newton observatory-I. The spacecraft and operations”. In: *Astronomy & Astrophysics* 365.1, pp. L1–L6.

Jenke P., Finger M., Wilson-Hodge C., and Camero-Arranz A. (2012). “ORBITAL DECAY AND EVIDENCE OF DISK FORMATION IN THE X-RAY BINARY PULSAR OAO 1657- 415”. In: *The Astrophysical Journal* 759.2, p. 124.

Jonker P. G. and Klis M. van der (2001). “The newly discovered X-ray pulsar 4U 1822-37”. In: *Two Years of Science with Chandra*, p. 41.

Kaaret P. (2021). “X-ray polarimetry”. In: *The WSPC Handbook of Astronomical Instrumentation: Volume 4: X-Ray Astronomical Instrumentation*. World Scientific, pp. 281–300.

Kaaret P. et al. (1990). “Stellar X-Ray Polarimeter: a focal plane polarimeter for the Spectrum X-Gamma mission”. In: *Optical Engineering* 29.7, pp. 773–780.

Kaastra J. and Bleeker J. (2016). “Optimal binning of X-ray spectra and response matrix design”. In: *Astronomy & Astrophysics* 587, A151.

Kabiraj S., Islam N., and Paul B. (2020). “Investigating a unique partial eclipse in the high-mass X-ray binary IGR J16393- 4643 with Swift-XRT”. In: *Monthly Notices of the Royal Astronomical Society* 491.1, pp. 1491–1497.

Kabiraj S. and Paul B. (2020). “Broad-band X-ray characteristics of the transient pulsar GRO J2058+ 42”. In: *Monthly Notices of the Royal Astronomical Society* 497.1, pp. 1059–1065.

Kamata Y. et al. (1990). “X-ray observations of OAO 1657-415 with Tenma and Ginga”. In: *Publications of the Astronomical Society of Japan* 42, pp. 785–792.

Kaper L., Lamers H., Ruymaekers E., Van den Heuvel E., and Zuiderwijk E. (1995). “Wray 977 (GX301-2): a hypergiant with pulsar companion”. In: *arXiv preprint astro-ph/9503003*.

Karpouzas K. et al. (2020). “The Comptonizing medium of the neutron star in 4U 1636- 53 through its lower kilohertz quasi-periodic oscillations”. In: *Monthly Notices of the Royal Astronomical Society* 492.1, pp. 1399–1415.

Kaur R., Paul B., Kumar B., and Sagar R. (2008). “A Study of the Long-Term Evolution of Quasi-Periodic Oscillations in the Accretion-Powered X-Ray Pulsar 4U 1626–67”. In: *The Astrophysical Journal* 676.2, p. 1184.

Kelley R. L., Rappaport S., and Ayasli S. (1983). “Discovery of 9.3 S X-ray pulsations from 2S 1553-542 and a determination of the orbit”. In: *Astrophysical Journal, Part 1 (ISSN 0004-637X), vol. 274, Nov. 15, 1983, p. 765-770.* 274, pp. 765–770.

Kii T., Hayakawa S., Nagase F., Ikegami T., and Kawai N. (1986). “Anisotropic X-ray transfer in a strongly magnetized plasma of the X-ray pulsar 4U 1626-67”. In: *Astronomical Society of Japan, Publications (ISSN 0004-6264), vol. 38, no. 5, 1986, p. 751-774.* 38, pp. 751–774.

Kislat F., Clark B., Beilicke M., and Krawczynski H. (2015). “Analyzing the data from X-ray polarimeters with Stokes parameters”. In: *Astroparticle Physics* 68, pp. 45–51.

Klis M. and Bonnet-Bidaud J. (1984). “The orbital parameters and the X-ray pulsation of VELA X-1 (4U 0900-40)”. In: *Astronomy and Astrophysics* 135, pp. 155–170.

Klis M. v. d. (1997). “Kilohertz quasi-periodic oscillations in low-mass X-ray binaries”. In: *Astronomical Time Series*. Springer, pp. 121–132.

– (2000). “Millisecond oscillations in X-ray binaries”. In: *Annual Review of Astronomy and Astrophysics* 38.1, pp. 717–760.

Klochkov D., Doroshenko V., et al. (2012). “Outburst of GX 304–1 monitored with INTEGRAL: positive correlation between the cyclotron line energy and flux”. In: *Astronomy & Astrophysics* 542, p. L28.

Klochkov D., Staubert R., et al. (2007). “INTEGRAL Observations of Her Xl”. In: *The Obscured Universe. Proceedings of the VI INTEGRAL Workshop*. Vol. 622, p. 461.

Klochkov, D., Santangelo, A., Staubert, R., and Ferrigno, C. (2008). “Giant outburst of EXO 2030+375: pulse-phase resolved analysis of INTEGRAL data”. In: *A&A* 491.3, pp. 833–840. DOI: 10.1051/0004-6361:200810673. URL: https://doi.org/10.1051/0004-6361:200810673.

Knoll G. F. (2010). *Radiation detection and measurement*. John Wiley & Sons.

Koh D. T. et al. (1997). “Rapid Spin-Up Episodes in the Wind-fed Accreting Pulsar GX 301–2”. In: *The Astrophysical Journal* 479.2, p. 933.

Koyama K., Kawada M., et al. (1991). “A new X-ray pulsar GS 2138+ 56 (Cepheus X-4)”. In: *Astrophysical Journal, Part 2-Letters (ISSN 0004-637X), vol. 366, Jan. 1, 1991, p. L19-L22.* 366, pp. L19–L22.

Koyama K., Tsunemi H., et al. (2007). “X-ray imaging spectrometer (XIS) on board Suzaku”. In: *Publications of the Astronomical Society of Japan* 59.sp1, S23–S33.

Kreykenbohm I., Kretschmar P., et al. (1998). “Vela X-1 as seen by RXTE”. In: *arXiv preprint astro-ph/9810282*.

Kreykenbohm I., Mowlavi N., et al. (2005). “Observation of V0332+ 53 Over the 2004/2005 Outburst with INTEGRAL”. In.

Kreykenbohm I., Pottschmidt K., et al. (2004). “GX 301-2 as Seen by INTEGRAL”. In.

Kreykenbohm, I. et al. (2002). “Confirmation of two cyclotron lines in Vela X-1”. In: *A&A* 395.1, pp. 129–140. DOI: 10.1051/0004-6361:20021181. URL: https://doi.org/10.1051/0004-6361:20021181.

Krimm H. A. et al. (2013). “The Swift/BAT hard X-ray transient monitor”. In: *The Astrophysical Journal Supplement Series* 209.1, p. 14.

Kuehnel M. et al. (2014). “Orbital parameters and spin evolution of RX J0520. 5-6932”. In: *The Astronomer’s Telegram* 5856, p. 1.

Kühnel M. et al. (2013). “GRO J1008- 57: an (almost) predictable transient X-ray binary”. In: *Astronomy & Astrophysics* 555, A95.

La Barbera A., Baushev A., et al. (2004). “A Study of Cen X-3 as Seen by INTEGRAL”. In: *5th INTEGRAL Workshop on the INTEGRAL Universe*. Vol. 552, p. 337.

La Barbera A., Burderi L., Di Salvo T., Iaria R., and Robba N. (2001). “The 0.1-100 keV spectrum of LMC X-4 in the high state: Evidence for a high-energy cyclotron absorption line”. In: *The Astrophysical Journal* 553.1, p. 375.

La Barbera, A., Santangelo, A., Orlandini, M., and Segreto, A. (2003). “A pulse phase-dependent spectroscopic study of Vela X-1 in the 8-100 keV band”. In: *A&A* 400.3, pp. 993–1005. DOI: 10.1051/0004-6361:20030010. URL: https://doi.org/10.1051/0004-6361:20030010.

La Barbera, A., Segreto, A., Santangelo, A., Kreykenbohm, I., and Orlandini, M. (2005). “A study of an orbital cycle of GX 301-2 observed by BeppoSAX”. In: *A&A* 438.2, pp. 617–632. DOI: 10.1051/0004-6361:20041509. URL: https://doi.org/10.1051/0004-6361:20041509.

Lai D. (1996). “Orbital decay of the PSR J0045–7319 binary system: Age of radio pulsar and initial spin of neutron star”. In: *The Astrophysical Journal* 466.1, p. L35.

Leahy D. A. and Kostka M. (Jan. 2008). “Stellar wind accretion in GX 301–2: evidence for a high-density stream”. In: *Monthly Notices of the Royal Astronomical Society* 384.2, pp. 747–754. ISSN: 0035-8711. DOI: 10.1111/j.1365-2966.2007.12754.x. eprint: https://academic.oup.com/mnras/article-pdf/384/2/747/3410647/mnras0384-0747.pdf. URL: https://doi.org/10.1111/j.1365-2966.2007.12754.x.

Leahy D. (1987). “Searches for pulsed emission-Improved determination of period and amplitude from epoch folding for sinusoidal signals”. In: *Astronomy and Astrophysics (ISSN 0004-6361), vol. 180, no. 1-2, June 1987, p. 275-277. NSERC-supported research.* 180, pp. 275–277.

Lecar M., Wheeler J. C., and McKee C. F. (1976). “Tidal circularization of the binary X-ray sources Hercules X-1 and Centaurus X-3”. In: *Astrophysical Journal, vol. 205, Apr. 15, 1976, pt. 1, p. 556-562.* 205, pp. 556–562.

Levine A., Rappaport S., Putney A., Corbet R., and Nagase F. (1991). “LMC X-4-GINGA observations and search for orbital period changes”. In: *The Astrophysical Journal* 381, pp. 101–109.

Levine A. M., Bradt H., et al. (1996). “First results from the all-sky monitor on the rossi x-ray timing explorer”. In: *The Astrophysical Journal* 469.1, p. L33.

Lewin W. H., Heuvel E. P. van den, and Paradijs J. van (1997). *X-ray Binaries*. Vol. 26. Cambridge University Press.

Li F. and Clark G. (1977). "SMC X-2 and SMC X-3". In: *International Astronomical Union Circular* 3154, p. 1.

Liu J. (2020). "On the spin-up events and spin direction of the X-ray pulsar GX 301-2". In: *Monthly Notices of the Royal Astronomical Society* 496.3, pp. 3991–3995.

Liu J., Ji L., et al. (2021). "Disc versus wind accretion in X-ray pulsar GX 301-2". In: *Monthly Notices of the Royal Astronomical Society* 504.2, pp. 2493–2500.

Liu Q., Wang W., et al. (2022). "Detection of a quasi-periodic oscillation at 40 mHz in Cen X-3 with Insight-HXMT". In: *Monthly Notices of the Royal Astronomical Society* 516.4, pp. 5579–5587.

Lomb N. R. (1976). "Least-squares frequency analysis of unequally spaced data". In: *Astrophysics and space science* 39, pp. 447–462.

Lund N. et al. (2003). "JEM–X: The X-ray monitor aboard INTEGRAL". In: *Astronomy & Astrophysics* 411.1, pp. L231–L238.

Lutovinov A., Tsygankov S., and Chernyakova M. (2012). "Strong outburst activity of the X-ray pulsar X Persei during 2001–2011". In: *Monthly Notices of the Royal Astronomical Society* 423.2, pp. 1978–1984.

Lutovinov A., Tsygankov S., Molkov S., et al. (2021). "SRG/ART-XC and NuSTAR Observations of the X-Ray pulsar GRO J1008–57 in the Lowest Luminosity State". In: *The Astrophysical Journal* 912.1, p. 17.

Lutovinov A., Tsygankov S., Revnivtsev M., et al. (2004). "Variability of X-ray pulsars in a hard energy band observed with INTEGRAL". In: *arXiv preprint astro-ph/0407350*.

Lutovinov A., Tsygankov S., Suleimanov V., et al. (2015). "Transient X-ray pulsar V 0332+ 53: pulse-phase-resolved spectroscopy and the reflection model". In: *Monthly Notices of the Royal Astronomical Society* 448.3, pp. 2175–2186.

Lutovinov A. A., Buckley D. A., Townsend L. J., Tsygankov S. S., and Kennea J. (2016). "2S 1553- 542: a Be/X-ray binary pulsar on the far side of the Galaxy". In: *Monthly Notices of the Royal Astronomical Society* 462.4, pp. 3823–3829.

Ma R. et al. (2022). "High energy millihertz quasi-periodic oscillations in 1A 0535+ 262 with Insight-HXMT challenge current models". In: *Monthly Notices of the Royal Astronomical Society* 517.2, pp. 1988–1999.

Maitra C. and Paul B. (June 2013a). "PULSE-PHASE-DEPENDENT VARIATIONS OF THE CYCLOTRON ABSORPTION FEATURES OF THE ACCRETING PULSARS A0535+26, XTE J1946+274, AND 4U 1907+09 WITH SUZAKU". In: *The Astrophysical Journal* 771.2, p. 96. DOI: 10.1088/0004-637x/771/2/96. URL: https://doi.org/10.1088/0004-637x/771/2/96.

– (2013b). "Pulse-phase-resolved Spectroscopy of Vela X-1 with Suzaku". In: *The Astrophysical Journal* 763.2, p. 79.

Maitra C., Paul B., and Naik S. (2012). “Timing and broad-band spectroscopy of 1A 1118- 61 with Suzaku”. In: *Monthly Notices of the Royal Astronomical Society* 420.3, pp. 2307–2317.

Makishima K., Mihara T., Ishida M., et al. (1990). “Discovery of a prominent cyclotron absorption feature from the transient X-ray pulsar X0331+ 53”. In: *Astrophysical Journal, Part 2-Letters (ISSN 0004-637X), vol. 365, Dec. 20, 1990, p. L59-L62.* 365, pp. L59–L62.

Makishima K., Mihara T., Nagase F., and Tanaka Y. (1999). “Cyclotron resonance effects in two binary X-ray pulsars and the evolution of neutron star magnetic fields”. In: *The Astrophysical Journal* 525.2, p. 978.

Makishima K., Kawai N., et al. (1984). “Discovery of a 437.5-s X-ray pulsation from 4U 1907+ 09”. In: *Astronomical Society of Japan, Publications (ISSN 0004-6264), vol. 36, no. 4, 1984, p. 679-689.* 36, pp. 679–689.

Malacaria C., Jenke P., et al. (2020). “The ups and downs of accreting X-ray pulsars: decade-long observations with the Fermi Gamma-ray burst monitor”. In: *The Astrophysical Journal* 896.1, p. 90.

Malacaria C., Kretschmar P., et al. (2021). “The X-ray pulsar XTE J1858+ 034 observed with NuSTAR and Fermi/GBM: spectral and timing characterization plus a cyclotron line”. In: *The Astrophysical Journal* 909.2, p. 153.

Malacaria C., Klochkov D., Santangelo A., and Staubert R. (2015). “Luminosity-dependent spectral and timing properties of the accreting pulsar GX 304- 1 measured with INTEGRAL”. In: *Astronomy & Astrophysics* 581, A121.

Mandal M. and Pal S. (2021). “Detection of Low-Frequency QPO From X-ray Pulsar XTE J1858+ 034 During Outburst in 2019 with NuSTAR”. In: *arXiv preprint arXiv:2101.09250*.

– (Jan. 2022). “Study of timing and spectral properties of the X-ray pulsar 1A 0535+262 during the giant outburst in 2020 November–December”. In: *Monthly Notices of the Royal Astronomical Society* 511.1, pp. 1121–1130. DOI: 10.1093/mnras/stac111. URL: https://doi.org/10.1093%2Fmnras%2Fstac111.

Manikantan H., Kumar M., Paul B., and Rana V. (2023). “Investigating the orbital evolution of the eccentric HMXB GX 301–2 using long-term X-ray light curves”. In: *Monthly Notices of the Royal Astronomical Society* 527.1, pp. 640–650.

Manikantan H., Paul B., and Rana V. (2023). “An investigation of the ‘10 keV feature’in the spectra of accretion powered X-ray pulsars with NuSTAR”. In: *Monthly Notices of the Royal Astronomical Society* 526.1, pp. 1–28.

Manikantan H., Paul B., Roy K., and Rana V. (2023). “Changes in the distribution of circumbinary material around the HMXB GX 301-2 during a rapid spin-up episode of the neutron star”. In: *Monthly Notices of the Royal Astronomical Society* 520.1, pp. 1411–1416.

Manzo, G. et al. (1997). “The high pressure gas scintillation proportional counter on-board the BeppoSAX X-ray astronomy satellite”. In: *Astron. Astrophys. Suppl. Ser.* 122.2, pp. 341–356. DOI: 10.1051/aas:1997139. URL: https://doi.org/10.1051/aas:1997139.

Marshall N. and Ricketts M. J. (1980). “Determination of a binary period for the variable X-ray source A1907+ 09”. In: *Monthly Notices of the Royal Astronomical Society* 193.1, 7P–13P.

Martínez Núnez, S. et al. (2003). "JEM-X observations of the Be/X-ray binary EXO 2030+375*". In: *A&A* 411.1, pp. L411–L414. DOI: 10.1051/0004-6361:20031205. URL: https://doi.org/10.1051/0004-6361:20031205.

Mason K. O. and Cordova F. A. (1982). "Infrared photometry of the X-ray binary 2A 1822-371-A model for the ultraviolet, optical, and infrared light curve". In: *The Astrophysical Journal* 262, pp. 253–262.

Mason K. O. and Córdova F. A. (1982). "Ultraviolet spectrophotometry of 2A 1822-371-A bulge on the accretion disk". In: *Astrophysical Journal, Part 1, vol. 255, Apr. 15, 1982, p. 603-609. Research supported by the US Department of Energy;* 255, pp. 603–609.

Mason K., Middleditch J., et al. (1980). "A 5.57 HR Modulation in the Optical Counterpart of 2S 1822-371". In: *Astrophysical Journal, Part 2-Letters to the Editor, vol. 242, Dec. 1, 1980, p. L109-L113. Research supported by the Miller Institute for Basic Research and US Department of Energy* 242, pp. L109–L113.

Mason K., Murdin P., Tuohy I., Seitzer P., and Branduardi-Raymont G. (1982). "Phase resolved optical spectroscopy of the compact X-ray binary 2A 1822–371". In: *Monthly Notices of the Royal Astronomical Society* 200.3, pp. 793–805.

Matsuoka M. et al. (Oct. 2009). "The MAXI Mission on the ISS: Science and Instruments for Monitoring All-Sky X-Ray Images". In: *Publications of the Astronomical Society of Japan* 61.5, pp. 999–1010. ISSN: 0004-6264. DOI: 10.1093/pasj/61.5.999. eprint: https://academic.oup.com/pasj/article-pdf/61/5/999/17453643/pasj61-0999.pdf. URL: https://doi.org/10.1093/pasj/61.5.999.

Mazeh T. and Shaham J. (1979). "The orbital evolution of close triple systems-The binary eccentricity". In: *Astronomy and Astrophysics* 77, pp. 145–151.

Mazzola S. et al. (2019). "Updated orbital ephemeris of the ADC source X 1822-371: a stable orbital expansion over 40 years". In: *Astronomy & Astrophysics* 625, p. L12.

McBride V. et al. (2007). "On the cyclotron line in Cepheus X-4". In: *Astronomy & Astrophysics* 470.3, pp. 1065–1070.

McClintock J. et al. (1977). "Optical candidates for two X-ray bursters and an X-ray pulsar". In: *Nature* 270.5635, pp. 320–321.

Meegan C., Fishman G., et al. (1992). "Spatial distribution of γ-ray bursts observed by BATSE". In: *Nature* 355.6356, pp. 143–145.

Meegan C., Lichti G., et al. (2009). "The Fermi gamma-ray burst monitor". In: *The Astrophysical Journal* 702.1, p. 791.

Meszaros P., Novick R., Szentgyorgyi A., Chanan G., and Weisskopf M. C. (1988). "Astrophysical implications and observational prospects of X-ray polarimetry". In: *The Astrophysical Journal* 324, pp. 1056–1067.

Middleditch J., Mason K., Nelson J., and White N. (1981). "4U 1626-67-A prograde spinning X-ray pulsar in a 2500 s binary system". In: *Astrophysical Journal*.

Mihara T., Makishima K., et al. (1991). “Discovery of a cyclotron resonance feature at 30 keV from the transient X-ray pulsar Cepheus X-4”. In: *Astrophysical Journal, Part 2-Letters (ISSN 0004-637X), vol. 379, Oct. 1, 1991, p. L61, L64.* 379, p. L61.

Mihara T. (1995). “Observational study of X-ray spectra of binary pulsars with Ginga”. PhD thesis. Cosmic Radiation Laboratory, Institute of Physical and Chemical Research.

Mihara T., Nakajima M., et al. (Nov. 2011). “Gas Slit Camera (GSC) onboard MAXI on ISS”. In: *Publications of the Astronomical Society of Japan* 63.sp3, S623–S634. ISSN: 0004-6264. DOI: 10.1093/pasj/63.sp3.S623. eprint: https://academic.oup.com/pasj/article-pdf/63/sp3/S623/17442673/pasj63-0S623.pdf. URL: https://doi.org/10.1093/pasj/63.sp3.S623.

Milgrom M. (1978). *On the nature of the galactic bulge X-ray sources*. Tech. rep. Weizmann Inst. of Science.

Miller M. C., Lamb F. K., and Psaltis D. (1998). “Sonic-point model of kilohertz quasi-periodic brightness oscillations in low-mass x-ray binaries”. In: *The Astrophysical Journal* 508.2, p. 791.

Molkov S., Lutovinov A., Tsygankov S., Mereminskiy I., and Mushtukov A. (2019). “Discovery of a Pulse-phase-transient Cyclotron Line in the X-Ray pulsar GRO J2058+ 42”. In: *The Astrophysical Journal Letters* 883.1, p. L11.

Mönkkönen J. et al. (2020). “Discovery of a retrogradely rotating neutron star in the X-ray pulsar GX 301–2”. In: *Monthly Notices of the Royal Astronomical Society* 494.2, pp. 2178–2182.

Morgan E., Remillard R., and Greiner J. (1997). “RXTE observations of QPOs in the black hole candidate GRS 1915+ 105”. In: *The Astrophysical Journal* 482.2, p. 993.

Motch C. and Janot-Pacheco E. (1987). “The optical counterpart of the X-ray transient EXO 2030+ 375”. In: *Astronomy and Astrophysics (ISSN 0004-6361), vol. 182, no. 2, Aug. 1987, p. L55-L58.* 182, pp. L55–L58.

Motta S., Rouco-Escorial A., Kuulkers E., Muñoz-Darias T., and Sanna A. (2017). “Links between quasi-periodic oscillations and accretion states in neutron star low-mass X-ray binaries”. In: *Monthly Notices of the Royal Astronomical Society* 468.2, pp. 2311–2324.

Mowlavi N. et al. (2006). “INTEGRAL observation of the high-mass X-ray transient V 0332+ 53 during the 2005 outburst decline”. In: *Astronomy & Astrophysics* 451.1, pp. 187–194.

Mukerjee K., Antia H., and Katoch T. (2020). “AstroSat Observations of GRO J2058+ 42 during the 2019 Outburst”. In: *The Astrophysical Journal* 897.1, p. 73.

Mukherjee U., Bapna S., Raichur H., Paul B., and Jaaffrey S. (2006). “Variable Quasi Periodic Oscillations during an outburst of the transient X-ray pulsar XTE J1858+ 034”. In: *Journal of Astrophysics and Astronomy* 27, pp. 25–35.

Mukherjee U., Raichur H., Paul B., Naik S., and Bhatt N. (2006). “Orbital evolution and orbital phase resolved spectroscopy of the HMXB pulsar 4U 1538-52 with RXTE-PCA and BeppoSAX”. In: *Journal of Astrophysics and Astronomy* 27.4, pp. 411–423.

Mukherjee U. and Paul B. (2004). “Orbital phase spectroscopy of GX 301-2 with RXTE-PCA”. In: *A&A* 427.2, pp. 567–573. DOI: 10.1051/0004-6361:20034407. URL: https://doi.org/10.1051/0004-6361:20034407.

Muleri F. (2014). “On the operation of X-ray polarimeters with a large field of view”. In: *The Astrophysical Journal* 782.1, p. 28.

Müller, S. et al. (2012). “The reawakening of the sleeping X-ray pulsar XTE J1946+274”. In: *A&A* 546, A125. DOI: 10.1051/0004-6361/201219580. URL: https://doi.org/10.1051/0004-6361/201219580.

Munoz-Darias T., Casares J., and Martìnez-Pais I. (2005). “The “k-correction” for irradiated emission lines in lmxbs: Evidence for a massive neutron star in x1822–371 (v691 cra)”. In: *The Astrophysical Journal* 635.1, p. 502.

Mushtukov A., Tsygankov S., et al. (2023). “X-ray polarimetry of X-ray pulsar X Persei: another orthogonal rotator?” In: *arXiv preprint arXiv:2303.17325*.

Mushtukov A. A., Suleimanov V. F., Tsygankov S. S., and Portegies Zwart S. (2021). “Spectrum formation in X-ray pulsars at very low mass accretion rate: Monte Carlo approach”. In: *Monthly Notices of the Royal Astronomical Society* 503.4, pp. 5193–5203.

Nabizadeh A. et al. (2019). “NuSTAR observations of wind-fed X-ray pulsar GX 301–2 during unusual spin-up event”. In: *Astronomy & Astrophysics* 629, A101.

Nabizadeh, Armin et al. (2019). “NuSTAR observations of wind-fed X-ray pulsar GX 301-2 during unusual spin-up event”. In: *A&A* 629, A101. DOI: 10.1051/0004-6361/201936045. URL: https://doi.org/10.1051/0004-6361/201936045.

Nagase F., Corbet R., et al. (1992). “Ginga observations of Centaurus X-3”. In: *Astrophysical Journal, Part 1 (ISSN 0004-637X), vol. 396, no. 1, Sept. 1, 1992, p. 147-160. Research supported by Royal Society and Japan Society for the Promotion of Science.* 396, pp. 147–160.

Nagase F., Hayakawa S., et al. (1982). “Observation of an outburst of the transient X-ray pulsar A0535+ 26 in 1980”. In: *Astrophysical Journal, Part 1, vol. 263, Dec. 15, 1982, p. 814-822.* 263, pp. 814–822.

Nagase F. (1989). “Accretion-powered X-ray pulsars”. In: *Astronomical Society of Japan, Publications (ISSN 0004-6264), vol. 41, no. 1, 1989, p. 1-79.* 41, pp. 1–79.

Naik S., Callanan P., Paul B., and Dotani T. (2006). “Broadband X-ray spectrum of KS 1947+300 with BeppoSAX”. In: *The Astrophysical Journal* 647.2, p. 1293.

Naik S. and Jaisawal G. K. (Apr. 2015). “Suzaku observation of Be/X-ray binary pulsar EXO 2030+375”. In: *Research in Astronomy and Astrophysics* 15.4, p. 537. DOI: 10.1088/1674-4527/15/4/007. URL: https://dx.doi.org/10.1088/1674-4527/15/4/007.

Naik S., Maitra C., Jaisawal G. K., and Paul B. (2013). “Timing and Spectral properties of Be/X-ray pulsar EXO 2030+ 375 during a Type I outburst”. In: *The Astrophysical Journal* 764.2, p. 158.

Naik S. and Paul B. (2003). “Spectral variations of the X-ray binary pulsar LMC X-4 during its long period intensity variation and a comparison with Her X-1”. In: *Astronomy & Astrophysics* 401.1, pp. 265–270.

– (2004a). “BeppoSAX observations of the accretion-powered X-ray pulsar SMC X-1”. In: *Astronomy & Astrophysics* 418.2, pp. 655–661.

– (2004b). “Timing and spectral studies of LMC X-4 in high and low states with BeppoSAX: detection of pulsations in the soft spectral component”. In: *The Astrophysical Journal* 600.1, p. 351.

– (2012). “Investigation of variability of iron emission lines in Centaurus X-3”. In: *arXiv preprint arXiv:1212.0949*.

Naik S., Paul B., Kachhara C., and Vadawale S. V. (2011). “Suzaku observation of the transient X-ray pulsar GRO J1008- 57”. In: *Monthly Notices of the Royal Astronomical Society* 413.1, pp. 241–248.

Nespoli E. and Reig P. (2010). “Discovery of a QPO in the X-ray pulsar 1A 1118-615: correlated spectral and aperiodic variability”. In: *arXiv preprint arXiv:1011.0564*.

Novick R., Weisskopf M. C., et al. (1978). “The OSO-8 mosaic graphite stellar X-ray polarimeter”. In: *New instrumentation for space astronomy*, pp. 127–130.

Novick R. and Wolff R. (1971). “A Large Area Thomson-Scattering Stellar X-Ray Polarimeter”. In: *Symposium-International Astronomical Union*. Vol. 41. Cambridge University Press, pp. 159–164.

Odaka H. et al. (2013). “Short-term Variability of X-Rays from Accreting Neutron Star Vela X-1. I. Suzaku Observations”. In: *The Astrophysical Journal* 767.1, p. 70.

Orlandini M., Dal Fiume D., et al. (1998). “BeppoSAX Observation of 4U 1626–67: Discovery of an AbsorptionCyclotron Resonance Feature”. In: *The Astrophysical Journal* 500.2, p. L163.

Orlandini M., Fiume D. D., Del Sordo S., et al. (1999). “The broad-band spectrum of OAO1657-415 with BeppoSAX: in search of cyclotron lines”. In: *arXiv preprint astro-ph/9908094*.

Orlandini M., Fiume D. D., Frontera F., et al. (1998). “The vela x-1 pulse-averaged spectrum as observed by bepposax”. In: *Astron. Astrophys.* 332, p. 121. arXiv: astro-ph/9711215.

Orlandini M. (2006). “Broad-band spectral properties of accreting X-ray binary pulsars”. In: *Advances in Space Research* 38.12, pp. 2742–2746.

Owens A., Oosterbroek T., and Parmar A. (1997). “The complex X-ray spectrum of the low-mass X-ray binary 4U 1626-67”. In: *arXiv preprint astro-ph/9706021*.

Pahari M. and Pal S. (2012). “RXTE observation of recent flaring activity from the transient X-ray pulsar 2S 1553- 542”. In: *Monthly Notices of the Royal Astronomical Society* 423.4, pp. 3352–3359.

Paizis A. et al. (2005). “Resolving the hard X-ray emission of GX 5-1 with INTEGRAL”. In: *Astronomy & Astrophysics* 443.2, pp. 599–608.

Parkes G., Mason K., Murdin P., and Culhane J. (1980). “A spectral study of Wray 977, the optical counterpart of the binary X-ray pulsar 4U 1223–62”. In: *Monthly Notices of the Royal Astronomical Society* 191.3, pp. 547–558.

Parmar A., Oosterbroek T., et al. (2000). “Broad-band BeppoSAX observation of the low-mass X-ray binary X1822-371”. In: *arXiv preprint astro-ph/0001407*.

Parmar A., White N., Stella L., Izzo C., and Ferri P. (1989). “The transient 42 second X-ray pulsar EXO 2030+ 375. I-The discovery and the luminosity dependence of the pulse period variations”. In: *Astrophysical Journal, Part 1 (ISSN 0004-637X), vol. 338, March 1, 1989, p. 359-372.* 338, pp. 359–372.

Paul B. (2017). “Neutron Stars in X-ray Binaries and their Environments”. In: *Journal of Astrophysics and Astronomy* 38, pp. 1–12.

– (2022). “The X-ray Polarimetry Satellite XPoSat”. In: *44th COSPAR Scientific Assembly. Held 16-24 July* 44, p. 1853.

Paul B., Nagase F., et al. (2002). “Nature of the Soft Spectral Component in the X-ray Pulsars SMC X-1 and LMC X-4”. In: *The Astrophysical Journal* 579.1, p. 411.

Paul B. and Naik S. (2011). “Transient high mass X-ray binaries”. In: *arXiv preprint arXiv:1110.4446*.

Paul B. and Rao A. (1998). “Quasi-periodic oscillations discovered in the new X-ray pulsar XTE J1858+ 034”. In: *arXiv preprint astro-ph/9805366*.

Peirano V. and Méndez M. (2022). “Lags of the kilohertz quasi-periodic oscillations in the transient source XTE J1701- 462”. In: *Monthly Notices of the Royal Astronomical Society* 513.2, pp. 2804–2813.

Petre R. and Serlemitsos P. J. (June 1985). “Conical imaging mirrors for high-speed x-ray telescopes”. In: *Appl. Opt.* 24.12, pp. 1833–1837. DOI: 10.1364/AO.24.001833. URL: https://opg.optica.org/ao/abstract.cfm?URI=ao-24-12-1833.

Petterson J. A. (1978). “On the occurrence of streams and disks in massive X-ray binary systems”. In: *Astrophysical Journal, Part 1, vol. 224, Sept. 1, 1978, p. 625-630.* 224, pp. 625–630.

Pike S. N. et al. (2019). “Observing the transient pulsations of SMC X-1 with NuSTAR”. In: *The Astrophysical Journal* 875.2, p. 144.

Pradhan P., Maitra C., and Paul B. (2020). “Is Superorbital Modulation in SMC X-1 Caused by Absorption in a Warped Precessing Accretion Disk?” In: *The Astrophysical Journal* 895.1, p. 10.

Pradhan P., Maitra C., Paul B., Islam N., and Paul B. (2014a). “Variations in the pulsation and spectral characteristics of OAO 1657- 415”. In: *Monthly Notices of the Royal Astronomical Society* 442.3, pp. 2691–2700.

Pradhan P., Maitra C., Paul B., Islam N., and Paul B. C. (2014b). “Variations in the pulsation and spectral characteristics of OAO 1657- 415”. In: *Monthly Notices of the Royal Astronomical Society* 442.3, pp. 2691–2700.

Pradhan P., Paul B., Bozzo E., Maitra C., and Paul B. C. (2021). “Comprehensive broad-band study of accreting neutron stars with Suzaku: Is there a bi-modality in the X-ray spectrum?” In: *Monthly Notices of the Royal Astronomical Society* 502.1, pp. 1163–1190.

Pravdo S. H. and Ghosh P. (June 2001). “An Orbital Light-Curve Model for GX 301–2”. In: *The Astrophysical Journal* 554.1, p. 383. DOI: 10.1086/321350. URL: https://dx.doi.org/10.1086/321350.

Qu J. L., Zhang S., Song L. M., and Falanga M. (2005). “Discovery of new quasi-periodic oscillations in the X-ray transient source V0332+ 53”. In: *The Astrophysical Journal Letters* 629.1, p. L33.

Raichur H. and Paul B. (2008). “Quasi-periodic oscillations in Cen X-3 and the long-term intensity variations”. In: *The Astrophysical Journal* 685.2, p. 1109.

– (2010a). “Apsidal motion in 4U 0115+ 63 and orbital parameters of 2S 1417- 624 and V0332+ 53”. In: *Monthly Notices of the Royal Astronomical Society* 406.4, pp. 2663–2670.

– (2010b). “Effect of pulse profile variations on measurement of eccentricity in orbits of Cen X-3 and SMC X-1”. In: *Monthly Notices of the Royal Astronomical Society* 401.3, pp. 1532–1539.

Raman G., Paul B., and Bhattacharya D. (2021). “AstroSat detection of a mHz quasi-periodic oscillation and cyclotron line in IGR J19294+ 1816 during the 2019 outburst”. In: *Monthly Notices of the Royal Astronomical Society* 508.4, pp. 5578–5586.

Rampy R. A., Smith D. M., and Negueruela I. (2009). “IGR J17544- 2619 IN DEPTH WITH SUZAKU: DIRECT EVIDENCE FOR CLUMPY WINDS IN A SUPERGIANT FAST X-RAY TRANSIENT”. In: *The Astrophysical Journal* 707.1, p. 243.

Rappaport S. and Joss P. (1977). “Accretion torques in X-ray pulsars”. In: *Nature* 266.5604, pp. 683–685.

Ray P. S. and Chakrabarty D. (Dec. 2002). “The Orbit of the High-Mass X-Ray Binary Pulsar 1E 1145.1–6141”. In: *The Astrophysical Journal* 581.2, p. 1293. DOI: 10.1086/344300. URL: https://dx.doi.org/10.1086/344300.

Read A. M. and Ponman T. J. (2003). “The XMM-Newton EPIC background: Production of background maps and event files”. In: *Astronomy & Astrophysics* 409.1, pp. 395–410.

Reig P. and Coe M. (1999). “X-ray spectral properties of the pulsar EXO 2030+ 375 during an outburst”. In: *Monthly Notices of the Royal Astronomical Society* 302.4, pp. 700–706.

Reig P., Negueruela I., Papamastorakis G., Manousakis A., and Kougentakis T. (2005). “Identification of the optical counterparts of high-mass X-ray binaries through optical photometry and spectroscopy”. In: *Astronomy & Astrophysics* 440.2, pp. 637–646.

Remillard R. A. and McClintock J. E. (2006). “X-ray properties of black-hole binaries”. In: *Annu. Rev. Astron. Astrophys.* 44, pp. 49–92.

Reynolds A., Owens A., Kaper L., Parmar A., and Segreto A. (1999). “A BeppoSAX observation of the massive x-ray binary 4U1700-37”. In: *arXiv preprint astro-ph/9904349*.

Rivers E. et al. (2009). “A comprehensive spectral analysis of the X-ray pulsar 4U 1907+ 09 from two observations with the Suzaku X-ray observatory”. In: *The Astrophysical Journal* 709.1, p. 179.

Robba N. R., Di Salvo T., Burderi L., La Barbera A., and Cusumano G. (2000). “BeppoSAX observation of the X-ray pulsar 4U 1538-52”. In: *AIP Conference Proceedings*. Vol. 510. 1. American Institute of Physics, pp. 213–216.

Rodes-Roca J. J., Bernabeu G., Magazzù A., Torrejon J. M., and Solano E. (2018). “IGR J19294+ 1816: a new Be-X-ray binary revealed through infrared spectroscopy”. In: *Monthly Notices of the Royal Astronomical Society* 476.2, pp. 2110–2116.

Rodes-Roca, J. J. et al. (2009). “The first cyclotron harmonic of 4U 1538-52”. In: *A&A* 508.1, pp. 395–400. DOI: 10.1051/0004-6361/200912815. URL: https://doi.org/10.1051/0004-6361/200912815.

Rodriguez J. et al. (2009). “The nature of the X-ray binary IGR J19294+ 1816 from INTEGRAL, RXTE, and Swift observations”. In: *Astronomy & Astrophysics* 508.2, pp. 889–894.

Rothschild R., Markowitz A., et al. (May 2013). “OBSERVATIONS OF THE HIGH-MASS X-RAY BINARY A 0535+26 IN QUIESCENCE”. In: *The Astrophysical Journal* 770.1, p. 19. DOI: 10.1088/0004-637x/770/1/19. URL: https://doi.org/10.1088/0004-637x/770/1/19.

Rothschild R. E., Kühnel M., et al. (2017). “Discovery and modelling of a flattening of the positive cyclotron line/luminosity relation in GX 304- 1 with RXTE”. In: *Monthly Notices of the Royal Astronomical Society* 466.3, pp. 2752–2779.

Roy J., Choudhury M., and Agrawal P. (2017). “Timing and spectral study of igr j19294+ 1816 with the rxte: The discovery of cyclotron features”. In: *The Astrophysical Journal* 848.2, p. 124.

Saavedra E. A., Fogantini F. A., Combi J. A., García F., and Chaty S. (2022). “A NuSTAR observation of the eclipsing binary system OAO 1657-415: The revival of the cyclotron line”. In: *Astronomy & Astrophysics* 659, A48.

Sartore N., Jourdain E., and Roques J. P. (June 2015). “THE INTEGRAL/SPI VIEW OF A0535+26 DURING THE GIANT OUTBURST OF 2011 FEBRUARY”. In: *The Astrophysical Journal* 806.2, p. 193. DOI: 10.1088/0004-637x/806/2/193. URL: https://doi.org/10.1088/0004-637x/806/2/193.

Sato N. et al. (1986). “Orbital elements of the binary X-ray pulsar GX 301-2”. In: *The Astrophysical Journal* 304, pp. 241–248.

Scargle J. D. (1982). “Studies in astronomical time series analysis. II-Statistical aspects of spectral analysis of unevenly spaced data”. In: *Astrophysical Journal, Part 1, vol. 263, Dec. 15, 1982, p. 835-853.* 263, pp. 835–853.

Schanne S. et al. (2007). “INTEGRAL Observations of the Vela Region Focusing on Vela X-1”. In: *arXiv preprint astro-ph/0701641*.

Schmidtke P. et al. (1996). “UV Observations of Three LMC Be-Star/X-ray Binaries”. In: *Publications of the Astronomical Society of the Pacific* 108.726, p. 668.

Schönherr G. et al. (2007). “A model for cyclotron resonance scattering features”. In: *Astronomy & Astrophysics* 472.2, pp. 353–365.

Schreier E. et al. (1972). “Evidence for the binary nature of Centaurus X-3 from UHURU X-ray observations”. In.

Schulz N. S. et al. (2001). “Double-peaked X-ray lines from the oxygen/neon-rich accretion disk in 4U 1626–67”. In: *The Astrophysical Journal* 563.2, p. 941.

Schurch M., Udalski A., and Coe M. (2008). “OGLE-III counterpart to SMC X-2 reveals 18.62 day binary period”. In: *The Astronomer’s Telegram* 1670, p. 1.

Seifina E., Titarchuk L., and Shaposhnikov N. (2016). “X-ray spectra of the high-mass X-ray binary 4U 1700-37 using BeppoSAX, Suzaku, and RXTE observations”. In: *The Astrophysical Journal* 821.1, p. 23.

Seitzer P. et al. (Sept. 1979). “S 1822-371”. In: *IAU Cirulars* 3406, p. 1.

Shakura N. I. and Sunyaev R. A. (1973). “Black holes in binary systems. Observational appearance.” In: *Astronomy and Astrophysics, Vol. 24, p. 337-355* 24, pp. 337–355.

Sharma P., Sharma R., Jain C., and Dutta A. (2022). “Timing and spectral analysis of HMXB OAO 1657-415 with NuSTAR”. In: *Monthly Notices of the Royal Astronomical Society* 509.4, pp. 5747–5755.

Sharma R., Jain C., Rikame K., and Paul B. (2023). “Broad-band mHz QPOs and spectral study of LMC X-4 with AstroSat”. In: *Monthly Notices of the Royal Astronomical Society* 519.2, pp. 1764–1770.

Shinoda K. et al. (1990). “Discovery of the quasi-periodic oscillations from the X-ray pulsar X1627-673”. In: *Astronomical Society of Japan, Publications (ISSN 0004-6264), vol. 42, no. 2, 1990, p. L27-L32.* 42, pp. L27–L32.

Shirke P., Bala S., Roy J., and Bhattacharya D. (2021). “A new measurement of the spin and orbital parameters of the high mass X-ray binary Centaurus X-3 using AstroSat”. In: *Journal of Astrophysics and Astronomy* 42.2, p. 58.

Shtykovsky A., Lutovinov A., Arefiev V., et al. (2017). “NuSTAR observations of the X-ray pulsar LMC X-4: A constraint on the magnetic field and tomography of the system in the fluorescent iron line”. In: *Astronomy Letters* 43.3, pp. 175–185.

Shtykovsky A. E., Lutovinov A. A., Tsygankov S. S., and Molkov S. V. (2019). “Discovery of a cyclotron absorption line in the transient X-ray pulsar XTE J1829- 098”. In: *Monthly Notices of the Royal Astronomical Society: Letters* 482.1, pp. L14–L18.

Singh N. et al. (2002). “New measurements of orbital period change in Cygnus X-3”. In: *Astronomy & Astrophysics* 392.1, pp. 161–167.

Soffitta P. et al. (2021). “The instrument of the imaging x-ray polarimetry explorer”. In: *The Astronomical Journal* 162.5, p. 208.

Staubert R. et al. (2019). “Cyclotron lines in highly magnetized neutron stars”. In: *Astronomy & Astrophysics* 622, A61.

Stella L., White N., et al. (1985). “The discovery of 4.4 second X-ray pulsations from the rapidly variable X-ray transient V0332+ 53”. In: *The Astrophysical Journal* 288, pp. L45–L49.

Stella L. and Vietri M. (1997). “Lense-Thirring precession and quasi-periodic oscillations in low-mass X-ray binaries”. In: *The Astrophysical Journal* 492.1, p. L59.

Stephen J., Caroli E., Silva R. da, and Foschini L. (2001). “Gamma-ray polarization measurements with INTEGRAL/IBIS”. In: *AIP Conference Proceedings*. Vol. 587. 1. American Institute of Physics, pp. 816–820.

Strohmayer T. E. et al. (1996). “Millisecond X-ray variability from an accreting neutron star system”. In: *The Astrophysical Journal* 469.1, p. L9.

Strüder L. et al. (2001). “The European photon imaging camera on XMM-Newton: the pn-CCD camera”. In: *Astronomy & Astrophysics* 365.1, pp. L18–L26.

Sturrock P. (1971). “A model of pulsars”. In: *Astrophysical Journal, vol. 164, p. 529* 164, p. 529.

Suchy S., Fürst F., et al. (2012). “BROADBAND SPECTROSCOPY USING TWO SUZAKU OBSERVATIONS OF THE HMXB GX 301- 2”. In: *The Astrophysical Journal* 745.2, p. 124.

Suchy S., Pottschmidt K., et al. (2008). “Pulse phase-resolved analysis of the high-mass X-ray binary Centaurus X-3 over two binary orbits”. In: *The Astrophysical Journal* 675.2, p. 1487.

Takahashi T. et al. (2007). “Hard X-ray detector (HXD) on board Suzaku”. In: *Publications of the Astronomical Society of Japan* 59.sp1, S35–S51.

Takeshima T., Corbet R., Marshall F., Swank J., and Chakrabarty D. (1998). “XTE J1858+034.” In: *International Astronomical Union Circular* 6826, p. 1.

Takeshima T., Dotani T., Mitsuda K., and Nagase F. (1994). “Discovery of the quasi-periodic oscillations from V0332+ 53”. In: *Astrophysical Journal, Part 1 (ISSN 0004-637X), vol. 436, no. 2, p. 871-874* 436, pp. 871–874.

Tamang R., Ghising M., Tobrej M., Rai B., and Paul B. C. (Aug. 2022). “Spectral and timing analysis of Be/X-ray binary EXO 2030+375 during its giant 2021 outburst”. In: *Monthly Notices of the Royal Astronomical Society* 515.4, pp. 5407–5415. ISSN: 0035-8711. DOI: 10.1093/mnras/stac2135. eprint: https://academic.oup.com/mnras/article-pdf/515/4/5407/45478298/stac2135.pdf. URL: https://doi.org/10.1093/mnras/stac2135.

Tanaka Y. (2005). “Observations of compact x-ray sources”. In: *Radiation Hydrodynamics in Stars and Compact Objects: Proceedings of Colloquium No. 89 of the International Astronomical Union Held at Copenhagen University June 11–20, 1985*. Springer, pp. 198–221.

Tananbaum H. a. et al. (1972). “Discovery of a periodic pulsating binary X-ray source in hercules from UHURU”. In: *Astrophysical Journal, vol. 174, p. L143* 174, p. L143.

Tauris T. M. and Heuvel E. P. J. van den (2006). "Formation and evolution of compact stellar X-ray sources". In: *Compact Stellar X-ray Sources*. Ed. by W. Lewin and M. van der Klis. Cambridge Astrophysics. Cambridge University Press, pp. 623–666. DOI: 10.1017/CBO9780511536281.017.

Tendulkar S. P. et al. (2014). "NuSTAR DISCOVERY OF A CYCLOTRON LINE IN THE BE/X-RAY BINARY RX J0520. 5- 6932 DURING OUTBURST". In: *The Astrophysical Journal* 795.2, p. 154.

Thompson T. W., Tomsick J. A., Rothschild R. E., Walter R., et al. (2006). "Orbital Parameters for the X-Ray Pulsar IGR J16393–4643". In: *The Astrophysical Journal* 649.1, p. 373.

Thorne K. S. and Zytkow A. (1977). "Stars with degenerate neutron cores. I-Structure of equilibrium models". In: *The Astrophysical Journal* 212, pp. 832–858.

Titarchuk L. (1994). "Generalized comptonization models and application to the recent high energy observations". In: *AIP Conference Proceedings*. Vol. 304. 1. American Institute of Physics, pp. 380–384.

Tobrej M., Rai B., Ghising M., Tamang R., and Paul B. C. (2023). "A high-mass X-ray binary pulsar 4U 1907+ 09 with multiple absorption-line features in the spectrum". In: *Monthly Notices of the Royal Astronomical Society* 518.4, pp. 4861–4869.

Tomar G., Pradhan P., and Paul B. (2021). "New measurements of the cyclotron line energy in Cen X-3". In: *Monthly Notices of the Royal Astronomical Society* 500.3, pp. 3454–3461.

Tomida H., Tsunemi H., Kimura M., Kitayama H., Matsuoka M., Ueno S., Kawasaki K., Katayama H., Miyaguchi K., Maeda K., et al. (2011a). "Solid-state slit camera (SSC) aboard MAXI". In: *Publications of the Astronomical Society of Japan* 63.2, pp. 397–405.

Tomida H., Tsunemi H., Kimura M., Kitayama H., Matsuoka M., Ueno S., Kawasaki K., Katayama H., Miyaguchi K., Maeda K., et al. (Apr. 2011b). "Solid-State Slit Camera (SSC) Aboard MAXI". In: *Publications of the Astronomical Society of Japan* 63.2, pp. 397–405. ISSN: 0004-6264. DOI: 10.1093/pasj/63.2.397. eprint: https://academic.oup.com/pasj/article-pdf/63/2/397/6036076/pasj63-0397.pdf. URL: https://doi.org/10.1093/pasj/63.2.397.

Trümper J., Kahabka P., Oegelman H., Pietsch W., and Voges W. (1986). "EXOSAT observations of the 35 day cycle of Hercules X-1 Evidence for neutron star precession". In: *Astrophysical Journal, Part 2-Letters to the Editor (ISSN 0004-637X), vol. 300, Jan. 15, 1986, p. L63-L67.* 300, pp. L63–L67.

Trümper J., Pietsch W., et al. (1978). "Evidence for strong cyclotron line emission in the hard X-ray spectrum of Hercules X-1". In: *Astrophysical Journal, Part 2-Letters to the Editor, vol. 219, Feb. 1, 1978, p. L105-L110. Deutsche Forschungsgemeinschaft* 219, pp. L105–L110.

Tsygankov S. S., Doroshenko V., Mushtukov A. A., Lutovinov A. A., and Poutanen J. (2019). "Study of the X-ray pulsar IGR J19294+ 1816 with NuSTAR: Detection of cyclotron line and transition to accretion from the cold disk". In: *Astronomy & Astrophysics* 621, A134.

Tsygankov S. S., Doroshenko V., Mushtukov A. A., Suleimanov V. F., et al. (2019). "Cyclotron emission, absorption, and the two faces of X-ray pulsar A 0535+ 262". In: *Monthly Notices of the Royal Astronomical Society: Letters* 487.1, pp. L30–L34.

Tsygankov S. S., Doroshenko V., Poutanen J., et al. (2022). “The X-ray polarimetry view of the accreting pulsar Cen X-3”. In: *The Astrophysical journal letters* 941.1, p. L14.

Tsygankov S. S., Lutovinov A. A., Krivonos R. A., et al. (2016). “NuSTAR discovery of a cyclotron absorption line in the transient X-ray pulsar 2S 1553- 542”. In: *Monthly Notices of the Royal Astronomical Society* 457.1, pp. 258–266.

Tsygankov S. S., Lutovinov A. A., Molkov S. V., et al. (2021). “X-ray pulsar XTE J1858+ 034: discovery of the cyclotron line and the revised optical identification”. In: *The Astrophysical Journal* 909.2, p. 154.

Tsygankov S. S., Rouco Escorial A., et al. (2019). “Dramatic spectral transition of X-ray pulsar GX 304- 1 in low luminous state”. In: *Monthly Notices of the Royal Astronomical Society: Letters* 483.1, pp. L144–L148.

Tsygankov S. and Lutovinov A. (2005a). “Long-term INTEGRAL and RXTE observations of the X-ray pulsar LMC X-4”. In: *Astronomy Letters* 31.6, pp. 380–387.

– (2005b). “Observations of the transient X-ray pulsar KS 1947+ 300 by the INTEGRAL and RXTE observatories”. In: *Astronomy Letters* 31, pp. 88–97.

Tsygankov S., Lutovinov A., Churazov E., and Sunyaev R. (2006). “V0332+ 53 in the outburst of 2004–2005: luminosity dependence of the cyclotron line and pulse profile”. In: *Monthly Notices of the Royal Astronomical Society* 371.1, pp. 19–28.

Turner M. J. et al. (1989). “The large area counter on Ginga”. In: *Astronomical Society of Japan, Publications (ISSN 0004-6264), vol. 41, no. 3, 1989, p. 345-372. Research supported by SERC.* 41, pp. 345–372.

Vadawale S. et al. (2018). “Phase-resolved X-ray polarimetry of the Crab pulsar with the AstroSat CZT Imager”. In: *Nature Astronomy* 2.1, pp. 50–55.

Van der Klis M. (1989). “Fourier techniques in X-ray timing”. In: *Timing neutron stars*. Springer, pp. 27–69.

VanderPlas J. T. (May 2018). “Understanding the Lomb–Scargle Periodogram”. In: *The Astrophysical Journal Supplement Series* 236.1, p. 16. DOI: 10.3847/1538-4365/aab766. URL: https://dx.doi.org/10.3847/1538-4365/aab766.

Varun, Maitra C., Pradhan P., Raichur H., and Paul B. (2019). “Probing the Cyclotron line characteristics of 4U 1538–522 using AstroSat-LAXPC”. In: *Monthly Notices of the Royal Astronomical Society: Letters* 484.1, pp. L1–L6.

Varun, Pradhan P., Maitra C., Raichur H., and Paul B. (2019). “Pulse Phase Variation of the Cyclotron Line in HMXB 4U 1907+ 09 with AstroSat LAXPC”. In: *The Astrophysical Journal* 880.1, p. 61.

Vasco D. et al. (2013). “Pulse phase and precession phase resolved spectroscopy of Hercules X-1: studying a representative Main-On with RXTE”. In: *Astronomy & Astrophysics* 550, A111.

Vasilopoulos G., Haberl F., Sturm R., Maggi P., and Udalski A. (2014). “Spectral and temporal properties of RX J0520. 5-6932 (LXP 8.04) during a type-I outburst”. In: *Astronomy & Astrophysics* 567, A129.

Verner D., Ferland G. J., Korista K., and Yakovlev D. (1996). “Atomic data for astrophysics. II. New analytic fits for photoionization cross sections of atoms and ions”. In: *arXiv preprint astro-ph/9601009*.

Vybornov V. et al. (2017). “Luminosity-dependent changes of the cyclotron line energy and spectral hardness in Cepheus X-4”. In: *Astronomy & Astrophysics* 601, A126.

Vybornov, V., Doroshenko, V., Staubert, R., and Santangelo, A. (2018). “Changes in the cyclotron line energy on short and long timescales in V 0332+53”. In: *A&A* 610, A88. DOI: 10.1051/0004-6361/201731750. URL: https://doi.org/10.1051/0004-6361/201731750.

Wang W. (2014a). “Temporal variations and spectral properties of the Be/X-ray pulsar GRO J1008—57 studied by INTEGRAL”. In: *Research in Astronomy and Astrophysics* 14.5, p. 565.

– (2014b). “Variations and correlations in cyclotron resonant scattering features of Vela X-1 studied by INTEGRAL”. In: *Monthly Notices of the Royal Astronomical Society* 440.2, pp. 1114–1124.

Watanabe S. et al. (2003). “Detection of a Fully Resolved Compton Shoulder of the Iron Kα Line in the Chandra X-Ray Spectrum of GX 301–2”. In: *The Astrophysical Journal* 597.1, p. L37.

Weisskopf M. C., Berthelsdorf R., et al. (1972). “A Graphite Crystal Polarimeter for Stellar X-Ray Astronomy”. In: *Review of Scientific Instruments* 43.7, pp. 967–976.

Weisskopf M. C., Cohen G., et al. (1976). “Measurement of the X-ray polarization of the Crab Nebula”. In: *Astrophysical Journal, vol. 208, Sept. 15, 1976, pt. 2, p. L125-L128.* 208, pp. L125–L128.

Weisskopf M. C., Elsner R., and O’Dell S. (2010). “On understanding the figures of merit for detection and measurement of x-ray polarization”. In: *Space Telescopes and Instrumentation 2010: Ultraviolet to Gamma Ray*. Vol. 7732. SPIE, pp. 98–102.

Weisskopf M. C., Ramsey B., et al. (2016). “The imaging x-ray polarimetry explorer (IXPE)”. In: *Results in Physics* 6, pp. 1179–1180.

Weisskopf M. C., Soffitta P., et al. (2022). “Imaging X-ray polarimetry explorer: prelaunch”. In: *Journal of Astronomical Telescopes, Instruments, and Systems* 8.2, pp. 026002–026002.

White N., Becker R., et al. (1981). “A 5.57 hour Modulation of the X-ray Flux from 4U 1822-37”. In: *The Astrophysical Journal* 247, pp. 994–1002.

White N., Swank J., and Holt S. (1983). “Accretion powered X-ray pulsars”. In: *Astrophysical Journal, Part 1 (ISSN 0004-637X), vol. 270, July 15, 1983, p. 711-734.* 270, pp. 711–734.

White N. E. and Holt S. (1982). “Accretion disk coronae”. In: *Astrophysical Journal, Part 1, vol. 257, June 1, 1982, p. 318-337.* 257, pp. 318–337.

Wijnands R. et al. (1997). “Discovery of kilohertz quasi-periodic oscillations in gx 17+ 2”. In: *The Astrophysical Journal* 490.2, p. L157.

Wilms J., Allen A., and McCray R. (2000). “On the absorption of X-rays in the interstellar medium”. In: *The Astrophysical Journal* 542.2, p. 914.

Wilson C. A., Finger M. H., and Camero-Arranz A. (2008a). “Outbursts large and small from EXO 2030+ 375”. In: *The Astrophysical Journal* 678.2, p. 1263.

Wilson C. A., Finger M. H., Coe M., Laycock S., and Fabregat J. (2002). “A decade in the life of EXO 2030+ 375: a multiwavelength study of an accreting X-ray pulsar”. In: *The Astrophysical Journal* 570.1, p. 287.

Wilson C. A., Weisskopf M. C., et al. (2005). “Discovery of a Be/X-ray Binary Consistent with the Position of GRO J2058+ 42”. In: *The Astrophysical Journal* 622.2, p. 1024.

Wilson C. A., Finger M. H., and Camero-Arranz A. (May 2008b). “Outbursts Large and Small from EXO 2030+375”. In: *The Astrophysical Journal* 678.2, p. 1263. DOI: 10.1086/587134. URL: https://dx.doi.org/10.1086/587134.

Wilson C. A., Finger M. H., Coe M. J., and Negueruela I. (Feb. 2003). “XTE J1946+274 = GRO J1944+26: An Enigmatic Be/X-Ray Binary”. In: *The Astrophysical Journal* 584.2, pp. 996–1007. DOI: 10.1086/345791. URL: https://doi.org/10.1086%2F345791.

Witte M. and Savonije G. (2001). “Tidal evolution of eccentric orbits in massive binary systems-II. Coupled resonance locking for two rotating main sequence stars”. In: *Astronomy & Astrophysics* 366.3, pp. 840–857.

Woo J. W., Clark G. W., Blondin J. M., Kallman T. R., and Nagase F. (1995). “Wind dynamics in SMC X-1. 2: GINGA and ROSAT observations”. In: *The Astrophysical Journal* 445, pp. 896–908.

Woo J. W., Clark G. W., Levine A. M., Corbet R. H., and Nagase F. (1996). “Orbital Decay, Spin-down, and Pulse-Phase–resolved Spectroscopy of LMC X-4 from GINGA and ROSAT Observations”. In: *The Astrophysical Journal* 467, p. 811.

Xiao G. et al. (2019). “Constant cyclotron line energy in Hercules X–1-Joint Insight-HXMT and NuSTAR observations”. In: *Journal of High Energy Astrophysics* 23, pp. 29–32.

Yamamoto T., Mihara T., et al. (2014). “Firm detection of a cyclotron resonance feature with Suzaku in the X-ray spectrum of GRO J1008- 57 during a giant outburst in 2012”. In: *Publications of the Astronomical Society of Japan* 66.3.

Yamamoto T., Sugizaki M., et al. (2011). “Discovery of a Cyclotron Resonance Feature in the X-ray Spectrum of GX 304- 1 with RXTE and Suzaku during Outbursts Detected by MAXI in 2010”. In: *Publications of the Astronomical Society of Japan* 63.sp3, S751–S757.

Zhang W., Lapidus I., White N., and Titarchuk L. (1996). “Kilohertz Quasi-periodic Intensity Oscillations from 4U 1636–536”. In: *The Astrophysical Journal* 469.1, p. L17.